

**PETROLOGICAL CHARACTERIZATION OF  
TOURMALINE BEARING ROCKS FROM PARTS OF  
SOUTH PURULIA SHEAR ZONE (SPSZ) AND  
SINGHBHUM SHEAR ZONE (SSZ): EVIDENCE OF  
EPISODIC BORON BEARING FLUID FLUX DURING  
REGIONAL METAMORPHISM**



**Thesis submitted to Jadavpur University  
for the degree of  
Doctor of Philosophy (Science)**

**SAYAN BISWAS  
Department of Geological Sciences  
Jadavpur University  
2022**



**CERTIFICATE FROM THE SUPERVISOR(S)**

This is to certify that the thesis entitled “PETROLOGICAL CHARACTERIZATION OF TOURMALINE BEARING ROCKS FROM PARTS OF SOUTH PURULIA SHEAR ZONE (SPSZ) AND SINGHBHUM SHEAR ZONE (SSZ): EVIDENCE OF EPISODIC BORON BEARING FLUID FLUX DURING REGIONAL METAMORPHISM” submitted by **Sri. Sayan Biswas** who got his name registered on **24/06/2013** for the award of **Ph.D. (Science)** degree of Jadavpur University, is absolutely based upon his own work under the supervision of **Professor Pulak Sengupta** and **Professor Sanjoy Sanyal** and that neither this thesis nor any part of it has been submitted for either any degree/ diploma or any other academic award anywhere before.

(Signature of Supervisors)

*Pulak Sengupta 19/7/22*

Prof. PULAK SENGUPTA

Department of Geological Sciences  
Jadavpur University  
Kolkata-700032

**Dr. Pulak Sengupta**  
Professor

Department of Geological Sciences  
Jadavpur University, Kolkata-700032

*Sanjoy Sanyal 19.07.2022*

Prof. SANJOY SANYAL

Department of Geological Sciences

Jadavpur University

Kolkata-700032

**Dr. Sanjoy Sanyal**  
Professor

Department of Geological Sciences  
Jadavpur University  
Kolkata: 700032, India

*Dedicated to.....*  
*My Daughter ISHIKA BISWAS*

## ACKNOWLEDGEMENT

My Ph. D. work was carried out with a full-time doctoral fellowship from the Council of Scientific and Industrial Research (CSIR) under the supervision of **Prof. Pulak Sengupta** and **Prof. Sanjoy Sanyal** from the Department of Geological Sciences, Jadavpur University.

The professors are thanked additionally for providing inspirational guidance to carry out the work. Their stimulating suggestions and encouragement in my professional and personal life have always helped me during all these years of my research tenure to complete my work.

I would like to thank the financial support from the University Grants Commission (UGC) during the tenure of my research work.

I extend my gratitude to all the faculty members, researchers and staff from the Department of Geological Sciences, Jadavpur University for their help and support. I express my utmost gratitude to the staff from the Research Section of Jadavpur University, for their assistance whenever needed.

I take this opportunity to thank **Prof. Subrata Karmakar** and **Prof. Subir Sarkar**, Department of Geological Sciences, Jadavpur University.

I take this opportunity to **Dr. Nandini Sengupta**, **Dr. Nandini Chattopadhyay** and **Dr. Sayan Ray** for their constant encouragement and numerous critical comments during my research work.

I am very much thankful to **Mr. Shyamal Sengupta**, **Mr. Sandip Nandy**, **Mr. Arindam Dutta**, **Mr. Sujit Tripathi** and **Ms. Arya Ghosh**, EPMA Laboratory, Central Petrology Laboratory, Geological Survey of India; **Dr. Debashis Upadhyay** and **Prof. Biswajit Mishra**, IIT Kharagpur; **Dr. Upama Dutta**, ISM Dhanbad; for providing me with the analytical facilities without which this work would have remained incomplete.

I am also grateful for the efforts made by my friends **Dr. Moumita Talukdar**, **Dr. Shreya Karmakar**, **Dr. Tapabrata Sarkar**, **Mr. Saikat Bhakta**, **Mr. Sunandan Basu**, and **Dr. Sambit Ghosh** for their encouragement, moral support and all sorts of help during this work.

I am also grateful to my junior colleagues **Dr. Priyadarshi Chowdhury, Dr. Anindita Dey, Dr. Subham Mukherjee, Dr. Enakshi Das** and **Ms. Maitraiye Chakraborty**, for assisting me in countless ways during the fieldwork, analysis and completion of this work. I am thankful to **Satabdi, Nivedita, Sirina, Arimita** and **Somdipta** for extending their helping hands.

I am also grateful to all my colleagues of Presidency University, Kolkata for their support, whenever needed.

Completion of this thesis would not have been possible without my wife, **Mrs. Trisrota Chaudhuri**. I thank her for all her support and for sticking by my side during all these years through the ups and downs of my life.

Lastly and most importantly, I would like to thank my family, without their help and inspiration the journey would have remained incomplete. My father, **Mr. Kshitischandra Biswas** and mother, **Mrs. Banani Biswas**, always supported and motivated me during this Ph.D. journey. I am also thankful to my younger brother, **Mr. Tuhin Biswas** for his love, unconditional support and continuous encouragement.

SAYAN BISWAS  
Department of Geological Sciences  
Jadavpur University, Kolkata

# CONTENTS

<b>ABSTRACT</b> .....	(i-ii)
<b>CHAPTER 1 : Introduction</b> .....	(1-26)
1.1 Background geology.....	2
1.2 Tourmaline as a petrogenetic indicator mineral.....	14
1.3 Tourmaline mineral chemistry.....	15
1.4 Occurrences of tourmaline bearing rocks across India.....	21
1.5 Present study area.....	23
1.6 Objective of the thesis.....	26
<b>CHAPTER 2: Tourmaline bearing rocks in and around Haripaldih</b> .....	(27-58)
2.1 Lithology and structure of the area.....	27
2.2 Field features of tourmaline bearing rocks.....	34
2.3 Petrographic description of tourmaline bearing rocks.....	36
2.4 Tourmaline mineral chemistry.....	39
2.5 Trace and REE concentrations of tourmaline.....	55
2.6 Summary.....	58
<b>CHAPTER 3: Tourmaline bearing rocks in and around Beldih</b> .....	(59-89)
3.1 Lithology and structure of the area.....	59
3.2 Field features of tourmaline bearing rocks.....	66
3.3 Petrographic description of tourmaline bearing rocks.....	69
3.4 Tourmaline mineral chemistry.....	73
3.5 Trace and REE concentrations of tourmaline.....	84
3.6 Summary.....	89
<b>CHAPTER 4: Tourmaline bearing rocks in and around Kutni</b> .....	(90-111)
4.1 Lithology and structure of the area.....	90
4.2 Field features of tourmaline bearing rocks.....	96
4.3 Petrographic description of tourmaline bearing rocks.....	98
4.4 Tourmaline mineral chemistry.....	101
4.5 Trace and REE concentrations of tourmaline.....	107

4.6 Summary.....	111
<b>CHAPTER 5: Tourmaline bearing rocks in and around Mukutmanipur.....</b>	<b>(112-152)</b>
5.1 Lithology and structure of the area.....	112
5.2 Field features of tourmaline bearing rocks.....	120
5.3 Petrographic description of tourmaline bearing rocks.....	124
5.4 Tourmaline mineral chemistry.....	128
5.5 Trace and REE concentrations of tourmaline.....	146
5.6 Summary.....	151
<b>CHAPTER 6: Tourmaline bearing rocks in and around Ujainpur .....</b>	<b>(153-189)</b>
6.1 Lithology and structure of the area.....	153
6.2 Field features of tourmaline bearing rocks.....	157
6.3 Petrographic description of tourmaline bearing rocks.....	160
6.4 Tourmaline mineral chemistry.....	166
6.5 Trace and REE concentrations of tourmaline.....	179
6.6 Summary.....	188
<b>CHAPTER 7: Discussion.....</b>	<b>(190-205)</b>
7.1 Summary of the tourmaline occurrences and the metasomatic reactions.....	190
7.2 REE characteristics of the tourmalines of the studied rocks.....	197
7.3 Significance of the trace element concentrations in the studied tourmaline bearing rocks.....	200
7.4 Timing of tourmaline mineralization.....	201
<b>References.....</b>	<b>(206-236)</b>
<b>Appendix I: Analytical procedures.....</b>	<b>(237-238)</b>
<b>Appendix II: Normalization of tourmaline and associated minerals.....</b>	<b>239</b>
<b>Appendix III: C space programme.....</b>	<b>(240-241)</b>
<b>Appendix IV: List of abbreviations used.....</b>	<b>242</b>

## ABSTRACT

*Tourmaline is an important borosilicate mineral, which has a complex chemical formula, high chemical resistance and a wide P-T stability field. Chemical composition of tourmaline is sensitive to ambient physicochemical conditions of its growth and thus provides valuable information about fluid-rock interaction in associated magmatic or hydrothermal systems, nature and evolution of its host rock.*

*The Eastern Indian Shield comprises of Paleo to Meso-Archean Singhbhum Craton towards the south and Meso-Proterozoic Chotanagpur Granite Gneissic Complex (CGGC) in the north. A multiphase-deformed and poly-metamorphosed volcano sedimentary succession of Palaeo- to Meso Proterozoic age known as the North Singhbhum Mobile Belt (NSMB) is juxtaposed between these two cratonic blocks. The NSMB is bound by two shear zones, viz. the South Purulia Shear Zone (SPSZ) in the north and the Singhbhum Shear Zone (SSZ) in the south. Both SPSZ and SSZ are characterized by regional shearing, hydrothermal activity and are known for hosting important polymetallic deposits. Intense infiltration driven metamorphism yielded several exotic rocks in SPSZ and SSZ including tourmaline mineralization. The SPSZ consists of schists (retrograded rocks of CGGC) and phyllites (Chandil formation of NSMB) that are highly deformed and hydrothermally altered. The SSZ is represented by an assemblage of polyphase-deformed, volcano-sedimentary assemblage of NSMB rocks. Notable tourmaline mineralization occurs within the schists, phyllite and pegmatites of SPSZ and kyanite-quartzite rocks of SSZ.*

*In the present study, a comprehensive field, petrographic, mineralogical and geochemical study of tourmaline-bearing rocks occurring at selected locations of SPSZ and SSZ is attempted. Within SPSZ, tourmaline mineralization occurs within pegmatite veins at Haripaldih area, muscovite/quartz-muscovite schist at Beldih area, mica-chlorite schist at Mukutmanipur area and phyllitic rocks at Kutni area. From field, textural and mineral compositions, two stages of tourmaline mineralization are identified in the SPSZ. The first stage of tourmaline mineralization (Gen-I) occurs within banded or laminated-quartz tourmaline rock within schistose rock and phyllite, where the tourmaline grains are oriented parallel to the  $S_1$  regional fabric. The second generation (Gen-II) of tourmaline is characterized by coarse, haphazardly oriented grains without any prior deformational features within the schistose rock and quartz vein. Therefore, it is inferred that the Gen-I tourmaline is syn-tectonic with respect to the regional deformation ( $D_1$ ) and Gen-II tourmaline postdates the latest deformation event in the area, i.e.  $D_3/F_3$ . However, another set of tourmaline mineralization is found within the pegmatite vein in Haripaldih area. These pegmatite veins are co deformed with the regional foliation i.e.,  $S_1$  fabric and tourmaline mineralization occurred as post tectonic with respect to  $S_1/D_1$  but prior or syn-tectonic with respect to  $D_2$ . The Gen-I tourmalines in Beldih and Mukutmanipur region belong to alkali group and majorly of schorl ( $X_{Mg}=0.43-0.57$ ) composition. Gen-I tourmalines from Kutni area belong to alkali to X-vacancy group and are foitite to Mg-foitite ( $X_{Mg}=0.46-0.58$ ) in composition. The*

variation of tourmaline composition of same generation (Gen-I) is attributed to difference in host rock lithology. Gen-II tourmaline grains are dravite ( $X_{Mg}=0.55-0.69$ ) in nature. Tourmalines in pegmatite in Haripaldih region belong to alkali group and their composition straddles boundary between schorl and dravite ( $X_{Mg}=0.40-0.52$ ). Major element composition suggests a low to moderate saline hydrothermal fluid was responsible for tourmaline mineralization across the SPSZ.

Around Ujainpur area of the SSZ, three generations of tourmaline mineralization were identified within the kyanite-quartzite. Gen-I tourmaline grains occur along the  $S_1$  fabric that cut across and replaced by medium to coarse grained tourmaline aggregates. The latter are assigned to Gen-II which also preferentially grows along the  $S_2$  shear foliation corresponding to the regional shear deformation ( $D_2$ ) in SSZ. Gen-II tourmalines are associated without (Gen-IIA) or with (Gen-IIB) dumortierite. Another set of tourmaline (Gen-III) vein cut across the  $S_2$  that are randomly oriented (post shearing or  $S_2$ ). Gen-I tourmalines belong alkali to X-vacancy group and dravite to Mg-foitite ( $X_{Mg}=0.72-0.90$ ) in composition. Gen IIA tourmalines belong to alkali group and dravite ( $X_{Mg}=0.62-0.71$ ) in composition. Both Gen IIB ( $X_{Mg}=0.48-0.61$ ) and Gen-III ( $X_{Mg}=0.35-0.45$ ) tourmalines belong to X-vacancy group and foitite to Mg-foitite in composition. Chemical composition of Ujainpur tourmalines, it is inferred a high to moderate saline hydrothermal fluid may have been responsible for tourmaline mineralization in SSZ.

Tourmaline from the kyanite-quartzite rocks of SSZ exhibit distinctly higher REE concentrations (up to 1029 ppm) compared to those of the SPSZ (up to 15ppm). The SPSZ tourmalines exhibit distinct LREE enrichment, prominent positive Eu anomaly and flat to marginally convex upward HREE with respect to chondrite. The tourmaline within kyanite-quartzite of SSZ exhibits overall flat LREE and HREE chondrite normalized patterns along with weak negative to positive Eu anomalies. Tourmaline with higher concentration of Ca in its structure can accommodate LREE than HREE. Tourmalines along SPSZ has a significant amount of Ca (0.10 to 0.35 apfu) and thus are enriched in LREE due to Ca-LREE substitution. Contrastingly, low Ca (0.02-0.07apfu) SSZ tourmalines explain absence of LREE-enrichment and no significant LREE/HREE fractionation. Tourmaline from both SPSZ and SSZ shows prominent depletion in LILE such as Rb and Ba. Notably. These tourmalines have near-crustal concentrations of Sr, Ni, Co, Zn, V and Sc. Tourmalines of SPSZ have lower concentrations of Li and Y compared to the SSZ tourmalines. These features indicate that a metamorphogenic fluid may have taken significant role in tourmaline mineralization in SPSZ. However, in SSZ, the fluid responsible for tourmaline mineralization was possibly a combination of external, granite derived fluid and internal, metamorphogenic fluid. Based on the existing geochronological database and the relation between tourmaline texture and deformation fabrics, the present study suggests that tourmaline mineralization in SPSZ is younger than ~0.93 Ga whereas tourmaline mineralization in SSZ hosted by kyanite-quartzite is definitely older than 1.0 Ga.

# CHAPTER 1

## Introduction

Fluid–rock interaction plays a crucial role in modifying the bulk composition of rocks exposed along shear zones through metasomatism due to enhanced permeability and concomitant fluid flow along crustal level conduits in different orogenic belts. Fluids in shear zones are not always in equilibrium with the wall rocks but to achieve equilibrium, infiltrating fluids due to shearing exchange mass and energy with the wall rocks. Through this process of fluid-rock interaction with the wall rock it can form exotic mineral assemblages including boron-bearing minerals and Cu-Fe-U-Au-REE ores. Therefore, the minerals present in and around as network of veins or patches within sheared country rock could provide valuable information about pressure-temperature and fluid evolution of orogenic belts. Tourmaline, the chief sink in boron, is one of those minerals which are formed due to fluid rock interaction in shear zone. It is a chemically resistant mineral that has a wide P-T stability field and a complex chemical formula that monitors the fluid composition and reflects the chemical environment in which it is generated (Henry and Dutrow, 1996). Tourmaline is commonly associated with and co-precipitated during the formation of numerous types of mineral deposits, including copper, silver-gold, tin (-tungsten), massive sulfide, and uranium deposits, other metasomatic bodies (Slack et al., 1984; Pirajno and Smithies, 1992; Slack, 1996; Xavier et al., 2008). Therefore, the study of tourmaline may give important information about the source, chemical composition of the associated fluids and the evolution of the associated rocks. A number of crustal scale shear zones are recognized in this East India shield area. East Indian Shield is mainly comprised Meso-Archean (ca. 3.4 – 3.0 Ga, Sharma et al., 1994) cratonic batholith of ‘Singhbhum Granite’ towards the south and the Meso-Neo Proterozoic Chotanagpur Granite Gneissic Complex (CGGC) in the north. The Palaeo- to Meso- Proterozoic poly-deformed (ca. 1.8 to 1.5 Ga) and poly-metamorphosed volcano-sedimentary pile (reviewed by Sengupta et al., 2000; Vapnik et al., 2007) known as the North Singhbhum Mobile Belt (NSMB) is sandwiched between the above two cratonic blocks (Mukhopadhyay, 1990; Saha, 1994; Gupta and Basu,

2000; Sarkar, 2000). The northern margin of the Singhbhum craton with North Singhbhum Mobile Belt is marked by a prominent ductile shear zone, known as Copper Belt Thrust (Dunn and Dey, 1942) or Singhbhum Shear Zone (SSZ) (Sarkar and Saha, 1962). The contact between North Singhbhum Mobile Belt in the south and Chhotanagpur Gneissic Complex in the north is also marked by a prominent brittle–ductile shear zone (Dunn and Dey, 1942; Bhattacharya, 1989) referred as South Purulia Shear Zone (SPSZ). Both SPSZ and SSZ is characterized by intense shearing, hydrothermal activity and localization of polymetallic deposits (Sarkar, 1984; Sarkar, 2000; Gupta and Basu, 2000; Sengupta, et al., 2005; Acharyya, et al., 2006; Vapnik, et al., 2007; Pal, et al., 2009; Sengupta, et al., 2011). Infiltration-driven metamorphism in the SPSZ and SSZ produced a number of exotic rocks including tourmaline mineralization. The main objective of the study is to investigate the field feature, petrography, geochemistry, origin and evolution of tourmaline-bearing rocks in parts of both SPSZ and SSZ. A further aim is to investigate the chemical variations among different generations of tourmaline for a better understanding of the evolution of boron-rich fluids that were responsible for tourmaline mineralization.

## **1.1 Background geology**

Singhbhum and the adjoining areas of East Indian shield are the most intensely studied parts of the Indian Precambrian. Dunn (1929), Jones (1934) and Dunn and Dey (1942) first carried out most authentic and systematic geological study of the singhbhum region. These pioneering works document a detailed account of the geology, stratigraphy, structure and economic minerals of the belt.

The main litho-stratigraphical domains in the East Indian Shield are (Fig 1.1a and Fig 1.1c):

- The Archaean Cratonic block represented by Singhbhum Granite batholith (SBG) with enclaves of Older Metamorphic Group (OMG) and Older Metamorphic Tonalite Gneiss (OMTG)
- Iron Ore Belts mainly comprise with the volcano-sedimentary sequence with BIF known as Iron Ore Group (IOG). They occur along the eastern, western and southern peripheries of the cratonic nucleus (Badampahar-Gorumahisani belt, Jamda-Koira-Noamundi belt and Tomka–Daitari belt).

- The North Singhbhum Mobile belt (NSMB) ( Chaibasa and Dhalbhum Formations, Dhanjori formations, Dalma formations, Chandil formation and their equivalents)
- The Chhotanagpur Granite Gneiss Complex with metasedimentary, Mafic ultramafic enclaves and granulite slivers.

The main lithostratigraphic units occurring south of the Chhotanagpur Gneissic Complex, as recognized by Dunn and Dey (1942) are Older Metamorphic Series, Iron Ore Series, Singhbhum Granite, Dhanjori and Dalma lavas, Soda Granite and basic and ultrabasic intrusives. Based on mutual field relationships and the tectono-metamorphic status of the different rock units, stratigraphic succession is given in Fig 1.1a (Mazumder 2005).

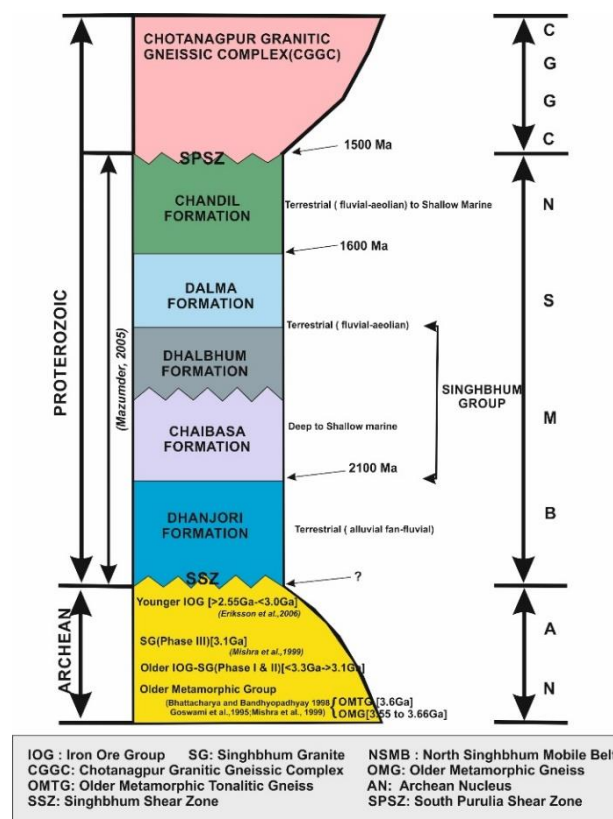


Fig1.1a: Stratigraphic succession of the East Indian Shield (reproduced from Mazumder 2005)

## Singhbhum Craton

The Singhbhum archean cratonic nucleus is an ovoid shaped body that exposes a vast tract of Precambrian rocks occupying an area of approximately 50,000 km<sup>2</sup>. Isotopic data from rocks of the Singhbhum craton indicate an age range from 3500 to 900 Ma (Mazumder et al., 2012). “Archean Nucleus” comprising meso- to neoproterozoic granitoid rocks, the meso- to neoproterozoic Iron Ore Group and other supracrustals (Mukhopadhyay, 2001 and Mazumder et al., 2012) (Fig 1.1c). Granitoid rocks in this region are called Singhbhum

granite (SBG A and SBG B) having innumerable large and small enclaves of older metamorphics (OMG) and trondjemite grading into tonalities (OMTG) which are comparable to the components of typical Archean greenstones. OMG, the older supracrustal comprises metamorphosed (amphibolite facies) pelitic, arenaceous, occasionally calcareous sediments and mafic-ultramafic rocks. The OMG rocks are intruded by OMTG which compositionally varies from biotite/hornblende-rich tonalite through trondhjemite to granodiorite and shows structural similarity with the OMG rocks (Sarkar and Saha, 1977; Sarkar and Saha, 1983; Saha, 1994). Detrital zircon of OMG yield age ( $^{207}\text{Pb}/^{206}\text{Pb}$  ion probe) 3.55, 3.4 and 3.2 Ga respectively (Goswami et al., 1995; Mishra et al., 1999). Sharma et al., 1994 reported OMG yield age of  $3305 \pm 60$  Ma (whole-rock Sm–Nd). Ghosh et al., 1996 reported the oldest age of OMTG which is 3.66 (Pb–Pb whole rock isochron). Mishra et al., 1999 noted  $^{207}\text{Pb}/^{206}\text{Pb}$  ages of zircons from the OMTG cluster around  $\sim 3.4$  Ga and  $\sim 3.2$  Ga. Acharyya et al., 2010 reported  $3448 \pm 19$  Ma and  $3527 \pm 17$  Ma U–Pb zircon ages from the OMTG and interpreted as  $\sim 3.4$  Ga age at the time of formation of the OMTG and 3.2 Ga as a metamorphic event that affected both the Older Metamorphic Group and Older Metamorphic Tonalite Gneiss (Acharyya et al., 2010). Hadean zircon xenocrysts have been reported in Singhbhum Craton by various authors. 4.03 to 4.24 Ga old xenocrysts were recorded from  $\sim 3.4$  Ga old TTGs of the OMTG suite by Chaudhuri et al., 2018. Other occurrences include zircon xenocrysts of 4.02 Ga age from modern sediment of Baitarani river (Miller et al., 2018) and 4.03 Ga age from  $\sim 3$  Ga old metasediment of simlipal volcano-sedimentary basin (Bhattacharjee et al., 2021). The SBG is a poly-component unit that belongs to three successive but closely related phases of emplacement and compositionally it varies from tonalite to granodiorite to granite (Saha, 1972; Saha et al., 1988). Phase I granites are relatively K-poor and granodiorite and trondhjemite in composition whereas Phase II and III granites are biotite granodiorite grading to adamellitic granites. Phase-I and Phase-II are known as SBG-A and Phase-III as SBG-B. Rafts and inclusions of OMG and OMTG are common within the SBG, which suggests OMG and OMTG are older than the SBG (Saha and Ray, 1984). Naqvi and Rogers, 1987, suggested the emplacement of SBG in multiple phases. It was later confirmed that SBG intruded in pulses over a period of 3.37–3.29 Ga (Mishra et al., 1999; Tait et al., 2011; Nelson et al., 2014; Upadhyay et al., 2014; Dey et al., 2017). The central part of the Singhbhum Craton is encircled by supracrustal rocks of the Paleoproterozoic Iron Ore Group (IOG). IOG comprises BIF with associated basic volcanic rocks and volcanogenic sediments. IOG is typical greenstone rocks with a thick pile of low-grade metamorphosed sediments, volcanics and mafic-ultramafic plutons. These IOG rocks are exposed in three belts i.e.,

Gorumahisani-Badampahar belt to the east, Tomka-Daitari belt to the south, and the Jamda-Koira belt to the west (Acharyya, 1993; Saha, 1994; Mukhopadhyay et al., 2001; Chakraborty and Majumder, 2002; Ghosh and Mukhopadhyay, 2007; Mukhopadhyay et al., 2012). The stratigraphic position of IOG is debatable. According to some workers IOG is intruded by SBG (Dunn and Dey, 1942; Sarkar and Saha, 1977; Saha, 1984), while others consider SBG as the basement of IOG (Mukhopadhyay; 1976; Banerji, 1977; Iyenger and Murty, 1982; Banerjee, 1982; Dasgupta et al., 1999).

### **North Singhbhum Mobile Belt (NSMB)**

The NSMB is a prominent Proterozoic mobile belt, that occurs between CGGC in the north and Singhbhum Craton in the south (Sarkar and Saha, 1962; Bose and Chakraborti, 1981; Gupta et al., 1980; Mukhopadhyay, 1988; Saha, 1994). The belt is about 50 km wide and 200 km long and with an average E-W trend (Fig 1.1c). It comprises a thick volcano-sedimentary sequence of pelites, psammopelites, mafic-ultramafic and acid lavas. The North Singhbhum Mobile Belt (NSMB) is delineated in its southern periphery by the famous Singhbhum Shear Zone (SSZ) characterized by intense ductile shearing and thrusting. North Singhbhum Fold Belt comprises the Dhanjori, Chaibasa, Dhalbhum, Dalma and Chandil Formations (Gupta and Basu, 1991; Gupta and Basu, 2000; Acharyya, 2003)

Sarkar et al., 1992 and Gupta and Basu, 2000, divided the NSMB into five broad lithostratigraphic domains:

**Domain I:** This domain comprises the earliest Proterozoic cover sediments of NSMB. This domain is fringing to the south and bounded by Singhbhum Shear Zone (SSZ). It comprises low-grade metamorphosed volcano-sedimentary formations including intracratonic sub-basins of Dhanjori and Ongarbira in the eastern and western parts of NSMB. The Simlipal volcanics in the east are considered to be the time equivalent of the Dhanjori volcanics.

**Domain II:** The rocks of the SSZ which is originally named Copper Thrust. It is an arcuate belt of high strain characterized by multiphase of deformation, intense ductile shearing, sodic magmatism, multiple metasomatic features and polymetallic mineralization.

**Domain III:** This domain occurred between SSZ and Dalma volcanics. The belt comprises the schistose medium-grade metamorphic (upper greenschist amphibolite facies) rock of Chaibasa and Dhalbhum formations. The metasedimentary packages of Chaibasa and

Dhalbhum formation are together considered as Singhbhum Group of rocks. Chaibasa formations rocks are commonly muscovite-quartz schists with biotite, chloritoid, garnet, kyanite and sillimanite which occur progressively in space and time and show Barrovian type metamorphism (Naha, 1965; Roy, 1966). An important rock type in this domain is kyanite-quartzite which occurs towards the southern parts. Within kyanite-quartzite schists, tourmaline occurs as alternating bands as local pockets. The Dhalbhum formation rocks are mainly phyllites that contain large porphyroblasts of andalusite and staurolite. These formations gradually merge northward into an overlying sequence of low-grade rocks comprising magnetite pelite, chlorite schist, carbon phyllite and orthoquartzite, forming a belt south of the Dalma (Mazumder, 2005).

**Domain IV:** This domain is the Dalma volcano-sedimentary belt. It comprises of low-grade metamorphosed predominantly basic and ultrabasic volcanic covering the Dalma Range and its extensions to the east and west. It is an arcuate ridge occurring almost along the middle of the North Singhbhum mobile belt.

**Domain V:** This low to medium grade metamorphosed volcano-sedimentary succession is known as the Chandil Formation (Ray et al., 1996; Mazumder, 2005) which lies in between the Dalma Range in the south and the CGGC in the north. The Chandil Formation includes metapelites, intercalated with lenses of quartzites, carbonaceous slate/phyllite, weakly metamorphosed felsic volcanic and volcanoclastic rocks (including vitric and lithic tuffs) and amphibolites (Bhattacharya, 1992; Bose, 1994; Ray et al., 1996; Singh, 1997; Singh, 1998; Sengupta et al., 2000, Mazumder, 2005). The litho-units of the Chandil Formation are markedly different from the underlying Dalma and Dhalbhum Formations (Domain III).

North Singhbhum Fold Belt was likely deposited in an intracontinental rift basin in a rapidly changing tectonic environment (Mazumder and Sarkar, 2004; Mazumder, 2005). The Dhanjori Group is represented by vesicular basalts (locally pillowed), and komatiite with intercalated arkose, feldspathic arenite-litharenite/lithic wacke, and pelitic metasediments (Mazumder and Sarkar, 2004) which are inferred to have been deposited mostly in alluvial to fluvial and partly in lacustrine (Mazumder and Sarkar, 2004). The Singhbhum Group is inferred to have been deposited in shallow to the deep marine environment (Chaibasa formation) with a later transition to mostly terrestrial (fluvial-aeolian) or shallow marine environment (Dhalbhum formation). The Dhanjori formation is conformably overlain by Chaibasa formation of the Singhbhum Group (Mazumder, 2005; De et al., 2015 and De et al.,

2016). According to Mazumder and Van Loon, 2012, Dalma volcanism took place under terrestrial conditions (largely subaerially). The Chandil felsic volcanism took place in a terrestrial (fluvial-aeolian) setting (Chatterjee et al., 2013), whereas fine-grained sandstones occurred at top of the Chandil succession are of shallow marine origin (Chatterjee et al., 2013). These rhyolites and associated felsic tuffs are ~1600 Ma old (Nelson et al., 2007; Reddy et al., 2009). The Singhbhum brittle-ductile shear zone (SSZ), cuts across rocks of the Iron ore Group, Dhanjori Group and the Singhbhum Group (Mazumder, 2005). Regionally three phases of deformation and two episodes of metamorphism (greenschist to amphibolite facies) are imprinted in the NSMB rocks (Ghosh and Sengupta 1987; Mukhopadhyay and Deb 1995; Bandyopadhyay 2003).

Generalized lithological and chronological events in the North Singhbhum Fold Belt (NSFB) and Singhbhum Shear Zone (SSZ) are given in the following Table 1.1b:

Table 1.1b: Generalized lithological and chronological events in the North Singhbhum Fold Belt (NSFB) and Singhbhum Shear Zone(SSZ).

Unit	Lithology	Metamorphism	Age
Chandil formation	Rhyolite, tuff, agglomerates, shale, C-shale	Low greenschist (Phyllite)	Thermal event: ~1.5 Ga <sup>8</sup> Rhyolite emplacement: ~1.63 Ga <sup>7,9</sup>
Dalma formation	Basic lava and volcano-clastic sediments of continental affinity	Green schist	Metamorphism (?): 1.6 Ga <sup>6</sup>
Dhalbhum formation	Sandstone, siltstone, orthoquartzite, shale, tuff of continental affinity	Green schist	Maximum depositional age: ≤1.76 Ga <sup>9</sup>
SSZ mélangé	Chlorite quartz schist, talc/actinolite schist, magnetite-apatite rock, Cu-U ores, tourmalinite, kyanite-bearing quartzite, chloritoid schist, etc.	Green schist to amphibolite	Shearing and hydrothermal alteration: 1.66–1.60 Ga <sup>5</sup> , ~1.0 Ga <sup>5</sup> , 0.97 Ga <sup>9</sup> Protolith formation: ~1.9 – 1.8 Ga <sup>5</sup>
Soda granite (only in SSZ)	Granitoids	Green schist to amphibolite hydrothermally altered	Hydrothermal alteration: ~1.66–1.60 Ga <sup>5</sup> Emplacement: ~2.2 Ga <sup>4</sup>
Chaibasa formation	Shale, sandstone, and orthoquartzite with minor basic to ultrabasic rocks Marine affinity	Greenschist to amphibolite	Metamorphism: ~1.6–1.3 Ga <sup>3</sup>
Dhanjori formation	Basic and dacitic lavas, quartzite minor shale, and basal conglomerate of continental affinity		Lava flow: ~2.1 Ga <sup>2</sup>
Archaean basement	Unconformity – metasedimentary rocks, tonalite, trondjhemite and granitoid intrusions		~2.8–>3.5 Ga <sup>1</sup>

Notes: <sup>1</sup>Reviewed in Mazumder et al., (2012); <sup>2</sup>Roy et al., (2002a); <sup>3</sup>Mahato et al., (2008); <sup>4</sup>Sarkar et al., (1986); <sup>5</sup>Pal and Rhede, (2013); <sup>6</sup>Rao and Rao, (1983); <sup>7</sup>Roy et al., (2002b); <sup>8</sup>Reddy et al., (2009); <sup>9</sup>Sengupta et al., (2000); <sup>9</sup>Olierook, et al.,(2019)

## **Singhbhum Shear Zone (SSZ)**

The E–W (in the west) to NNW–SSE (in the east) trending, arc shaped, ~ 200-km-long and 1-5 km wide intensely polydeformed Singhbhum Shear Zone (SSZ) occurs in between Singhbhum craton in the south and NSMB in the north (Fig 1.1c, reviewed in Dunn and Dey, 1942; Mahato et al. 2008; Pal et al. 2010; Sengupta et al. 2011; Sarkar and Gupta 2012). The detailed geology of the Archaean Singhbhum nucleus and the fringing NSFB is discussed earlier. The Singhbhum brittle-ductile shear zone (SSZ), cuts across the rocks of the Iron Ore Group, Dhanjori Group and Singhbhum Group. Along this Singhbhum Shear Zone (SSZ), extensive occurrences of mylonites and phyllonites which is developed close to the contact between the fold belt and the Archaean nucleus (Sarkar and Saha, 1977). The typical rocks in the SSZ are kyanite-quartzite, apatite-magnetite rock, kyanite-mica schist, quartz-chlorite schist, amphibole-chlorite schist, quartz-sericite schist, talc schist, biotite-muscovite schist, conglomerate, tourmalinite, soda granite/feldspathic schist and mylonitized granite which are highly deformed and sheared (Sarkar, 1984; Saha, 1994; Mukhopadhyay and Deb, 1995). The asymmetrical folds and other shear-sense criteria, like mica fish, asymmetric tails of pressure shadows, and shear bands, indicate thrust-type movement (top to the south) (Ghosh and Sengupta, 1987; Mukhopadhyay and Deb, 1995). Superposed deformations, along with several phases of ductile shearing, led to the development of conspicuous down dip mineral lineation. Intense ductile shear deformation in the SSZ provided conduits for different generations of hydrothermal fluids which metasomatized the pre-existing rocks and formed economic deposits of phosphate, Cu-Fe sulfides and U-ores that are associated with tourmalinization, muscovitization, and ferruginization (Sengupta et al., 2005; Sengupta et al., 2011; Sengupta et al., 2012; Sarkar and Gupta, 2012). In SSZ there is evidence of K, Na, and B-metasomatism (Dunn and Dey, 1942; Banerji and Talapatra, 1966; Talapatra, 1968; Ghosh, 1972; Banerjee, 1982; Sarkar, 1984; Bhattacharya et al., 1992; Sengupta et al., 2005; Pal et al., 2009; Sengupta et al., 2011) which formed different types of rocks like feldspathic schist /soda granite, biotite schist, chlorite schist and tourmalinite. But the source of the hydrothermal fluids is still debatable. There are many theories which include metamorphic fluid, magmatic fluid, evaporite-derived/ basinal brine and seawater (Dunn and Dey, 1942; Sarkar, 1984; Changkakoti et al., 1987; Mishra and Singh, 2003; Mishra et al., 2003; Pal et al., 2010; Patel et al., 2021).

There are three phases of deformation. Primary compositional banding ( $S_0$ ) is rarely observed within the SSZ due to several phases of intense shearing. In places, relict reclined

isoclinal folds which defined by an earlier schistosity ( $S_1$ ) is observed (Ghosh and Sengupta, 1987; Mukhopadhyay and Deb, 1995). This  $S_1$  plane were formed by the first phase of deformation ( $D_1$ ). The dominant planar structure of the SSZ and NSMB is a pervasive regional schistosity ( $S_2$ ) mainly defined by phyllosilicates mineral of E-W to ESE-WNW strikes which are formed due to  $D_2$  deformation. The evidence of shearing diminishes northward i.e outside of the SSZ, but the deformational history is similar. The mylonitic foliation which is developed in SSZ is parallel to the regional schistosity ( $S_2$ ). Therefore, the main phase of shearing is coeval with the second phase of deformation ( $D_2$ ) (Ghosh and Sengupta, 1987; Ghosh and Sengupta, 1990; Mukhopadhyay and Deb, 1995). The regional schistosity ( $S_2$ ) was deformed and showed a gentle upright fold during the third phase of deformation ( $D_3$ ) (Ghosh and Sengupta, 1987; Mukhopadhyay and Deb, 1995). The shear zone rocks underwent two different events ( $M_1$  and  $M_2$ ) of metamorphism (Sarkar 1984; Sengupta et al., 2005). The  $M_1$  event is distinguished by the development of porphyroblast such as chloritoid, garnet, and staurolite in pelitic schists, kyanite in kyanite-quartzite and kyanite-mica schist, and amphibole in mafic schists. The phyllosilicates in the schistose rock which define the  $S_2$  are developed during  $M_1$  metamorphism. The porphyroblasts grow over the  $S_2$  plane which indicates that  $M_1$  metamorphism outlasted the main phase of shearing.  $M_2$  event is distinguished by retrogression and hydration of phases. There are no significant differences between the P-T conditions of,  $M_1$  and  $M_2$  events (Bandyopadhyay, 2003). According to Sengupta et al., 2005, the first phase of metamorphism ( $M_1$ ) took place 1.5–1.7 Ga at  $480 \pm 40$  °C and  $6.4 \pm 0.4$  kbar. However, Mishra and Singh, 2003, reported from the fluid inclusions study near Jaduguda mine area that the ore mineralization that occurred along SSZ was at distinctly lower temperatures (300–450 °C). Rao and Rao, 1983, obtained a 1.6 Ga U-Pb age of uraninite and inferred that this is the age of the main phase of shearing in the SSZ. Moreover, according to Pal and Rhede, 2013, the protolith of the uranium ores was formed during the time span of 1.9–1.8 Ga (U-Th-Pb chemical ages of uraninite). This protolith of uranium ores was sheared and changed its composition at ~ 1.66 Ga (dominant) and ~ 1.0 Ga (minor impression) due to infiltration of hydrothermal fluids.

### **Chotonagpur Granitic Gneissic Complex (CGGC)**

The granite and granite gneiss with patches of high grade supracrustals commonly known as Chhotanagpur Granitic Gneissic Complex (CGGC), lying to the north of the NSMB, occupies a vast area (Mukhopadhyay, 1984) (Fig1.1c). The Proterozoic CGGC is an

east–west-trending subarcuate belt of the East Indian Shield that covers approximately 10000 km<sup>2</sup> (reviewed in Mahadevan, 1992; Acharyya, 2003; Sharma, 2009). The southern margin of the CGGC is marked by an E-W to ENE–WSW-trending crustal-scale brittle–ductile shear zone, which is variously named as the Tamar–Porapahar–Khatra Fault Zone (TPKF: Mahadevan, 2002) or the Northern Shear Zone (NSZ: Kumar et al., 1978) or the South Purulia Shear Zone (SPSZ: Mazumdar, 1988). The CGGC is covered in the north by the Gangetic alluvium, and in the east by the Mesozoic Rajmahal trap basalt. In the west the CGGC is covered by Gondwana deposits of the Son-Mahanadi Valley, and supracrustal rocks and granitoids of the Palaeoproterozoic Mahakoshal Group of the Central Indian Tectonic Zone (CITZ). CGGC represents granulite-gneiss terrain largely composed of granitic rocks with numerous enclaves of meta-pelites of varying composition. It also includes calc silicates, marble, quartzites, amphibolites, gabbro-norites, alkaline rocks, ultramafics, anorthosites, charnockites, pyroxene granulites and skarn rocks. The granitic rocks vary in composition from granite through grannodiorite to tonalite. The gneissic rocks vary widely from fine to coarse grained to porphyritic types and have a diverse chemical composition (Ghose, 1983; Ghose et al., 1990; Singh and De, 1990). A large part of the CGGC is occupied by different variants of migmatites (Mazumder, 1988) depending on the nature of parent rocks. Generally, rocks of CGGC show high-grade amphibolite facies to granulite facies Metamorphism (Bhattacharya, 1976; Bhattacharya, 1982; Ghose, 1983). The metamorphic grade decreases from north to south in the CGGC (Banerji., 1991). Typical granulite facies rocks like khondalite, leptynite and charnockite along with porphyritic and augen type granites are found in the northern part of the CGGC (Sen, 1947; Sen and Manna, 1976). A massif type anorthosite occurs within the granulite facies rocks near Bankura in the eastern part of the CGGC, well known as “Bengal Anorthosite” (Chatterjee, 1936; Roy, 1977). The stratigraphic position of the CGGC is not yet clear due to the lack of radiometric age data. The existing age data suggest geological evolution of CGGC is spanning from 1700 to 800 Ma. However, the latest geochronological and petrological published data indicates that there are three major phases of deformation-metamorphism experienced by the CGGC. The first two deformations are the most intense and penetrative and are also coaxial. (Ghosh and Sengupta, 1999; Maji et al., 2008; Chatterjee et al., 2010; Sanyal and Sengupta, 2012; Mukherjee et al., 2017). The oldest metamorphic event recorded by metapelitic enclaves within the granitoids (ultra-high temperature metamorphism at moderate pressure) (Sanyal and Sengupta, 2012), yield an age of ~1650 Ma (Dey et al., 2017). The intrusion of the porphyritic granite in the western and northern part of CGGC gave age between 1750-1660 Ma (Chatterjee and Ghose,

2011; Saikia et al., 2017). Emplacement age of the massif anorthosite in the south-eastern part of CGGC yields an age of  $1550\pm 12$  (U-Pb zircon data). Ray Barman and Bishui, 1994, reported age of intrusion of the syenitic body in the eastern part of the terrane near Dumka is  $1457\pm 63$  Ma (Rb- Sr isochron). Much younger intrusion of mafic dykes and followed by an amphibolite grade metamorphic event found in CGGC with an age of 870-780 Ma (Chatterjee et al., 2010; Sanyal and Sengupta, 2012).

### **South Purulia Shear Zone (SPSZ)**

The ~ E W to ESE–WNW trending SPSZ (Fig 1.1c), also known as Tamar-Porapahar lineament of the east Indian shield occurs at the interface between two crustal blocks with contrasting geological and geochronological characteristics (reviewed in Mahadevan 1992; Acharyya et al. 2006; Mahato et al. 2008; Sanyal and Sengupta 2012). The southern block, referred to as the North Singhbhum Mobile Belt (NSMB) which have been metamorphosed in greenschist to amphibolites facies by ca. 1.5–1.8 Ga tectonothermal events (Sengupta et al., 2000; Mahato et al. 2008; Pal and Rhede, 2013). The northern block, referred to as Meso- to Neoproterozoic Chotanagpur Granite Gneiss Complex (CGGC), consists of granite gneisses with enclaves of metapelite, metabasic and metacalcareous rocks (Acharyya et. al., 2006; Gupta and Basu, 2000; Sanyal and Sengupta 2012) which have been metamorphosed amphibolite to granulite facies. The status of this lineament has been widely debated and is variably described as a ‘boundary fault’ (Ball, 1881), ‘zone of trench faults and shears’ (Mazumder, 1988), ‘thrust contact’ (Banerjee, 1985), ‘Khatra- Tamar overthrust’ (Mahadevan, 1992), ‘Rift Zone’ (Ghosh Roy and Sengupta, 1993). The arcuate SPSZ (Fig. 1.1) roughly 150 km long and 4-6 km wide, zone continues from Porapahar in the east to Tamar in the west through Khariduar and Beldih (Saha, 1994). This shear zone has affected both the supracrustal rock of Chandil formation of NSMB and granitoids of CGGC and is converted into mylonites along the SPSZ (Chatterjee et al., 2013; Mazumder, 2005; Chakrabarty and Sen, 2010). Along the shear zone, it preserves a mylonitic fabric as well as breccia development in some restricted stretches. Therefore, SPSZ is mostly ductile to brittle-ductile in nature (Pyne, 1992; Bhattacharya, 1989; Acharyya and Roy, 2006; Gupta and Basu, 2000; Acharjee et al., 2016). The rock types exposed along SPSZ are mostly tuffaceous phyllite, metapelitic schists that are intruded by a suite of rocks ranging from tourmalinites, ultramafics, carbonatite-apatite, granitoids, alkali granites and nepheline-bearing syenite

which are also strongly deformed and metamorphosed and hydrothermally altered along with the other rock types (Acharyya et al., 2006; Acharjee et al., 2016). The rocks of the area were subjected to metamorphism from greenschist to amphibolite facies (Dunn and Dey, 1942; Mehra and Banerjee, 1974; Kumar et al., 1978). The SPSZ, which affects the rocks of both NSF and CGGC, shows ductile deformation with late rejuvenation in a brittle regime (Acharyya et al., 2006; Talukdar et al., 2012; Acharjee et al., 2016). Hydrothermal alteration during brittle deformation accompanied by ferruginisation, kaolinization and silicification was noted in many places and localization of polymetallic deposits of U-apatite-iron oxide (Sarkar, 1984; Sarkar, 2000; Gupta and Basu, 2000; Acharyya et al., 2006; Vapnik et al., 2007; Talukdar et al., 2012). In Chandil formation rhyolites and associated felsic tuffs are ~1600 Ma old (Nelson et al., 2007; Reddy et al., 2009). Reddy et al., 2009 reported that the emplacement age of nepheline-bearing syenite in Sushina from the western part is ~0.93 Ga (U-Pb zircon). It also provides the timing of the rift activity i.e around 0.93 Ga (Reddy et al., 2009; Chatterjee et al., 2013). Intense deformation, shear, and metamorphism of this early rock ensemble mark the closure of the rift zone (Acharyya et al., 2006; Ray et al., 2012; Talukdar et al., 2012).

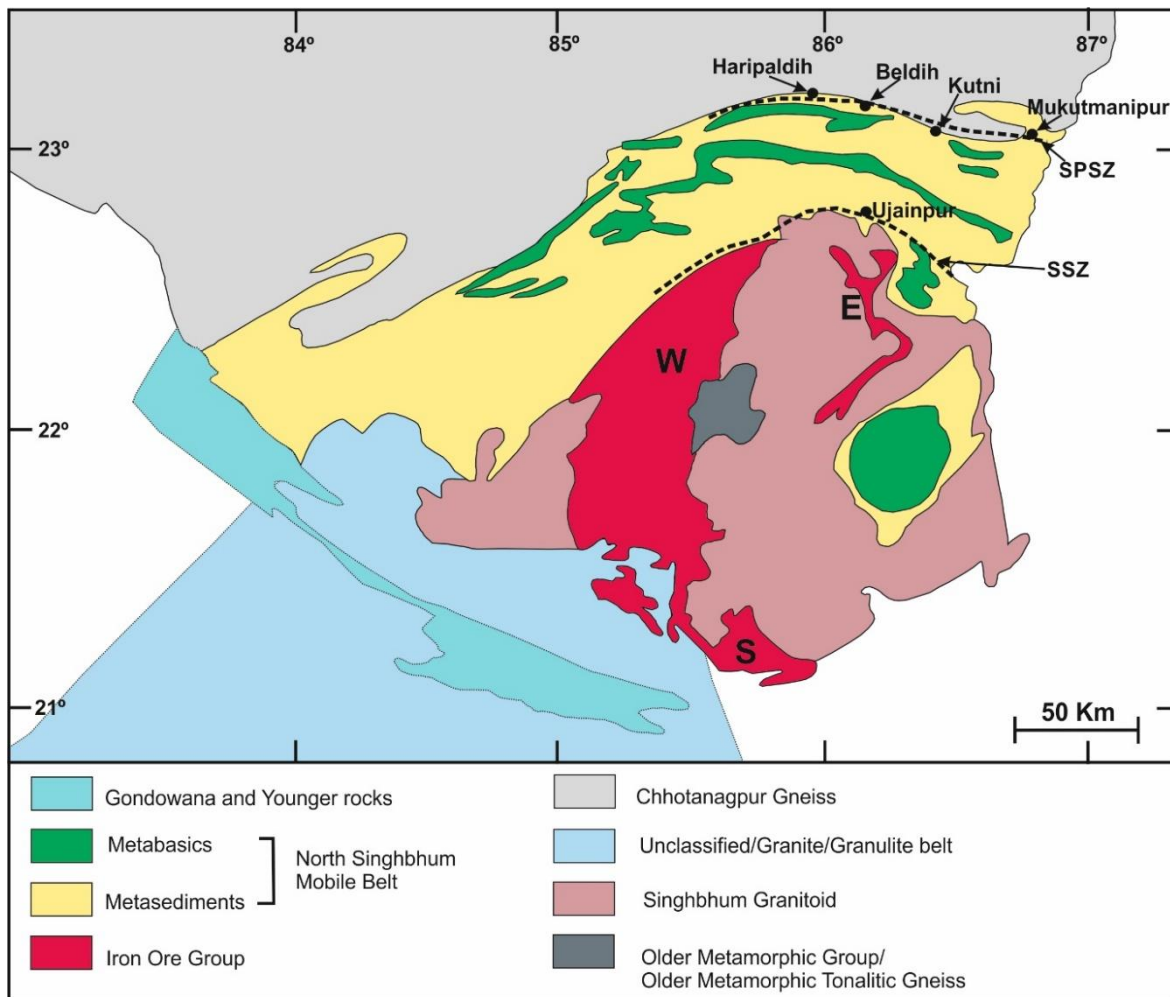


Fig 1.1c: Lithological map of East Indian Craton (modified after Mukhopadhyay, 2001). Locations of study areas are marked in the map.

## 1.2 Tourmaline as a petrogenetic indicator mineral

Tourmaline (9-10.5% B<sub>2</sub>O<sub>3</sub>) is the most important boron mineral in the earth's crust, occurring in various lithologies. Tourmaline's large stability range, in both pressure and temperature (near-surface to granulite-facies conditions), facilitates this widespread occurrence. Its presence in the diagenetic zone of sedimentary basins and in near-surface hydrothermal deposits suggests that the lower limits of stability is 150°C and 100 MPa (Henry et al., 1999; Moore et al., 2004). From the experimental study, the upper thermal stability has been constrained of tourmaline between 725°C and 950°C (Morgan and London, 1989; Holtz and Johannes, 1991; Krosse, 1995; Wolf and London, 1997; von Goerne et al., 1999; Spicer et al., 2004; Ota et al., 2008a; London, 2011; van Hinsberg, 2011). Tourmaline has a wide physical and chemical stability because of its widely varying composition. Thus, it can occur in rocks of widely varying compositions, from sedimentary, hydrothermal, metamorphic, and magmatic (Henry and Dutrow, 1996; Slack 1996; Henry et al., 1999; Marschall et al., 2009). Tourmaline forms in a wide variety of tectonic settings, including as a diagenetic mineral in buried sedimentary basins, as a gangue mineral in ore deposits, associated with the contact, regional and subduction-related metamorphism, in metasomatism, and as a significant mineral typically crystallizing in fractionated igneous bodies (Morgan and London, 1989; Henry and Dutrow, 1996; Slack, 1996; London et al., 1996; Henry et al., 1999; Nakano and Nakamura, 2001; Roda-Robles et al., 2012). The common occurrence of tourmaline mineralization in rocks subjected to metasomatism by boron-bearing fluids (Morgan and London, 1989; Dutrow et al., 1999; Marschall et al., 2006; Marocchi et al., 2011).

Tourmaline is mainly an elongate mineral, having a prismatic shape with well-defined crystal faces (Ford and Dana, 1932), although it also occurs as equidimensional grains and masses (Henry et al., 1999; Slack, 1996). In hand specimen tourmaline occur in different colors from colorless to red, green, blue, pink, brown and, most commonly, black (Ford and Dana, 1932; Rustemeyer, 2003; Beurlen et al., 2011). It also commonly shows strong color zoning (optical zoning), both parallel and perpendicular to the long axis under a petrographic microscope. Tourmaline has strong anisotropy along the prism axis (c axis) for distinctly different properties of the opposite poles of the grain which gives its strong piezo- and pyroelectric properties (Lang, 1974; Dietrich, 1985; Sperlich, 1990; Sperlich et al., 1996; Lang, 2005). The most characteristic property of tourmaline is the negligible rates of intracrystalline element diffusion over geologic time for major and trace elements in its

structure, which is evidenced by sharp compositional and isotopic breaks that have persisted during prolonged periods even at elevated temperature (Voll, 1969; van Hinsberg and Marschall, 2007; van Hinsberg and Schumacher, 2007; van Hinsberg et al., 2011). Because of these characteristics, the compositional variation in even a single zoned crystal may contain significant petrogenetic information (Agrosi et al., 2006; Dutrow and Henry, 2000; Henry et al., 1999; van Hinsberg and Marschall, 2007; van Hinsberg and Schumacher, 2007; van Hinsberg et al., 2006). So, it can preserve chemical signatures of earlier periods of growth. Therefore, tourmaline is useful for tracking the compositional evolution of igneous and metamorphic rocks, and as well as a monitor of fluid infiltration. So, tourmaline can be used to discriminate among different environments of tourmaline formation and possible boron sources (e.g., Henry and Guidotti, 1985, Jiang, 1998, Jiang et al., 1999). The tourmaline crystal structure can accommodate trace elements of widely varying ionic charge and radius, making the tourmaline an excellent monitor of the trace-element evolution of its local environment of growth (Slack, 1982; Beaty et al., 1988; Robinson et al., 1988; Clarke et al., 1989; Pirajno and Smithies, 1992). Tourmaline is commonly associated and co-precipitated during the formation of various types of mineral deposits including copper, silver-gold, tin (-tungsten), massive sulfide, uranium deposits and other metasomatic bodies (Slack et al., 1984; Pirajno and Smithies, 1992; Slack, 1996; Xavier et al., 2008; Raith et al., 2004). Boron isotopes in tourmaline have been used to fingerprint the source and evolution of mineralizing fluids. So, the Tourmaline acts as a pathfinder element to trace different metallogenesis of various hydrothermal deposits (Palmer and Swihart, 1996; Xavier et al., 2008).

### 1.3 Tourmaline mineral chemistry

Tourmaline is a complex borosilicate mineral. It is characterized by extensive chemical substitutions, and thus compositionally diverse members. This chemical complexity makes tourmaline a variable indicator of in its local chemical environment. Its general structural composition can be expressed by:

$\text{XY}_3\text{Z}_6(\text{T}_6\text{O}_{18})(\text{BO}_3)_3\text{V}_3\text{W}$ , following Hawthorne and Henry, (1999), where the site coordinations and elements at the different sites are as follows:

$^{\text{IX}}\text{X}$ :  $\text{Na}^{1+}$ ,  $\text{Ca}^{2+}$ ,  $\square$  (vacancy),  $\text{K}^{1+}$ ,  $\text{Pb}^{2+}$

$^{\text{VI}}\text{Y}$ :  $\text{Mg}^{2+}$ ,  $\text{Fe}^{2+}$ ,  $\text{Al}^{3+}$ ,  $\text{Li}^{1+}$ ,  $\text{Ti}^{4+}$ ,  $\text{Mn}^{2+}$ ,  $\text{Fe}^{3+}$ ,  $\text{Zn}^{2+}$

**<sup>VI</sup>Z:** Al<sup>3+</sup>, Cr<sup>3+</sup>, Fe<sup>3+</sup>, Mg<sup>2+</sup>, Fe<sup>2+</sup>

**<sup>IV</sup>T:** Si<sup>4+</sup>, B<sup>3+</sup>, Al<sup>3+</sup>

**<sup>III</sup>B:** B<sup>3+</sup>

**<sup>III</sup>V:** OH<sup>1-</sup>, O<sup>2-</sup>

**<sup>III</sup>W:** OH<sup>1-</sup>, F<sup>1-</sup>, O<sup>2-</sup>

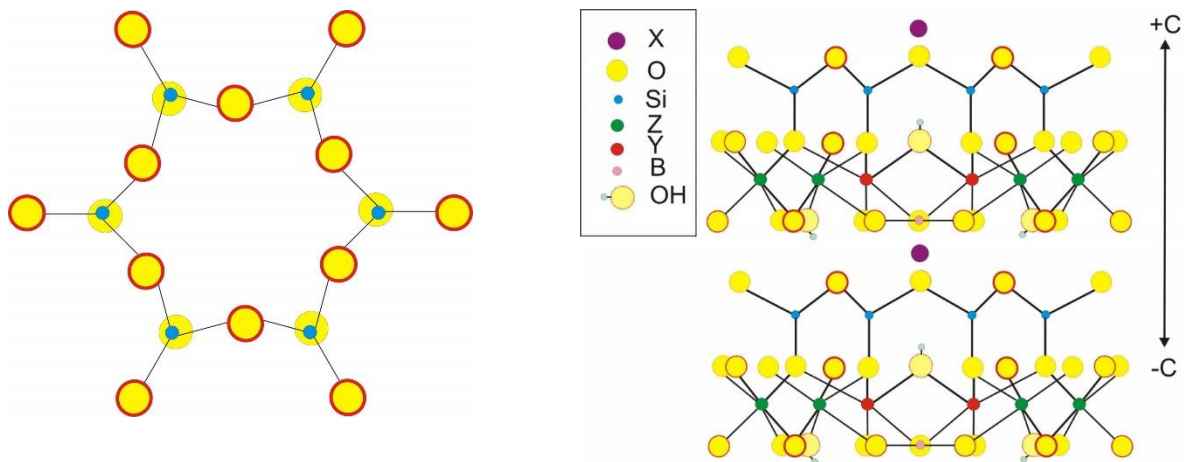


Fig 1.3.1a: Tourmaline crystal structure by Henry and Dutrow, 1996; Hawthorne and Henry, 1999

Tourmaline is a ring-silicate mineral. Tourmaline mineral unit cell consists of a six-fold ring of tetrahedra (T sites) on top of a concentric arrangement of three Y-site and six Z-site octahedra. Six TO<sub>4</sub> tetrahedra join corners to form a [T<sub>6</sub>O<sub>18</sub>] ring (Fig1.3.1a). There are two types of octahedral sites; the Z site which is slightly larger, and more distorted than the Y site (Bosi and Lucchesi, 2007). Within the six-fold ring, all tetrahedra point toward the layer of octahedra, and this arrangement results in the polar characteristics of tourmaline, because it prohibits the presence of symmetry elements perpendicular to the long axis. The X site is a nine-coordinated polyhedron and is located on top of the six-fold ring. Three trigonal boron polyhedra are further present within the layer of octahedra which is roughly perpendicular to the c axis. The octahedral Y and Z-sites contain a variety of di-, tri- and tetravalent cations. The Z site is typically occupied by Al but a significant amount of Fe<sup>2+</sup>, Fe<sup>3+</sup>, Mg<sup>2+</sup>, Cr<sup>3+</sup> and V<sup>3+</sup> can replace Al. The larger Y site tolerates extensive and diverse substitutions involving monovalent, divalent, trivalent and tetravalent cations like Mg<sup>2+</sup>, Fe<sup>2+</sup>, Al<sup>3+</sup>, Li<sup>1+</sup>, Ti<sup>4+</sup>, Mn<sup>2+</sup>,

$\text{Fe}^{3+}$ ,  $\text{Zn}^{2+}$ . The X site usually contains variable amount of  $\text{Na}^{1+}$ ,  $\text{K}^{1+}$ ,  $\text{Ca}^{2+}$  and may also accommodate vacancies “□” (Foit and Rosenberg, 1977). The X-site vacancies are calculated assuming  $\text{Ca} + \text{Na} + \text{K} + \text{X-vacancies} = 1$ . Al is first assigned to the Z-site, followed by the Y-site. Al is also present in the T-site, if the T site is not completely filled up by Si. Boron is in regular triangular coordination and has no apparent substitutions. There are two types of anion sites (V-site and W-site), which can contain not only  $\text{O}^{2-}$ , but also  $\text{OH}^{1-}$  and F. In the hydroxyl site,  $\text{O}^{2-}$  can substitute for  $\text{OH}^{1-}$  (Nemec, 1969; Foit and Rosenberg, 1977),  $\text{F}^{1-}$  and  $\text{O}^{2-}$  are present in the W-site, and the rest of the W-site and the V-site are occupied by  $(\text{OH})^{-1}$ . The Cl contents are generally negligible (Henry and Dutrow, 1996; Hawthorne and Henry, 1999). So, Tourmaline incorporates in its structure a wide variety of elements such as mono-, di-, tri-, and tetravalent cations as well as mono- and divalent anions. For the chemical diversity, W. L. Bragg refers to tourmaline as a “garbage-can mineral” (Bragg, 1937).

Tourmaline chemical composition is considered in terms of its end members. There are fourteen IMA recognized species. The generalized formulae of different tourmaline end-members are presented in Table 1.3.2a. Ternary systems for primary groups are used for general tourmaline-species designation. The primary division (Fig 1.3.1a) is made according to the dominant occupancy of the X site, which divides as the alkali-tourmaline group, calcic-tourmaline group, or the X-vacant-tourmaline group (modified after Henry et al., 2011). The generalized tourmaline species can be identified based on  $\text{Mg}/(\text{Mg} + \text{Fe}^{2+})$  vs.  $\square/(\square + \text{Na})$  ratios (Fig 1.3.1b). The solid solution in tourmaline is ubiquitous due to simple or coupled substitutions. Table 1.3.2b summarizes common exchange vectors in tourmaline. Exchange vectors are used to represent the composition of tourmaline in a two-dimensional projection. The main purposes are to clarify the chemical variability among the different groups of tourmalines and to decipher some specific ionic substitutions in the tourmaline.

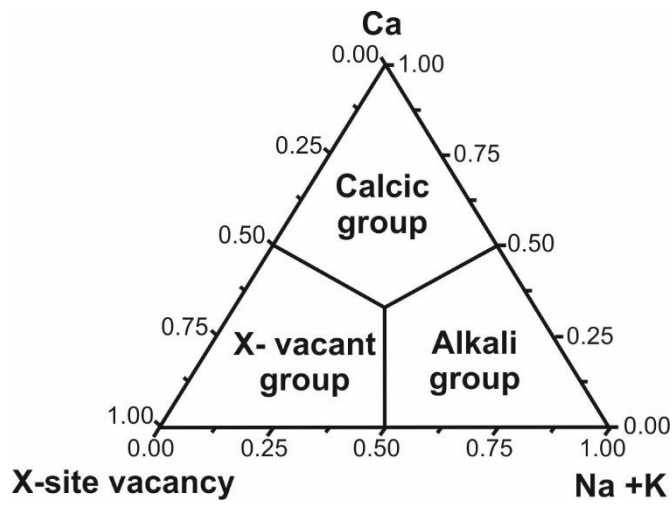


Fig 1.3.1b: Ternary systems for primary groups (X-site occupancy) used for general tourmaline-species designation (after Hawthorne and Henry, 1999).

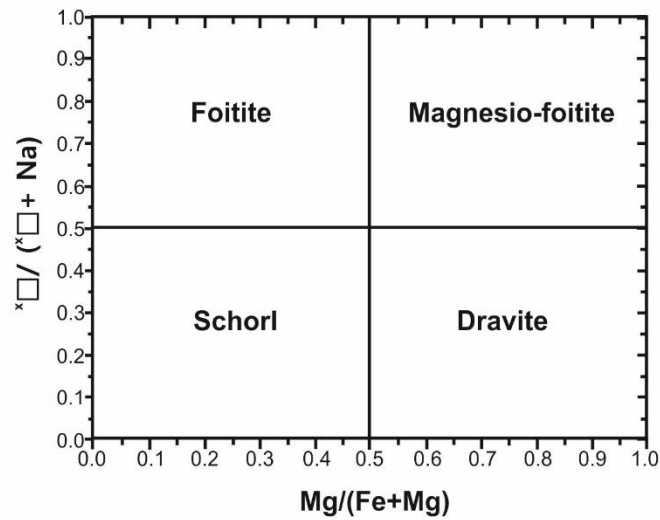


Fig1.3.1c: The generalized tourmaline species are identified based on  $Mg/(Mg + Fe)$  vs.  $\square/(\square + Na)$  ratios (after Henry et al., 2003) ( $\square$  - X-site vacancy).

Table 1.3.2a: Tourmaline end members and classifications from Hawthorne and Henry (1999).

Alkali tourmaline:

Species	(X)	(Y <sub>3</sub> )	(Z <sub>6</sub> )	T <sub>6</sub> O <sub>18</sub>	(BO <sub>3</sub> ) <sub>3</sub>	V <sub>3</sub>	W
Elbaite	Na	Li <sub>1.5</sub> Al <sub>1.5</sub>	Al <sub>6</sub>	Si <sub>6</sub> O <sub>18</sub>	(BO <sub>3</sub> ) <sub>3</sub>	(OH) <sub>3</sub>	(OH)
Olenite	Na	Al <sub>3</sub>	Al <sub>6</sub>	Si <sub>6</sub> O <sub>18</sub>	(BO <sub>3</sub> ) <sub>3</sub>	O <sub>3</sub>	(OH)
Dravite	Na	Mg <sub>3</sub>	Al <sub>6</sub>	Si <sub>6</sub> O <sub>18</sub>	(BO <sub>3</sub> ) <sub>3</sub>	(OH) <sub>3</sub>	(OH)
Chromdravite	Na	Mg <sub>3</sub>	Cr <sub>6</sub>	Si <sub>6</sub> O <sub>18</sub>	(BO <sub>3</sub> ) <sub>3</sub>	(OH) <sub>3</sub>	(OH)
Schorl	Na	(Fe <sup>2+</sup> ) <sub>3</sub>	Al <sub>6</sub>	Si <sub>6</sub> O <sub>18</sub>	(BO <sub>3</sub> ) <sub>3</sub>	(OH) <sub>3</sub>	(OH)
Buergerite	Na	(Fe <sup>3+</sup> ) <sub>3</sub>	Al <sub>6</sub>	Si <sub>6</sub> O <sub>18</sub>	(BO <sub>3</sub> ) <sub>3</sub>	O <sub>3</sub>	F
Povondraite	Na	(Fe <sup>3+</sup> ) <sub>3</sub>	(Fe <sup>3+</sup> ) <sub>4</sub> Mg <sub>2</sub>	Si <sub>6</sub> O <sub>18</sub>	(BO <sub>3</sub> ) <sub>3</sub>	(OH) <sub>3</sub>	O
Vanadiumdravite	Na	Mg <sub>3</sub>	Al <sub>6</sub>	Si <sub>6</sub> O <sub>18</sub>	(BO <sub>3</sub> ) <sub>3</sub>	(OH) <sub>3</sub>	(OH)

Calcic tourmaline:

Species	(X)	(Y <sub>3</sub> )	(Z <sub>6</sub> )	T <sub>6</sub> O <sub>18</sub>	(BO <sub>3</sub> ) <sub>3</sub>	V <sub>3</sub>	W
Liddicoatite	Ca	Li <sub>2</sub> Al	Al <sub>6</sub>	Si <sub>6</sub> O <sub>18</sub>	(BO <sub>3</sub> ) <sub>3</sub>	(OH) <sub>3</sub>	F
Uvite	Ca	Mg <sub>3</sub>	MgAl <sub>5</sub>	Si <sub>6</sub> O <sub>18</sub>	(BO <sub>3</sub> ) <sub>3</sub>	(OH) <sub>3</sub>	F
Feruvite	Ca	(Fe <sup>3+</sup> ) <sub>3</sub>	MgAl <sub>5</sub>	Si <sub>6</sub> O <sub>18</sub>	(BO <sub>3</sub> ) <sub>3</sub>	(OH) <sub>3</sub>	F

X-site vacant tourmaline:

Species	(X)	(Y <sub>3</sub> )	(Z <sub>6</sub> )	T <sub>6</sub> O <sub>18</sub>	(BO <sub>3</sub> ) <sub>3</sub>	V <sub>3</sub>	W
Rossa-manite	□	Li <sub>2</sub> Al	Al <sub>6</sub>	Si <sub>6</sub> O <sub>18</sub>	(BO <sub>3</sub> ) <sub>3</sub>	(OH) <sub>3</sub>	F
Foitite	□	(Fe <sup>2+</sup> ) <sub>2</sub>	Al <sub>6</sub>	Si <sub>6</sub> O <sub>18</sub>	(BO <sub>3</sub> ) <sub>3</sub>	(OH) <sub>3</sub>	F
Magnesian-foitite	□	Mg <sub>2</sub> Al	Al <sub>6</sub>	Si <sub>6</sub> O <sub>18</sub>	(BO <sub>3</sub> ) <sub>3</sub>	(OH) <sub>3</sub>	F

□ - This symbol represents an X-site vacancy.

Table 1.3.2b. Common substitutions within and between sites including a compilation of exchange vectors after Henry and Guidotti (1985) and Henry and Dutrow (1996).

Substitutions*	Exchange vectors
${}^Y\text{Mg} = {}^Y\text{Fe}^{2+}$	$\text{Fe}^{2+}\text{Mg}_{-1}$
${}^Y\text{Mn} = {}^Y\text{Fe}^{2+}$	$\text{Fe}^{2+}\text{Mn}_{-1}$
${}^Z\text{Al} = {}^Z\text{Fe}^{3+}$	$\text{Fe}^{3+}\text{Al}_{-1}$
${}^Z\text{Al} = {}^Z\text{Cr}^{3+}$	$\text{CrAl}_{-1}$
${}^{O(1)}\text{OH}^- = {}^{O(1)}\text{F}^-$	$\text{F(OH)}_{-1}$
$2{}^Y\text{Fe}^{2+} = {}^Y\text{Li} + {}^Y\text{Al}$ (Elbaite substitution)	$\text{LiAlFe}^{2+}_{-1}$
${}^X\text{Na} + 2{}^Y\text{Mg} = {}^X\text{□}^{**} + {}^Y\text{Al}$ (Alkali-defect substitution)	$\text{□AlNa}_{-1}\text{Mg}_{-1}$
${}^X\text{Na} + {}^Y\text{Mg} + {}^{O(1)}\text{OH}^- = {}^X\text{□} + 2{}^Y\text{Al} + {}^{O(1)}\text{O}^{2-}$ (Aluminobuergerite substitution)	$\text{□Al}_2\text{ONa}_{-1}\text{Mg}_{-2}(\text{OH})_{-1}$
${}^Y\text{Mg} + {}^{O(3)}\text{OH}^- = {}^Y\text{Al} + {}^{O(3)}\text{O}^{2-}$ (Buergerite substitution)	$\text{AlOMg}_{-1}(\text{OH})_{-1}$
${}^Y\text{Fe}^{2+} + {}^{O(3)}\text{OH}^- = {}^Y\text{Fe}^{3+} + {}^{O(3)}\text{O}^{2-}$ (Buergerite substitution)	$\text{Fe}^{3+}\text{OFe}^{2+}_{-1}(\text{OH})_{-1}$
${}^Y\text{Mg} + {}^T\text{Si} = {}^Y\text{Al} + {}^T\text{Al}$ (Tshermaks substitution)	$\text{Al}_2\text{Mg}_{-1}\text{Si}_{-1}$
$2{}^Y\text{Al} = {}^Y\text{Mg} + {}^Y\text{Ti}$ (Uvite substitution)	$\text{MgTiAl}_{-1}$
${}^X\text{Na} + {}^Y\text{Al} = {}^X\text{Ca} + {}^Y\text{Mg}$ (Uvite substitution)	$\text{CaMgNa}_{-1}\text{Al}_{-1}$
${}^X\text{□} + {}^Y\text{Al} + {}^{O(1)}\text{OH}^- = {}^X\text{Ca} + {}^Y\text{Mg} + {}^{O(1)}\text{O}^{2-}$	$\text{CaMgO(OH)}_{-1}\text{□}_{-1}\text{Al}_{-1}(\text{OH})_{-1}$
$2{}^Y\text{Mg} + {}^Z\text{Al} + {}^{O(1)}\text{OH}^- = 2{}^Y\text{Al} + {}^Z\text{Mg} + {}^{O(1)}\text{O}^{2-}$	$\text{CaMgO(OH)}_{-1}\text{□}_{-1}\text{Al}_{-1}(\text{OH})_{-1}$

\*Superscripts denote specific crystallographic sites.

\*\*□ - This symbol represents an X-site vacancy.

## 1.4 Occurrences of tourmaline bearing rocks across India

There are several occurrences of tourmaline-bearing rocks reported in India which are systematically depicted in the following Table:

Table 1.4 Stratigraphy, host rock, mineral associations of the tourmaline occurrences in India.

Locality	Stratigraphy	Host rock types	Tourmaline composition	Reference
Zanskar, Kulu, Lahoul and Kishtwar-Kashmir (NW India)	Miocene leucogranites	Garnet, tourmaline and muscovite bearing granites locally contain biotite, apatite or kyanite	-----	Searle and Fryer, 1986
Ambaji-Deri mineralized zone, South Delhi fold belt, Rajasthan	Proterozoic	in association pyrite and biotite in a tourmalinite band in metachert	Dravite in composition	Deb et al., 1997
Rampura-Agucha Rajasthan	Palaeo Proterozoic Bhilwara Belt	In association sphalerite, galena, quartz and feldspar(Ore body), hosted by graphite-mica sillimanite-schist	Dravite in composition	Hiiller and Gandhi, 1997
		In pegmatite	Schorl in composition	
Badiya, Kanyaluka, Pathargora, Surda, and Rakha Mines, Tetuldanga Singhbhum shear zone(SSZ), Singhbhum, Jharkhand	Paleo to Meso Proterozoic	tourmalinite enclosed by quartz-chlorite schist	alkali group and straddle the boundary between schorl-dravite	Sengupta et al., 2005
		tourmaline-rich assemblage kyanite-muscovite schist /Kyanite-quartzite	alkali group and are classified under dravite series	
		tourmaline-rich assemblage in mylonitized granite(Soda-Granite)	alkali group and are classified under dravite series	
Hira Buddini gold mine,Karnataka	Late Archean granite-greenstone belt	tourmaline-rich clusters or zones within the wall rock (Metabasalt and metadacites)	straddle the boundary between schorl-dravite	Krienitz et al., 2008
Agucha, Kayar and Dariba areas in central Rajasthan	Paleoproterozoic	tourmaline-rich assemblage kyanite-muscovite schist /Kyanite-quartzite	alkali group and are classified under dravite series	Fareeduddin et al., 2010
Jaduguda, Singhbhum Shear zone(SSZ),Singhbhum,Jharkhand	Paleo to Meso Proterozoic	Tourmaline-bearing rocks like quartz-tourmaline rock, quartz-sulphide vein, biotite schist, chlorite schist and meta-conglomerate	alkali group and are dravite in composition	Pal et al., 2010
Gangotri Granite, Garhwal Higher Himalaya	Late Cenozoic	Gangotri granite ( quartz+ Kfeldspar+plagioclase+tourmaline+muscovite + biotite + garnet + beryl)	Alkali Group and are Schorl in composition	Jowhar, 2010

Singhbhum Shear zone(SSZ),Singhbhum,Jharkhand	Paleo to Meso Proterozoic	tourmaline-rich assemblage in kyanite-muscovite schist /Kyanite-quartzite	Early generation are alkali rich and classified under dravite series, later generation are in vacancy group and classified under foitite/oxy foitite series	Sengupta et al., 2011
Guddarangavanahalli (G.R.Halli), western Dharwar craton, southern India, Karnataka	Late Archean	tourmaline-rich assemblage in mylonitized granite(Soda-Granite)	alkali group and are classified under dravite	Gupta et al., 2014
		tourmaline-rich assemblage in biotite-muscovite schist	alkali group and are classified under dravite	
Hutti,Hira-Buddini and Uti gold mine,Karntaka	Late Archean	Hutti: (1) along the biotite-chlorite– defined mylonitic foliation, inclusions of tourmaline within pyrite and arsenopyrite (2) as tourmaline-calcite microveins within rocks	Tourmaline is Dravite in composition	Hazarika et al., 2015
		Hira-Buddini: (1) tourmaline veins that replace amphiboles accompanied by sulfides and calcite, with minor titanite, ilmenite, and apatite(host:metabasalt)	Tourmaline composition straddles the boundary between schorl-dravite series	
		Uti: Tourmalines grew along the biotite-muscovite-defined foliation metapelites containing garnet, quartz, plagioclase	Tourmaline is dravite in composition	
Bihar Mica Belt,Bihar	Mesoproterozoic	Mica pegmatites from the Bihar Mica Belt	Tourmaline are schorl in composition	Hazarika et al., 2016
Mashak Pahar, Bankura district, West Bengal	Proterozoic	migmatized quartz tourmaline gneiss and quartz tourmaline veins	All are in alkali group and tourmaline compositions from dravite to schorl	Acharjee et al., 2016
Bastipadu, Kurnool, Andhra Pradesh	Paleoproterozoic to Mesoproterozoic granitoids	Tourmaline-bearing leucogranite occurs as a pluton with pegmatitic veins intruding the Archaean granodiorite	alkali group and mainly schorl in composition	Mishra et al., 2018
Bhukia gold deposit, Aravalli-Delhi Belt	Proterozoic	calc-silicate and quartz-albite rocks	All the generations of tourmaline are alkali rich, First generation of tourmaline is dravite in character, while second and third generations of	Hazarika et al., 2019

			tourmaline are schorl in character	
Balda and Motiya in Aravalli Delhi Belt in western India	Proterozoic	Tourmaline-wolframite-bearing quartz veins associated with S-type granites	Tourmaline belongs to the alkali group and schorl in character	Ghosh et al., 2021
Mohuldih and Bagjata along Singhbhum shear zone(SSZ), Singhbhum, Jharkhand	Paleo to Meso Proterozoic	Mohuldih: Tourmaline bearing quartz-chlorite-sericite-schist Bagjata: Tourmaline-bearing quartz-biotite-chlorite-muscovite schists	Pre-tectonic and post tectonic tourmalines are schorl to dravite in composition	Patel et al., 2021
Hutti-Maski greenstone belt And Kolar greenstone belt of the Eastern Dharwar Craton in southern India.	Late Archean	tourmaline occurs in the gold mineralized metabasalt and non-mineralized metabasalt	Tourmalines in mineralized metabasalt are alkali-rich and dravite in composition. Whereas tourmalines in the nonmineralized metabasalt are calcic rich and dravite to Ferruvite in composition	Hazarika et al., 2021

## 1.5 Present study area

SPSZ occurs as a crustal scale lineament that affected both the rock types of CGGC and Chandil formation of NSMB. Whereas, SSZ occurs between two cationic blocks i.e Singhbhum craton in the south and NSMB in the north. The SPSZ and SSZ are both ductile shear zones, characterized by intense shearing along with hydrothermal activity that developed different polymetallic deposits. Shearing in both the shear zones caused infiltration of different generations of hydrothermal fluids, which metasomatized the pre-existing rock and formed different hydrothermal mineralization including tourmaline mineralization. In SPSZ, Biswas et al., 2013 and Acharjee et al., 2016, reported tourmaline mineralization near Mukutmanipur area, Bankura. There are several occurrences of tourmaline-bearing rocks that have been addressed by many authors (Mukhopadhyay and Deb, 1995; Sengupta et al., 2005; Sengupta et al., 2011; Pal et al., 2010; Patel et al., 2021) along SSZ. Detailed field, the petrographic study of tourmaline in SPSZ is lacking. A clear understanding of the relationship between multiple generations of tourmaline mineralization with deformation events is also lacking. Similarly, a detailed account of major and trace element data in SPSZ is also not available. More Major elements data on tourmaline has been generated in SSZ but

trace element data on tourmaline is very rare. However, considering the vast area and complex history of deformation and mineralization, a notable knowledge gap still remains regarding tourmaline mineralization in these two important shear zones. Most of the previous studies have focused on tourmaline mineralization in single mineralization belt, such as SPSZ or SSZ. However, no attempt has been done to compare or correlate the mineralization patterns between these two belts. This would elucidate the crustal evolution and fluid-rock interaction pattern throughout the prolonged period of deformation and shearing event in this area during Proterozoic.

For the present study, some specific areas (Fig 1.5a). were chosen along SPSZ and SSZ to understand the evolution of tourmaline mineralization. Here, four specific locations along SPSZ were selected. between the stretch of Haripaldih in the west to the Mukutmanipur in the extremity east. These areas are a) Haripaldih area in the west, b) Beldih area at the center, c) Kutni area to the east and d) Mukutmanipur area to the extreme east (Fig 1.5a). Detailed mapping has been done (1:12,500) to delineate the field relations among the different rocks along with their structural attributes. Tourmaline-bearing rocks are formed both within the CGGC and NSMB. In the Haripaldih sector, tourmaline mineralization occurred within the CGGC rock which is situated slightly north of the SPSZ (Fig 1.5a). In the Beldih area, tourmaline mineralization occurred within the CGGC rock which falls within the shear zone (SPSZ) along the boundary between CGGC and NSMB (Fig 1.5a). In the Kutni area, tourmaline mineralization occurred in Chandil formation rocks belonging to NSMB located in the southern part of SPSZ (Fig 1.5a). In the Mukutmanipur area, tourmaline mineralization occurred in CGGC rock which is situated northern part of SPSZ (Fig 1.5a). These four sectors were selected to understand the effects of tourmaline mineralization in different types of host rocks belonging to both CGGC and NSMB. Also, these locations were specifically selected to understand the effects of tourmaline mineralization as we progress from away towards the lineament of SPSZ. Apart from these, tourmaline mineralization at Ujainpur which is located in the western part of SSZ (Fig 1.5b) was also studied in detail. This area was selected to understand the structural and lithological control of tourmaline mineralization in the evolutionary (both structural and mineralogical) context of SSZ which is different from SPSZ. An attempt was also made to establish the relationship and the role of boron metasomatism during the formation of SPSZ and SSZ. The different tourmaline bearing and associated rocks are described in detail in different chapters in different areas as follows.

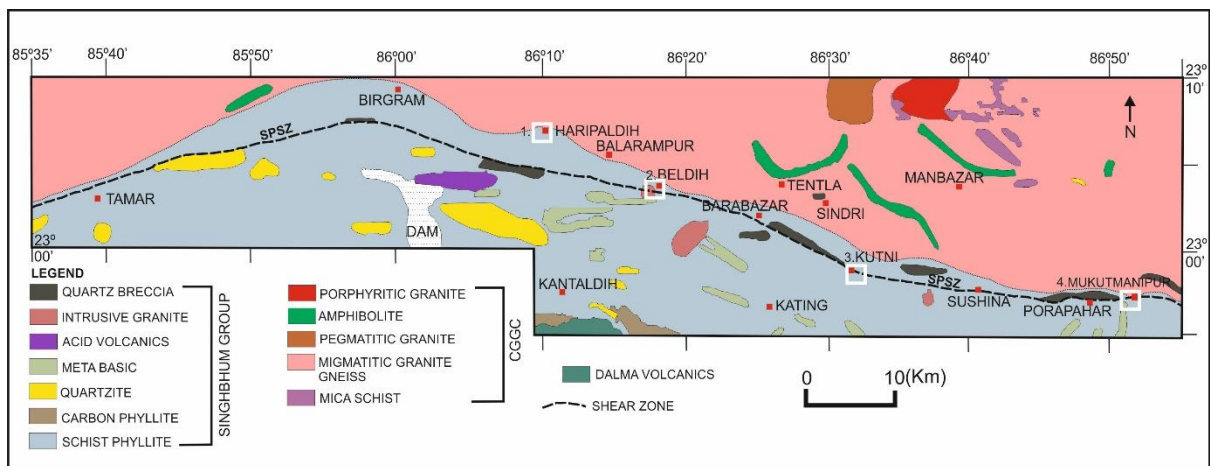


Fig 1.5a: Generalized map of the SPSZ from Tamar to Porapahar showing the study area (Modified after Dunn and Dey, 1942). Locations of study areas are marked on the map.

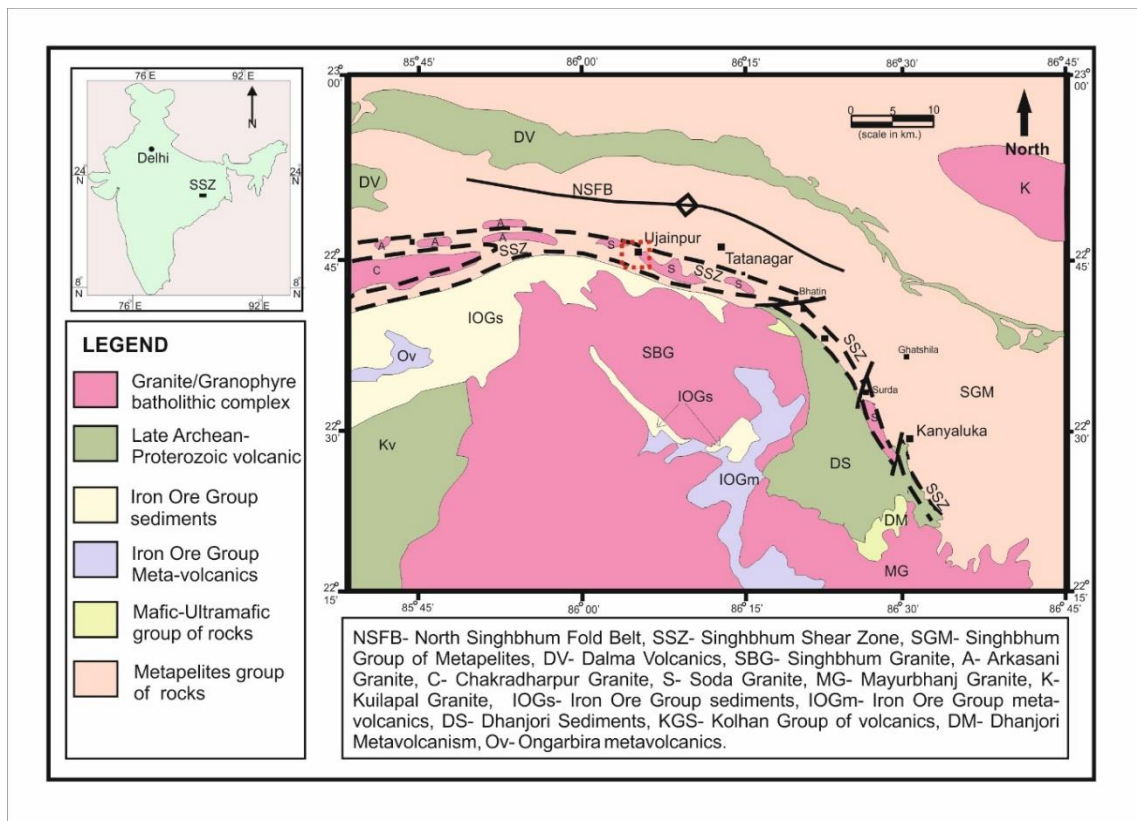


Fig 1.5b: Geological map of Singhbhum Shear Zone (SSZ) (Modified after Sengupta et al., 2011). The study area (Ujainpur) is shown on the map.

## 1.6 Objective of the thesis

In the present study areas of the SPSZ and SSZ different types of tourmaline-bearing rocks are chosen for detailed petrography, and geochemistry study to understand the origin and evolution of these tourmaline-bearing rocks.

### Objectives of my present study:

- Understanding the relationship between different rocks related to tourmaline mineralization in study areas (parts of the SPSZ and SSZ).
- Understanding the structural characters of different tourmaline-rich rocks and associated lithologies.
- Determination of relative timing of formation of tourmaline with respect to successive deformation and/or alteration events.
- Characterising tourmalines of different generations with respect to major and trace element characters to understand the source and conditions of tourmaline formation.
- Comparison of tourmaline mineralization between the SPSZ and SSZ.

The present work was started with a thorough study of literatures related to the topic and previous work related to the study area. This was followed by detailed fieldwork and mapping of the important areas on 1:25,000 scale. Traverses were taken across the shear zone to understand the change of mineralization pattern with changing the intensity of deformation. Fieldwork included the collection of structural data and an extensive collection of samples both from tourmaline mineralized rocks and associated other rocks. The collected samples were carried to the laboratory and prepared for analysis. Thin sections were made for a detailed petrography study. Electron Probe Microscope Analysis (EPMA) and LA-ICPMS analysis were done for the phase chemistry study of tourmaline and associated minerals.

# CHAPTER 2

## Tourmaline bearing rocks in and around Haripaldih

Haripaldih village is located 10 km west from Barabhum rail station in Purulia district, West Bengal. The position of the Haripaldih area is shown in the map of Fig 1.5a. This area is situated in the north of the SPSZ (Fig 1.5a). The detailed geological description of the area is dealt in the subsequent section.

### 2.1 Lithology and structure of the area

The major lithological distribution in and around Haripaldih area is shown in Fig 2.1.1. The northern group includes high-grade granite gneisses which are the parts of Chotanagpur Granite Gneiss Complex (CGGC) extending from E to W. This zone is highly metamorphosed granitic rock showing gneissic banding. In different domain, contrasting compositional character is recorded. This lithounit is medium to coarse grained leucocratic felsic layer (quartz + feldspar) and medium to coarse grained melanocratic layer with biotite (Fig 2.1.2a). Muscovite schists or quartz muscovite schist and its variants formed the major country rock towards the south of granite gneiss. Muscovite schist or quartz muscovite schist mainly occurs as low-lying detached outcrops mostly exposed along the nalah sections and low-lying paddy fields. Within this quartz muscovite schist, patches of muscovite schist have occurred. This schistose zone is nearly 1.5 to 2 km wide and runs parallel to the boundary of CGGC in nearly E-W direction. Muscovite schist are medium to coarse grained, leucocratic in nature. In many places, quartz content increases and represented the rock as quartz-muscovite schist (Fig 2.1.2b). Sometimes, distinct interbanding of quartzose and micaceous units are observed. The rock is highly foliated and being defined by the phyllosilicate minerals and the quartz-mica interbanding (Fig 2.1.2c). Hardness of the rock varies depending on quartz content, quartz rich bands are extremely hard, foliations being almost absent within these bands while the mica-rich layers are very friable. The granite gneiss which is the part of CGGC, affected by the shear zone and retrograded into muscovite schist or quartz muscovite schist (Chattopadhyay et al., 2016). Rarely, segregations of bladed kyanite of centimeter to decimeter scale is present within

this quartz muscovite schist (Fig 2.1.2d). There are numerous pegmatite veins intrusions found near Haripaldih area. Pegmatites are mainly hosted by the muscovite schist or quartz-muscovite schist. At places, biotite is also present along with muscovite within these rocks. However, biotite is less abundant than muscovite and thus these rocks are identified as biotite-muscovite schist. Pegmatite veins are medium to coarse grained, leucocratic (Fig 2.1.2e, 2.1.2i and 2.1.2j). This pegmatite veins thickness varies from place to place (centimeter to meter). There are two generations of pegmatite veins are found. Most pervasive pegmatite veins run parallel to the general trend of schistose host rock (E-W trend) (Fig 2.1.2e) while in some localities pegmatite veins show a low angle cross cut relationship with schistose rock (Fig 2.1.2f). The pegmatite veins which are parallel to the foliation define by muscovite schist or quartz- muscovite schist are deformed and folded (Fig 2.1.2g). The pegmatite veins sometimes show pinch and swell structures due to the layer parallel stretching (Fig 2.1.2h). Pegmatite vein is mainly composed of quartz, K-feldspar and muscovite. K-feldspars, muscovite, and quartz are coarse-grained of centimetre dimension (Fig 2.1.2i). Quartz content varies from place to place. Occasionally, the feldspar clasts are fractured indicative of deformation (Fig 2.1.2i). In places aggregates of mica (>3cm) formed as mica books (Fig 2.1.2j). Foliation plane is not developed in the pegmatite veins. Occasionally, relicts of schistose host rocks are found within pegmatite vein (Fig 2.1.2e). Locally, tourmaline mineralisation is noted within these pegmatite veins (Fig 2.1.2g). Tourmaline bearing pegmatite are described in detail in next section. Quartzite is exposed as isolated outcrops in high contour and elevated hillocks, linearly arranged along a general E-W trend, immediately south of the muscovite schist or quartz-muscovite schist. Quartzite is gray in colour and shows saccaroidal texture due to recrystallization of primary quartz grains (Fig 2.1.2k). In places, mylonitic foliation develops in quartzite which is defined by stretched grains of quartz. Phyllite is the most dominant and aerially persistent unit towards the south of quartzite. The rock is grey to greenish grey in colour and extremely fine grained (Fig 2.1.2l). The rock is finely foliated (defined by flaky minerals) and highly sheared. The southernmost group i.e quartzite and phyllite are parts of the North Singhbhum Fold Belt (Chandil Fm of NSFB).

There are no primary structures preserved in and around Haripaldih area. The rocks in this region suffered at least three phases of deformation. The first phase of deformation ( $D_1$ ), produce the  $F_1$  folds whose axial planar schistosity ( $S_1$ ) is the most prominent planar fabric occurring as the regional schistosity of the study area, irrespective of lithology. The second phase of deformation ( $D_2$ ) produce  $F_2$  folds defined by the folding of the  $S_1$  planes. The third

phase of deformation ( $D_3$ ) produce the  $F_3$  folds defined by the large broad warps of the resistant lithounits.

The most prominent planar structure that regional schistosity ( $S_1$ ), shown by muscovite schist having a general E-W strike of  $80^\circ$ - $100^\circ$  and dipping steeply ( $70^\circ$ -  $80^\circ$ ) towards north (Fig 2.1.2e). In places, dip amount is nearly vertical. The regional ( $S_1$ ) foliation is also prominent in phyllite having a E-W strike of  $90^\circ$ -  $100^\circ$  and dipping steeply ( $65^\circ$ - $80^\circ$ ) towards north (Fig 2.1.2l). Locally the attitude of the regional foliation is changed due to folding of the  $S_1$ . First generation or  $F_1$  folds are defined by the quartz veins (Fig 2.1.2m) whose axial planes are parallel to the schistosity of the rock. The  $F_1$  is mostly asymmetric, sometimes with thickened hinges. The  $F_1$  fold of quartz vein plunges  $25^\circ \rightarrow 95^\circ$ . The attitude of  $F_1$  axial plane is  $105^\circ/75^\circ$  N. The  $F_1$  folds are thus steeply inclined low plunging tight folds. The  $F_2$  folds are defined by well-developed puckers in muscovite schist, folding of pegmatite veins along with host muscovite schist. The  $F_2$  fold measured from the pucker axis in muscovite schist plunges  $20^\circ \rightarrow 100^\circ$  (Fig 2.1.2b). The  $F_2$  fold measured from folded pegmatite veins in muscovite schist plunges  $30^\circ \rightarrow 95^\circ$ . The attitude of  $F_2$  axial plane of pegmatite veins within muscovite schists is  $95^\circ/70^\circ$  N (Fig 2.1.2g). The  $F_2$  folds are steeply inclined low to moderate plunging tight folds. Therefore, the axial planes of  $F_1$  and  $F_2$  folds are almost parallel. A third generation of open folds ( $F_3$ ), is defined by broad warps of the schistosity within the muscovite schists. These  $F_3$  folds axial plane is tending towards N-S direction. Therefore, in the study area  $F_1$  and  $F_2$  are coaxial and  $F_3$  occurs as a cross fold. Extensional structures defined by the discordant and concordant (with respect to  $S_1$ ) quartz veins within muscovite schist rocks are observed in the area. The concordant and discordant quartz veins exhibit pinch-and-swell and boudinage structures due to layer parallel extension (Fig 2.1.2n). On average this quartz vein trends  $10^\circ$ , thus it is mainly along the  $F_3$  axial plane. So the intrusion of these quartz veins possibly occurred due to the extension in the hinge area of the  $F_3$  fold.

The pegmatite veins have intruded parallel to the foliation ( $S_1$ ) of host muscovite schist or quartz muscovite schist. Relict traces of host muscovite schist are found within the pegmatite vein. Pegmatite veins are deformed and folded (i.e.,  $F_2$ ) along with the host muscovite schist. These features indicate that the intrusion of pegmatite veins is post tectonic with respect to the regional deformation ( $D_1/S_1$ ).

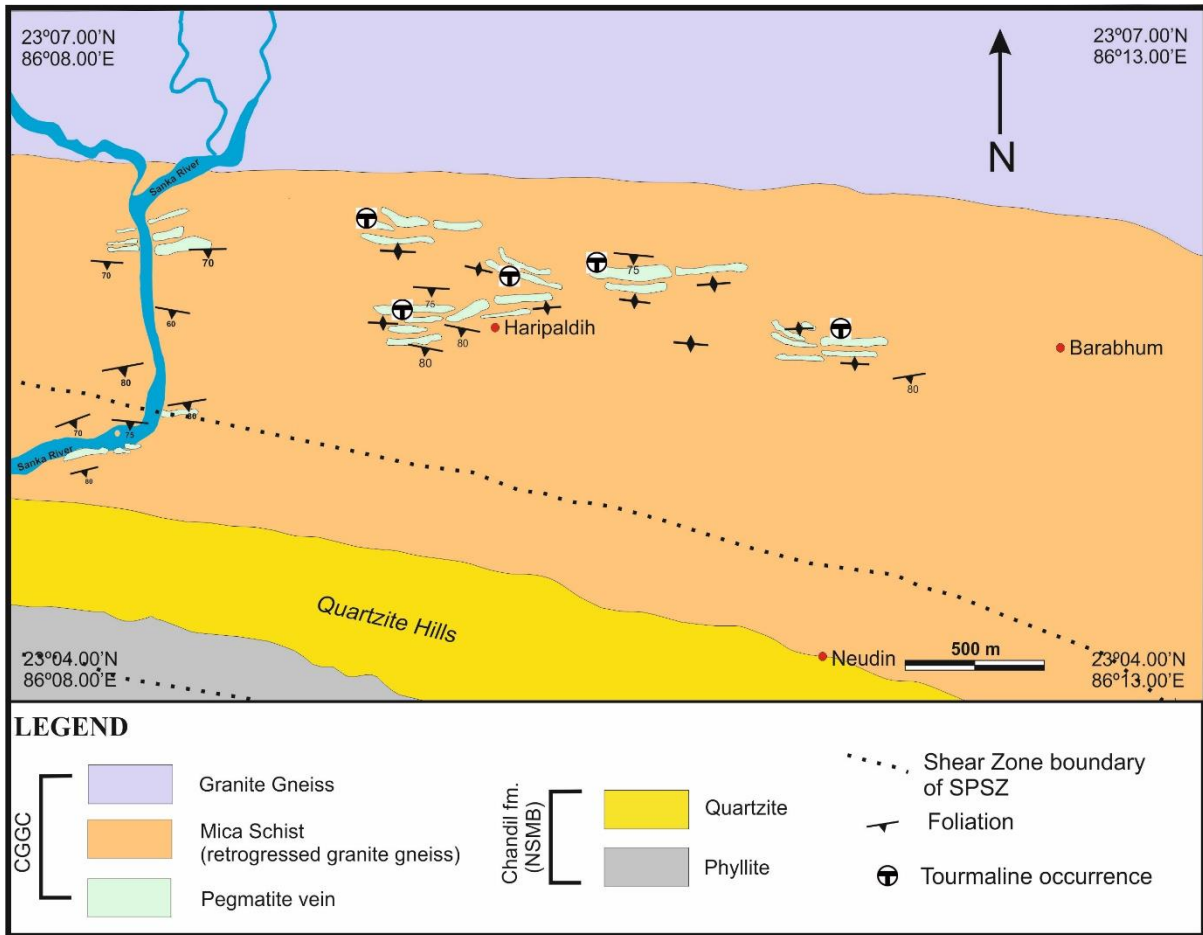


Fig 2.1.1: Lithological map of Haripaldih area, Purulia [ Modified after BRNS funded research project (Sanction no.2008/36/36-BRNS), entitled "Pressure-Temperature-fluid evolution in parts of SPSZ- Implication for boron metasomatism and U-Fe-Cu-P Mineralisation", P.I Pulak Sengupta, 2014]

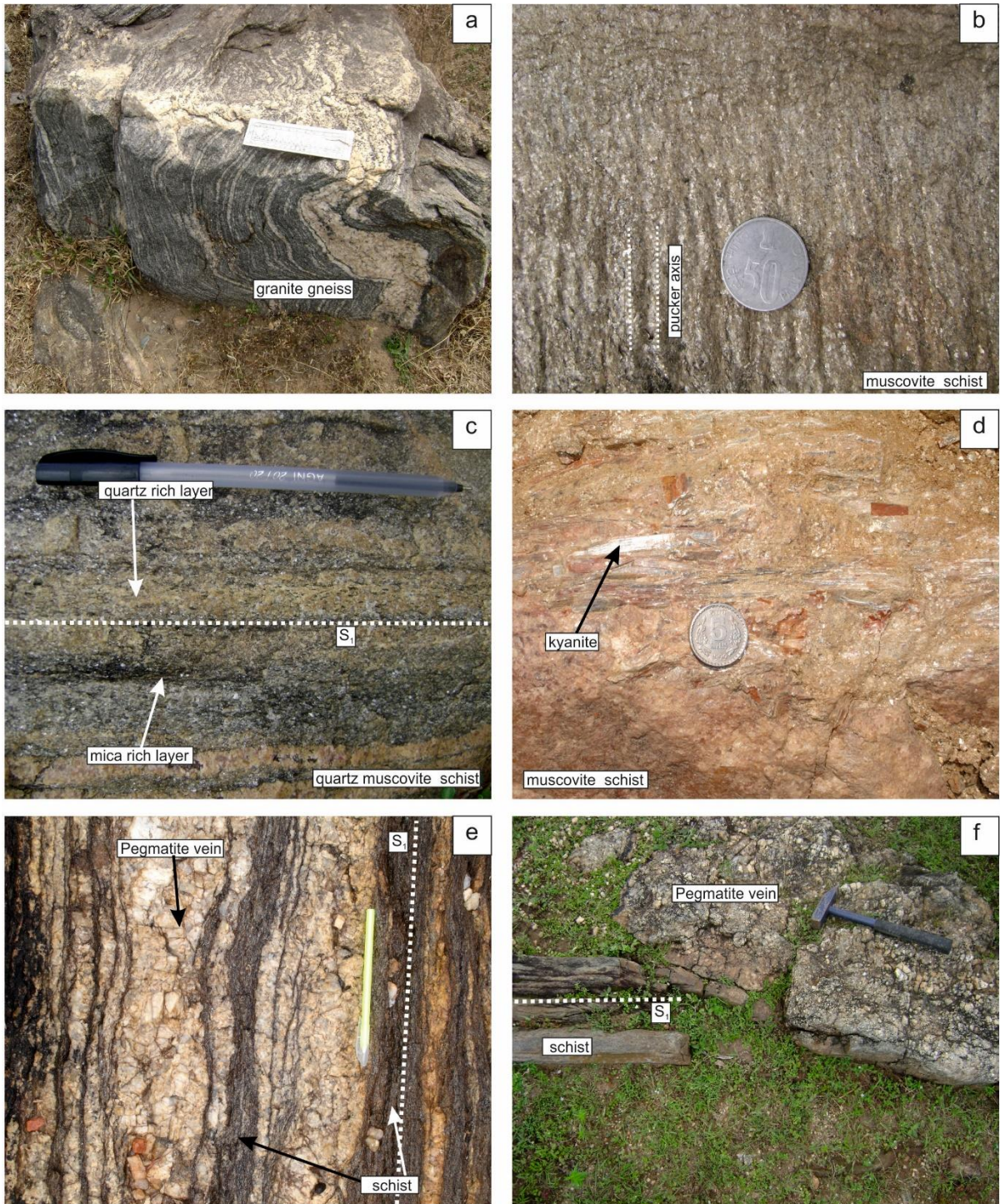


Fig 2.1.2a: Granite gneiss showing gneissic banding, medium to coarse grained leucocratic felsic layer and medium to coarse grained melanocratic layer. Fig 2.1.2b: Muscovite schist are medium to coarse grained, foliation being defined by the phyllosilicate minerals. Pucker axis define by  $F_2$ . Fig 2.1.2c: Quartz muscovite schist showing distinct interbanding of quartzose and micaceous units. Fig 2.1.2d :Segregations of bladed kyanite of centimeter to decimeter scale is present within this quartz muscovite schist. Fig 2.1.2e: Pegmatite veins are run parallel to the general trend of schistose host rock. Relict of schistose host rock is found within the pegmatite. Fig 2.1.2f: Pegmatite veins are show a low angle cross cut relationship with schistose rock.

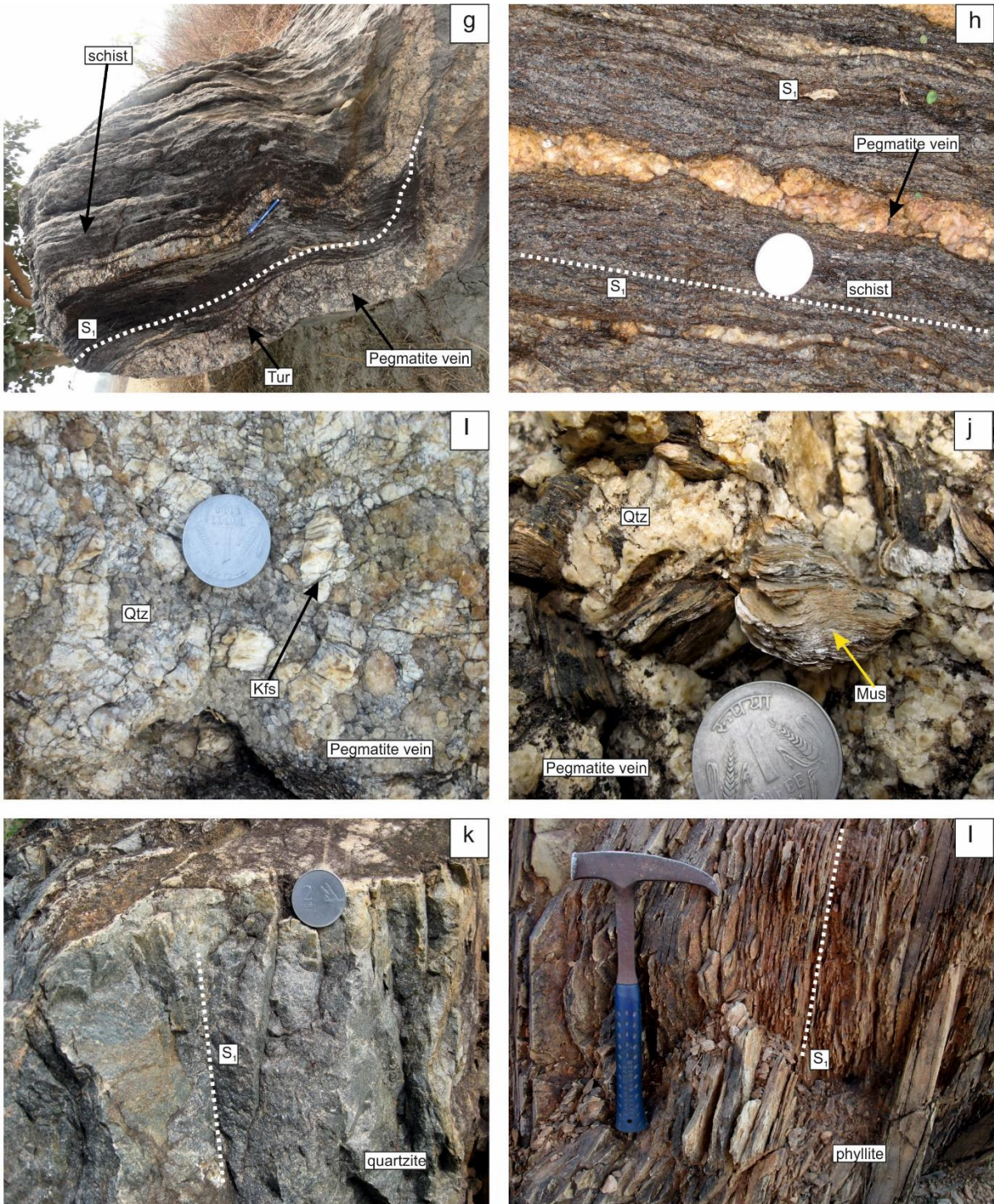


Fig 2.1.2g: The pegmatite veins which are parallel to the foliation defined by muscovite schist or quartz-muscovite schist are deformed and folded ( $F_2$ ). Fig 2.1.2h: Pegmatite veins sometimes show pinch and swell structures due to the layer parallel stretching. Fig 2.1.2i: Pegmatite veins are mainly composed of coarse grained quartz, K-feldspar and muscovite. Fig 2.1.2j: In pegmatite, aggregates of mica ( $>3\text{cm}$ ) formed as mica books. Fig 2.1.2k: Quartzite is gray in colour and sheared. Fig 2.1.2l: Phyllite is finely foliated (defined by flaky minerals) and highly sheared.

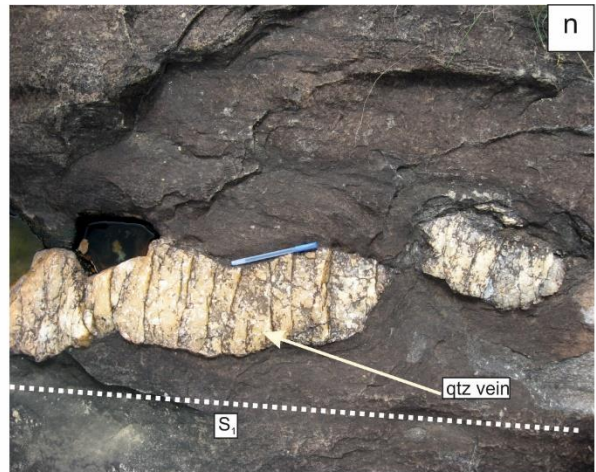
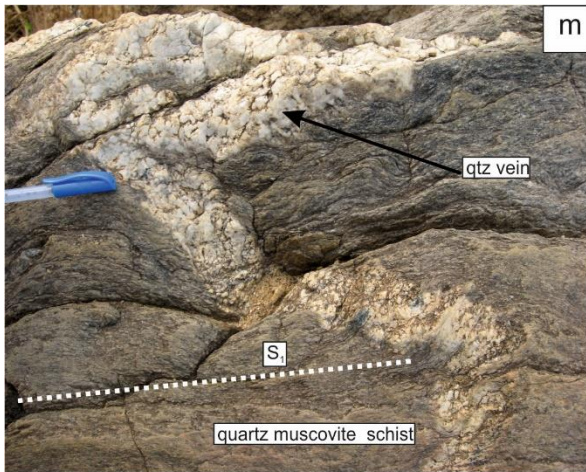


Fig 2.1.2m:  $F_1$  folds are defined by quartz veins within quartz muscovite schist. Fig 2.1.2n: Extensional structures defined by the concordant (with respect to  $S_1$ ) quartz veins within in quartz muscovite schist.

## 2.2 Field features of tourmaline bearing rocks

Tourmaline mineralization occurs within the pegmatite vein hosted in muscovite schist or quartz muscovite schist exposed near Haripaldih village. Tourmalines are seen within the pegmatite veins which intrude along the foliation plane ( $S_1$ ) of muscovite schist/quartz muscovite schist in the study area. Whereas pegmatite veins which are cut across the foliation ( $S_1$ ) are barren in terms of tourmaline mineralization. Within the pegmatite veins tourmaline mineralization is not pervasive but localized.

Based on the size and morphology of tourmaline and the relation of the tourmaline-bearing aggregates with the host rock, three distinct modes of occurrence are established.

**Mode 1:** In pegmatite veins, fine to medium tourmaline aggregates occur in form of mesoscopic veins (0.5- 3 cm thick) (Fig 2.2a). These veins are laterally impersistent and can trace laterally for few meters. Tourmaline veins are lenticular in shape and thickness varies from place to place. These tourmaline rich veins are made up of tourmaline (>50-60 volume %) and quartz. In places, tourmaline rich veins are thickened and occur as pockets (Fig 2.2a). Under hand lens, tourmaline grains within these veins are not showing any preferred orientation. In places, tourmaline veins show pinch and swell structures (Fig 2.2a).

**Mode 2:** In this mode, medium to coarse, disseminated tourmaline aggregates occur within the pegmatite veins. These tourmaline grains are acicular in shape and occur as patches within the pegmatite (Fig 2.2b). Instead of making straight boundary contact with the coarse, euhedral grains of quartz and K-feldspar, the tourmaline occurs as aggregates following the grain boundaries of pegmatite assemblages, i.e. quartz and K-Feldspar and appear as network in the outcrop scale (Fig 2.2b). In places, tourmaline grains grow over the K-feldspar grain of pegmatite. Occasionally massive tourmaline rich aggregates partially engulf the primary assemblage of pegmatite, leaving relicts of quartz and K-feldspar (Fig 2.2c). It indicates that the tourmaline has formed after crystallization of pegmatite veins.

**Mode 3:** In this rare mode of occurrence, tourmaline crystals show forming a patch within pegmatites and show distinct mineral lineation (Fig 2.2d). Coarse grain tourmaline (2-5cm along long axis) shows oriented parallel growth along the movement plane and the lineation is formed. The lineation plunges  $35^\circ \rightarrow 105^\circ$  which is parallel to the  $F_2$  fold seen in pegmatite veins. So the tourmaline mineralisation may occur post  $S_1/D_1$  and syn  $F_2/D_2$ .

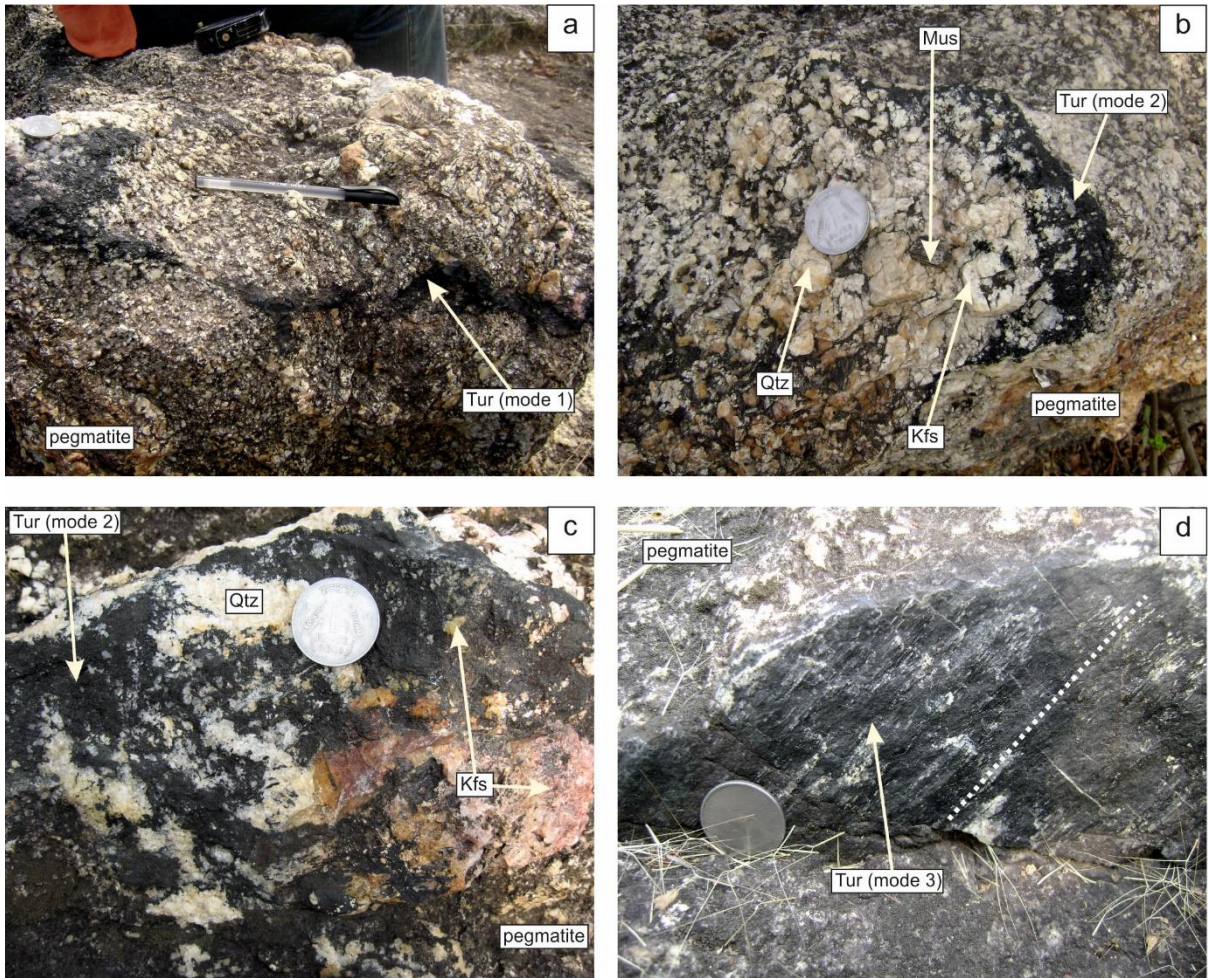


Fig 2.2a: In mode-1, fine to medium tourmaline aggregates occur in form of mesoscopic veins within pegmatite. Fig 2.2b: In mode 2 medium to coarse tourmaline aggregates with disseminated grains occur within pegmatite vein. Fig 2.2c: In mode 2, occasionally massive tourmaline rich aggregates partially engulf and leaving relics of pegmatitic assemblages. Fig 2.2d: In mode 3, tourmaline crystals show distinct mineral lineation.

## 2.3 Petrographic description of tourmaline bearing rocks

The main mineral constituents in pegmatites are quartz+ microcline+ muscovite ± tourmaline. Quartz, being the main constituent mineral of pegmatite veins, occupies more the 50 vol% and shows serrated grain boundaries. Post crystalline deformational features such as, undulose extinction, formation of sub-grains, marginal recrystallization are common in quartz grains (Fig 2.3a). Microcline grains are deformed, partially recrystallized and being replaced by muscovite. (Fig 2.3a and 2.3e). Muscovite grains show dynamic recrystallization (Fig 2.3a). Primary magmatic textures of pegmatite veins are completely obliterated due to intense deformation.

Tourmaline grains occur both as veins and as disseminated aggregates within pegmatite. The mode-1 association tourmaline occurs as veins or patches. Mode 1, while observed under microscope, show variable concentrations of tourmaline, normally 20% to 70% by volume. These tourmaline grains are associated with microcline, muscovite and quartz at the boundary (Fig 2.3a and Fig 2.3c), whereas within the vein tourmaline are associated with quartz (Fig 2.3b). Tourmalines are medium to coarse grained with variable grain size (0.2-2mm along long axis) and prismatic in habit (Fig 2.3b). These grains are euhedral to subhedral with a combination of straight boundaries (Fig 2.3a and 2.3b). In thin sections, at places both prismatic and basal sections of tourmaline grains are found (Fig 2.3b). This feature suggests that the tourmaline grains are randomly oriented. In places, tourmaline grains grow over the microcline-quartz-muscovite assemblage and appear to replace them (Fig 2.3c). Commonly, tourmaline grains show strong pleochroism in the shades of green to dark green. Prismatic tourmaline grains show strong optical zoning with a bluish green core and a greenish brown rim (Fig 2.3b). These grains are formed without any prior orientation but are highly fractured (Fig 2.3a, 2.3b and 2.3c). In mode-2 association, tourmaline aggregates with disseminated grains occur within pegmatite veins. Microcline, muscovite and quartz form the matrix of the rock where coarse grain (0.5mm-5mm along long axis) tourmaline occurs as cluster (Fig 2.3e). In places, tourmaline grains are associated with ilmenite (fig 2.3d). Resorbed quartz grains are included in the prismatic to acicular tourmaline (Fig 2.3d). Commonly, tourmaline grains show strong pleochroism in the shades of light green-green-dark green with faint optical zoning in prismatic sections (Fig 2.3d). Tourmaline grains are highly fractured and show bending due to the deformation (Fig 2.3d). Extensive replacement of microcline by muscovite and clots of tourmaline are recorded (Fig 2.3e). In mode 3, medium to coarse tourmaline grains are associated with quartz. Tourmaline grains are acicular, prismatic and equant in habit. These

grains are mostly euhedral to subhedral with a combination of straight and irregular grain boundaries (Fig 2.3f). Commonly, tourmaline grains show strong pleochroism in the shades of light green-green-dark green with strong optical zoning with a bluish green core and a greenish brown rim (Fig 2.3f)

Tourmaline grains grow over the microcline-quartz-muscovite assemblage of pegmatite and replace them. Thus, the tourmaline grains are formed after pegmatite crystallization.

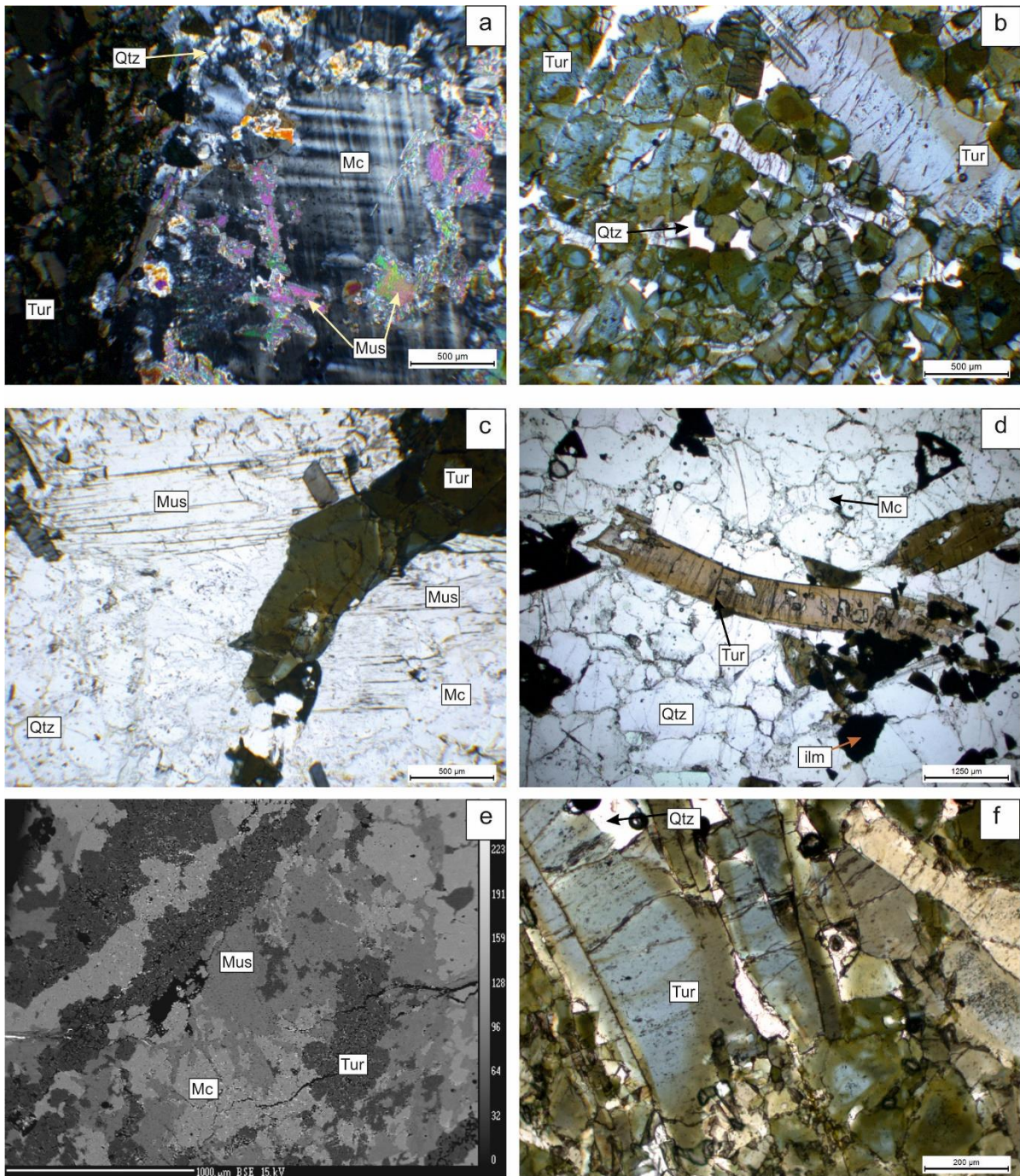


Fig 2.3a: The main mineral constituents in pegmatites are quartz+ microcline+ muscovite ± tourmaline. Quartz, microcline and muscovite shows post crystalline deformation features(under CPL). Fig 2.3b:Both prismatic and basal sections of tourmaline grains are found which indicate that the tourmaline grains are randomly oriented. Fig 2.3c:Tourmaline grains grow over the microcline-quartz-muscovite assemblage and appear to replace them. Fig 2.3d: Fractured tourmaline grains show bending at places due to the deformation. Fig 2.3e:Extensive replacement of microcline by muscovite and clots of tourmaline are recorded(under BSE image).Fig 2.3f: Prismatic tourmaline grains show strong optical zoning with a bluish green core and a greenish brown rim .

## 2.4 Tourmaline mineral chemistry

The standard analytical procedures of major elements analysis and normalization of tourmaline and associate minerals are given in appendix I and II respectively. Representative microprobe analyses of tourmaline are given in Table 2.4.3a. Overall, T sites of tourmalines in pegmatite are nearly filled with Si ( $5.96 \pm 0.05$  apfu, Table 2.4.3a). The Z site of the tourmaline is completely filled up with Al. The Al in apfu of the tourmaline compositions exceeds 6 ( $6.31 \pm 0.15$  apfu) suggesting that some Al must be present in Y site. The Al is higher in core ( $6.46 \pm 0.05$  apfu) than in the Rim ( $6.22 \pm 0.09$  apfu). The Ti in tourmaline structure is higher in the rim ( $0.09 \pm 0.01$  apfu) than in the core ( $0.04 \pm 0.03$  apfu). X-site vacancy, estimated from the measured Na + Ca + K contents, is  $0.24 \pm 0.09$  apfu. X-vacancy is higher in the core ( $0.32 \pm 0.04$  apfu) than in the rim ( $0.19 \pm 0.05$  apfu) of the tourmaline grain. Tourmaline Ca content in their structure ( $0.1 \pm 0.04$  apfu). Core ( $0.07 \pm 0.01$  apfu) compositions is less calcic than the rim ( $0.13 \pm 0.03$  apfu). In terms of the Ca-X-site vacancy-Na+K diagram (Fig 2.4.1.a), all tourmaline grains are plots in the “Alkali group”. By and large, the core compositions of the tourmaline are Ca-poor and X-vacancy rich. In the X/(X + Na) vs.  $X_{Mg}$  diagram (Fig 2.4.1.b) tourmaline grains straddles the boundary between schorl and dravite where  $X_{Mg} = (Mg/Mg+Fe^{2+})$ . Though there exists a compositional overlap between core and rim compositions, the rim compositions are more magnesium and have less X- site vacancies relative to the core compositions. An antipathetic relation between X- vacancy and  $X_{Mg}$  was noted.  $X_{Mg}$  is higher in the rim ( $0.48 \pm 0.02$  apfu) than the core ( $0.44 \pm 0.01$  apfu). Fig 2.4.2a is a line traverse that shows the compositional variation across optical zoning of a tourmaline grain. The optical zoning coincides with significant compositional zoning. In Al<sub>total</sub>-vs- X-site vacancy diagram (Fig 2.4.1c), the spread of tourmaline compositions show that the chemical substitution was dominated and expressed by the exchange vectors towards  $\square Al(NaR)_{-1}$  ( $r^2 = 0.64$ ) where  $R = Fe^{2+} + Mg$ . From the compositional traverse variation diagram it can be confirmed that the  $\square Al(NaR)_{-1}$  ( $r^2 = 0.84$ ) is more dominant substitution (Fig 2.4.2b). In Al vs Fe+Mg diagram it is also evident that the compositions of tourmaline show more affinity to the exchange vector  $\square Al(NaR)_{-1}$  and  $AlO[R(OH)]_{-1}$  ( $r^2 = 0.90$ ) (Fig 2.4.1d). It is also noted from the compositional traverse variation diagram of Al vs Fe+Mg+Ti shows stronger influence of  $AlO[R(OH)]_{-1}$  ( $r^2 = 0.94$ ) (Fig 2.4.2.c) exchange vector. In Xvac vs Ca compositional traverse variation diagram, it shows that lesser extent  $CaRO[\square Al(OH)]_{-1}$  ( $r^2 = 0.65$ ) exchange vector substitution occurs from core to rim (Fig 2.4.2. d). In the  $[R_1 (=Na + Ca) + R_2 (=Fe^{2+} + Mg + Mn)]$  vs.  $[R_3 (=Al + 1.33 \times Ti)]$  plot (Fig 2.4.1.e), tourmaline compositions fall within the upper

half of the parallelogram formed by the lines joining the positions of the tourmaline species. Compositions show more affinity to the exchange vector  $\square\text{Al}(\text{NaR})_{-1}$ . No distinct substitution in terms of Fe- Mg is noted along the vector  $\text{MgFe}_{-1}$ (Fig 2.4.1.f and 2.4.2e).

The  $X_{\text{Kfs}}$  value of the K-feldspar varies from ~0.95-0.98. Muscovite  $\text{FeO}_t$  content varies from 0.61 to 2.59 wt%. Muscovite shows significant amount of pyrophyllite component (~25 mol %). Ilmenite shows nearly end member composition. Compositions of K-feldspar, muscovite and ilmenite are presented in Table 2.4.3b.

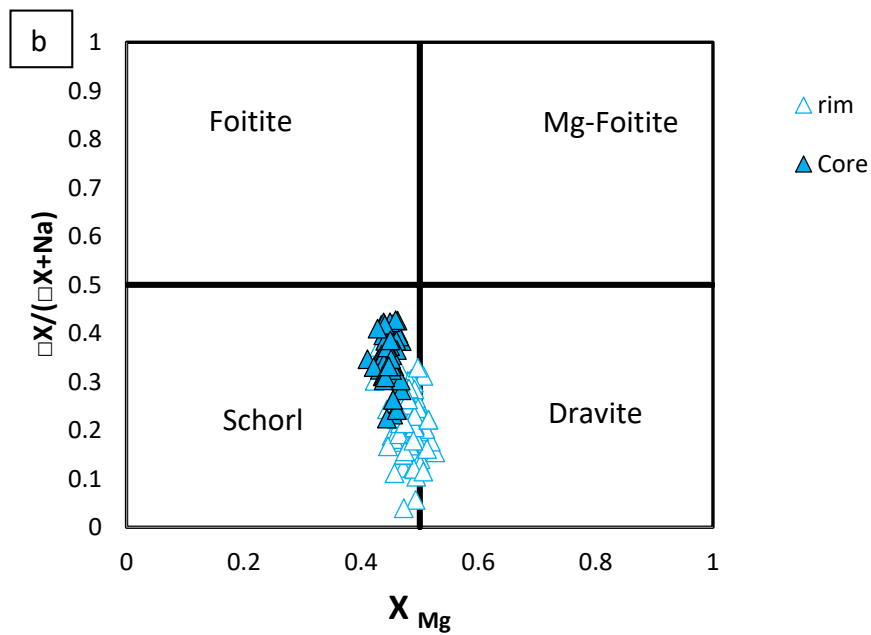
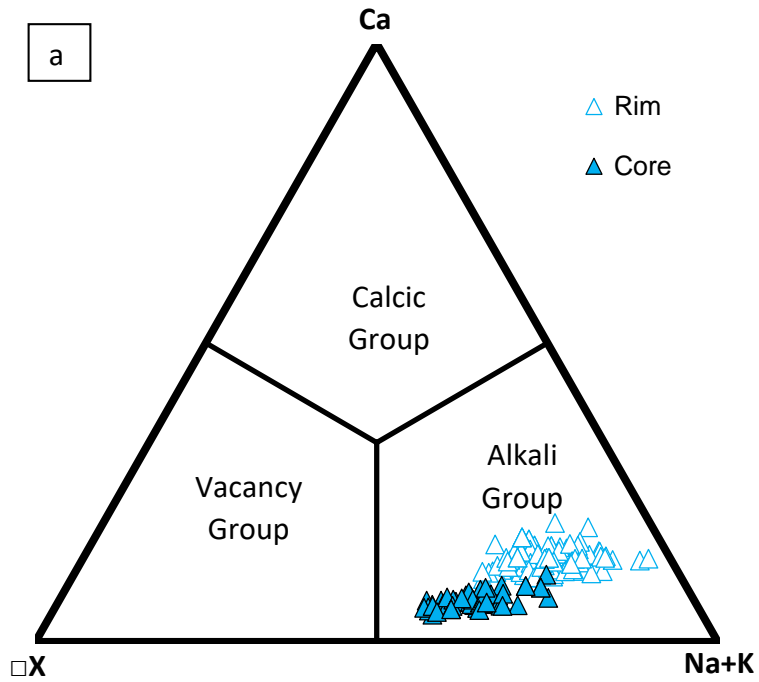


Fig 2.4.1.a Principal tourmaline groups based on the classification scheme of Hawthorne and Henry (1999). Tourmaline are Alkali rich. Fig 2.4.1.b Nomenclature diagram of tourmaline based on X-site vacancy/(X-site vacancy + Na) vs.  $Mg/(Mg + Fe^{2+})$  plot after Henry et al. (2003). Tourmaline grains composition straddles the boundary between schorl and dravite.

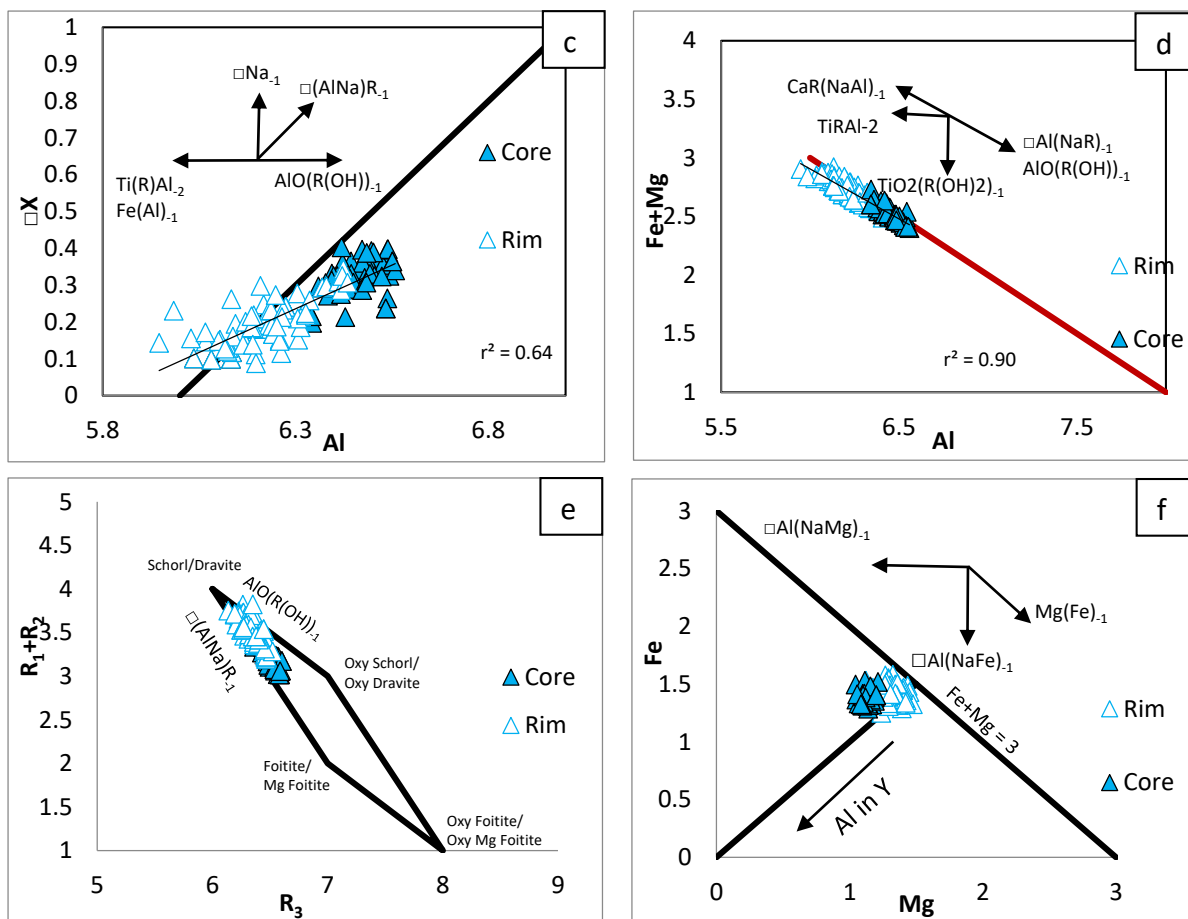


Fig 2.4.1c: In  $Al_{total}$ -vs- X-site vacancy diagram, compositions of tourmaline show more affinity to the exchange vector  $\square Al(NaR)_{-1}$  than the exchange vector  $AlO[R(OH)]_{-1}$ . Fig 2.4.1d In  $Al$  vs  $Fe+Mg$  diagram it is also evident that the compositions of tourmaline show more affinity to the exchange vector  $\square Al(NaR)_{-1}$  and  $AlO[R(OH)]_{-1}$ . Fig 2.4.1e: In the  $[R_1 (=Na + Ca) + R_2 (=Fe^{2+} + Mg + Mn)]$  vs.  $[R_3 (=Al + 1.33 \times Ti)]$  plot, tourmaline compositions fall within the upper half of the parallelogram formed by the lines joining the positions of the tourmaline species. Compositions show more affinity to the exchange vector  $\square Al(NaR)_{-1}$  than the exchange vector  $AlO[R(OH)]_{-1}$ . Fig 2.4.1f: Tourmaline compositions in pegmatitic assemblage form a cluster in  $Fe$ - $Mg$  diagram which implies that no strong substitution trend parallels to vector  $MgFe_{-1}$ .

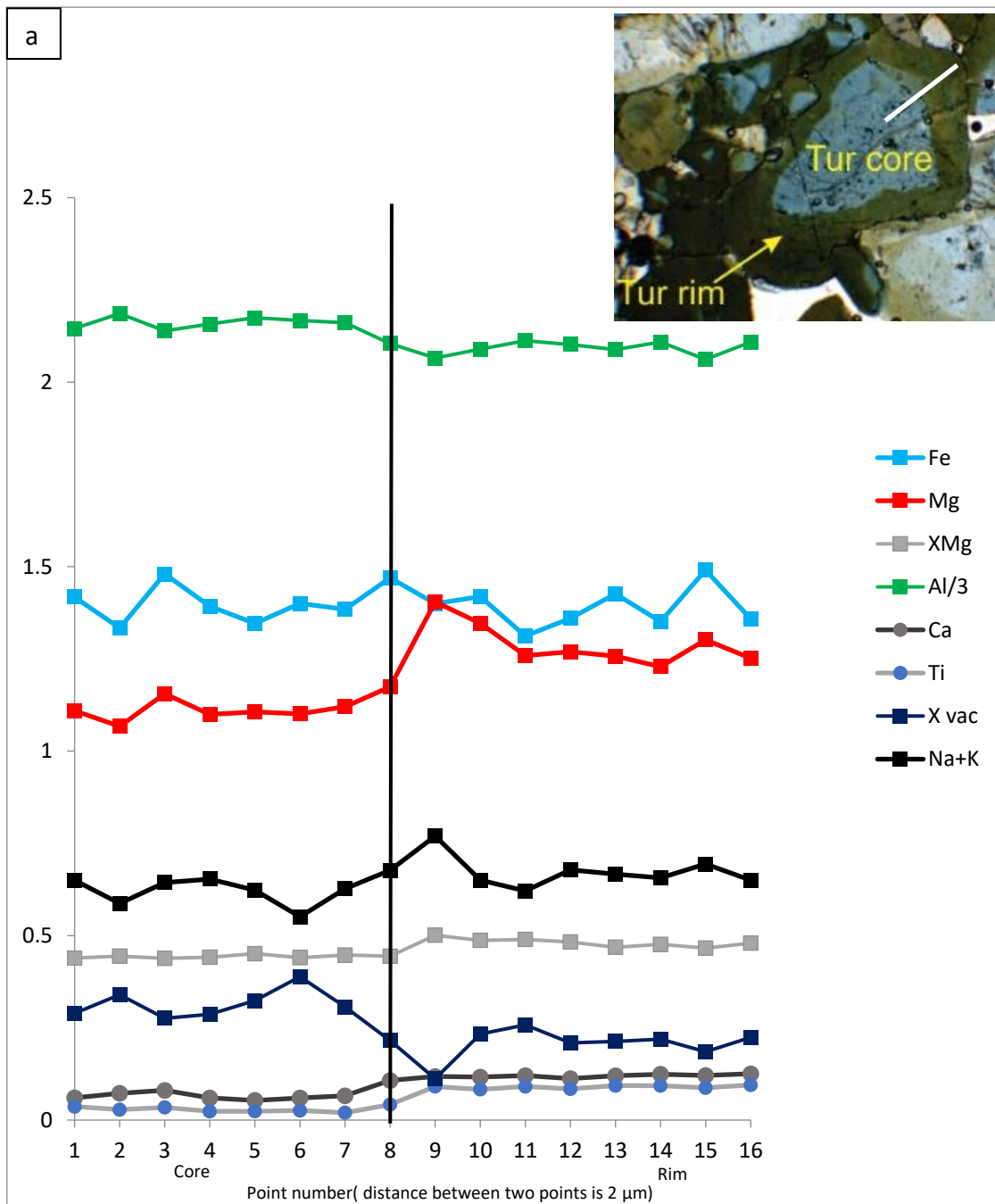


Fig 2.4.2a: Plot of compositional variations from the bluish green colour core and greenish brown in colour rim of a single zoned tourmaline grain in host Pegmatite.  $X_{Mg} = Mg/(Fe^{2+} + Mg)$ . Zero on the X-axis represents the starting point of the compositional traverse from the bluish green colour core. Photomicrograph of the zoned tourmaline and the traverse path is shown by the solid line (plane polarized light). Al is plotted as Al/3.

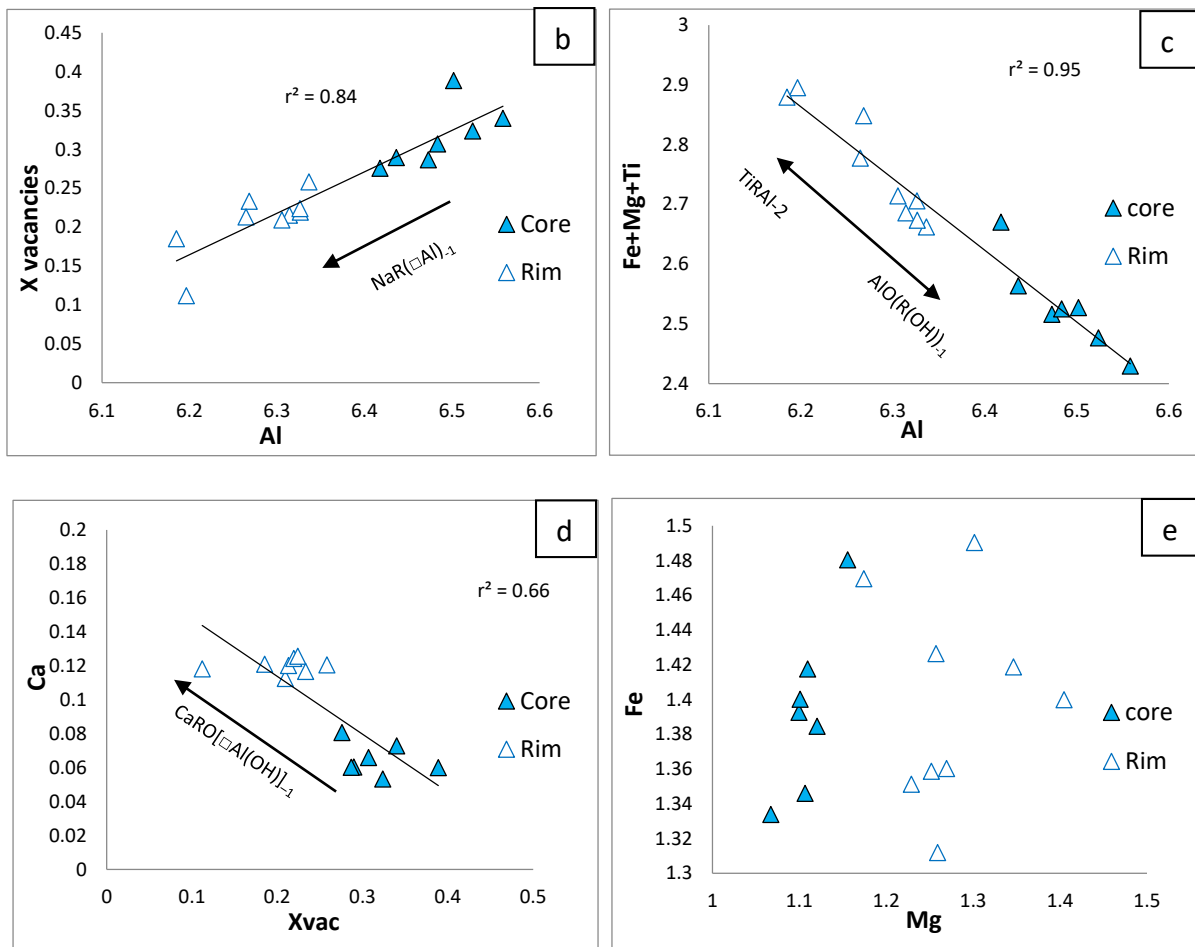


Fig 2.4.2b: Plot of data from the traverse of the zoned grain in terms of X-site vacancy vs. total Al showing positive ( $r^2 = 0.84$ ) correlations. Fig 2.4.2c: Plot of data from the traverse of the zoned grain in terms of Fe+Mg+Ti vs. total Al and shows strong correlations negative ( $r^2 = 0.95$ ). Fig 2.4.2d: Plot of data from the traverse of the zoned grain in terms of Ca vs. X-vac negative ( $r^2 = 0.65$ ) moderate correlations. Fig 2.4.2e: Plot of data from the traverse of the zoned tourmaline grain in terms of Fe vs. Mg showing no correlations.

Table 2.4.3a: Representative EPMA analysis of Tourmaline.

Sample no.	BR2E2	BR2E2	BR2E2	BR2E2	BR2E2	BR2E2	BR2E1	BR2E1	BR2E1	BR2E1	BR2E1	BR2E1	BR2E1	BR2E1	BR2E1	BR2E1	BR2E1	BR2E1	BR2E1	BR2E1
Point	92 / 1	93 / 1	95 / 1	97 / 1	102 / 1.	103 / 1	1 / 1	4 / 1	9 / 1	13 / 1	6 / 1	6 / 2	6 / 3	6 / 4	6 / 5	6 / 6	6 / 7	6 / 8	6 / 9	6 / 10
Core/Rim	core	core	core	core	core	core	core	core	core	core	core	core	core	core	core	core	core	core	core	core
Al <sub>2</sub> O <sub>3</sub>	33.28	33.80	32.95	33.17	33.43	32.29	32.24	33.19	33.11	32.74	32.96	33.01	33.04	33.22	33.07	33.18	33.08	32.74	33.00	32.61
FeO	10.34	9.65	10.02	10.36	10.78	10.90	9.98	9.46	10.00	10.00	9.48	9.38	9.19	9.52	9.74	9.85	9.59	10.04	9.87	9.94
TiO <sub>2</sub>	0.25	0.18	0.48	0.25	0.19	0.44	0.56	0.28	0.31	0.22	0.28	0.24	0.26	0.31	0.26	0.26	0.39	0.47	0.28	0.45
SiO <sub>2</sub>	36.16	36.22	36.06	36.01	35.45	35.13	35.80	36.17	35.91	36.41	36.26	36.22	36.44	36.15	36.20	36.31	36.26	36.02	36.33	36.10
K <sub>2</sub> O	0.02	0.02	0.02	0.04	0.02	0.03	0.06	0.05	0.05	0.05	0.04	0.03	0.04	0.02	0.04	0.09	0.05	0.07	0.07	0.07
CaO	0.36	0.35	0.44	0.42	0.32	0.63	0.39	0.35	0.39	0.45	0.39	0.36	0.38	0.33	0.38	0.39	0.40	0.44	0.38	0.39
Na <sub>2</sub> O	1.96	2.12	1.99	2.22	1.91	2.12	1.90	1.68	1.71	1.87	1.65	1.74	1.78	1.78	1.79	1.84	1.77	1.80	1.80	1.91
Cr <sub>2</sub> O <sub>3</sub>	0.05	0.03	0.00	0.06	0.04	0.04	0.04	0.04	0.00	0.00	0.03	0.00	0.04	0.10	0.00	0.00	0.04	0.00	0.00	0.00
MnO	0.00	0.00	0.08	0.00	0.01	0.09	0.00	0.00	0.00	0.01	0.00	0.11	0.07	0.08	0.02	0.02	0.01	0.00	0.00	0.03
MgO	4.72	4.78	4.82	4.85	4.22	4.88	4.42	4.40	4.56	4.59	4.57	4.55	4.56	4.64	4.52	4.40	4.59	4.82	4.52	4.69
B <sub>2</sub> O <sub>3</sub> *	10.60	10.65	10.57	10.61	10.48	10.44	10.40	10.49	10.50	10.53	10.50	10.49	10.52	10.54	10.52	10.55	10.54	10.53	10.54	10.51
Total	97.74	97.80	97.43	97.99	96.85	96.99	95.79	96.11	96.54	96.87	96.16	96.13	96.32	96.69	96.54	96.89	96.72	96.93	96.79	96.70
Si(T)	5.94	5.94	5.95	5.92	5.89	5.85	6.00	6.00	5.96	6.00	6.00	6.00	6.00	5.99	6.00	6.00	6.00	5.97	6.00	6.00
Al(T)	0.06	0.06	0.05	0.08	0.11	0.15	0.00	0.00	0.04	0.00	0.00	0.00	0.00	0.01	0.00	0.00	0.00	0.03	0.00	0.00
B(T)	3.00	3.00	3.00	3.00	3.00	3.00	3.00	3.00	3.00	3.00	3.00	3.00	3.00	3.00	3.00	3.00	3.00	3.00	3.00	3.00
Al(Z)	6.00	6.00	6.00	6.00	6.00	6.00	6.00	6.00	6.00	6.00	6.00	6.00	6.00	6.00	6.00	6.00	6.00	6.00	6.00	6.00
Al(Y)	0.39	0.48	0.36	0.35	0.43	0.20	0.41	0.54	0.44	0.44	0.50	0.51	0.53	0.47	0.49	0.50	0.48	0.36	0.47	0.39
Ti(Y)	0.03	0.02	0.06	0.03	0.02	0.06	0.07	0.04	0.04	0.03	0.04	0.03	0.03	0.04	0.03	0.03	0.05	0.06	0.04	0.06
Cr(Y)	0.01	0.00	0.00	0.01	0.01	0.01	0.01	0.01	0.00	0.00	0.00	0.00	0.01	0.01	0.00	0.00	0.01	0.00	0.00	0.00
Fe(Y)	1.42	1.32	1.38	1.42	1.50	1.52	1.41	1.32	1.39	1.39	1.33	1.31	1.29	1.32	1.36	1.37	1.33	1.39	1.37	1.38
Mn(Y)	0.00	0.00	0.01	0.00	0.00	0.01	0.00	0.00	0.00	0.00	0.00	0.02	0.01	0.01	0.00	0.00	0.00	0.00	0.00	0.00
Mg(Y)	1.16	1.17	1.19	1.19	1.04	1.21	1.11	1.10	1.13	1.14	1.14	1.13	1.14	1.15	1.12	1.09	1.14	1.19	1.12	1.16
K(X)	0.00	0.00	0.00	0.01	0.00	0.01	0.01	0.01	0.01	0.01	0.01	0.01	0.01	0.00	0.01	0.02	0.01	0.01	0.01	0.01
Ca(X)	0.06	0.06	0.08	0.07	0.06	0.11	0.07	0.06	0.07	0.08	0.07	0.06	0.07	0.06	0.07	0.07	0.07	0.08	0.07	0.07
Na(X)	0.62	0.67	0.63	0.70	0.61	0.68	0.62	0.54	0.55	0.60	0.53	0.56	0.57	0.57	0.57	0.59	0.57	0.58	0.58	0.61
X vacancies	0.31	0.26	0.28	0.21	0.33	0.20	0.30	0.39	0.37	0.31	0.39	0.37	0.35	0.37	0.35	0.32	0.35	0.33	0.34	0.30
X <sub>Mg</sub>	0.45	0.47	0.46	0.45	0.41	0.44	0.44	0.45	0.45	0.45	0.46	0.46	0.47	0.46	0.45	0.44	0.46	0.46	0.45	0.46

Note: Atomic proportions based on ΣT+Z+Y cations = 15. X<sub>Mg</sub> = Mg/(Fe<sup>2+</sup> + Mg).

\* B<sub>2</sub>O<sub>3</sub> calculated assuming B to be 3 atoms per formula unit.

Table 2.4.3a: Representative EPMA analysis of Tourmaline(continued).

Sample no.	BR2E1	BR2E1	BR2E1	BR2E1	BR2E1	BR2E1	BR2E1	BR2E1	BR3C	BR3C	BR2E1	BR3C								
Point	6 / 11	109 / 1	110 / 1	36 / 1	36 / 2	36 / 3	36 / 4	36 / 5	31 / 1	33 / 1	36 / 11	36 / 12	36 / 13	36 / 14	36 / 15	36 / 16	36 / 17	36 / 18	36 / 19	43 / 1
Core/Rim	core	core	core	core	core	core	core	core	core	core	core	core	core	core	core	core	core	core	core	core
Al <sub>2</sub> O <sub>3</sub>	32.49	33.09	33.05	33.13	32.83	33.32	32.89	33.21	33.23	33.76	32.98	32.94	33.09	33.35	32.97	32.75	33.24	32.74	32.83	31.89
FeO	9.72	10.29	10.15	10.20	10.20	9.95	10.33	10.51	10.16	9.95	10.72	10.35	10.25	10.54	10.10	9.97	10.23	10.35	10.20	10.81
TiO <sub>2</sub>	0.61	0.64	0.44	0.24	0.34	0.31	0.40	0.35	0.08	0.17	0.28	0.31	0.31	0.31	0.35	0.36	0.37	0.35	0.45	0.01
SiO <sub>2</sub>	35.86	35.84	35.96	36.03	36.22	36.27	36.25	36.10	36.16	36.58	36.02	36.71	36.07	36.23	35.97	36.28	35.92	36.15	36.14	35.23
K <sub>2</sub> O	0.04	0.01	0.03	0.07	0.02	0.03	0.06	0.08	0.02	0.02	0.06	0.03	0.06	0.02	0.06	0.06	0.05	0.05	0.07	0.05
CaO	0.53	0.08	0.01	0.42	0.34	0.36	0.43	0.35	0.38	0.26	0.47	0.50	0.45	0.36	0.37	0.40	0.37	0.39	0.41	0.50
Na <sub>2</sub> O	1.95	2.08	1.96	1.72	1.80	1.92	1.84	1.87	1.87	1.75	1.82	1.90	1.93	1.90	1.89	1.85	1.94	1.90	1.89	1.84
Cr <sub>2</sub> O <sub>3</sub>	0.05	0.00	0.00	0.07	0.02	0.02	0.00	0.07	0.09	0.14	0.00	0.01	0.03	0.00	0.03	0.00	0.01	0.03	0.05	0.28
MnO	0.08	0.39	0.40	0.00	0.00	0.01	0.04	0.00	0.00	0.04	0.06	0.04	0.10	0.03	0.00	0.03	0.14	0.01	0.00	0.00
MgO	4.79	4.39	4.44	4.46	4.52	4.57	4.54	4.62	4.39	4.29	4.71	4.72	4.76	4.63	4.66	4.63	4.74	4.60	4.48	4.42
B <sub>2</sub> O <sub>3</sub> *	10.49	10.55	10.52	10.52	10.52	10.59	10.56	10.60	10.53	10.64	10.57	10.65	10.58	10.63	10.53	10.53	10.58	10.53	10.53	10.29
Total	96.61	97.36	96.96	96.86	96.81	97.35	97.34	97.76	96.91	97.60	97.69	98.16	97.63	98.00	96.93	96.86	97.59	97.10	97.05	95.32
Si(T)	5.98	5.92	5.95	5.97	6.00	5.98	5.99	5.93	5.99	6.00	5.93	6.00	5.94	5.94	5.96	6.00	5.91	5.99	5.99	5.96
Al(T)	0.02	0.08	0.05	0.03	0.00	0.02	0.01	0.07	0.01	0.00	0.07	0.00	0.06	0.06	0.04	0.00	0.09	0.01	0.01	0.04
B(T)	3.00	3.00	3.00	3.00	3.00	3.00	3.00	3.00	3.00	3.00	3.00	3.00	3.00	3.00	3.00	3.00	3.00	3.00	3.00	3.00
Al(Z)	6.00	6.00	6.00	6.00	6.00	6.00	6.00	6.00	6.00	6.00	6.00	6.00	6.00	6.00	6.00	6.00	6.00	6.00	6.00	6.00
Al(Y)	0.36	0.36	0.39	0.45	0.42	0.46	0.40	0.37	0.49	0.54	0.33	0.38	0.36	0.38	0.40	0.42	0.36	0.38	0.41	0.32
Ti(Y)	0.08	0.08	0.05	0.03	0.04	0.04	0.05	0.04	0.01	0.02	0.03	0.04	0.04	0.04	0.04	0.05	0.05	0.04	0.06	0.00
Cr(Y)	0.01	0.00	0.00	0.01	0.00	0.00	0.00	0.01	0.01	0.02	0.00	0.00	0.00	0.00	0.00	0.00	0.00	0.00	0.01	0.04
Fe(Y)	1.35	1.42	1.40	1.41	1.42	1.37	1.43	1.44	1.41	1.37	1.48	1.42	1.41	1.44	1.40	1.39	1.41	1.43	1.42	1.53
Mn(Y)	0.01	0.05	0.06	0.00	0.00	0.00	0.01	0.00	0.00	0.01	0.01	0.01	0.01	0.00	0.00	0.00	0.02	0.00	0.00	0.00
Mg(Y)	1.19	1.08	1.09	1.10	1.12	1.12	1.12	1.13	1.08	1.05	1.16	1.16	1.17	1.13	1.15	1.15	1.16	1.14	1.11	1.11
K(X)	0.01	0.00	0.01	0.01	0.00	0.01	0.01	0.02	0.00	0.00	0.01	0.01	0.01	0.00	0.01	0.01	0.01	0.01	0.01	0.01
Ca(X)	0.09	0.01	0.00	0.07	0.06	0.06	0.08	0.06	0.07	0.05	0.08	0.09	0.08	0.06	0.07	0.07	0.07	0.07	0.07	0.09
Na(X)	0.63	0.66	0.63	0.55	0.58	0.61	0.59	0.59	0.60	0.55	0.58	0.60	0.61	0.60	0.60	0.59	0.62	0.61	0.60	0.60
X vacancies	0.27	0.32	0.36	0.36	0.36	0.32	0.32	0.33	0.33	0.40	0.32	0.31	0.29	0.33	0.32	0.32	0.31	0.31	0.31	0.30
X <sub>Mg</sub>	0.47	0.43	0.44	0.44	0.44	0.45	0.44	0.44	0.44	0.43	0.44	0.45	0.45	0.44	0.45	0.45	0.45	0.44	0.44	0.42

Note: Atomic proportions based on ΣT+Z+Y cations = 15. X<sub>Mg</sub> = Mg/(Fe<sup>2+</sup> + Mg).

\* B<sub>2</sub>O<sub>3</sub> calculated assuming B to be 3 atoms per formula unit.

Table 2.4.3a: Representative EPMA analysis of Tourmaline(continued).

Sample no.	BR3B	BR3B	BR3B	BR3B	BR3B	BR3B	BR3B	BR3B	BR3B	BR3B	BR3B	BR3B	BR3B	BR3B	BR3B	BR3B	BR3B	BR 3B	BR2E2	BR2E2
Point	7 / 1	9 / 1	11 / 1	13 / 1	16 / 1	58 / 1	58 / 2	58 / 3	58 / 4	58 / 5	58 / 6	58 / 7	58 / 17	58 / 18	58 / 17	58 / 18	8 / 1	54	83 / 1	84 / 1
Core/Rim	core	core	core	core	core	core	core	core	core	core	core	core	core	core	core	core	core	core	rim	rim
Al <sub>2</sub> O <sub>3</sub>	33.79	33.23	33.40	33.42	32.70	32.63	33.87	31.03	33.04	32.94	33.37	32.92	32.22	32.48	32.22	32.48	33.99	33.42	31.52	31.52
FeO	9.68	10.25	10.23	9.54	9.81	10.13	9.71	10.09	10.02	9.58	10.13	9.91	10.05	9.22	10.05	9.22	10.43	9.54	10.08	10.08
TiO <sub>2</sub>	0.26	0.24	0.14	0.22	0.39	0.29	0.23	0.26	0.19	0.19	0.21	0.16	0.54	0.40	0.54	0.40	0.33	0.22	0.89	0.89
SiO <sub>2</sub>	36.69	36.17	36.65	36.37	36.04	36.14	37.15	33.70	36.11	36.28	36.13	35.84	35.84	35.79	35.84	35.79	37.13	36.37	35.79	35.79
K <sub>2</sub> O	0.03	0.04	0.02	0.00	0.00	0.05	0.05	0.04	0.06	0.06	0.04	0.04	0.07	0.02	0.07	0.02	0.02	0.00	0.05	0.05
CaO	0.30	0.38	0.33	0.31	0.32	0.34	0.42	0.43	0.34	0.30	0.34	0.37	0.51	0.52	0.51	0.52	0.29	0.31	0.81	0.81
Na <sub>2</sub> O	1.72	2.00	1.71	1.82	1.68	1.99	1.84	1.87	2.00	1.90	1.70	1.92	2.11	2.05	2.11	2.05	1.79	1.82	2.18	2.18
Cr <sub>2</sub> O <sub>3</sub>	0.05	0.03	0.03	0.00	0.00	0.00	0.00	0.00	0.00	0.00	0.00	0.00	0.00	0.00	0.00	0.00	0.04	0.00	0.05	0.05
MnO	0.07	0.07	0.02	0.07	0.05	0.00	0.09	0.00	0.08	0.00	0.00	0.03	0.03	0.02	0.03	0.02	0.02	0.07	0.02	0.02
MgO	4.43	4.46	4.48	4.38	4.67	4.45	4.36	4.42	4.44	4.42	4.47	4.50	4.82	4.31	4.82	4.31	4.38	4.38	5.73	5.73
B <sub>2</sub> O <sub>3</sub> *	10.66	10.57	10.63	10.55	10.47	10.48	10.74	9.92	10.52	10.49	10.55	10.45	10.47	10.37	10.47	10.37	10.79	10.55	10.54	10.54
Total	97.68	97.44	97.64	96.68	96.13	96.50	98.46	91.76	96.80	96.16	96.94	96.14	96.66	95.18	96.66	95.18	99.21	96.68	97.66	97.66
Si(T)	6.00	5.97	6.00	6.00	6.00	6.00	6.00	5.91	6.00	6.00	5.97	5.99	5.98	6.00	5.98	6.00	6.00	6.00	5.92	5.92
Al(T)	0.00	0.03	0.00	0.00	0.00	0.00	0.00	0.09	0.00	0.00	0.03	0.01	0.02	0.00	0.02	0.00	0.00	0.00	0.08	0.08
B(T)	3.00	3.00	3.00	3.00	3.00	3.00	3.00	3.00	3.00	3.00	3.00	3.00	3.00	3.00	3.00	3.00	3.00	3.00	3.00	3.00
Al(Z)	6.00	6.00	6.00	6.00	6.00	6.00	6.00	6.00	6.00	6.00	6.00	6.00	6.00	6.00	6.00	6.00	6.00	6.00	6.00	6.00
Al(Y)	0.54	0.44	0.47	0.55	0.42	0.44	0.56	0.33	0.47	0.52	0.47	0.47	0.33	0.53	0.33	0.53	0.48	0.55	0.07	0.07
Ti(Y)	0.03	0.03	0.02	0.03	0.05	0.04	0.03	0.03	0.02	0.02	0.03	0.02	0.07	0.05	0.07	0.05	0.04	0.03	0.11	0.11
Cr(Y)	0.01	0.00	0.00	0.00	0.00	0.00	0.00	0.00	0.00	0.00	0.00	0.00	0.00	0.00	0.00	0.00	0.01	0.00	0.01	0.01
Fe(Y)	1.33	1.42	1.41	1.33	1.37	1.42	1.33	1.48	1.39	1.35	1.40	1.38	1.40	1.32	1.40	1.32	1.41	1.33	1.40	1.40
Mn(Y)	0.01	0.01	0.00	0.01	0.01	0.00	0.01	0.00	0.01	0.00	0.00	0.00	0.00	0.00	0.00	0.00	0.00	0.01	0.00	0.00
Mg(Y)	1.08	1.10	1.10	1.09	1.16	1.11	1.07	1.16	1.10	1.11	1.10	1.12	1.20	1.10	1.20	1.10	1.06	1.09	1.41	1.41
K(X)	0.01	0.01	0.00	0.00	0.00	0.01	0.01	0.01	0.01	0.01	0.01	0.01	0.01	0.00	0.01	0.00	0.00	0.00	0.01	0.01
Ca(X)	0.05	0.07	0.06	0.05	0.06	0.06	0.07	0.08	0.06	0.05	0.06	0.07	0.09	0.09	0.09	0.09	0.05	0.05	0.14	0.14
Na(X)	0.54	0.64	0.54	0.58	0.54	0.64	0.58	0.63	0.64	0.61	0.54	0.62	0.68	0.67	0.68	0.67	0.56	0.58	0.70	0.70
X vacancies	0.40	0.29	0.40	0.36	0.40	0.29	0.34	0.28	0.29	0.32	0.39	0.31	0.22	0.24	0.22	0.24	0.39	0.36	0.15	0.15
X <sub>Mg</sub>	0.45	0.44	0.44	0.45	0.46	0.44	0.44	0.44	0.44	0.45	0.44	0.45	0.46	0.45	0.46	0.45	0.43	0.45	0.50	0.50

Note: Atomic proportions based on ΣT+Z+Y cations = 15. X<sub>Mg</sub> = Mg/(Fe<sup>2+</sup> + Mg).

\* B<sub>2</sub>O<sub>3</sub> calculated assuming B to be 3 atoms per formula unit.

Table 2.4.3a: Representative EPMA analysis of Tourmaline(continued).

Sample no.	BR2E2	BR2E2	BR2E2	BR2E2	BR2E2	BR2E1	BR2E2													
Point	89 / 1	90 / 1	91 / 1	100 / 1	101 / 1	6 / 12	6 / 13	6 / 14	6 / 15	6 / 16	6 / 17	6 / 18	6 / 19	6 / 20	36 / 6	36 / 7	36 / 8	36 / 9	36 / 10	82 / 1
Core/Rim	rim	rim	rim	rim	rim	rim	rim	rim	rim	rim	rim	rim	rim	rim	rim	rim	rim	rim	rim	rim
Al <sub>2</sub> O <sub>3</sub>	30.69	30.20	31.42	31.30	31.30	31.82	32.33	32.37	31.75	31.20	31.63	31.77	31.21	31.60	30.89	32.95	32.73	33.05	32.68	31.15
FeO	10.77	10.28	10.73	10.20	10.24	9.81	9.98	9.97	9.94	9.74	9.76	9.77	9.57	9.42	10.57	10.16	10.19	10.53	10.24	9.83
TiO <sub>2</sub>	0.98	1.13	0.79	0.76	0.75	0.92	0.61	0.45	0.64	0.93	0.87	0.94	0.99	0.89	0.33	0.29	0.26	0.25	0.27	0.78
SiO <sub>2</sub>	35.24	35.11	35.28	35.60	35.05	35.85	35.69	36.23	35.49	35.92	35.65	35.64	35.73	35.55	35.87	36.32	36.44	36.34	35.98	36.02
K <sub>2</sub> O	0.05	0.07	0.04	0.05	0.02	0.04	0.04	0.05	0.06	0.07	0.06	0.06	0.05	0.07	0.05	0.07	0.04	0.05	0.04	0.06
CaO	1.07	0.84	0.85	0.82	0.77	0.75	0.59	0.47	0.68	0.83	0.94	0.91	0.96	0.90	0.39	0.44	0.36	0.38	0.44	0.77
Na <sub>2</sub> O	2.16	2.24	2.31	2.26	2.08	1.92	1.84	1.90	1.93	2.09	1.90	1.98	1.93	2.04	1.95	1.88	2.01	1.82	1.83	2.18
Cr <sub>2</sub> O <sub>3</sub>	0.00	0.07	0.00	0.00	0.00	0.00	0.00	0.03	0.03	0.00	0.00	0.00	0.00	0.00	0.00	0.10	0.00	0.03	0.02	0.02
MnO	0.03	0.04	0.05	0.04	0.00	0.00	0.00	0.05	0.01	0.00	0.08	0.02	0.02	0.00	0.00	0.02	0.01	0.00	0.03	0.06
MgO	5.40	5.52	5.82	5.76	5.47	4.99	4.80	4.65	5.19	5.45	5.42	5.49	5.37	5.49	4.35	4.64	4.56	4.47	4.49	5.79
B <sub>2</sub> O <sub>3</sub> *	10.39	10.31	10.50	10.49	10.36	10.47	10.45	10.50	10.41	10.47	10.47	10.50	10.43	10.45	10.25	10.58	10.55	10.58	10.47	10.51
Total	96.78	95.81	97.79	97.28	96.04	96.57	96.33	96.67	96.13	96.70	96.78	97.08	96.26	96.41	94.65	97.45	97.15	97.50	96.49	97.17
Si(T)	5.92	5.95	5.84	5.92	5.89	6.00	5.96	6.00	5.95	6.00	5.95	5.93	6.00	5.96	6.00	5.99	6.00	5.99	6.00	5.99
Al(T)	0.08	0.05	0.16	0.08	0.11	0.00	0.04	0.00	0.05	0.00	0.05	0.07	0.00	0.04	0.00	0.01	0.00	0.01	0.00	0.01
B(T)	3.00	3.00	3.00	3.00	3.00	3.00	3.00	3.00	3.00	3.00	3.00	3.00	3.00	3.00	3.00	3.00	3.00	3.00	3.00	3.00
Al(Z)	6.00	5.99	5.97	6.00	6.00	6.00	6.00	6.00	6.00	6.00	6.00	6.00	6.00	6.00	6.00	6.00	6.00	6.00	6.00	6.00
Al(Y)	0.01	0.00	0.00	0.05	0.10	0.27	0.33	0.38	0.22	0.16	0.17	0.16	0.18	0.20	0.30	0.40	0.42	0.41	0.42	0.09
Ti(Y)	0.12	0.14	0.10	0.10	0.09	0.12	0.08	0.06	0.08	0.12	0.11	0.12	0.13	0.11	0.04	0.04	0.03	0.03	0.03	0.10
Cr(Y)	0.00	0.01	0.00	0.00	0.00	0.00	0.00	0.00	0.00	0.00	0.00	0.00	0.00	0.00	0.00	0.01	0.00	0.00	0.00	0.00
Fe(Y)	1.51	1.46	1.49	1.42	1.44	1.37	1.39	1.39	1.39	1.36	1.36	1.36	1.34	1.32	1.53	1.40	1.42	1.45	1.43	1.37
Mn(Y)	0.00	0.01	0.01	0.01	0.00	0.00	0.00	0.01	0.00	0.00	0.01	0.00	0.00	0.00	0.00	0.00	0.00	0.00	0.00	0.01
Mg(Y)	1.35	1.39	1.44	1.43	1.37	1.24	1.20	1.16	1.30	1.36	1.35	1.36	1.34	1.37	1.12	1.14	1.13	1.10	1.12	1.43
K(X)	0.01	0.02	0.01	0.01	0.00	0.01	0.01	0.01	0.01	0.01	0.01	0.01	0.01	0.01	0.01	0.01	0.01	0.01	0.01	0.01
Ca(X)	0.19	0.15	0.15	0.15	0.14	0.13	0.11	0.08	0.12	0.15	0.17	0.16	0.17	0.16	0.07	0.08	0.06	0.07	0.08	0.14
Na(X)	0.70	0.73	0.74	0.73	0.68	0.62	0.59	0.61	0.62	0.67	0.61	0.63	0.62	0.66	0.64	0.60	0.64	0.58	0.59	0.70
X vacancies	0.10	0.10	0.10	0.12	0.18	0.24	0.29	0.30	0.24	0.17	0.21	0.19	0.19	0.17	0.28	0.31	0.29	0.34	0.32	0.15
X <sub>Mg</sub>	0.47	0.49	0.49	0.50	0.49	0.48	0.46	0.45	0.48	0.50	0.50	0.50	0.50	0.51	0.42	0.45	0.44	0.43	0.44	0.51

Note: Atomic proportions based on ΣT+Z+Y cations = 15. X<sub>Mg</sub> = Mg/(Fe<sup>2+</sup> + Mg).

\* B<sub>2</sub>O<sub>3</sub> calculated assuming B to be 3 atoms per formula unit.

Table 2.4.3a: Representative EPMA analysis of Tourmaline(continued).

Sample no.	BR2E2	BR2E2	BR2E2	BR2E2	BR2E2	BR2E1	BR2E1	BR2E1	BR2E1	BR2E1	BR2E1	BR2E1	BR2E1	BR2E1	BR2E1	BR2E1	BR2E1	BR2E1	BR2E1	BR2E1
Point	85 / 1	94 / 1	96 / 1	98 / 1	99 / 1	2/1	3/1	6 / 15	6 / 16	6 / 17	6 / 18	6 / 19	6 / 20	7 / 1	8 / 1	10 / 1	11 / 1	12 / 1	14 / 1	15 / 1
Core/Rim	rim	rim	rim	rim	rim	rim	rim	rim	rim	rim	rim	rim	rim	rim	rim	rim	rim	rim	rim	rim
Al <sub>2</sub> O <sub>3</sub>	30.91	32.01	31.14	31.30	30.42	30.94	30.24	31.75	31.20	31.63	31.77	31.21	31.60	29.93	31.02	31.74	30.87	30.95	32.93	31.16
FeO	10.28	10.37	9.50	10.63	8.77	10.04	10.95	9.94	9.74	9.76	9.77	9.57	9.42	11.22	9.81	9.93	10.39	10.10	10.21	10.75
TiO <sub>2</sub>	1.00	0.71	0.80	0.77	0.43	1.01	1.24	0.64	0.93	0.87	0.94	0.99	0.89	1.13	0.83	0.97	0.96	0.88	0.23	0.88
SiO <sub>2</sub>	35.53	35.67	35.75	35.87	33.86	35.42	35.37	35.49	35.92	35.65	35.64	35.73	35.55	35.74	35.43	35.80	35.74	35.74	36.50	35.42
K <sub>2</sub> O	0.04	0.04	0.04	0.04	0.04	0.07	0.07	0.06	0.07	0.06	0.06	0.05	0.07	0.06	0.08	0.03	0.10	0.04	0.03	0.06
CaO	0.88	0.67	0.87	0.85	0.70	0.84	0.88	0.68	0.83	0.94	0.91	0.96	0.90	1.11	0.86	0.92	0.90	0.85	0.43	0.94
Na <sub>2</sub> O	2.14	2.25	2.20	2.17	2.09	1.97	2.06	1.93	2.09	1.90	1.98	1.93	2.04	1.99	1.93	1.82	2.01	2.10	1.92	2.17
Cr <sub>2</sub> O <sub>3</sub>	0.09	0.04	0.02	0.00	0.00	0.03	0.02	0.03	0.00	0.00	0.00	0.00	0.00	0.02	0.00	0.00	0.05	0.00	0.00	0.00
MnO	0.00	0.07	0.04	0.00	0.00	0.00	0.02	0.01	0.00	0.08	0.02	0.02	0.00	0.02	0.05	0.06	0.00	0.01	0.00	0.00
MgO	5.84	5.19	5.93	5.70	5.31	5.35	5.07	5.19	5.45	5.42	5.49	5.37	5.49	5.27	5.39	5.35	5.64	5.30	4.54	5.49
B <sub>2</sub> O <sub>3</sub> *	10.47	10.52	10.47	10.54	9.94	10.37	10.34	10.41	10.47	10.47	10.50	10.43	10.45	10.39	10.36	10.51	10.47	10.41	10.58	10.46
Total	97.18	97.54	96.76	97.87	91.56	96.04	96.26	96.13	96.70	96.78	97.08	96.26	96.41	96.88	95.76	97.13	97.13	96.38	97.37	97.33
Si(T)	5.92	5.92	5.97	5.93	5.95	5.97	5.98	5.95	6.00	5.95	5.93	6.00	5.96	6.00	5.98	5.95	5.96	6.00	6.00	5.90
Al(T)	0.08	0.08	0.03	0.07	0.05	0.03	0.02	0.05	0.00	0.05	0.07	0.00	0.04	0.00	0.02	0.05	0.04	0.00	0.00	0.10
B(T)	3.00	3.00	3.00	3.00	3.00	3.00	3.00	3.00	3.00	3.00	3.00	3.00	3.00	3.00	3.00	3.00	3.00	3.00	3.00	3.00
Al(Z)	5.98	6.00	6.00	6.00	6.00	6.00	6.00	6.00	6.00	6.00	6.00	6.00	6.00	5.95	6.00	6.00	6.00	6.00	6.00	6.00
Al(Y)	0.00	0.18	0.09	0.03	0.26	0.11	0.01	0.22	0.16	0.17	0.16	0.18	0.20	0.00	0.15	0.17	0.02	0.14	0.43	0.03
Ti(Y)	0.13	0.09	0.10	0.10	0.06	0.13	0.16	0.08	0.12	0.11	0.12	0.13	0.11	0.14	0.11	0.12	0.12	0.11	0.03	0.11
Cr(Y)	0.01	0.01	0.00	0.00	0.00	0.00	0.00	0.00	0.00	0.00	0.00	0.00	0.00	0.00	0.00	0.00	0.01	0.00	0.00	0.00
Fe(Y)	1.43	1.44	1.33	1.47	1.29	1.41	1.55	1.39	1.36	1.36	1.36	1.34	1.32	1.58	1.38	1.38	1.45	1.42	1.42	1.50
Mn(Y)	0.00	0.01	0.01	0.00	0.00	0.00	0.00	0.00	0.00	0.01	0.00	0.00	0.00	0.00	0.01	0.01	0.00	0.00	0.00	0.00
Mg(Y)	1.45	1.28	1.47	1.40	1.39	1.34	1.28	1.30	1.36	1.35	1.36	1.34	1.37	1.32	1.36	1.32	1.40	1.33	1.12	1.36
K(X)	0.01	0.01	0.01	0.01	0.01	0.01	0.02	0.01	0.01	0.01	0.01	0.01	0.01	0.01	0.02	0.01	0.02	0.01	0.01	0.01
Ca(X)	0.16	0.12	0.15	0.15	0.13	0.15	0.16	0.12	0.15	0.17	0.16	0.17	0.16	0.20	0.15	0.16	0.16	0.15	0.08	0.17
Na(X)	0.69	0.72	0.71	0.69	0.71	0.64	0.67	0.62	0.67	0.61	0.63	0.62	0.66	0.65	0.63	0.58	0.65	0.68	0.61	0.70
X vacancies	0.15	0.15	0.13	0.15	0.15	0.19	0.16	0.24	0.17	0.21	0.19	0.19	0.17	0.14	0.20	0.25	0.17	0.16	0.31	0.12
X <sub>Mg</sub>	0.50	0.47	0.53	0.49	0.52	0.49	0.45	0.48	0.50	0.50	0.50	0.50	0.51	0.46	0.49	0.49	0.49	0.48	0.44	0.48

Note: Atomic proportions based on ΣT+Z+Y cations = 15. X<sub>Mg</sub> = Mg/(Fe<sup>2+</sup> + Mg).

\* B2O3 calculated assuming B to be 3 atoms per formula unit.

Table 2.4.3a: Representative EPMA analysis of Tourmaline(continued).

Sample no.	BR2E1	BR2E1	BR2E1	BR2E1	BR2E1	BR2E1	BR2E1	BR3C	BR3C	BR3C	BR3C	BR3C	BR3B	BR3B	BR3B	BR3B	BR3B	BR3B	BR3B	BR3B
Point	16 / 1	36 / 20	105 / 1	106 / 1	107 / 1	108 / 1	111 / 1	32 / 1	34 / 1	40 / 1	41 / 1	42 / 1	2 / 1	58 / 8	58 / 9	58 / 10	58 / 11	58 / 12	58 / 13	58 / 14
Core/Rim	rim	rim	rim	rim	rim	rim	rim	rim	rim	rim	rim	rim	rim	rim	rim	rim	rim	rim	rim	rim
Al <sub>2</sub> O <sub>3</sub>	31.28	31.87	31.36	30.79	31.35	31.50	31.55	31.78	31.83	31.91	31.70	31.10	31.87	31.61	31.34	31.72	31.49	31.90	32.06	32.02
FeO	10.39	10.44	11.30	11.26	11.09	9.71	10.17	9.63	9.71	9.80	9.56	10.30	9.71	10.37	9.98	10.12	9.19	9.70	10.29	9.64
TiO <sub>2</sub>	1.03	0.67	0.37	1.27	0.62	0.83	1.05	0.00	0.00	0.22	0.00	0.10	0.75	0.33	0.72	0.66	0.71	0.67	0.75	0.74
SiO <sub>2</sub>	35.69	35.88	35.58	35.85	35.10	34.91	34.90	35.76	35.76	36.44	35.52	35.18	36.14	35.97	35.17	35.04	35.81	35.60	35.93	36.00
K <sub>2</sub> O	0.05	0.02	0.04	0.06	0.05	0.07	0.03	0.05	0.04	0.05	0.05	0.03	0.04	0.03	0.04	0.05	0.06	0.03	0.07	0.05
CaO	0.91	0.63	0.92	0.04	0.01	0.06	0.02	0.71	0.76	0.62	0.63	0.78	0.70	0.60	0.66	0.65	0.67	0.63	0.68	0.70
Na <sub>2</sub> O	2.19	2.04	2.14	2.34	2.24	2.33	2.13	2.32	2.20	2.17	2.12	2.05	1.99	2.07	2.35	1.97	1.87	2.08	2.04	2.01
Cr <sub>2</sub> O <sub>3</sub>	0.04	0.00	0.05	0.00	0.02	0.00	0.00	0.51	0.61	0.55	0.47	0.56	0.00	0.00	0.00	0.00	0.00	0.00	0.00	0.00
MnO	0.09	0.05	0.06	0.76	0.92	0.98	0.76	0.06	0.00	0.00	0.00	0.02	0.07	0.00	0.07	0.07	0.01	0.08	0.02	0.00
MgO	5.56	5.18	5.10	5.25	5.23	5.60	5.25	5.37	5.40	5.27	5.06	5.26	5.31	4.65	5.62	5.39	4.95	5.08	5.09	4.92
B <sub>2</sub> O <sub>3</sub> *	10.53	10.51	10.45	10.51	10.40	10.38	10.37	10.45	10.47	10.57	10.35	10.31	10.53	10.39	10.40	10.38	10.35	10.43	10.54	10.48
Total	97.76	97.29	97.37	98.13	97.03	96.37	96.23	96.64	96.78	97.60	95.46	95.69	97.11	96.02	96.35	96.05	95.11	96.20	97.47	96.56
Si(T)	5.92	5.95	5.93	5.91	5.82	5.82	5.83	5.98	5.96	6.00	6.00	5.94	6.00	6.00	5.90	5.87	6.00	5.97	5.96	6.00
Al(T)	0.08	0.05	0.07	0.09	0.18	0.18	0.17	0.02	0.04	0.00	0.00	0.06	0.00	0.00	0.10	0.13	0.00	0.03	0.04	0.00
B(T)	3.00	3.00	3.00	3.00	3.00	3.00	3.00	3.00	3.00	3.00	3.00	3.00	3.00	3.00	3.00	3.00	3.00	3.00	3.00	3.00
Al(Z)	6.00	6.00	6.00	5.89	5.96	6.00	6.00	6.00	6.00	6.00	6.00	6.00	6.00	6.00	6.00	6.00	6.00	6.00	6.00	6.00
Al(Y)	0.04	0.18	0.10	0.00	0.00	0.01	0.03	0.24	0.22	0.24	0.31	0.13	0.24	0.31	0.09	0.14	0.34	0.27	0.22	0.33
Ti(Y)	0.13	0.08	0.05	0.16	0.08	0.10	0.13	0.00	0.00	0.03	0.00	0.01	0.09	0.04	0.09	0.08	0.09	0.08	0.09	0.09
Cr(Y)	0.01	0.00	0.01	0.00	0.00	0.00	0.00	0.07	0.08	0.07	0.06	0.07	0.00	0.00	0.00	0.00	0.00	0.00	0.00	0.00
Fe(Y)	1.44	1.45	1.58	1.55	1.54	1.35	1.42	1.35	1.35	1.36	1.35	1.45	1.35	1.47	1.40	1.42	1.31	1.36	1.43	1.35
Mn(Y)	0.01	0.01	0.01	0.11	0.13	0.14	0.11	0.01	0.00	0.00	0.00	0.00	0.01	0.00	0.01	0.01	0.00	0.01	0.00	0.00
Mg(Y)	1.37	1.28	1.27	1.29	1.29	1.39	1.31	1.34	1.34	1.30	1.27	1.32	1.31	1.17	1.40	1.35	1.26	1.27	1.26	1.23
K(X)	0.01	0.00	0.01	0.01	0.01	0.01	0.01	0.01	0.01	0.01	0.01	0.01	0.01	0.01	0.01	0.01	0.01	0.01	0.01	0.01
Ca(X)	0.16	0.11	0.16	0.01	0.00	0.01	0.00	0.13	0.14	0.11	0.11	0.14	0.12	0.11	0.12	0.12	0.12	0.11	0.12	0.12
Na(X)	0.70	0.65	0.69	0.75	0.73	0.76	0.69	0.75	0.71	0.69	0.69	0.67	0.64	0.67	0.76	0.64	0.61	0.67	0.65	0.65
X vacancies	0.13	0.23	0.14	0.23	0.26	0.22	0.30	0.12	0.15	0.19	0.19	0.18	0.23	0.22	0.11	0.23	0.26	0.21	0.21	0.22
X <sub>Mg</sub>	0.49	0.47	0.45	0.45	0.46	0.51	0.48	0.50	0.50	0.49	0.49	0.48	0.49	0.44	0.50	0.49	0.49	0.48	0.47	0.48

Note: Atomic proportions based on ΣT+Z+Y cations = 15. X<sub>Mg</sub> = Mg/(Fe<sup>2+</sup> + Mg).

\* B<sub>2</sub>O<sub>3</sub> calculated assuming B to be 3 atoms per formula unit.

Table 2.4.3a: Representative EPMA analysis of Tourmaline(continued).

Sample no.	BR3B	BR3B	BR3B	BR3B	BR3B	BR3B	BR3B	BR3B	BR3B	BR3B	BR3B	BR3B	BR3B	BR3B	BR3B	BR3B	BR3B	BR3B	BR3B	BR3B
Point	58 / 15	58 / 16	58 / 19	58 / 20	25 / 1	59 / 1	59 / 2	59 / 3	59 / 4	59 / 5	59 / 6	59 / 7	59 / 8	59 / 9	59 / 10	59 / 11	59 / 12	59 / 13	59 / 14	59 / 15
Core/Rim	rim	rim	rim	rim	rim	rim	rim	rim	rim	rim	rim	rim	rim	rim	rim	rim	rim	rim	rim	rim
Al <sub>2</sub> O <sub>3</sub>	31.06	31.81	30.67	31.24	31.05	31.49	31.58	31.77	31.54	31.68	29.87	31.54	30.34	31.63	31.69	31.94	32.34	31.87	31.82	31.82
FeO	10.55	9.63	9.87	9.67	9.92	9.79	9.43	9.50	10.33	10.29	10.25	9.91	9.05	10.35	9.97	9.86	10.28	10.35	9.88	10.10
TiO <sub>2</sub>	0.69	0.75	0.66	0.69	0.79	0.81	0.74	0.71	0.77	0.60	0.72	0.69	0.74	0.66	0.74	0.61	0.82	0.72	0.77	0.80
SiO <sub>2</sub>	35.14	35.37	34.45	35.28	35.64	35.75	35.61	35.48	36.02	35.39	33.29	35.22	33.78	35.34	35.34	36.13	36.35	36.22	35.21	35.64
K <sub>2</sub> O	0.07	0.05	0.08	0.04	0.09	0.02	0.03	0.00	0.04	0.04	0.02	0.05	0.01	0.01	0.06	0.03	0.07	0.03	0.03	0.04
CaO	0.67	0.70	0.75	0.74	0.84	0.76	0.66	0.62	0.72	0.66	0.76	0.76	0.76	0.68	0.64	0.66	0.66	0.75	0.73	0.77
Na <sub>2</sub> O	2.08	1.97	2.29	2.22	1.89	2.08	1.86	2.11	2.09	2.18	2.22	2.49	2.22	2.24	2.29	1.90	1.86	2.04	2.06	1.91
Cr <sub>2</sub> O <sub>3</sub>	0.00	0.00	0.00	0.00	0.00	0.00	0.00	0.00	0.00	0.00	0.00	0.00	0.00	0.00	0.00	0.00	0.00	0.00	0.00	0.00
MnO	0.00	0.01	0.11	0.06	0.00	0.00	0.00	0.00	0.04	0.04	0.00	0.00	0.00	0.04	0.00	0.00	0.03	0.03	0.16	0.00
MgO	5.17	4.98	5.41	5.70	5.21	5.05	5.43	5.24	4.97	5.02	4.84	5.41	4.88	5.42	5.01	5.23	5.05	5.13	4.92	4.92
B <sub>2</sub> O <sub>3</sub> *	10.32	10.37	10.18	10.38	10.37	10.42	10.40	10.40	10.48	10.40	9.87	10.41	9.94	10.44	10.39	10.51	10.62	10.56	10.38	10.44
Total	95.75	95.64	94.47	96.02	95.80	96.17	95.74	95.83	97.00	96.30	91.84	96.48	91.72	96.81	96.13	96.87	98.08	97.70	95.96	96.44
Si(T)	5.94	5.97	5.90	5.93	6.00	6.00	5.98	5.96	6.00	5.94	5.89	5.92	5.96	5.90	5.95	6.00	5.98	5.99	5.93	5.97
Al(T)	0.06	0.03	0.10	0.07	0.00	0.00	0.02	0.04	0.00	0.06	0.11	0.08	0.04	0.10	0.05	0.00	0.02	0.01	0.07	0.03
B(T)	3.00	3.00	3.00	3.00	3.00	3.00	3.00	3.00	3.00	3.00	3.00	3.00	3.00	3.00	3.00	3.00	3.00	3.00	3.00	3.00
Al(Z)	6.00	6.00	6.00	6.00	6.00	6.00	6.00	6.00	6.00	6.00	6.00	6.00	6.00	6.00	6.00	6.00	6.00	6.00	6.00	6.00
Al(Y)	0.12	0.29	0.10	0.12	0.19	0.25	0.22	0.26	0.22	0.22	0.11	0.17	0.28	0.12	0.24	0.26	0.24	0.21	0.25	0.26
Ti(Y)	0.09	0.10	0.09	0.09	0.10	0.10	0.09	0.09	0.10	0.08	0.10	0.09	0.10	0.08	0.09	0.08	0.10	0.09	0.10	0.10
Cr(Y)	0.00	0.00	0.00	0.00	0.00	0.00	0.00	0.00	0.00	0.00	0.00	0.00	0.00	0.00	0.00	0.00	0.00	0.00	0.00	0.00
Fe(Y)	1.49	1.36	1.41	1.36	1.40	1.38	1.32	1.34	1.44	1.45	1.52	1.39	1.34	1.44	1.40	1.37	1.41	1.43	1.39	1.42
Mn(Y)	0.00	0.00	0.02	0.01	0.00	0.00	0.00	0.00	0.01	0.01	0.00	0.00	0.00	0.01	0.00	0.00	0.00	0.00	0.02	0.00
Mg(Y)	1.30	1.25	1.38	1.43	1.31	1.27	1.36	1.31	1.24	1.26	1.28	1.35	1.28	1.35	1.26	1.30	1.24	1.26	1.24	1.23
K(X)	0.02	0.01	0.02	0.01	0.02	0.00	0.01	0.00	0.01	0.01	0.00	0.01	0.00	0.00	0.01	0.01	0.01	0.01	0.01	0.01
Ca(X)	0.12	0.13	0.14	0.13	0.15	0.14	0.12	0.11	0.13	0.12	0.14	0.14	0.14	0.12	0.11	0.12	0.12	0.12	0.13	0.14
Na(X)	0.68	0.64	0.76	0.72	0.61	0.67	0.60	0.68	0.67	0.71	0.76	0.81	0.75	0.72	0.74	0.61	0.59	0.65	0.67	0.62
X vacancies	0.19	0.22	0.09	0.14	0.22	0.19	0.27	0.21	0.19	0.17	0.09	0.05	0.10	0.15	0.13	0.27	0.28	0.21	0.19	0.24
X <sub>Mg</sub>	0.47	0.48	0.49	0.51	0.48	0.48	0.51	0.50	0.46	0.47	0.46	0.49	0.49	0.48	0.47	0.49	0.47	0.47	0.47	0.46

Note: Atomic proportions based on ΣT+Z+Y cations = 15. X<sub>Mg</sub> = Mg/(Fe<sup>2+</sup> + Mg).

\* B<sub>2</sub>O<sub>3</sub> calculated assuming B to be 3 atoms per formula unit.

Table 2.4.3a: Representative EPMA analysis of Tourmaline(continued).

Sample no.	BR3B	BR3B	BR3B	BR3B	BR3B	BR3B	BR 3B	BR 3B	BR3B	BR3B	BR3B	BR3B	BR3B							
Point	59 / 20	59 / 21	59 / 22	59 / 23	59 / 24	59 / 25	57	59	3 / 1	5 / 1	3 / 1	4 / 1	5 / 1	6 / 1	10 / 1	14 / 1	15 / 1	17 / 1	18 / 1	
Core/Rim	rim	rim	rim	rim	rim	rim	rim	rim	rim	rim	rim	rim	rim	rim	rim	rim	rim	rim	rim	rim
Al <sub>2</sub> O <sub>3</sub>	29.89	32.13	31.82	31.29	30.20	32.02	31.05	31.60	30.91	30.75	32.24	31.86	31.62	31.78	31.84	31.61	30.67	31.62	32.02	
FeO	9.39	9.78	9.88	9.73	10.29	9.86	9.92	9.47	10.01	10.74	9.94	10.02	10.15	10.24	10.04	10.22	10.54	8.71	9.39	
TiO <sub>2</sub>	0.79	0.67	0.80	0.88	0.91	0.74	0.79	0.74	0.79	0.76	0.74	0.76	0.78	0.75	0.76	0.53	0.81	0.67	0.96	
SiO <sub>2</sub>	33.54	36.21	35.47	35.42	33.51	35.13	35.64	35.64	35.23	35.72	35.88	36.10	36.05	35.79	36.34	36.37	35.54	35.80	35.80	
K <sub>2</sub> O	0.04	0.02	0.08	0.08	0.02	0.06	0.09	0.04	0.06	0.07	0.03	0.07	0.05	0.05	0.05	0.01	0.09	0.03	0.03	
CaO	0.75	0.72	0.84	0.78	0.75	0.73	0.84	0.70	0.77	0.78	0.71	0.76	0.76	0.83	0.68	0.80	0.97	0.60	0.66	
Na <sub>2</sub> O	2.22	1.90	1.88	1.84	2.45	2.18	1.89	2.06	2.16	2.21	1.95	1.90	2.13	2.03	2.04	1.98	1.85	2.05	1.83	
Cr <sub>2</sub> O <sub>3</sub>	0.00	0.00	0.00	0.00	0.00	0.00	0.00	0.00	0.00	0.00	0.01	0.00	0.08	0.02	0.00	0.10	0.03	0.00	0.02	
MnO	0.06	0.09	0.08	0.01	0.15	0.00	0.00	0.02	0.02	0.00	0.05	0.00	0.07	0.00	0.10	0.28	0.03	0.12	0.06	
MgO	5.40	5.11	5.09	4.99	5.18	5.30	5.21	5.13	5.24	5.45	5.38	5.22	5.50	5.44	5.17	5.30	5.01	4.83	5.20	
B <sub>2</sub> O <sub>3</sub> *	9.93	10.54	10.43	10.33	10.03	10.43	10.37	10.40	10.31	10.43	10.56	10.53	10.56	10.53	10.57	10.56	10.33	10.33	10.48	
Total	92.01	97.17	96.37	95.35	93.49	96.45	95.80	95.80	95.50	96.91	97.49	97.22	97.75	97.46	97.59	97.76	95.87	94.76	96.45	
Si(T)	5.90	6.00	5.94	6.00	5.83	5.88	6.00	6.00	5.97	5.98	5.93	5.99	5.96	5.93	6.00	6.00	6.00	6.00	5.97	
Al(T)	0.10	0.00	0.06	0.00	0.17	0.12	0.00	0.00	0.03	0.02	0.07	0.01	0.04	0.07	0.00	0.00	0.00	0.00	0.03	
B(T)	3.00	3.00	3.00	3.00	3.00	3.00	3.00	3.00	3.00	3.00	3.00	3.00	3.00	3.00	3.00	3.00	3.00	3.00	3.00	
Al(Z)	6.00	6.00	6.00	6.00	6.00	6.00	6.00	6.00	6.00	6.00	6.00	6.00	6.00	6.00	6.00	6.00	6.00	6.00	6.00	
Al(Y)	0.09	0.28	0.23	0.25	0.02	0.20	0.19	0.28	0.15	0.04	0.20	0.22	0.12	0.14	0.22	0.16	0.13	0.41	0.27	
Ti(Y)	0.10	0.08	0.10	0.11	0.12	0.09	0.10	0.09	0.10	0.10	0.09	0.09	0.10	0.09	0.09	0.07	0.10	0.09	0.12	
Cr(Y)	0.00	0.00	0.00	0.00	0.00	0.00	0.00	0.00	0.00	0.00	0.00	0.00	0.01	0.00	0.00	0.01	0.00	0.00	0.00	
Fe(Y)	1.38	1.36	1.38	1.38	1.50	1.38	1.40	1.34	1.42	1.50	1.37	1.39	1.40	1.42	1.39	1.41	1.49	1.25	1.31	
Mn(Y)	0.01	0.01	0.01	0.00	0.02	0.00	0.00	0.00	0.00	0.00	0.01	0.00	0.01	0.00	0.01	0.04	0.00	0.02	0.01	
Mg(Y)	1.41	1.26	1.27	1.26	1.34	1.32	1.31	1.29	1.32	1.36	1.32	1.29	1.36	1.34	1.28	1.31	1.27	1.24	1.29	
K(X)	0.01	0.00	0.02	0.02	0.00	0.01	0.02	0.01	0.01	0.01	0.01	0.01	0.01	0.01	0.01	0.00	0.02	0.01	0.01	
Ca(X)	0.14	0.13	0.15	0.14	0.14	0.13	0.15	0.13	0.14	0.14	0.13	0.13	0.13	0.15	0.12	0.14	0.17	0.11	0.12	
Na(X)	0.75	0.61	0.61	0.60	0.82	0.70	0.61	0.67	0.71	0.71	0.62	0.61	0.68	0.65	0.65	0.63	0.60	0.67	0.59	
X vacancies	0.10	0.26	0.23	0.24	0.03	0.15	0.22	0.20	0.14	0.13	0.25	0.24	0.18	0.19	0.22	0.23	0.20	0.22	0.29	
X <sub>Mg</sub>	0.51	0.48	0.48	0.48	0.47	0.49	0.48	0.49	0.48	0.47	0.49	0.48	0.49	0.49	0.48	0.48	0.46	0.50	0.50	

Note: Atomic proportions based on ΣT+Z+Y cations = 15. X<sub>Mg</sub> = Mg/(Fe<sup>2+</sup> + Mg).

\* B<sub>2</sub>O<sub>3</sub> calculated assuming B to be 3 atoms per formula unit.

Table 2.4.3a: Representative EPMA analysis of Tourmaline(continued).

Sample no.	BR3B	BR3B	BR3B	BR 3B					
Point	21 / 1 .	24 / 1 .	26 / 1 .	53	55	56	58	60	61
Core/Rim	rim	rim	rim	rim	rim	rim	rim	rim	rim
Al <sub>2</sub> O <sub>3</sub>	31.60	31.53	30.67	30.67	31.61	30.67	30.67	31.53	32.02
FeO	9.47	9.89	9.44	10.54	10.22	10.54	9.44	9.89	9.86
TiO <sub>2</sub>	0.74	0.81	0.81	0.81	0.53	0.81	0.81	0.81	0.74
SiO <sub>2</sub>	35.64	35.93	36.44	35.54	36.37	35.54	36.44	35.93	35.13
K <sub>2</sub> O	0.04	0.09	0.08	0.09	0.01	0.09	0.08	0.09	0.06
CaO	0.70	0.79	0.78	0.97	0.80	0.97	0.78	0.79	0.73
Na <sub>2</sub> O	2.06	2.05	2.04	1.85	1.98	1.85	2.04	2.05	2.18
Cr <sub>2</sub> O <sub>3</sub>	0.00	0.00	0.00	0.03	0.10	0.03	0.00	0.00	0.00
MnO	0.02	0.08	0.03	0.03	0.28	0.03	0.03	0.08	0.00
MgO	5.13	5.01	5.62	5.01	5.30	5.01	5.62	5.01	5.30
B <sub>2</sub> O <sub>3</sub> *	10.40	10.46	10.46	10.33	10.56	10.33	10.46	10.46	10.43
Total	95.80	96.64	96.37	95.87	97.76	95.87	96.37	96.64	96.45
Si(T)	6.00	6.00	6.00	6.00	6.00	6.00	6.00	6.00	5.88
Al(T)	0.00	0.00	0.00	0.00	0.00	0.00	0.00	0.00	0.12
B(T)	3.00	3.00	3.00	3.00	3.00	3.00	3.00	3.00	3.00
Al(Z)	6.00	6.00	6.00	6.00	6.00	6.00	6.00	6.00	6.00
Al(Y)	0.28	0.24	0.13	0.13	0.16	0.13	0.13	0.24	0.20
Ti(Y)	0.09	0.10	0.10	0.10	0.07	0.10	0.10	0.10	0.09
Cr(Y)	0.00	0.00	0.00	0.00	0.01	0.00	0.00	0.00	0.00
Fe(Y)	1.34	1.39	1.34	1.49	1.41	1.49	1.34	1.39	1.38
Mn(Y)	0.00	0.01	0.00	0.00	0.04	0.00	0.00	0.01	0.00
Mg(Y)	1.29	1.25	1.42	1.27	1.31	1.27	1.42	1.25	1.32
K(X)	0.01	0.02	0.02	0.02	0.00	0.02	0.02	0.02	0.01
Ca(X)	0.13	0.14	0.14	0.17	0.14	0.17	0.14	0.14	0.13
Na(X)	0.67	0.66	0.66	0.60	0.63	0.60	0.66	0.66	0.70
X vacancies	0.20	0.18	0.19	0.20	0.23	0.20	0.19	0.18	0.15
X <sub>Mg</sub>	0.49	0.47	0.51	0.46	0.48	0.46	0.51	0.47	0.49

Note: Atomic proportions based on  $\Sigma T+Z+Y$  cations = 15.  $X_{Mg} = Mg/(Fe^{2+} + Mg)$ .

\* B<sub>2</sub>O<sub>3</sub> calculated assuming B to be 3 atoms per formula unit.

Table 2.4.3b: Representative EPMA analysis of muscovite, Kfeldspar and ilmenite

Sample No	BR2E2	BR2E2	BR 3b	BR3b	BR 3c	BR 3c	BR 3c	BR2E2	BR2E3	BR2E4	BR3C
DataSet/Point	87 / 1	88 / 1	2 / 1	4 / 1	37 / 1	38 / 1	47 / 1	80 / 1	81 / 1	86 / 1	56
Mineral	Muscovite	Kfeldspar	Kfeldspar	Kfeldspar	ilmenite						
SiO <sub>2</sub>	45.94	46.07	45.66	45.71	46.50	47.16	46.17	63.18	64.56	63.37	0.01
TiO <sub>2</sub>	0.05	0.01	0.10	0.00	0.05	0.05	0.00	0.00	0.00	0.00	50.87
Al <sub>2</sub> O <sub>3</sub>	36.91	37.76	35.00	34.98	34.89	35.65	34.25	18.39	18.44	18.20	0.05
Cr <sub>2</sub> O <sub>3</sub>	0.00	0.01	0.00	0.02	0.00	0.00	0.00	0.00	0.02	0.00	0.05
FeO	0.62	0.51	1.37	1.78	2.10	2.04	2.59	0.00	0.00	0.01	45.12
MnO	0.07	0.00	0.00	0.00	0.02	0.03	0.02	0.00	0.01	0.07	2.08
CaO	0.00	0.00	0.03	0.00	0.00	0.00	0.02	0.00	0.00	0.00	0.03
MgO	0.35	0.19	0.37	0.37	0.45	0.34	0.47	0.00	0.01	0.00	0.06
Na <sub>2</sub> O	0.27	0.27	0.37	0.29	0.21	0.27	0.34	0.35	0.57	0.26	0.03
K <sub>2</sub> O	11.24	11.20	10.57	11.28	11.83	11.61	11.20	16.85	16.51	17.20	0.01
P <sub>2</sub> O <sub>5</sub>	0.00	0.00	0.00	0.00	0.00	0.00	0.00	0.03	0.00	0.00	0.00
Total	95.45	96.02	93.47	94.43	96.05	97.15	95.06	98.81	100.12	99.11	98.37
Normalization basis	11(O)	8(O)	8(O)	8(O)	3(O)						
Si	3.05	3.03	3.10	3.09	3.10	3.10	3.11	2.97	2.99	2.98	0.00
Ti	0.00	0.00	0.01	0.00	0.00	0.00	0.00	0.00	0.00	0.00	0.99
Al	2.89	2.93	2.80	2.79	2.74	2.76	2.72	1.02	1.01	1.01	0.00
Cr	0.00	0.00	0.00	0.00	0.00	0.00	0.00	0.00	0.00	0.00	0.00
Fe	0.03	0.03	0.08	0.10	0.12	0.11	0.15	0.00	0.00	0.00	0.97
Mn	0.00	0.00	0.00	0.00	0.00	0.00	0.00	0.00	0.00	0.00	0.05
Ca	0.00	0.00	0.00	0.00	0.00	0.00	0.00	0.00	0.00	0.00	0.00
Mg	0.03	0.02	0.04	0.04	0.04	0.03	0.05	0.00	0.00	0.00	0.00
Na	0.03	0.03	0.05	0.04	0.03	0.03	0.04	0.03	0.05	0.02	0.00
K	0.95	0.94	0.91	0.97	1.01	0.97	0.96	1.01	0.97	1.03	0.00
P	0.00	0.00	0.00	0.00	0.00	0.00	0.00	0.00	0.00	0.00	0.00
K/(K+Ca+Na)	0.96	0.96	0.95	0.96	0.97	0.97	0.95				
X <sub>Ca</sub>								0.00	0.00	0.00	
X <sub>Na</sub>								0.03	0.05	0.02	
X <sub>K</sub>								0.97	0.95	0.98	

## 2.5 Trace and REE concentrations of tourmaline

The distribution of trace and rare earth elements (REE) in tourmaline is closely related to their petrogenesis. To study and compare the REE element concentrations of tourmaline belonging to different generations were normalized with chondritic values (McDonough and Sun, 1995). However, trace and REE concentrations of these tourmalines were also normalized with respect to the upper continental crust values (UCC; Rudnic and Gao, 2003) to check their enrichment or depletion with respect to the more enriched crust.

The 14 numbers of REE (La - Lu) are plotted in a spider diagram by normalizing each REE concentration in mineral with chondrite data (McDonough and Sun, 1995) with LREE (more incompatible) at the left, MREE at the center & HREE (less incompatible) to the right of the diagram. In chondrite normalized REE spectra, tourmalines from pegmatite show LREE enrichment, distinct positive Eu anomaly and HREE depletion (Fig 2.5.1a). The LREE patterns for core and rim show similar negative slope, although rim is more enriched than the core. Both core and rim show similar distinctly positive Eu anomaly ( $Eu/Eu^*=4.81-22.16$ ) with  $(La/Lu)_{CN} = 15.40-182.43$  ( $La/Lu > 1$ ). Both core and rim are depleted in HREE than chondrites and their concentrations are slightly irregular but nearly equivalent. The HREE shows negative slope. The  $REE_{total}$  contents at the core varies from 2.16 ppm to 2.74 ppm (average  $2.30 \pm 0.31$  ppm) and corresponding rim  $REE_{total}$  content varies from 4.67 ppm to 6.73 ppm (average  $5.86 \pm 0.70$  ppm). Thus, the rim is enriched in  $REE_{total}$  than the core composition (Fig 2.5.1a).

In UCC normalized multielement plot (Rudnick and Gao, 2003), significant depletion in LIL elements such as Rb, Ba is noted (Fig 2.5.1b). Within HFS elements, notable depletion of elements such as Hf and Zr and moderate depletion in Th is observed. However, a sharp positive anomaly in Sc and Ti are noted. These samples show a slightly concave upward pattern in HREE-Y and a prominent positive Eu anomaly. These samples also exhibit LREE enrichment showing a positive sloped pattern. Ta is relatively enriched than Nb. Here, the core and rim compositions are indistinguishable in terms of compatible elements, i.e. Co, Ni and HREE-Y (Fig 2.5.1b).

Representative LA-ICP-MS trace-element analyses (in ppm) of tourmaline are given in Table 2.5.2a.

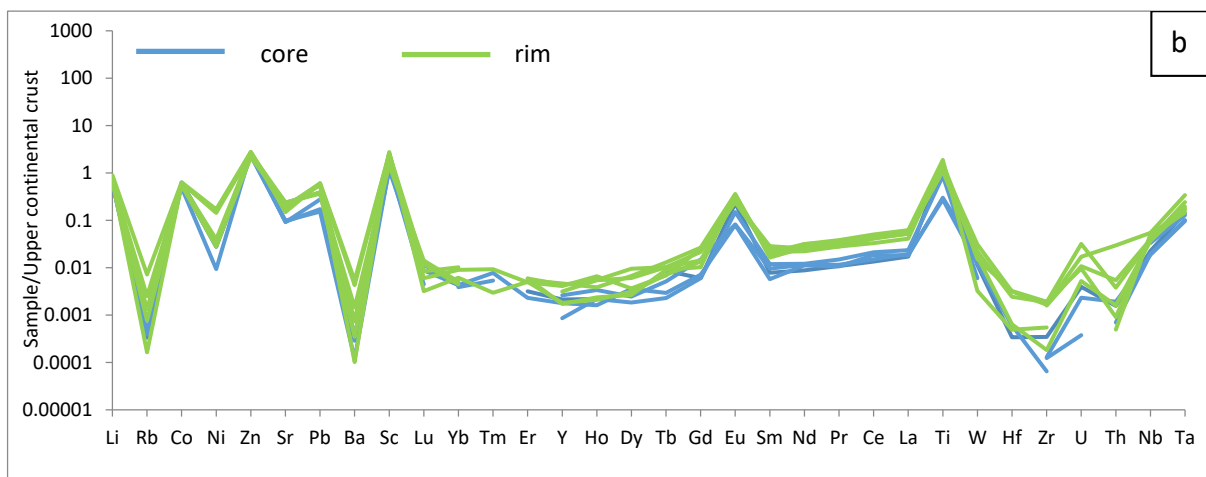
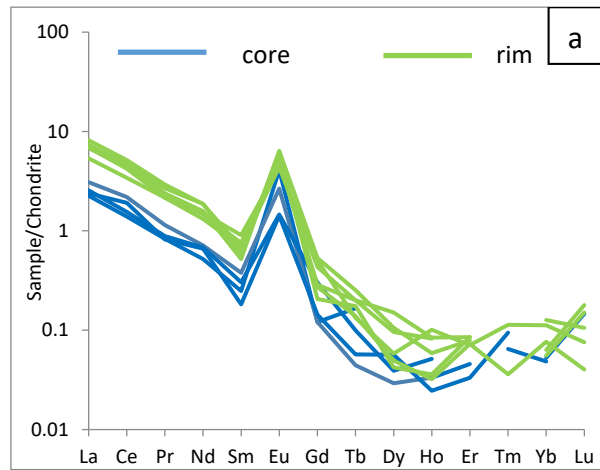


Fig 2.5.1a: Chondrite normalized (McDonough and Sun, 1995) REE spider diagram of tourmaline. (Blue –core: Green-rim) in pegmatite. Fig 2.5.1b: Upper continental crust (UCC) normalized (Rudnick and Gao, 2003) multielement diagram for tourmaline (Blue –core: Green-rim) within pegmatite.[The gaps in the spidergrams represent element concentrations that are below detection limit]

Table 2.5.2a: Representative LA-ICP-MS trace-element analyses (in ppm) of tourmaline

Sample no.	BR 3B	BR 3B	BR 3c	BR 3c	BR 3B	BR 3B	BR 3B	BR 3B	BR 3c	BR 3c
Mineral	Tourmaline									
Point	53	56	29	31	55	61	58	60	30	33
Core/Rim	Core	Core	Core	Core	Rim	Rim	Rim	Rim	Rim	Rim
La	0.53	0.73	0.61	0.56	1.93	1.27	1.61	1.74	1.69	1.63
Ce	0.85	1.34	0.95	1.17	3.16	2.09	2.71	2.84	2.99	2.58
Pr	0.08	0.11	0.08	0.08	0.27	0.20	0.22	0.25	0.22	0.20
Nd	0.24	0.33	0.31	0.30	0.85	0.60	0.72	0.85	0.69	0.67
Sm	0.04	0.06	0.05	0.03	0.09	0.10	0.08	0.10	0.13	0.11
Eu	0.23	0.15	0.08	0.08	0.35	0.25	0.36	0.29	0.25	0.28
Gd	0.02	0.02	0.06	0.03	0.04	0.10	0.11	0.05	0.09	0.06
Tb	0.01	0.00	0.00	0.00	0.01	0.00	0.01	0.01	0.01	0.01
Dy	bdl	0.01	0.01	0.01	0.01	0.01	0.03	0.01	0.04	0.02
Ho	0.00	0.00	0.00	0.00	0.00	0.01	0.00	0.00	0.00	0.00
Er	0.01	bdl	bdl	0.01	0.01	0.01	0.01	0.01	0.01	bdl
Tm	bdl	bdl	0.00	0.00	bdl	0.00	bdl	0.00	bdl	bdl
Yb	0.01	bdl	0.01	0.01	0.01	0.02	0.02	0.01	0.01	bdl
Lu	0.00	0.00	bdl	bdl	0.00	0.00	0.00	0.00	0.00	bdl
Total REE	2.02	2.74	2.16	2.28	6.73	4.67	5.88	6.16	6.13	5.57
Eu anomaly	22.17	10.68	4.81	8.75	15.53	7.39	12.15	10.88	6.51	9.60
Li	15.05	15.46	14.28	14.24	16.24	21.47	17.59	16.03	14.86	22.78
Sc	22.98	20.36	17.51	16.22	35.95	35.73	35.72	38.72	20.44	31.27
Ti	5821.82	3319.67	1060.35	1154.66	7249.80	6065.93	4894.75	5446.21	4256.22	4223.38
V	bdl									
Co	9.78	8.55	10.91	10.38	9.95	11.01	10.71	10.63	9.47	10.01
Ni	1.30	0.44	1.54	1.58	1.32	8.04	7.13	6.76	1.37	1.87
Zn	152.43	178.10	155.52	160.03	184.41	187.21	164.59	182.55	142.77	172.32
Rb	0.03	bdl	0.03	0.03	0.01	0.59	0.11	0.20	0.06	bdl
Sr	74.91	29.37	31.50	30.11	64.91	47.79	62.15	55.59	73.15	76.31
Y	0.05	0.02	0.05	0.04	0.04	0.09	0.10	0.04	0.09	0.07
Zr	0.07	0.02	0.01	0.03	0.11	0.36	0.32	0.37	0.31	0.04
Nb	0.27	0.40	0.23	0.23	0.60	0.45	0.65	0.55	0.48	0.44
Mo	0.04	0.08	0.04	0.04	0.08	0.05	0.06	0.09	0.03	0.06
Ag	0.03	0.01	0.01	0.02	bdl	0.09	0.01	0.01	0.02	0.01
Ba	0.22	bdl	0.08	0.18	0.06	3.40	2.71	0.46	0.91	0.22
Hf	0.00	bdl	0.00	bdl	0.00	0.01	0.02	0.02	bdl	0.00
Ta	0.13	0.12	0.09	0.09	0.15	0.16	0.31	0.13	0.22	0.18
W	0.02	0.01	0.02	0.04	0.01	0.04	0.06	0.03	0.04	0.03
Pb	6.49	4.71	2.61	2.92	9.37	10.28	10.32	9.75	6.67	6.22
Th	0.02	bdl	0.01	0.02	0.01	0.04	0.31	0.01	0.06	0.02
U	0.01	0.00	bdl	0.01	bdl	0.09	0.05	0.03	0.03	0.01

bdl: below detection limit

## 2.6 Summary

Tourmaline mineralization in Haripaldih area is found within pegmatite veins. These pegmatite veins are hosted within the muscovite schist and quartz muscovite schist. The major pegmatite veins are occurred along the foliation plane ( $S_1$ ) define by muscovite schist and quartz muscovite schist. The intrusion of pegmatite veins is to post- tectonic with respect to  $S_1/D_1$ . Pegmatite veins are folded and showing  $F_2$  fold. From the field, petrography study it can be deciphered that the tourmaline mineralization occurred after the pegmatite crystallization i.e post  $S_1/D_1$  and pre to syn  $F_2/D_2$ . Tourmaline grains are alkali rich in composition and schorl to dravite in character. There is a significant variation of optical zoning which coincides with compositional zoning in tourmaline core to rim composition. The rim compositions are more magnesium and less X-vacancies relative to the core compositions The rim of the tourmaline grain significantly higher  $REE_{total}$  than the core. In chondrite normalized REE diagram, tourmaline grains show LREE enrichment with a strong negative slope, distinct positive Eu anomaly and HREE depletion.

# CHAPTER 3

## Tourmaline bearing rocks in and around Beldih

Beldih village is located 10 km south-east from Balarampur town in Purulia district, West Bengal. The position of the Beldih area is shown in the map of Fig 1.5a. Geologically, Beldih falls inside the SPSZ and situated central part of SPSZ (Fig 1.5a). The detailed geological description of the area is dealt in the subsequent section.

### 3.1 Lithology and structure of the area

The major lithological distribution in and around Beldih area is shown in Fig 3.1.1. The area exposes rocks of CGGC in the north and NSMB towards the southern part of the mapped area (Fig 3.1.1). The CGGC rocks are represented by various felsic gneisses towards extreme north while muscovite schist/ quartz muscovite schist are the dominant lithotypes that form low lying outcrops near the central part of the map where the shear fabric is best developed. Muscovite schists are medium to fine grained (Fig 3.1.2b). In most places, it is pale gray and buff coloured and rich in muscovite and quartz. Quartz/muscovite ratio shows wide variation from place to place or in a single hand specimen. With the increase in quartz content, the muscovite schist (>60% muscovite) grades to quartz muscovite schist(<10% muscovite) (Fig 3.1.2a). In many places, alternate quartz rich and mica rich bandings of variable thickness (1cm -3cm) are observed (Fig 3.1.2b) The prominent foliation plane present in this rock is the regional schistosity and is defined by the oriented muscovite grains. In some places, puckers on the muscovite are developed (Fig 3.1.2b). Tourmaline mineralisation is noted in the muscovite schist or quartz muscovite schist which will be described in the next segment. The low-grade metamorphites of NSMB (Chandil formation) appear south of muscovite schist/ quartz muscovite schist and are represented by quartzite and phyllite. Quartzite is a dark grey coloured extremely fine-grained rock that suffered deformation and is weakly foliated (Fig 3.1.2c). The phyllite is the most dominant and aerially persistent unit towards the south of the muscovite schist or quartz muscovite schist. They are grey to greenish grey in colour and extremely fine grained. The rock is not very tough, finely foliated and highly sheared (Fig

3.1.2d). Flaky minerals like muscovite, biotite and chlorite are dominantly present in this rock. The foliations are mainly defined by these flaky minerals. At places phyllite changes to tough and compact welded tuff near the western and southern part of Beldih. The rock is extremely fine grained and tough with fine alternating laminae of a white and a black layer (Fig 3.1.2e). The phyllites of NSMB are intruded by an aegerine-bearing peralkaline granite (Biramdih Granite) near west central part of the mapped area whose boundary outcrops can be traced upto south of Beldih Mine area (Fig 3.1.2f). A small lenticular body of carbonatite-apatite rock has ultimately intruded the Biramdih Granite and phyllite in the Beldih area and causes some alkali metasomatic changes (Fenitization) of the country rock. In Beldih and adjoining areas the carbonatite released fluid has converted the granitic rock into ultramafic patches/pods with networks of carbonate veins through desilicification and addition of Mg-Fe-Ca (Proximal Fenitization). Ultramafic rock with ramifying veins of carbonatite having varying thickness forms the southern boundary of the Beldih mine. The rock appears dark green to black with white carbonate minerals occurring as veins or pods (Fig 3.1.2g). Whereas, in places pure carbonatite bands occur with a few small pods of ultramafic rock (Fig 3.1.2h). In the distal part towards the west, fresh exposures of peralkaline granite exhibit occasional presence of deformed dark coloured metasomatic intrusive veins with a light-coloured halo around. These alkali amphibole-albite rich veins are the product of distal fenitization related to carbonatite emplacement near Beldih (Fig 3.1.2f). The Apatite rich rock associated with carbonatite was being mined for phosphate in Beldih Mine area and shows brecciation, ferruginization and silicification. The proportion of iron-oxide and apatite varies widely ranging from apatite-rich rock to iron oxide-rich rocks with manganese oxide. In places, in beldih mine monomineralic apatite rock with vug fills of silica are seen (Fig. 3.1.2j). Apatite rich rocks are restricted within the Beldih mine that are enclosed by green and white clay deposits. The kaolinite rocks are very soft, fine grained and friable and highly altered. Ultramafic rock is transformed into kaolinite, due to low temperature hydrothermal alteration (Fig 3.1.2i). A deformed ultramafic rock that forms an E-W trending narrow band south of Fatehpur occurs as an intrusive within NSMB. They are composed of amphibole, pyroxene and biotite with very little feldspar (Fig 3.1.2k). Within this ultramafic no carbonatites veins are found.

There are no primary structures preserved in and around Beldih area. The rocks in this region suffered at least three phases of deformation. The first phase of deformation ( $D_1$ ), produce the  $F_1$  folds whose axial planar schistosity ( $S_1$ ) is the most prominent planar fabric occurring as the regional schistosity of the study area, irrespective of lithology. The second phase of deformation ( $D_2$ ) produces  $F_2$  folds defined by the folding of the  $S_1$  planes. The third

phase of deformation ( $D_3$ ) produces the  $F_3$  folds defined by the large broad warps of the resistant lithounits.

The most prominent planar structure that regional schistosity ( $S_1$ ), shown by muscovite schist having a general E-W strike of  $85^\circ$ - $100^\circ$  and dipping steeply ( $75^\circ$ - $80^\circ$ ) towards north (Fig 3.1.2a and 3.1.2b). The regional ( $S_1$ ) foliation is also prominent within peralkaline granite, welded tuff, phyllite, quartzite and mafic ultramafic rocks. Locally the attitude of the regional foliation is changed due to folding of the  $S_1$ . In many places localization of strain develops a strong shear foliation which is almost parallel to the regional foliation ( $S_1$ ). C and S shear fabrics are identified in phyllite and welded tuffs (Fig 3.1.2l).

First generation or  $F_1$  folds are defined by the quartz veins (Fig 3.1.2m), and amphibole rich (Fig 3.1.2f) veins, whose axial planes are parallel to the schistosity of the rocks.  $F_1$  are mostly asymmetric with thickened hinges and longer limbs sometimes become parallel to the foliation. The  $F_1$  fold defined by quartz vein plunges  $30^\circ \rightarrow 95^\circ$ . The attitude of  $F_1$  axial plane is  $110^\circ/75^\circ$  N. The  $F_1$  folds are thus steeply inclined moderately plunging tight folds. The  $F_2$  folds are defined by well-developed puckers in muscovite schist (Fig 3.1.2b), folding of compositional banding of quartz muscovite schists (Fig 3.1.2a) and welded tuffs. The  $F_2$  fold measured from the pucker axis in muscovite schist plunges  $20^\circ \rightarrow 100^\circ$ . The attitude of  $F_2$  axial plane in muscovite schists is  $100^\circ/85^\circ$  N. The  $F_2$  folds are steeply inclined low plunging tight folds. Therefore, the axial planes of  $F_1$  and  $F_2$  folds are almost parallel. So, it is not clearly understood that the shear fabric which is parallel to the regional foliation in some strain localised areas is the product of the late stage  $D_1$  deformation or the primary  $S_2$  surface. A third generation of open folds ( $F_3$ ), defined by broad warps of the schistosity with in the muscovite schists and phyllite. These  $F_3$  folds axial plane is tending towards SE-NW direction. Therefore, in the study area  $F_1$  and  $F_2$  are coaxial and  $F_3$  occurs as a cross fold. Extensional structures defined by the discordant and concordant (with respect to  $S_1$ ) quartz veins within the phyllite, welded tuff and mica schist rocks are observed in the area. The concordant veins exhibit pinch-and-swell structures, while the discordant veins are sometime boudinaged with angular boudin necks (Fig 3.1.2n). On an average these discordant quartz vein trends  $305^\circ$  which is mainly along the axial plane of  $F_3$ . Thus, the intrusion of these quartz veins possibly occurred due to the extension of in the hinge area of  $F_3$  fold.

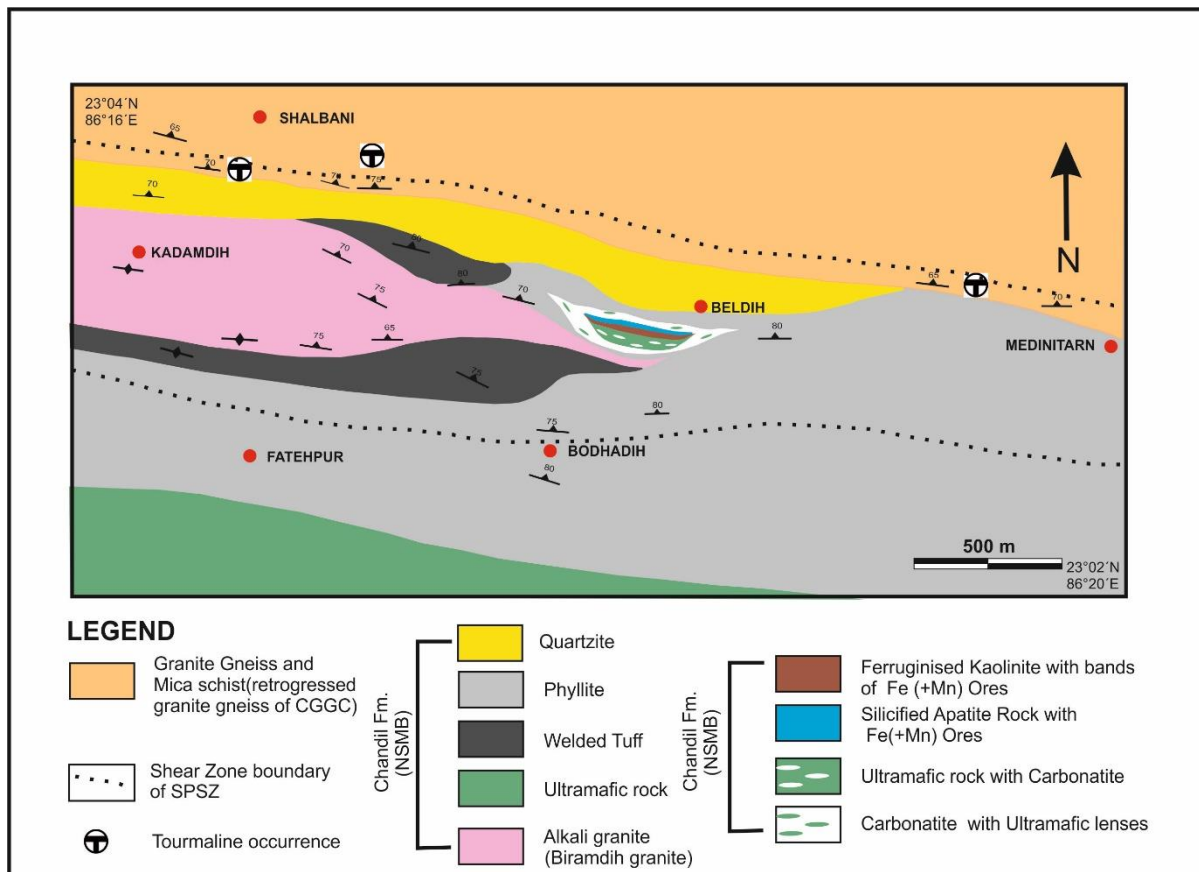


Fig 3.1.1: Lithological map of Beldih area, Purulia [Modified after BRNS funded research project (Sanction no.2008/36/36-BRNS), entitled “Pressure-Temperature-fluid evolution in parts of SPSZ- Implication for boron metasomatism and U-Fe-Cu-P Mineralisation”, P.I Pulak Sengupta, 2014]

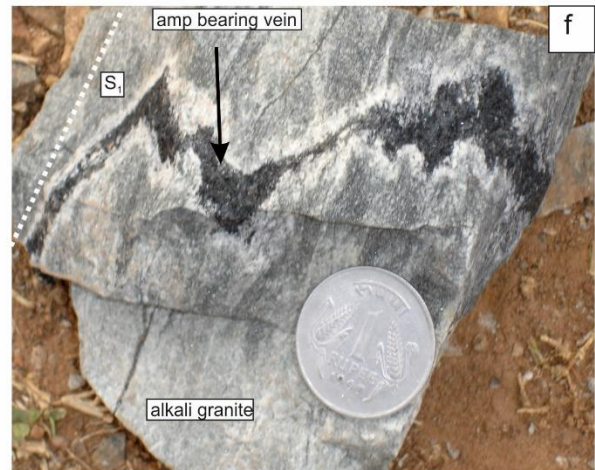
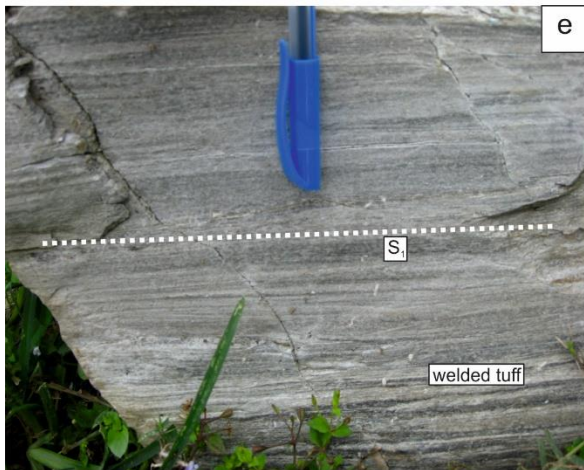
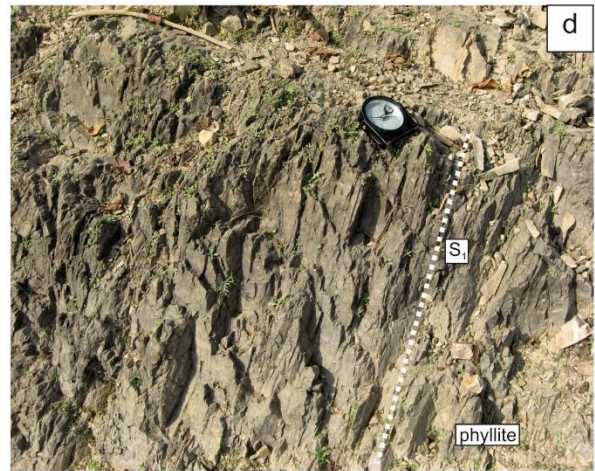
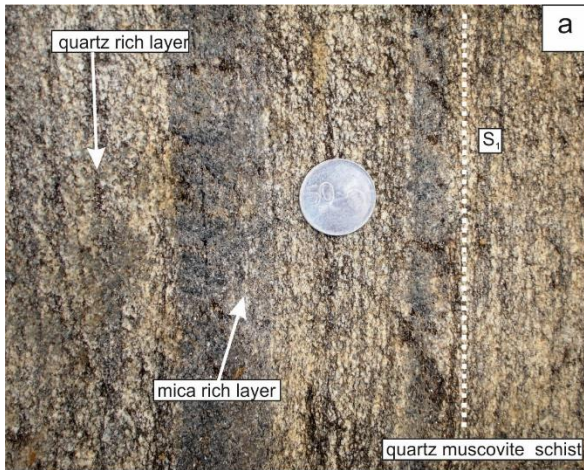


Fig 3.1.2a: quartz muscovite schist is alternate quartz rich and mica rich bandings of variable thickness (1cm - 3cm). Fig 3.1.2 b: Prominent foliation plane present in muscovite schist which is the parallel to regional schistosity ( $S_1$ ). Puckers are also present. Fig 3.1.2c: Quartzite is a dark grey coloured extremely fine grained rock, weakly foliated and highly sheared. Fig 3.1.2d: The phyllite is grey to greenish grey in colour, extremely fine grained and foliation is parallel to regional schistosity ( $S_1$ ). Fig 3.1.2e: Welded tuff is extremely fine grained and tough with fine alternating laminae of a white and a black layer. Fig 3.1.2f: Alkali granite is grey in appearance and tough extremely fine grained, sheared, composed predominantly of albite with some quartz. It contains numerous greenish black veins of amphibole.

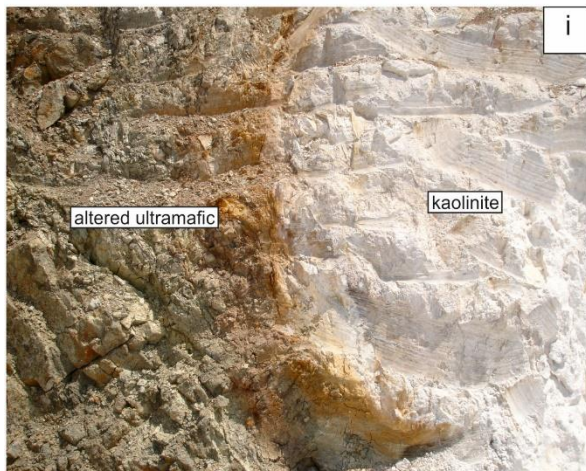
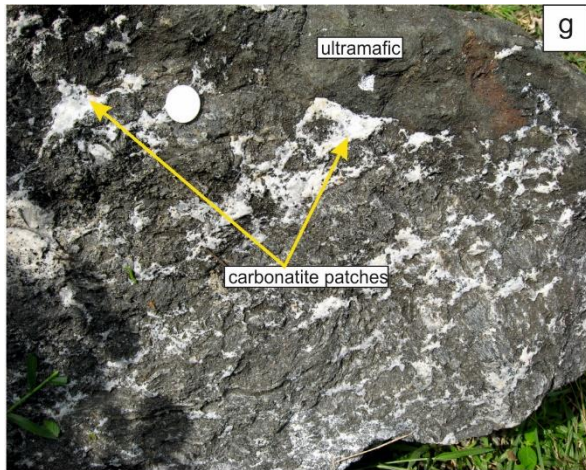


Fig 3.1.2g: Ultramafic rocks with ramifying veins of carbonatite having varying thickness forms in Beldih mine. Fig 3.1.2 h: Pure carbonatite rocks with a few small pods of ultramafic rock. Fig 3.1.2i: Sharp contact is present between the kaolinised zone and the altered ultramafic. Fig 3.1.2j: Apatite rich rock with vug fills of silica. Fig 3.1.2k: The ultramafic rocks near Fatehpur are melanocratic, extremely fine grained and composed of amphibole, pyroxene and biotite with very little feldspar. Fig 3.1.2l: C and S shear fabrics are identified in welded tuffs.

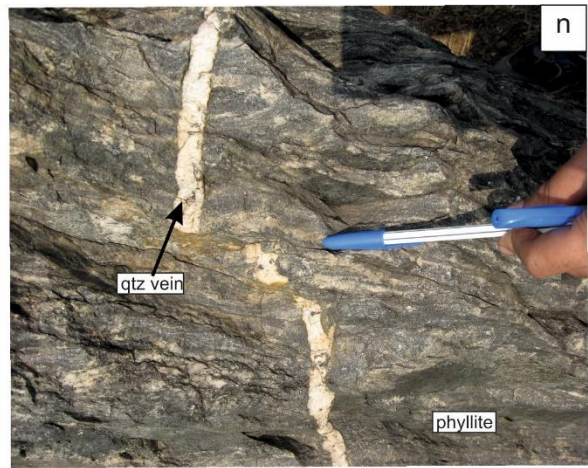
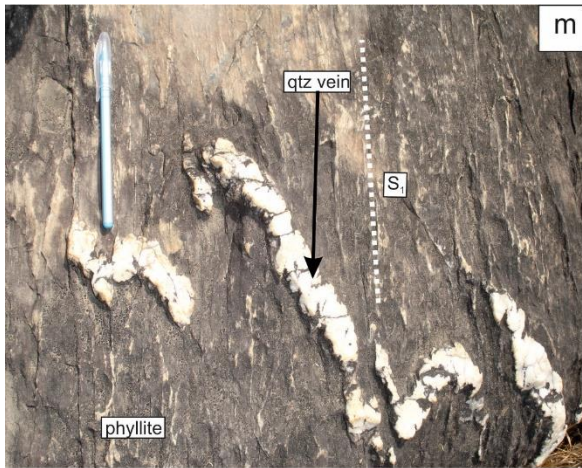


Fig 3.1.2 m: Asymmetric  $F_1$  fold are defined by quartz veins with thickened hinges and longer limbs sometimes become parallel to the foliation plane( $S_1$ ). Fig 3.1.2n: Extensional structures defined by the discordant quartz veins.

### 3.2 Field features of tourmaline bearing rocks

Minor occurrences of disseminated tourmaline grains are found in almost all the rock types of the area. However, in muscovite schist and quartz-muscovite schist tourmaline occurs in profusion in different modes and concentrations and is rightly considered as the host rocks for tourmaline in this area. The tourmaline occurrences within muscovite schist are not pervasive but rather is localized. Tourmaline in muscovite schist and quartz-muscovite schist mainly occur in north of the Beldih mine near Shalboni area and north –west near Medinitar area (Fig 3.1.1). Tourmaline-bearing muscovite schist or quartz muscovite schist samples were collected where the modal volume of tourmaline exceeds 10%.

Based on the size and morphology of tourmaline and the relation of the tourmaline-bearing aggregates with the host rock, three distinct modes of occurrence are established.

**Mode 1:** In muscovite schist, very fine grained, oriented aggregate of tourmaline occurs in form of thin, mesoscopic bands (0.1-0.5 cm thick). They commonly either occur as laterally impersistent lenticular stringers, veins, laminations that are parallel to the regional foliation ( $S_1$ ) defined by enclosing muscovite schist or as patches within the muscovite schist (Fig 3.2a, 3.2b). The stringers of tourmaline rich band are mm-thick and can trace laterally for few centimetres. All the tourmaline within the lensoid aggregates are very fine grained yet oriented in the direction of schistosity ( $S_1$ ). The tourmaline grains are so fine grained that identification of individual grains under naked eye is very difficult. Only one occurrence of fine-grained tourmaline vein is observed within muscovite schist (Fig 3.2b) which is also oriented parallel to  $S_1$  and associated tourmaline bands as well. Number of tourmaline bands is more in the quartz-tourmaline schist than in the quartz poor muscovite schists. Corroded patches of muscovite- and quartz muscovite schist are present in the thicker tourmaline bands (Fig. 3.2a). The tourmaline bands that are parallel to the pervasive schistosity( $S_1$ ) in muscovite- to quartz muscovite schists are folded by  $F_2$  folds (Fig 3.2a). Rarely, thin (0.5-1 mm thick; 1-2 cm long), fine-grained tourmaline veins are found cross cutting the  $S_1$  foliation and the foliation-parallel tourmaline bands (Fig 3.2a). Due to the discontinuous nature of these veins, relation between the  $F_2$  folds with them in the outcrop is not clear. Therefore, it is understood that these veins formed post  $S_1$  but their relation with the later deformation events could not be established. Tourmaline grains occurring within veins/bands/stringers that are oriented parallel to  $S_1$  are syn-tectonic regarding regional foliation ( $S_1$ ).

**Mode 2:** Another mode of tourmaline is coarse acicular (1-5cm along long axis) disseminated grains that occur within muscovite schist. In this mode the tourmaline grains occur as localised clusters of randomly oriented crystals within host quartz muscovite schist (Fig3.2c) cut across the pervasive  $S_1$  foliation. Locally rosette cluster of tourmaline grains growing over  $S_1$  fabric are found to remain unaffected by regional  $F_2$  and  $F_3$  folding. These tourmaline grains are post deformational regarding  $S_1$  and  $D_3/F_3$ .

**Mode 3:** In this mode, fine grained, oriented aggregate of tourmaline grains form moderately thick laterally persistent bands (thickness of bands 5mm-2cm) that are parallel to the  $S_1$  schistosity. All the tourmaline grains within the band are oriented parallel to  $S_1$  fabric (Fig 3.2d). This mode is found in both muscovite and quartz-muscovite schist and is designated as mode-3. In muscovite schist, such mode is rarely found in association with mode 1 tourmaline stringers (Fig 3.2b), while in quartz muscovite schist, multiple bands of mode 3 tourmaline are found to alternate with quartz rich bands giving a banded tourmaline-quartz “Schorl rock” type appearance (Fig 3.2d). Comparing the features of first and third modes, it appears that volume proportion of tourmaline has an inverse relation with that of muscovite within the rock. The tourmaline formation is syn tectonic regarding regional foliation ( $S_1$ ).

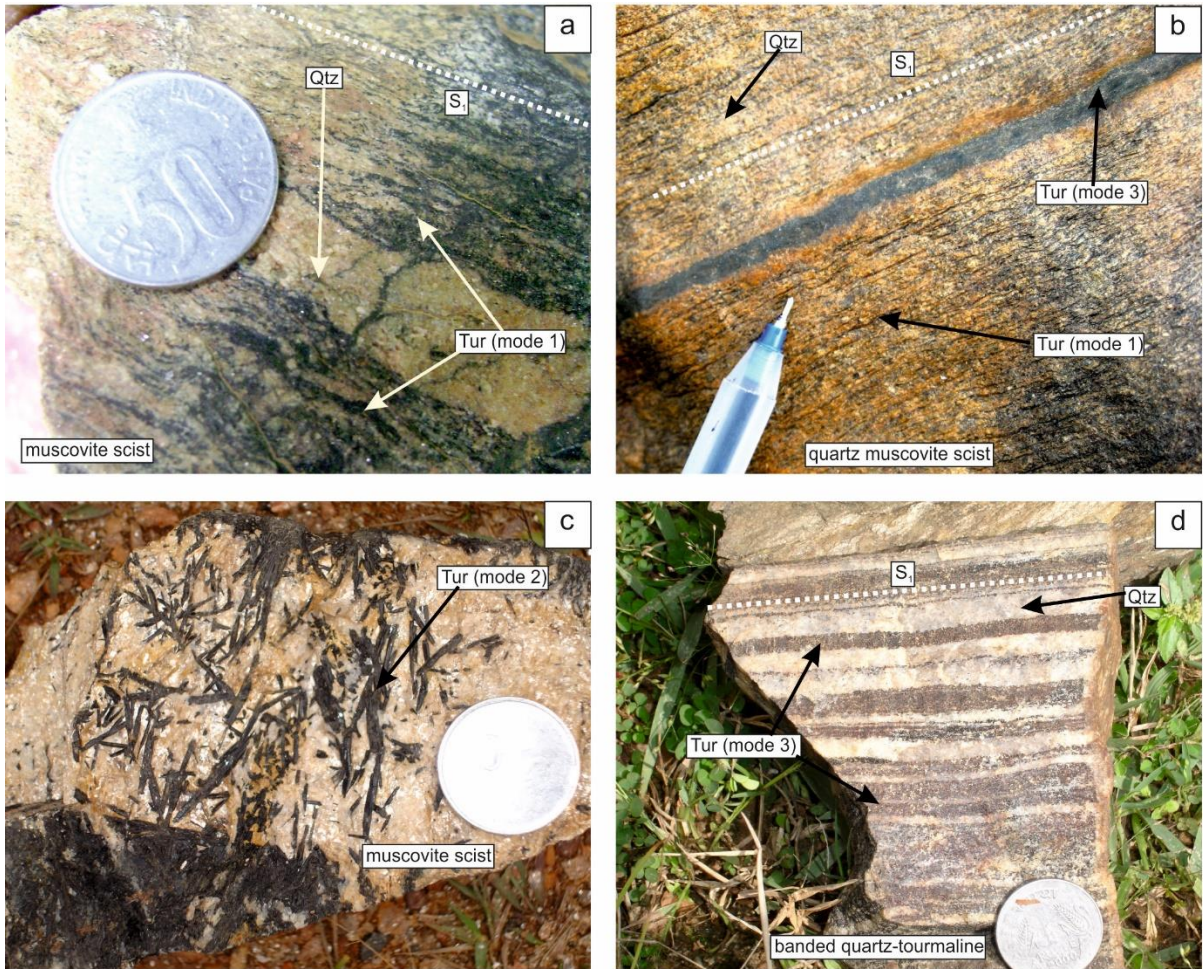


Fig 3.2a: In mode-1 aggregates of fine grained tourmaline occur as bands preferentially oriented along the foliation planes ( $S_1$ ) within muscovite schist. Fig 3.2b: In mode 1 association, tourmaline occurs as laterally impersistent lenticular stringers within host quartz muscovite schist. Fig 3.2c: In mode 2 association, tourmaline is coarse acicular (1-5cm along long axis) disseminated grains that occur within muscovite schist. Fig 3.2d: In mode 3 association, tourmaline occur in banded quartz-tourmaline rock defined by alternate tourmaline- rich and quartz-rich band oriented parallel to the  $S_1$  foliation.

### 3.3 Petrographic description of tourmaline bearing rocks

The host rock muscovite schist constitutes of quartz, muscovite, microcline, plagioclase feldspar with accessory ilmenite (Fig 3.3a). The volume proportion of microcline and plagioclase is <10% (Fig 3.3b). Plagioclase grains show tapered twin lamellae due to deformation. Microcline grains are subhedral in shape and deformation lamellae seen under CPL (Fig 3.3b). In places, muscovite grain which are defining foliation grows over the microcline (Fig 3.3b). This texture suggests the muscovite maybe produced due to metamorphism. The muscovite grains euhedral to subhedral in shape and show dynamic recrystallization and oriented parallel to the schistosity ( $S_1$ ) (Fig 3.3b and 3.3e). Quartz grains are subhedral to anhedral (up to 4 mm by 2.5 mm), elongated showing undulose extinction and marginal-recrystallization (Fig 3.3b and 3.3e). Foliation is defined by both elongated quartz grains and muscovite flakes (Fig 3.3a,3.3b and 3.3c). Foliation is crenulated forming  $F_2$ -microfolds within the muscovite schists (Fig 3.3a). Schistosity bends around the elliptical quartz grains (Fig 3.3c). S-C fabric is observed within muscovite schist which indicates that the rock is sheared (Fig 3.3a).

Based on the morphology and relation with the host rock there are three different modes of occurrences of tourmaline (Mode 1, Mode 2 and Mode 3) as described in the previous section.

The mode-1 association, while observed under microscope, show variable concentrations of tourmaline, normally 20% to 50% by volume. These tourmaline grains are associated with muscovite and quartz. However, mode-1 tourmaline grains can be divided into two different sub-categories based on their grain size and texture. One category is characterized by discrete or isolated, medium-grained (1-5 mm), subhedral or skeletal grains (Fig 3.3c and Fig 3.3e). These grains are rich in quartz inclusion and are associated with ilmenite (Fig 3.3c). The tourmaline grains show strong pleochroism in the shades of light green to dark greenish brown without optical zoning (Fig 3.3c). Another category, which is more pervasive, is characterized by fine-grained aggregates of tourmaline (Fig 3.3d) forming tourmaline-rich bands clearly visible under microscope. The tourmaline grains show strong pleochroism in the shades of light green to dark greenish brown without optical zoning. Tourmalines of both categories are oriented parallel to the schistosity plane ( $S_1$ ) and fractured. Therefore, tourmaline grains from both the categories are syn-tectonic to  $S_1$  and in spite of different appearances, they are designated as Gen-I (first generation) tourmaline.

The mode-2 association tourmaline grains are coarse, acicular subhedral to euhedral in shape, disseminated within muscovite schist and cut across the foliation ( $S_1$ ). Ilmenite and quartz occur in interstitial spaces. Tourmaline grains are haphazardly oriented and also characterized by extremely variable grain size (0.2-2mm along long axis) without any fracturing (Fig 3.3f). These grains do not show any prior deformational feature. The tourmaline grains show pleochroism in the shades of light green to deep green with strong optical zoning characterized by bluish green core and light green rim (Fig 3. 3f). So these tourmalines are certainly post deformational with respect to  $S_1$  fabric development and probably post- $D_3/F_3$  as well. These tourmaline grains are designated as Gen-II (second generation).

In mode-3 association the tourmaline grains occur within banded quartz tourmaline rock. In these domains major mineral coexisting with tourmalines is quartz and <10 volume % of muscovite (Fig 3.3g). These rocks are typically characterized by alternate tourmaline- rich bands and tourmaline-deficient (quartz rich) bands. Tourmaline rich bands are almost solely composed of fine grained (50 to 200  $\mu\text{m}$ ) tourmaline grains (> 70-80 % volume) and minor quartz. In places, tourmaline is associated with muscovite within tourmaline rich band (Fig 3.3h). Subhedral to euhedral aggregates of small grains of tourmaline that form bands oriented parallel to the  $S_1$  fabric (Fig 3.3g and 3.3h). Tourmaline grains are deep green to greenish brown in colour under microscope without optical zoning (PPL). Elliptical shaped, recrystallized quartz grains are seen within this banded rock (Fig 3.3g). In this mode tourmaline grains are designated as Gen -I (first generation) as these grains are syn- tectonic to  $S_1$ .

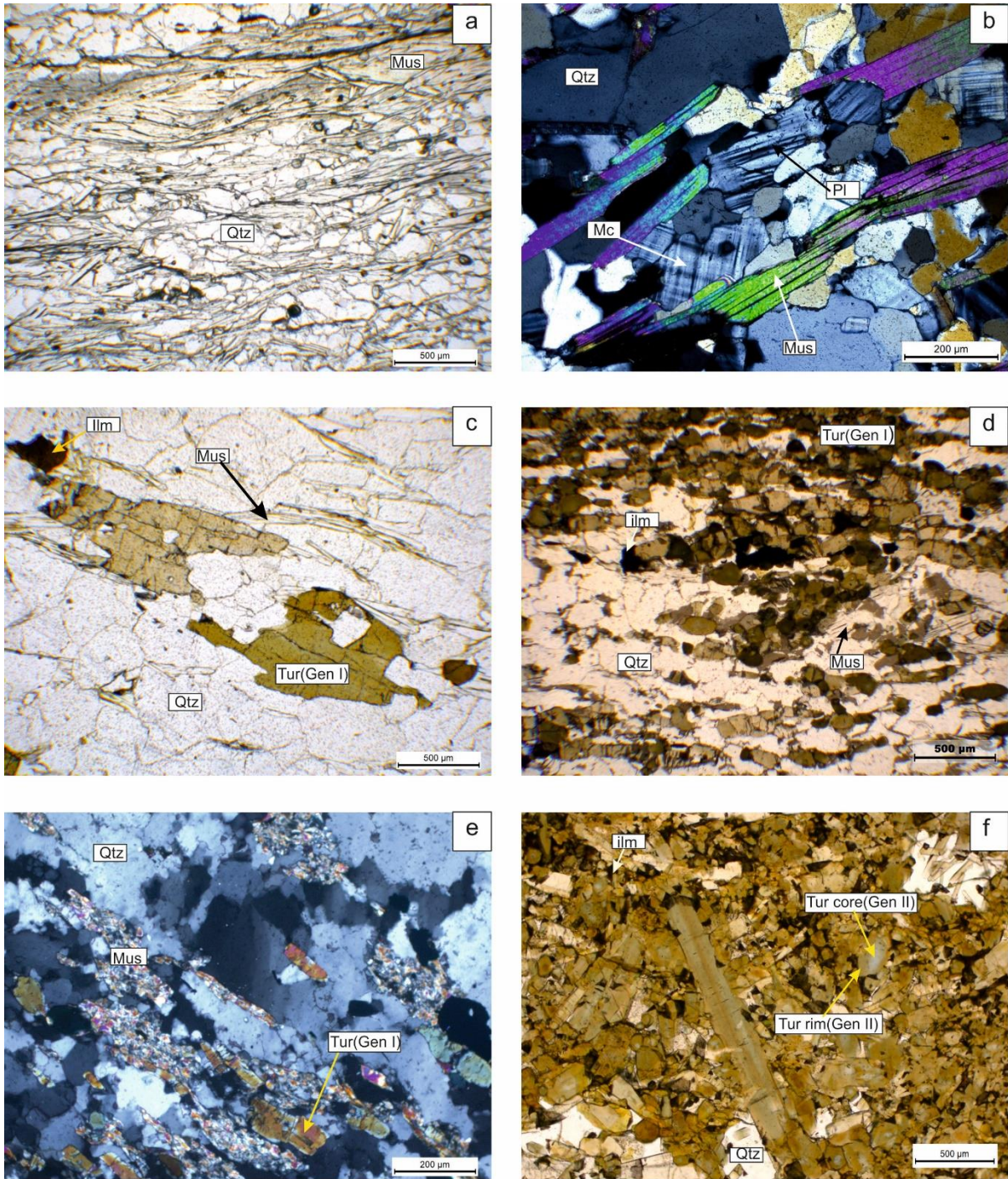


Fig 3.3a: The host rock muscovite schist constitutes of quartz, muscovite, microcline, plagioclase feldspar and foliation defined by muscovite flakes. Fig 3.3b: Plagioclase and microcline grains show deformation lamellae within muscovite schist (under CPL). Fig 3.3c: Gen I tourmaline occur as discrete or isolated, medium-grained, subhedral or skeletal in shape within muscovite schist in mode 1 association. Fig 3.3d: Gen I tourmaline is characterized by fine-grained aggregates of grains forming tourmaline-rich bands clearly visible under microscope in mode 1 association. Fig 3.3e: Muscovite grains show dynamic recrystallisation and tourmaline grains are oriented parallel to the  $S_1$  fabric in mode 1 association(under CPL). Fig 3.3f: Gen II tourmaline grains are haphazardly oriented and also characterized by extremely variable grain size without any fracturing in mode 2 association.

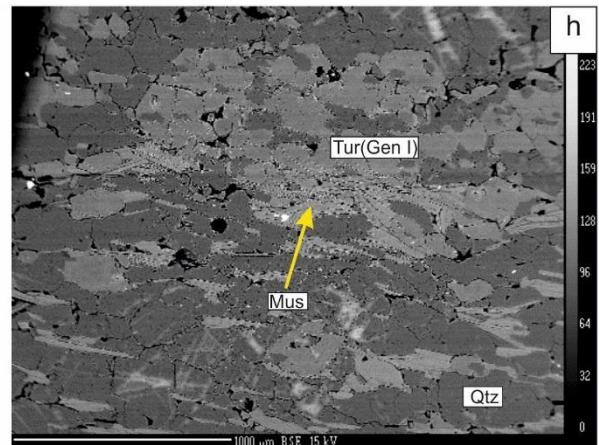
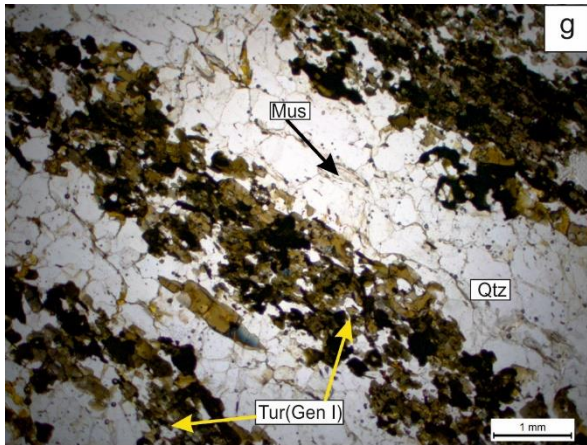


Fig 3.3g: Gen I fine grained tourmaline aggregates occur in banded quartz tourmaline rock and oriented parallel to  $S_1$  fabric in mode 3 association. Fig 3.3h: In banded quartz tourmaline rock, Gen I tourmaline grains are associated with muscovite (under BSE image)(mode 3 association).

### 3.4 Tourmaline mineral chemistry

The standard analytical procedures of major elements analysis and normalization of tourmalines are given in appendix I and II. In view of the petrographic studies, the tourmalines that form bands, laterally impersistent lenticular stringers, veins, laminations and oriented parallel to  $S_1$  schistosity will be designated as generation 1 (Gen-I, in mode 1, 3). Whereas, the randomly oriented tourmaline grain without any prior deformation features are designated as generation II (Gen-II, in mode 2).

Overall, T sites of tourmaline structure is nearly filled with Si ( $5.94 \pm 0.03$  apfu; Table 3.4.3a). The Z site of the tourmaline is completely filled up with Al. The Al in apfu of the tourmaline compositions exceeds 6 ( $6.28 \pm 0.12$  apfu) suggesting that some Al must be present in the Y site. Al content is higher in Gen-I ( $6.34 \pm 0.04$  apfu) than in the Gen-II ( $6.25 \pm 0.13$  apfu) tourmaline structure. Ti in tourmaline structure is nearly similar in Gen-I ( $0.09 \pm 0.03$  apfu) and Gen-II ( $0.08 \pm 0.04$  apfu). X-site vacancy, estimated from the measured Na+ Ca + K contents is  $0.20 \pm 0.06$  apfu. X vacancy is higher in Gen-I ( $0.21 \pm 0.04$  apfu) than in the Gen-II ( $0.18 \pm 0.04$  apfu) tourmaline structure. Ca in Gen-I ( $0.16 \pm 0.04$  apfu) tourmaline is lower than the Gen-II ( $0.18 \pm 0.05$  apfu). In terms of the Ca-X-site vacancy-Na+K diagram (Fig 3.4.1a), all tourmaline grains are plots in the “Alkali group”. Some of the tourmaline rim compositions from Gen-II are richer in Ca. In the  $X/(X + Na)$  vs.  $X_{Mg}$  diagram (Fig 3.4.1b) tourmaline grain straddles the boundary between schorl and dravite where  $X_{Mg} = Mg/Mg+Fe^{2+}$ .  $X_{Mg}$  in Gen-I ( $0.50 \pm 0.07$  apfu) tourmaline is lower than the Gen-II ( $0.60 \pm 0.09$  apfu). The core and the rim composition of Gen-I tourmaline is overlapping and straddle in boundary between schorl and dravite. Whereas, Gen-II tourmaline core composition straddles the boundary between schorl and dravite but the rim composition is dravite. There are a distinct  $X_{Mg}$  increases from core to rim in Gen-II tourmaline. There is significant variation in tourmaline compositions in Fe and Mg content between Gen-I and Gen-II. The  $Fe^{2+}$  contents shows a variations of: Gen-I ( $1.30 \pm 0.18$  apfu) > Gen-II ( $1.05 \pm 0.02$  apfu). Mg contents shows a variations of : Gen-I ( $1.10 \pm 0.09$  apfu) < Gen-II ( $1.64 \pm 0.30$  apfu). Representative microprobe analyses of tourmaline are given in Table 3.4.3a.

Tourmaline shows extensive chemical substitutions and is expressed by different exchange vectors. Gen-I and Gen-II tourmaline show strong substitution trend parallel to vector  $MgFe_{-1}$  (Fig 3.4.1.c) ( $r^2=0.95$ ), but tourmaline compositions fall slightly below the line  $Fe^{2+} + Mg = 3$  indicates substitution of Al in the Y-site. In  $Al_{total}$ -vs- X-site vacancy diagram (Fig 3.4.1d) the spread of tourmaline compositions show that the chemical substitution was

dominated and expressed by the  $\square\text{Al}(\text{NaR})_{-1}$  exchange vectors ( $r^2 = 0.53$ ) where  $R = \text{Fe}^{2+} + \text{Mg}$ . In the  $[\text{R}_1 (= \text{Na} + \text{Ca}) + \text{R}_2 (= \text{Fe}^{2+} + \text{Mg} + \text{Mn})]$  vs.  $[\text{R}_3 (= \text{Al} + 1.33 \times \text{Ti})]$  plot (Fig 3.4.1.e), tourmaline compositions of all the generations fall within the upper half of the parallelogram formed by the lines joining the positions of the tourmaline species. The spread of tourmaline compositions shows that the chemical substitution was dominated and expressed by the exchange vectors vector  $\square\text{Al}(\text{NaR})_{-1}$ . In Al vs Fe+Mg diagram (Fig 3.4.1f) it is also evident that the compositions of tourmaline show more affinity to the exchange vector  $\square\text{Al}(\text{NaR})_{-1}$  and  $\text{AlO}[\text{R}(\text{OH})]_{-1}$  ( $r^2 = 0.87$ ).

Fig 3.4.2a is a line traverse that shows the compositional variation across optical zoning of a tourmaline grain. In host muscovite schist Generation-II (Gen-II) tourmaline grains display strong optical zoning characterized by bluish green cores and green rims. Tourmaline grain core is enriched with Fe, Al, X-vac whereas the rim is enriched in Ca, Ti, Mg (Fig 3.4.2a). To clarify the chemical substitutions core to rim, the compositional data have been plotted in several different diagrams. In Fe vs Mg diagram a prominent Fe-Mg substitution occurs (Fig 3.4.2b) and shows strong substitution trend parallel to vector  $\text{MgFe}_{-1}$  ( $r^2 = 0.97$ ). In  $\text{Al}_{\text{total}}$  vs X vacancy diagram the spread of tourmaline compositions shows that the chemical substitution was dominated and expressed by the exchange vectors  $\square\text{Al}(\text{NaR})_{-1}$  with  $r^2 = 0.73$  (Fig 3.4.2c). The array of data in the Fe + Mg + Ti vs.  $\text{Al}_{\text{total}}$  diagram (Fig 3.4.2e) also suggests that the bluish green cores to green rims tourmaline Al content became poorer and substitution occurs along the  $\text{TiRAl}_{-2}$  exchange vector ( $r^2 = 0.99$ ). In Xvac vs Ca diagram (Fig 3.4.2d) it shows that the substitution occurs lesser extent along the  $\text{CaRO}[\square\text{Al}(\text{OH})]_{-1}$  exchange vector from core to rim substitution ( $r^2 = 0.74$ ).

Muscovite  $\text{FeO}_t$  content varies from 1.22 to 3.44 wt% in muscovite schist or quartz muscovite schist. Muscovite shows a significant amount of pyrophyllite component (~25 mol %). Plagioclase feldspar grains are oligoclase in composition ( $\text{Ab}_{74-77}$ ). The  $X_{\text{Kfs}}$  value of the K-feldspar varies from ~0.91-0.93. Ilmenite shows nearly end-member composition. Compositions of muscovite, plagioclase feldspar, K-feldspar and ilmenite are presented in Table 3.4.3b.

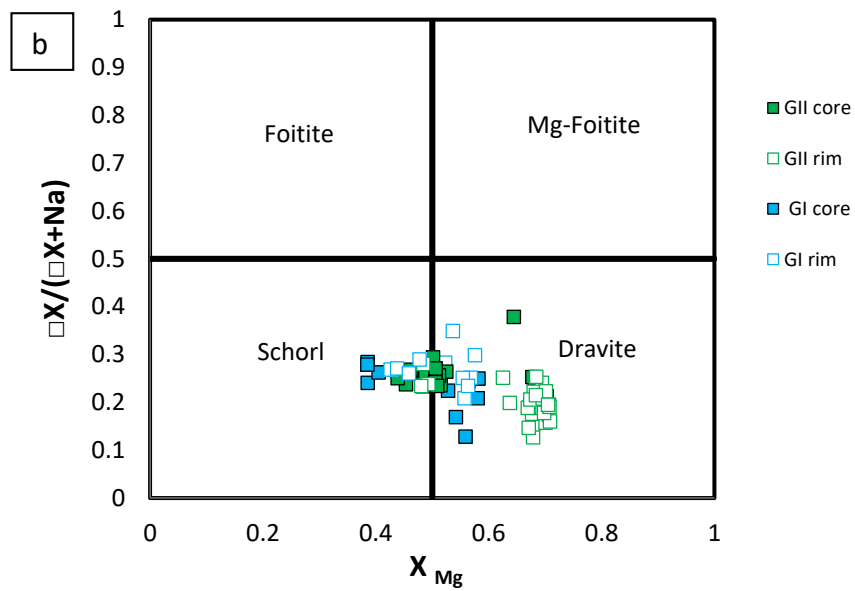
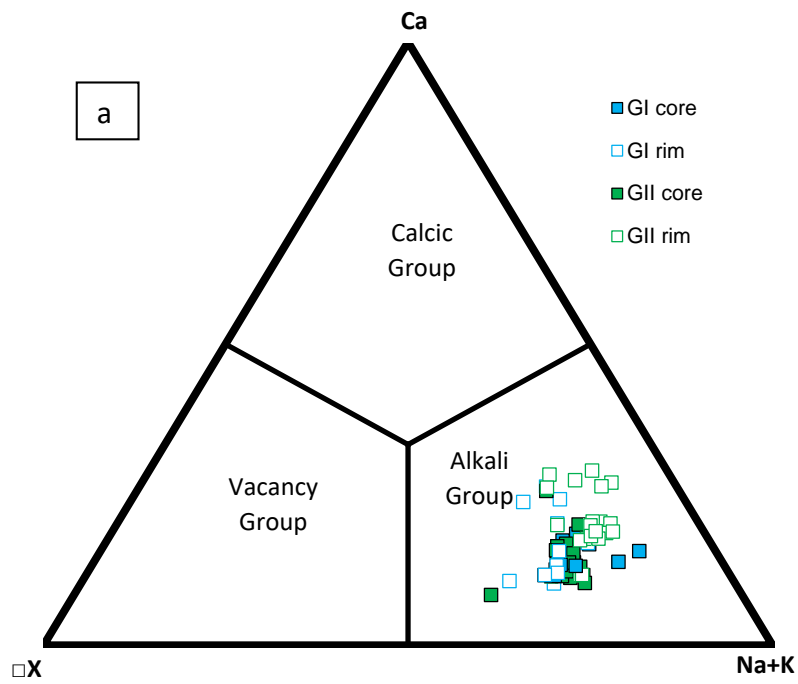


Fig 3.4.1.a : Principal tourmaline groups based on the classification scheme of Hawthorne and Henry (1999). Fig 3.4.1.b Nomenclature diagram of tourmaline based on X-site vacancy/(X-site vacancy + Na) vs. Mg/(Mg + Fe<sup>2+</sup>) plot after Henry et al. (2003).

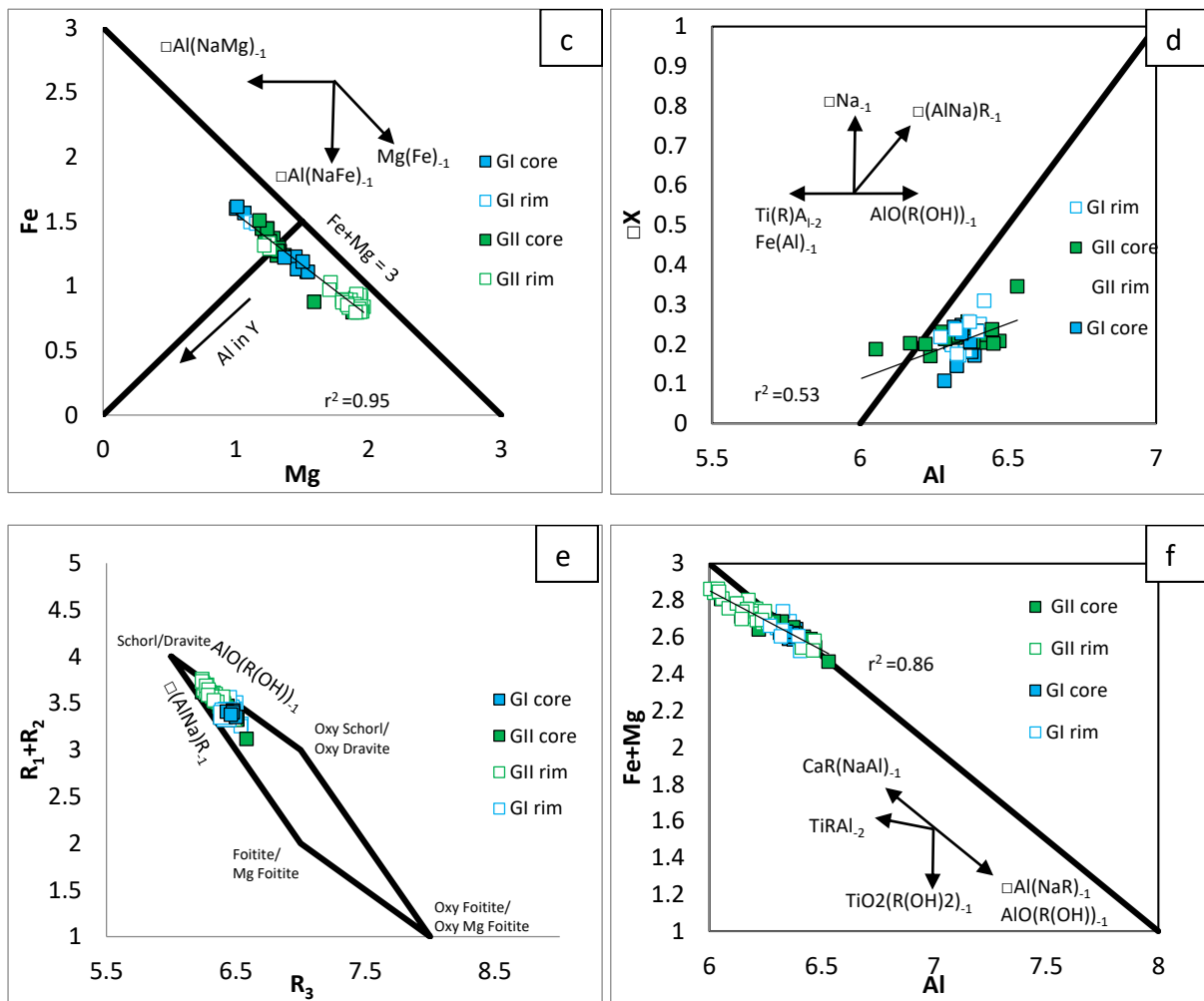


Fig 3.4.1.c: Tourmaline compositions in muscovite schist in Fe vs Mg diagram a prominent Fe-Mg substitution occurs, shows strong substitution trend parallel to vector  $Mg(Fe)_{-1}$ . Fig 3.4.1.d In  $Al_{total}$ -vs- X-site vacancy diagram, compositions of tourmaline show more affinity to the exchange vector  $Al(NaR)_{-1}$ . Fig 3.4.e: In the  $[R_1 (=Na + Ca) + R_2 (=Fe^{2+} + Mg + Mn)]$  vs.  $[R_3 (=Al + 1.33 \times Ti)]$  plot, tourmaline compositions fall within the upper half of the parallelogram formed by the lines joining the positions of the tourmaline species. Compositions show more affinity to the exchange vector exchange vector  $Al(NaR)_{-1}$ . Fig 2.3.1.f: In Al vs Fe+Mg diagram it is also evident that the compositions of tourmaline show more affinity to the exchange vector  $Al(NaR)_{-1}$  and  $AIO[R(OH)]_{-1}$ .

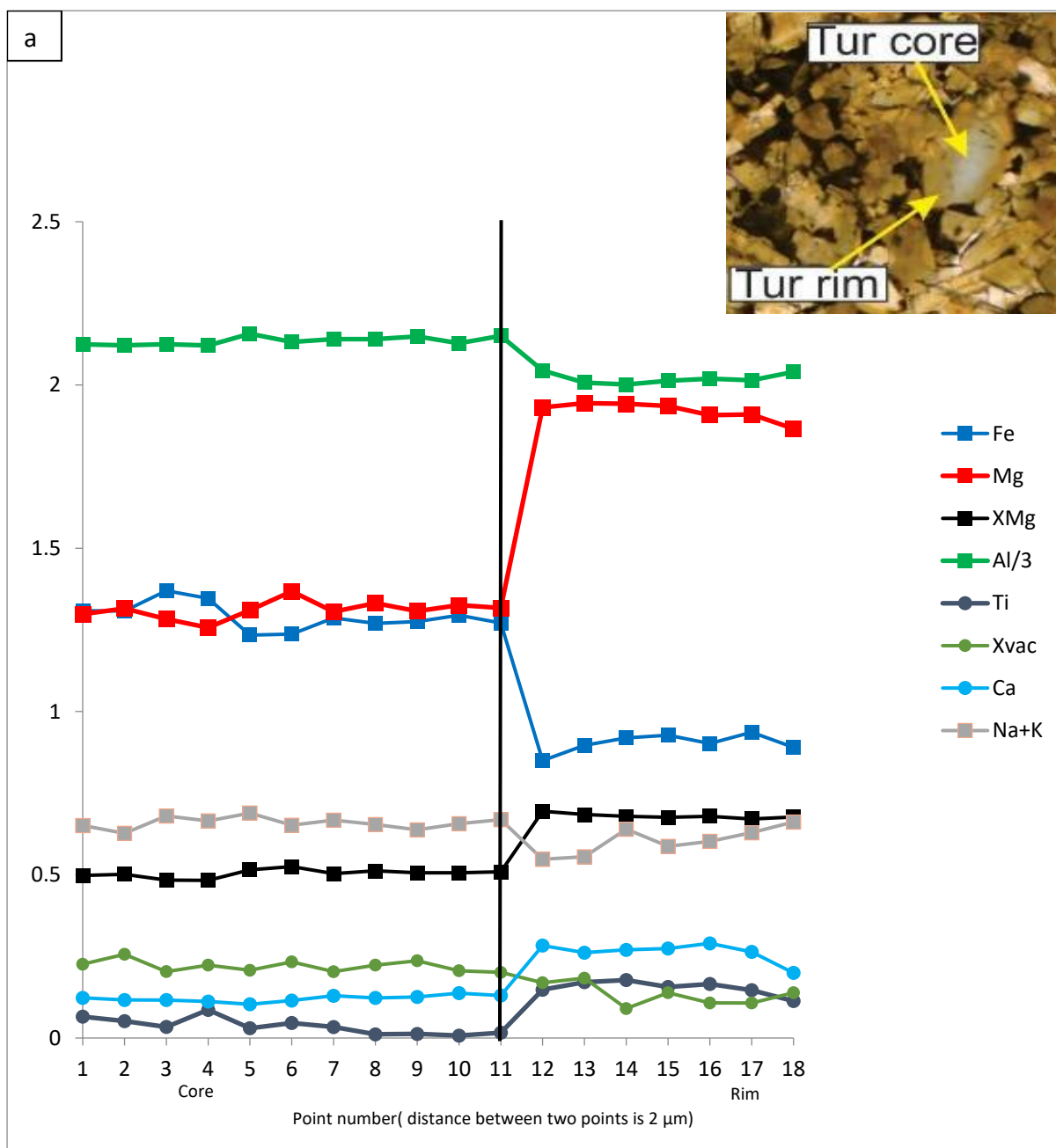


Fig 3.4.2.a: Plot of compositional variations of Gen-II tourmaline from the bluish green colour core and green in colour rim of a single zoned tourmaline grain in host muscovite schist.  $X_{Mg} = Mg/(Fe^{2+} + Mg)$ . Zero on the X-axis represents the starting point of the compositional traverse from the bluish green colour core. Photomicrograph of the zoned tourmaline and the traverse path is shown by the solid line (plane polarized light). Al is plotted as Al/3.

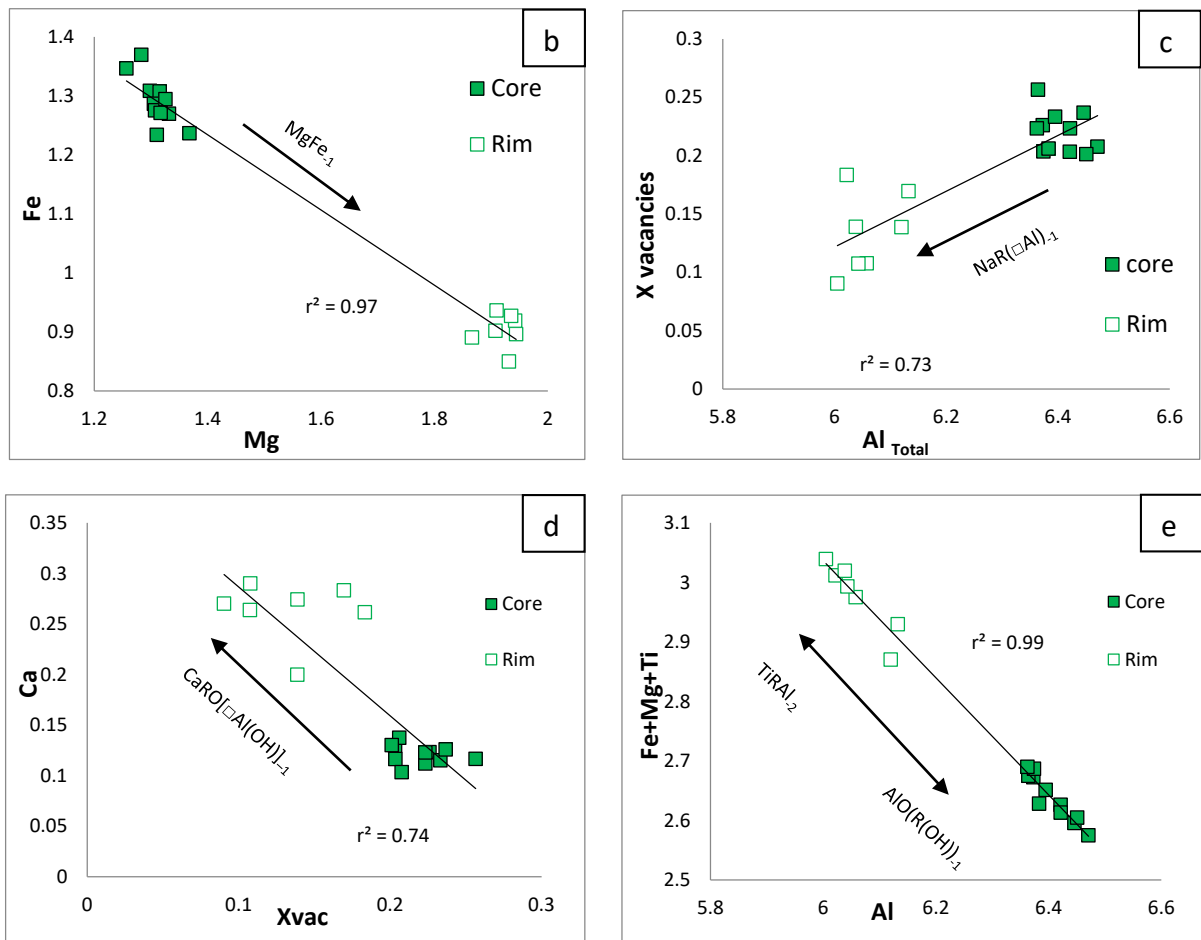


Fig 3.4.2b: Plot of data from the traverse of the Gen-II zoned tourmaline grain in terms of Fe vs. Mg showing strong correlations ( $r^2 = 0.97$ ). Fig 3.4.2.c: Plot of data from the traverse of the zoned grain in terms of X-site vacancy vs.  $Al_{total}$  showing positive ( $r^2 = 0.73$ ) correlations. Fig 3.4.2d: Plot of data from the traverse of the zoned grain in terms of Ca vs. X-vac negative ( $r^2 = 0.74$ ) moderate correlations. Fig 3.4.2e: Plot of data from the traverse of the zoned grain in terms of Fe+Mg+Ti vs.  $Al_{Total}$  negative ( $r^2 = 0.99$ ) strong correlations.

Table 3.4.3a : Representative EPMA analysis of tourmaline.

Generation	Gen I	Gen I	Gen I	Gen I	Gen I	Gen I	Gen I	Gen I	Gen I	Gen I	Gen I	Gen I	Gen I	Gen I	Gen I	Gen I	Gen I	Gen I	Gen I	Gen I	
Sample no.	BR1/1	BR1/1	BR1/1	BR1/1	BR28B	BR28B	BR28B	BR28B	BR28B	BR28B	BR 1/1	BR 1/1	BR 1/1	BR 1/1	BR28B	BR28B	BR28B	BR28B	BR28B	BR28B	
Point	4 / 1	12 / 1	6 / 1	13 / 1	79 / 1	81 / 1	83 / 1	85 / 1	87 / 1	89 / 1	9 / 1	10 / 1	2/1	5/1	80 / 1	82 / 1	84 / 1	86 / 1	88 / 1	90 / 1	
Core/Rim	core	core	core	core	core	core	core	core	core	core	rim	rim									
Al <sub>2</sub> O <sub>3</sub>	31.84	31.89	31.79	31.70	32.16	32.67	32.38	32.38	32.26	32.32	31.88	31.84	31.51	31.73	32.48	32.62	32.25	32.01	33.19	31.81	
FeO	11.32	11.33	11.05	11.41	8.78	7.99	8.11	8.02	8.59	8.72	10.50	10.52	10.20	9.55	8.35	8.64	8.32	8.05	8.68	8.46	
TiO <sub>2</sub>	0.37	0.49	0.39	0.49	0.90	0.26	0.88	1.03	1.07	1.08	0.71	0.56	0.41	0.14	0.87	0.83	0.94	1.09	0.72	0.97	
SiO <sub>2</sub>	35.08	35.45	35.30	35.42	35.26	35.72	35.66	35.80	35.64	35.12	34.66	35.35	35.56	35.95	35.16	35.74	35.56	35.36	36.09	35.05	
K <sub>2</sub> O	0.05	0.06	0.02	0.06	0.03	0.06	0.05	0.04	0.04	0.05	0.01	0.03	0.04	0.00	0.03	0.06	0.04	0.01	0.04	0.05	
CaO	0.73	0.64	0.74	0.64	0.78	0.95	0.93	0.99	0.89	1.04	0.73	0.67	0.87	0.65	1.49	0.58	0.96	1.34	0.61	1.13	
Na <sub>2</sub> O	1.99	1.92	1.95	1.93	2.21	2.03	1.95	1.93	2.29	1.94	1.93	1.96	1.90	1.93	1.71	1.98	2.03	1.66	1.82	1.82	
Cr <sub>2</sub> O <sub>3</sub>	0.00	0.01	0.00	0.01	0.00	0.00	0.00	0.00	0.00	0.00	0.00	0.03	0.06	0.02	0.00	0.00	0.00	0.00	0.00	0.00	
MnO	0.06	0.06	0.03	0.06	0.00	0.10	0.06	0.01	0.00	0.17	0.06	0.06	0.05	0.03	0.07	0.11	0.01	0.05	0.00	0.00	
MgO	3.99	3.99	4.22	4.01	5.83	6.21	5.89	6.27	6.11	5.48	4.38	4.60	4.85	4.90	6.17	5.32	5.88	6.13	5.64	5.90	
B <sub>2</sub> O <sub>3</sub> *	10.30	10.36	10.33	10.34	10.48	10.54	10.52	10.59	10.59	10.47	10.26	10.37	10.36	10.36	10.53	10.51	10.51	10.49	10.64	10.40	
Total	95.73	96.20	95.82	96.07	96.43	96.53	96.43	97.06	97.48	96.39	95.12	95.99	95.81	95.26	96.86	96.39	96.50	96.19	97.43	95.59	
Si(T)	5.96	5.98	5.97	5.99	5.88	5.92	5.94	5.91	5.89	5.88	5.90	5.96	6.00	6.00	5.84	5.95	5.93	5.90	5.92	5.90	
Al(T)	0.08	0.05	0.06	0.05	0.15	0.11	0.11	0.13	0.16	0.17	0.13	0.08	0.04	0.00	0.20	0.09	0.13	0.14	0.11	0.15	
B(T)	3.00	3.00	3.00	3.00	3.00	3.00	3.00	3.00	3.00	3.00	3.00	3.00	3.00	3.00	3.00	3.00	3.00	3.00	3.00	3.00	
Al(Z)	6.00	6.00	6.00	6.00	6.00	6.00	6.00	6.00	6.00	6.00	6.00	6.00	6.00	6.00	6.00	6.00	6.00	6.00	6.00	6.00	
Al(Y)	0.25	0.25	0.24	0.23	0.13	0.24	0.19	0.13	0.08	0.15	0.23	0.21	0.19	0.27	0.11	0.26	0.16	0.11	0.28	0.12	
Ti(Y)	0.05	0.06	0.05	0.06	0.11	0.03	0.11	0.13	0.13	0.14	0.09	0.07	0.05	0.02	0.11	0.10	0.12	0.14	0.09	0.12	
Cr(Y)	0.00	0.00	0.00	0.00	0.00	0.00	0.00	0.00	0.00	0.00	0.00	0.00	0.01	0.00	0.00	0.00	0.00	0.00	0.00	0.00	
Fe(Y)	1.61	1.60	1.56	1.61	1.23	1.11	1.13	1.11	1.19	1.22	1.49	1.48	1.44	1.36	1.16	1.20	1.16	1.12	1.19	1.19	
Mn(Y)	0.01	0.01	0.00	0.01	0.00	0.01	0.01	0.00	0.00	0.02	0.01	0.01	0.01	0.00	0.01	0.02	0.00	0.01	0.00	0.00	
Mg(Y)	1.01	1.00	1.06	1.01	1.45	1.53	1.46	1.54	1.50	1.37	1.11	1.15	1.22	1.24	1.53	1.32	1.46	1.53	1.38	1.48	
K(X)	0.01	0.01	0.00	0.01	0.01	0.01	0.01	0.01	0.01	0.01	0.00	0.01	0.01	0.00	0.01	0.01	0.01	0.00	0.01	0.01	
Ca(X)	0.13	0.12	0.13	0.12	0.14	0.17	0.16	0.17	0.16	0.18	0.13	0.12	0.16	0.12	0.26	0.10	0.17	0.24	0.11	0.20	
Na(X)	0.65	0.62	0.64	0.63	0.71	0.65	0.62	0.61	0.73	0.62	0.63	0.64	0.62	0.63	0.55	0.63	0.65	0.53	0.58	0.59	
X vacancies	0.21	0.25	0.23	0.24	0.14	0.17	0.20	0.20	0.11	0.18	0.23	0.24	0.22	0.26	0.18	0.25	0.17	0.23	0.31	0.20	
X <sub>Mg</sub>	0.39	0.39	0.40	0.39	0.54	0.58	0.56	0.58	0.56	0.53	0.43	0.44	0.46	0.48	0.57	0.52	0.56	0.58	0.54	0.55	

Note: Atomic proportions based on ΣT+Z+Y cations = 15. X<sub>Mg</sub> = Mg/(Fe<sup>2+</sup> + Mg).

\* B<sub>2</sub>O<sub>3</sub> calculated assuming B to be 3 atoms per formula unit.

Table 3.4.3a : Representative EPMA analysis of tourmaline(continued).

Generation	Gen I	Gen II																		
Sample no.	BR28B	BR 38																		
Point	95 / 1	1 / 1	1 / 2	1 / 3	1 / 4	1 / 5	1 / 6	1 / 7	1 / 8	1 / 9	1 / 10	1 / 11	5 / 1	7 / 1	11 / 1	14 / 1	16 / 1	16 / 2	16 / 3	16 / 4
Core/Rim	rim	core																		
Al <sub>2</sub> O <sub>3</sub>	31.87	32.27	32.11	32.22	32.38	32.77	32.68	32.71	32.61	32.41	32.32	32.69	33.91	31.55	30.90	31.95	31.67	32.18	30.86	31.32
FeO	8.49	9.34	9.30	9.76	9.66	8.81	8.91	9.24	9.09	9.04	9.24	9.08	6.41	6.22	6.51	5.74	10.20	10.09	10.09	10.15
TiO <sub>2</sub>	0.74	0.52	0.41	0.27	0.69	0.24	0.37	0.27	0.09	0.10	0.06	0.13	0.31	0.95	1.12	0.95	0.34	0.74	0.95	0.51
SiO <sub>2</sub>	34.62	35.53	35.43	35.32	35.60	35.55	35.84	35.68	35.65	35.32	35.65	35.49	36.50	36.57	36.09	36.04	35.04	35.81	35.01	35.15
K <sub>2</sub> O	0.05	0.04	0.05	0.06	0.06	0.07	0.01	0.09	0.03	0.00	0.05	0.05	0.02	0.02	0.02	0.00	0.04	0.06	0.03	0.02
CaO	1.35	0.69	0.65	0.65	0.63	0.58	0.65	0.73	0.69	0.70	0.77	0.73	0.48	0.96	1.45	1.14	0.91	0.89	0.84	0.75
Na <sub>2</sub> O	1.76	1.99	1.90	2.06	2.03	2.09	2.03	2.02	2.01	1.96	2.00	2.04	1.80	1.97	1.73	1.98	1.87	1.90	1.95	1.92
Cr <sub>2</sub> O <sub>3</sub>	0.00	0.00	0.00	0.05	0.00	0.00	0.04	0.00	0.06	0.00	0.06	0.00	0.01	0.00	0.00	0.00	0.06	0.00	0.13	0.00
MnO	0.06	0.02	0.03	0.04	0.10	0.00	0.00	0.08	0.02	0.00	0.06	0.03	0.00	0.00	0.02	0.00	0.05	0.05	0.09	0.02
MgO	6.15	5.20	5.25	5.13	5.06	5.25	5.53	5.26	5.35	5.20	5.31	5.28	6.53	7.48	7.68	7.62	4.91	4.91	4.70	4.88
B <sub>2</sub> O <sub>3</sub> *	10.37	10.43	10.38	10.40	10.48	10.44	10.52	10.50	10.45	10.36	10.43	10.44	10.69	10.61	10.54	10.58	10.31	10.51	10.24	10.27
Total	95.46	96.03	95.51	95.96	96.69	95.80	96.58	96.58	96.05	95.09	95.95	95.96	96.66	96.33	96.06	96.00	95.40	97.14	94.89	94.99
Si(T)	5.83	5.95	5.96	5.93	5.93	5.95	5.95	5.94	5.95	5.96	5.97	5.94	5.96	6.00	6.00	5.97	5.93	5.96	5.99	5.98
Al(T)	0.20	0.09	0.07	0.10	0.10	0.09	0.08	0.09	0.08	0.08	0.06	0.10	0.07	0.01	0.05	0.09	0.09	0.08	0.06	0.06
B(T)	3.00	3.00	3.00	3.00	3.00	3.00	3.00	3.00	3.00	3.00	3.00	3.00	3.00	3.00	3.00	3.00	3.00	3.00	3.00	3.00
Al(Z)	6.00	6.00	6.00	6.00	6.00	6.00	6.00	6.00	6.00	6.00	6.00	6.00	6.00	6.00	5.95	6.00	6.00	6.00	6.00	6.00
Al(Y)	0.10	0.25	0.26	0.25	0.22	0.34	0.28	0.29	0.31	0.33	0.28	0.32	0.43	0.08	0.00	0.10	0.20	0.19	0.11	0.19
Ti(Y)	0.09	0.07	0.05	0.03	0.09	0.03	0.05	0.03	0.01	0.01	0.01	0.02	0.04	0.12	0.14	0.12	0.04	0.09	0.12	0.07
Cr(Y)	0.00	0.00	0.00	0.01	0.00	0.00	0.01	0.00	0.01	0.00	0.01	0.00	0.00	0.00	0.00	0.00	0.01	0.00	0.02	0.00
Fe(Y)	1.20	1.31	1.31	1.37	1.35	1.23	1.24	1.29	1.27	1.28	1.29	1.27	0.88	0.86	0.90	0.79	1.44	1.40	1.44	1.44
Mn(Y)	0.01	0.00	0.00	0.01	0.01	0.00	0.00	0.01	0.00	0.00	0.01	0.00	0.00	0.00	0.00	0.00	0.01	0.01	0.01	0.00
Mg(Y)	1.54	1.30	1.32	1.28	1.26	1.31	1.37	1.31	1.33	1.31	1.33	1.32	1.59	1.85	1.90	1.88	1.24	1.22	1.20	1.24
K(X)	0.01	0.01	0.01	0.01	0.01	0.01	0.00	0.02	0.01	0.00	0.01	0.01	0.00	0.00	0.00	0.00	0.01	0.01	0.01	0.00
Ca(X)	0.24	0.12	0.12	0.12	0.11	0.10	0.11	0.13	0.12	0.13	0.14	0.13	0.08	0.17	0.26	0.20	0.16	0.16	0.15	0.14
Na(X)	0.57	0.64	0.62	0.67	0.65	0.67	0.65	0.65	0.65	0.64	0.65	0.66	0.57	0.63	0.55	0.63	0.61	0.61	0.64	0.63
X vacancies	0.18	0.23	0.26	0.20	0.22	0.21	0.23	0.20	0.22	0.24	0.21	0.20	0.35	0.20	0.19	0.17	0.22	0.22	0.20	0.23
X <sub>Mg</sub>	0.56	0.50	0.50	0.48	0.48	0.52	0.53	0.50	0.51	0.51	0.51	0.51	0.64	0.68	0.68	0.70	0.46	0.46	0.45	0.46

Note: Atomic proportions based on ΣT+Z+Y cations = 15. X<sub>Mg</sub> = Mg/(Fe<sup>2+</sup> + Mg).

\* B<sub>2</sub>O<sub>3</sub> calculated assuming B to be 3 atoms per formula unit.

Table 3.4.3a : Representative EPMA analysis of tourmaline(continued).

Generation	Gen II																			
Sample no.	BR 38																			
Point	16 / 5	1 / 12	1 / 13	1 / 14	1 / 15	1 / 16	1 / 17	1 / 18	1 / 19	1 / 20	1 / 21	1 / 22	1 / 23	1 / 24	1 / 25	1 / 26	1 / 27	1 / 28	1 / 29	1 / 30
Core/Rim	core	rim																		
Al <sub>2</sub> O <sub>3</sub>	31.83	31.43	30.74	30.64	31.00	30.83	30.76	31.01	32.73	32.38	32.49	31.51	31.78	31.92	31.72	31.71	31.52	31.78	31.84	31.69
FeO	10.75	6.14	6.45	6.61	6.71	6.47	6.72	6.36	9.49	9.17	9.30	7.34	5.85	6.22	6.07	5.74	5.78	5.80	5.98	6.43
TiO <sub>2</sub>	0.88	1.19	1.37	1.42	1.26	1.32	1.17	0.90	0.14	0.40	0.16	0.70	0.69	0.82	0.58	0.87	0.82	0.69	0.93	0.77
SiO <sub>2</sub>	35.22	35.81	35.88	35.81	35.95	35.72	35.79	36.33	35.35	35.64	35.45	35.60	36.20	35.98	35.92	36.19	36.08	35.99	35.74	35.79
K <sub>2</sub> O	0.06	0.06	0.07	0.08	0.04	0.05	0.02	0.06	0.00	0.05	0.03	0.04	0.05	0.04	0.02	0.08	0.05	0.06	0.05	0.06
CaO	0.77	1.61	1.48	1.53	1.56	1.64	1.49	1.13	0.64	0.65	0.65	1.12	1.17	1.17	1.15	1.06	1.07	1.13	1.00	1.00
Na <sub>2</sub> O	1.97	1.68	1.69	1.95	1.82	1.85	1.95	2.03	1.97	2.06	2.07	1.84	2.04	2.01	2.10	2.07	2.11	1.99	2.01	2.05
Cr <sub>2</sub> O <sub>3</sub>	0.03	0.00	0.01	0.00	0.02	0.07	0.00	0.00	0.02	0.00	0.00	0.00	0.05	0.00	0.06	0.00	0.00	0.00	0.07	0.00
MnO	0.08	0.08	0.02	0.02	0.00	0.03	0.00	0.07	0.03	0.05	0.07	0.03	0.10	0.00	0.10	0.00	0.00	0.06	0.02	0.02
MgO	4.72	7.83	7.85	7.84	7.86	7.68	7.69	7.48	5.00	5.01	4.83	6.88	7.95	7.71	7.98	7.77	7.90	7.86	7.47	7.39
B <sub>2</sub> O <sub>3</sub> *	10.42	10.58	10.53	10.55	10.59	10.53	10.51	10.53	10.41	10.42	10.38	10.45	10.62	10.60	10.58	10.59	10.56	10.56	10.53	10.51
Total	96.73	96.41	96.09	96.45	96.81	96.19	96.10	95.90	95.78	95.83	95.43	95.51	96.50	96.47	96.28	96.08	95.89	95.92	95.64	95.71
Si(T)	5.90	5.93	5.96	5.95	5.94	5.95	5.96	6.00	5.93	5.99	5.98	5.95	5.96	5.94	5.93	5.99	5.98	5.96	5.94	5.96
Al(T)	0.13	0.12	0.08	0.10	0.11	0.11	0.09	0.01	0.10	0.06	0.07	0.08	0.08	0.11	0.10	0.06	0.07	0.08	0.10	0.09
B(T)	3.00	3.00	3.00	3.00	3.00	3.00	3.00	3.00	3.00	3.00	3.00	3.00	3.00	3.00	3.00	3.00	3.00	3.00	3.00	3.00
Al(Z)	6.00	5.96	5.89	5.85	5.89	5.89	5.90	6.00	6.00	6.00	6.00	6.00	6.00	6.00	6.00	6.00	6.00	6.00	6.00	6.00
Al(Y)	0.13	0.00	0.00	0.00	0.00	0.00	0.00	0.02	0.34	0.30	0.35	0.09	0.05	0.06	0.04	0.07	0.05	0.08	0.09	0.09
Ti(Y)	0.11	0.15	0.17	0.18	0.16	0.17	0.15	0.11	0.02	0.05	0.02	0.09	0.09	0.10	0.07	0.11	0.10	0.09	0.12	0.10
Cr(Y)	0.00	0.00	0.00	0.00	0.00	0.01	0.00	0.00	0.00	0.00	0.00	0.00	0.01	0.00	0.01	0.00	0.00	0.00	0.01	0.00
Fe(Y)	1.51	0.85	0.90	0.92	0.93	0.90	0.94	0.89	1.33	1.29	1.31	1.03	0.81	0.86	0.84	0.79	0.80	0.80	0.83	0.89
Mn(Y)	0.01	0.01	0.00	0.00	0.00	0.00	0.00	0.01	0.00	0.01	0.01	0.00	0.01	0.00	0.01	0.00	0.00	0.01	0.00	0.00
Mg(Y)	1.18	1.93	1.94	1.94	1.94	1.91	1.91	1.87	1.25	1.25	1.21	1.71	1.95	1.90	1.96	1.92	1.95	1.94	1.85	1.83
K(X)	0.01	0.01	0.01	0.02	0.01	0.01	0.00	0.01	0.00	0.01	0.01	0.01	0.01	0.01	0.00	0.02	0.01	0.01	0.01	0.01
Ca(X)	0.14	0.28	0.26	0.27	0.27	0.29	0.26	0.20	0.11	0.12	0.12	0.20	0.21	0.21	0.20	0.19	0.19	0.20	0.18	0.18
Na(X)	0.64	0.53	0.54	0.62	0.58	0.59	0.62	0.65	0.64	0.67	0.67	0.59	0.65	0.64	0.67	0.66	0.67	0.63	0.64	0.66
X vacancies	0.21	0.17	0.18	0.09	0.14	0.11	0.11	0.14	0.25	0.21	0.21	0.20	0.14	0.15	0.12	0.14	0.13	0.15	0.17	0.15
X <sub>Mg</sub>	0.44	0.69	0.68	0.68	0.68	0.68	0.67	0.68	0.48	0.49	0.48	0.63	0.71	0.69	0.70	0.71	0.71	0.71	0.69	0.67

Note: Atomic proportions based on ΣT+Z+Y cations = 15. X<sub>Mg</sub> = Mg/(Fe<sup>2+</sup> + Mg).

\* B<sub>2</sub>O<sub>3</sub> calculated assuming B to be 3 atoms per formula unit.

Table 3.4.3a: Representative EPMA analysis of tourmaline(continued).

Generation	Gen II	Gen II	Gen II							
Sample no.	BR 38	BR 38	BR 38							
Point	8 / 1	13 / 1	15 / 1	16 / 6	16 / 7	16 / 8	16 / 9	16 / 10	16 / 11	16 / 12
Core/Rim	rim	rim	rim							
Al <sub>2</sub> O <sub>3</sub>	31.95	31.94	31.64	32.09	32.31	31.40	31.63	32.15	31.87	31.57
FeO	6.24	7.00	6.39	6.30	6.08	6.07	5.94	6.19	5.84	5.74
TiO <sub>2</sub>	0.79	0.97	0.74	0.89	0.93	1.00	0.88	0.74	0.84	1.00
SiO <sub>2</sub>	36.01	36.01	35.97	35.87	35.95	36.04	36.04	36.29	36.67	36.51
K <sub>2</sub> O	0.07	0.02	0.03	0.06	0.03	0.04	0.04	0.04	0.01	0.06
CaO	0.99	1.03	1.07	1.08	1.12	1.26	1.14	1.06	1.25	1.10
Na <sub>2</sub> O	1.98	2.05	2.04	1.99	2.00	1.99	1.93	2.00	2.01	2.02
Cr <sub>2</sub> O <sub>3</sub>	0.01	0.00	0.05	0.12	0.00	0.00	0.05	0.07	0.09	0.11
MnO	0.04	0.01	0.06	0.00	0.00	0.06	0.01	0.02	0.00	0.00
MgO	7.44	6.91	7.26	7.31	7.80	7.88	7.83	7.51	7.95	7.71
B <sub>2</sub> O <sub>3</sub> *	10.57	10.58	10.52	10.58	10.66	10.58	10.57	10.64	10.71	10.63
Total	96.09	96.52	95.77	96.29	96.88	96.32	96.06	96.71	97.24	96.45
Si(T)	5.96	5.96	5.99	5.94	5.90	5.96	5.96	5.97	6.00	6.00
Al(T)	0.08	0.09	0.06	0.11	0.14	0.08	0.08	0.08	0.05	0.03
B(T)	3.00	3.00	3.00	3.00	3.00	3.00	3.00	3.00	3.00	3.00
Al(Z)	6.00	6.00	6.00	6.00	6.00	5.99	6.00	6.00	6.00	6.00
Al(Y)	0.11	0.10	0.10	0.10	0.07	0.00	0.05	0.11	0.04	0.05
Ti(Y)	0.10	0.12	0.09	0.11	0.11	0.12	0.11	0.09	0.10	0.12
Cr(Y)	0.00	0.00	0.01	0.02	0.00	0.00	0.01	0.01	0.01	0.01
Fe(Y)	0.86	0.97	0.89	0.87	0.83	0.84	0.82	0.85	0.80	0.79
Mn(Y)	0.01	0.00	0.01	0.00	0.00	0.01	0.00	0.00	0.00	0.00
Mg(Y)	1.84	1.71	1.80	1.80	1.91	1.94	1.93	1.84	1.94	1.90
K(X)	0.01	0.00	0.01	0.01	0.01	0.01	0.01	0.01	0.00	0.01
Ca(X)	0.17	0.18	0.19	0.19	0.20	0.22	0.20	0.19	0.22	0.19
Na(X)	0.63	0.65	0.65	0.63	0.63	0.63	0.61	0.63	0.63	0.64
X vacancies	0.18	0.16	0.15	0.16	0.17	0.14	0.18	0.17	0.15	0.15
X <sub>Mg</sub>	0.68	0.64	0.67	0.67	0.70	0.70	0.70	0.68	0.71	0.71

Note: Atomic proportions based on  $\Sigma T+Z+Y$  cations = 15.  $X_{Mg} = Mg/(Fe^{2+} + Mg)$ .

\* B<sub>2</sub>O<sub>3</sub> calculated assuming B to be 3 atoms per formula unit.

Table 3.4.3b: Representative EPMA analysis of muscovite, Kfeldspar, plagioclase feldspar and ilmenite.

Sample No	BR28 B	BR17	BR17	BR17	BR 17	BR 17	BR 40F	BR 40F	BR 40F	BR 40F				
DataSet /Point	91 / 1	92 / 1	93 / 1	94 / 1	96 / 1	46 / 1	47 / 1	49 / 1	45 / 1	50 / 1	39/1	43/1	41/1	51/1
Mineral	Muscovite	Kfeldspar	Kfeldspar	Plagioclase	Plagioclase	illmanite	illmanite							
SiO <sub>2</sub>	46.05	45.63	46.42	45.83	45.49	46.43	46.95	46.73	65.51	65.07	62.10	63.43	0.01	0.05
TiO <sub>2</sub>	0.96	1.05	0.62	0.90	0.61	0.63	0.51	0.57	0.02	0.00	0.00	0.00	50.37	50.26
Al <sub>2</sub> O <sub>3</sub>	33.55	33.34	34.28	33.81	34.06	32.44	32.76	33.08	19.06	18.72	23.12	22.33	0.05	0.00
Cr <sub>2</sub> O <sub>3</sub>	0.00	0.00	0.00	0.00	0.00	0.00	0.00	0.00	0.00	0.00	0.00	0.02	0.05	0.03
FeO	1.52	1.48	1.42	1.28	1.22	3.33	3.26	3.44	0.00	0.05	0.09	0.00	45.72	45.67
MnO	0.02	0.00	0.00	0.00	0.00	0.02	0.00	0.12	0.00	0.12	0.02	0.00	2.08	1.84
CaO	0.00	0.00	0.00	0.00	0.00	0.00	0.00	0.00	0.00	0.00	5.51	4.82	0.05	0.11
MgO	0.98	0.90	0.95	0.83	0.72	1.27	1.15	1.30	0.02	0.00	0.04	0.01	0.06	0.06
Na <sub>2</sub> O	0.71	0.65	0.68	0.80	0.63	0.37	0.42	0.41	0.94	0.75	8.92	9.31	0.03	0.08
K <sub>2</sub> O	10.55	10.70	10.76	10.59	10.41	10.69	10.60	10.94	15.39	15.33	0.10	0.12	0.01	0.00
P <sub>2</sub> O <sub>5</sub>	0.00	0.00	0.00	0.00	0.00	0.00	0.00	0.00	0.00	0.00	0.00	0.00	0.00	0.00
Total	94.34	93.75	95.13	94.04	93.14	95.27	95.65	96.59	100.94	100.04	99.90	100.04	98.49	98.10
Normalization basis	11(O)	8(O)	8(O)	8(O)	8(O)	3(O)	3(O)							
Si	3.11	3.10	3.10	3.10	3.10	3.13	3.15	3.11	2.99	3.00	2.75	2.80	0.00	0.00
Ti	0.05	0.05	0.03	0.05	0.03	0.03	0.03	0.03	0.00	0.00	0.00	0.00	0.98	0.98
Al	2.67	2.67	2.70	2.70	2.74	2.58	2.59	2.60	1.03	1.02	1.21	1.16	0.00	0.00
Cr	0.00	0.00	0.00	0.00	0.00	0.00	0.00	0.00	0.00	0.00	0.00	0.00	0.00	0.00
Fe	0.09	0.08	0.08	0.07	0.07	0.19	0.18	0.19	0.03	0.06	0.06	0.03	0.99	0.99
Mn	0.00	0.00	0.00	0.00	0.00	0.00	0.00	0.01	0.00	0.00	0.00	0.00	0.05	0.04
Ca	0.00	0.00	0.00	0.00	0.00	0.00	0.00	0.00	0.00	0.00	0.26	0.23	0.00	0.00
Mg	0.10	0.09	0.09	0.08	0.07	0.13	0.11	0.13	0.00	0.00	0.00	0.00	0.00	0.00
Na	0.09	0.09	0.09	0.10	0.08	0.05	0.05	0.05	0.08	0.07	0.77	0.80	0.00	0.00
K	0.91	0.93	0.92	0.91	0.90	0.92	0.91	0.93	0.90	0.90	0.01	0.01	0.00	0.00
P	0.00	0.00	0.00	0.00	0.00	0.00	0.00	0.00	0.00	0.00	0.00	0.00	0.00	0.00
X <sub>An</sub>									0.00	0.00	0.25	0.22		
X <sub>Ab</sub>									0.08	0.07	0.74	0.77		
X <sub>Kfs</sub>									0.92	0.93	0.01	0.01		

### 3.5 Trace and REE concentrations of tourmaline

In chondrite normalized REE spectra (McDonough and Sun, 1995), Gen-I tourmalines show (Fig 3.5.1a) overall LREE enrichment but with a variable range (i.e ~1-10 X chondrite for La). Both core and rim show uniform negative slope for LREE pattern with overlapping ranges. Both core and rim exhibit prominent positive Eu anomaly ( $\text{Eu}/\text{Eu}^* = 8.61-26.58$ ) with  $(\text{La}/\text{Lu})_{\text{CN}} = 1.66-291.46$  ( $\text{La}/\text{Lu} > 1$ ). However, HREE concentrations in the core are more consistent whereas the rim shows more variability. HREE patterns for both core and rim are irregular, i.e. zig jagged. The difference between them is that the HREE pattern in the rim is nearly flat while the core shows a distinctly concave up pattern showing Yb or Lu enrichment. The rims also have higher HREE concentrations than the core. The rim of the tourmaline grain shows higher  $\text{REE}_{\text{total}}$  contents than the core. The  $\text{REE}_{\text{total}}$  contents at the core vary from 1.51 ppm to 14.67 ppm (average  $9.32 \pm 5.32$  ppm) and corresponding rim  $\text{REE}_{\text{total}}$  contents vary from 2.34 ppm to 14.41 ppm (average  $8.02 \pm 5.27$  ppm). Thus, there is an overlapping of  $\text{REE}_{\text{total}}$  concentration between core and rim (Fig 3.5.1a).

In chondrite normalized REE spider diagram (McDonough and Sun, 1995), the Gen-II tourmalines (Fig 3.5.1b) show negatively sloped LREE with near (1-2 X chondrite) to below-chondritic LREE concentration (0.1 X chondrite). They show notably positive Eu anomaly ( $\text{Eu}/\text{Eu}^* = 13.50-48.78$ ) with  $(\text{La}/\text{Lu})_{\text{CN}} = 5.43-49.57$  ( $\text{La}/\text{Lu} > 1$ ). HREE concentrations are near to below chondritic (1 to 0.1 X chondrite) that show flat to slightly concave up HREE pattern. The core and rim show overlapping ranges and similar patterns here. The  $\text{REE}_{\text{total}}$  content at the core varies from 1.46 ppm to 2.44 ppm (average  $2.03 \pm 0.50$  ppm) and the corresponding rim  $\text{REE}_{\text{total}}$  content varies from 1.93 ppm to 2.88 ppm (average  $2.53 \pm 0.35$  ppm).

In the upper continental crust (UCC) normalized multielement diagram (UCC data from Rudnick and Gao, 2003) of Gen-I tourmaline is shown in Fig 3.5.1c. The Gen-I tourmalines show prominent depletion in LILE such as Rb and Ba and moderate depletion in Sr compared to UCC. Compatible and metal elements such as Ni, Co, Zn and V, Sc concentrations are consistent and closer to UCC values. Both core and rim show subcrustal REE and Y values. However, the core exhibits gradual enrichment in heavier REEs where the rim shows near consistent concentration. Both core and rim show minor enrichment in Tb and notable positive Eu anomaly. Core and rim show flat to positive sloped LREE pattern showing LREE enrichment. All the spots show notable enrichment in Ti. The HFSE concentrations, i.e. Hf, Zr,

They are mostly irregular showing near or depleted patterns with respect to the UCC. Both core and rim show enrichment of Ta with respect to Nb.

In upper continental crust (UCC) normalized multielement diagram (UCC data from Rudnick and Gao, 2003) of Gen-II tourmaline is shown in Fig 3.5.1d. The pattern is nearly similar to the Gen-I tourmalines although certain differences exist. The core and rim compositions are nearly indistinguishable which makes the overall pattern more regular. Depletion in certain LILE, viz. Rb and Ba are more prominent than Gen-I tourmalines. LREE and HREE patterns for both core and rim are flat and moderately depleted ( $\sim 0.1-0.01 \times$  chondrite) with respect to the UCC. This is in contrast with the Gen-I tour which shows enrichment in both lighter and heavier REEs. The LREE concentrations in Gen-II tourmalines are very regular and consistent within a narrower compositional range. The positive Tb, Eu and Ti anomalies are noted in Gen II as well and their intensities are similar to Gen-I tourmalines. The HFSE concentration is enriched in U and Th compared to Gen-I.

Representative LA-ICP-MS trace-element analyses (in ppm) of tourmaline are given in Table 3.5.2a.

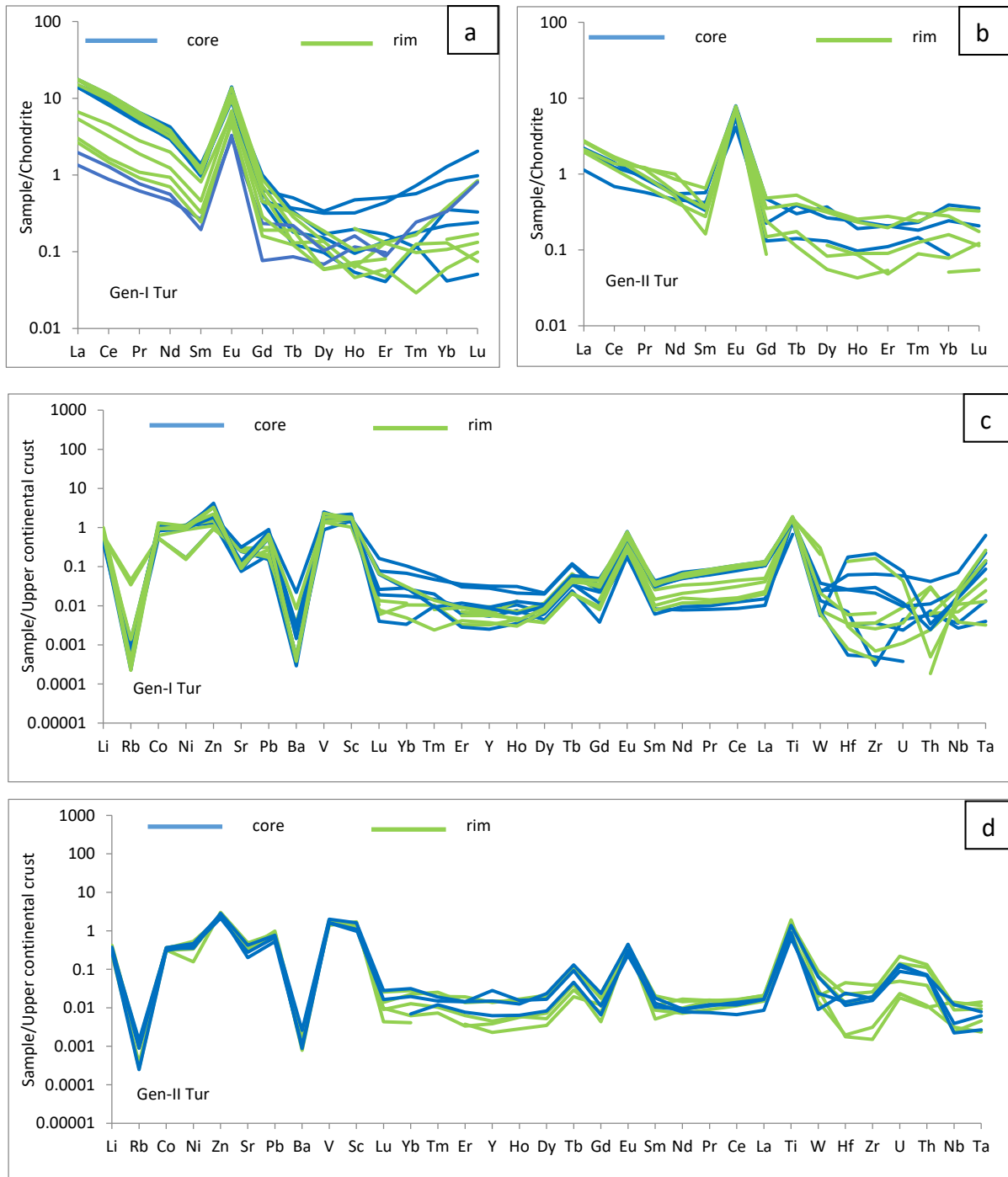


Fig 3.5.1a: Chondrite normalized (McDonough and Sun, 1995) REE spider diagram of Gen-I tourmaline (Blue–core: Green-rim) in muscovite schist/quartz muscovite schist. Fig 3.5.1b: Chondrite normalized (McDonough and Sun S, 1995) REE spider diagram of Gen-II tourmaline (Blue –core: Green-rim) in muscovite schist. Fig 3.5.1c: Upper continental crust (UCC) normalized (Rudnick and Gao, 2003) multi-element diagram for Gen-I tourmaline (Blue –core : Green-rim) within muscovite schist/quartz muscovite schist. Fig 3.5.1d: Upper continental crust (UCC) normalized (Rudnick and Gao, 2003) multi-element diagram for Gen-II tourmaline (Blue –core : Green-rim) within muscovite schist.[The gaps in the spidergrams represent element concentrations that are below detection limit]

Table 3.5.2a: Representative LA-ICPMS trace element analysis (in ppm) of tourmaline.

Sample no.	BR 1/1	BR 1/1	BR 28 B	BR 1/1	BR 1/1	BR 1/1					
Mineral	Tourmaline										
Point	4	10	2	4	7	9	12	5	9	11	
Generation	Gen I										
Core/Rim	core	rim	rim	rim							
La	0.46	0.32	3.30	3.31	3.28	4.16	3.51	1.57	1.27	0.63	
Ce	0.79	0.54	4.98	5.40	5.16	6.85	6.19	2.81	1.96	0.90	
Pr	0.07	0.06	0.44	0.45	0.46	0.61	0.52	0.26	0.18	0.09	
Nd	0.26	0.21	1.38	1.38	1.33	1.93	1.47	0.91	0.56	0.32	
Sm	0.03	0.04	0.16	0.14	0.15	0.20	0.17	0.12	0.07	0.04	
Eu	0.19	0.17	0.60	0.69	0.79	0.57	0.52	0.35	0.39	0.30	
Gd	0.02	0.05	0.09	0.11	0.13	0.20	0.09	0.09	0.06	0.03	
Tb	0.00	0.01	0.01	0.01	0.02	0.01	0.00	0.01	0.00	0.00	
Dy	0.02	0.03	0.08	0.04	0.08	0.04	0.02	0.05	bdl	0.01	
Ho	0.01	0.01	0.02	0.01	0.03	0.01	0.00	0.01	0.01	0.00	
Er	0.02	0.01	0.07	0.02	0.08	0.03	0.01	0.02	0.02	0.01	
Tm	bdl	0.01	0.02	0.00	0.01	0.00	0.00	0.00	bdl	0.00	
Yb	bdl	0.05	0.21	0.04	0.14	0.06	0.01	bdl	0.02	0.02	
Lu	bdl	0.02	0.05	0.01	0.02	0.01	0.00	0.00	0.00	0.00	
Total REE	1.87	1.52	11.40	11.61	11.68	14.68	12.51	6.22	4.56	2.35	
Eu anomaly	24.31	12.26	14.15	16.05	16.77	8.51	11.77	9.96	18.34	26.01	
Li	11.08	15.10	12.99	14.41	15.55	11.95	14.51	23.88	13.19	15.11	
Sc	20.71	32.70	23.76	19.26	20.05	21.85	30.83	21.11	14.27	26.16	
Ti	2567.36	5629.52	5594.90	6042.09	6168.09	6295.70	7088.18	6888.83	6691.55	6442.29	
V	84.91	120.57	213.41	201.14	243.49	156.80	187.08	139.31	132.20	184.53	
Co	15.43	4.84	20.37	19.19	19.94	15.63	14.29	16.09	10.82	9.34	
Ni	52.10	4.70	50.46	45.31	43.57	53.68	44.20	54.88	41.20	7.84	
Zn	88.01	34.58	145.07	123.43	136.13	248.60	281.66	99.36	74.32	63.00	
Rb	0.11	205.27	0.02	0.08	0.08	0.07	0.05	0.08	0.11	3.73	
Sr	24.24	40.50	31.02	44.50	100.16	28.36	25.96	43.91	94.64	85.19	
Y	0.11	0.16	0.59	0.18	0.67	0.19	0.05	0.20	0.13	0.07	
Zr	0.70	1.49	41.51	5.69	12.50	4.03	0.10	0.70	0.50	0.13	
Nb	0.03	5.20	0.19	0.21	0.85	0.31	0.26	0.05	0.05	0.13	
Mo	0.02	0.02	0.10	0.06	0.05	0.06	0.09	0.02	bdl	0.02	
Ag	0.02	0.01	0.05	0.31	0.23	0.08	0.02	0.01	0.01	0.02	
Ba	0.33	87.66	0.28	13.83	0.91	1.98	1.65	0.32	0.24	2.26	
Hf	0.02	0.07	0.93	0.14	0.33	0.14	0.00	0.02	0.02	0.02	
Ta	0.00	0.25	0.08	0.11	0.57	0.20	0.13	0.00	bdl	0.01	
W	bdl	30.15	0.01	0.07	0.04	0.05	0.01	0.01	bdl	0.57	
Pb	3.36	2.94	8.84	13.09	15.13	11.46	11.29	4.63	5.27	3.42	
Th	0.08	0.47	0.04	0.03	0.44	0.12	bdl	0.32	0.30	0.03	
U	0.01	0.02	0.21	0.03	0.16	0.03	0.00	0.02	0.01	0.00	

bdl: below detection limit

Table 3.5.2a: Representative LA-ICPMS trace element analysis (in ppm) of tourmaline (continued).

Sample no.	BR 28 B	BR 28 B	BR 28 B	BR 60(i)							
Mineral	Tourmaline										
Point	1	8	11	36	38	46	37	39	40	44	45
Generation	Gen I	Gen I	Gen I	Gen II							
Core/Rim	rim	rim	rim	core	core	core	rim	rim	rim	rim	rim
La	4.07	3.55	4.17	0.51	0.27	0.52	0.63	0.50	0.46	0.65	0.64
Ce	6.19	5.85	6.91	0.75	0.42	0.87	0.97	0.84	0.71	1.00	1.03
Pr	0.54	0.50	0.61	0.09	0.05	0.08	0.11	0.11	0.06	0.09	0.11
Nd	1.61	1.43	1.75	0.25	0.21	0.25	0.46	0.39	0.20	0.24	0.27
Sm	0.18	0.17	0.16	0.08	0.06	0.05	0.05	0.10	0.04	0.02	0.05
Eu	0.77	0.54	0.61	0.45	0.23	0.32	0.41	0.42	0.39	0.43	0.44
Gd	0.18	0.12	0.15	0.09	0.04	0.03	0.07	0.10	0.02	0.03	0.05
Tb	0.01	0.00	0.01	0.01	0.01	0.01	0.01	0.02	bdl	0.01	0.00
Dy	0.03	0.03	0.03	0.09	0.07	0.03	0.08	0.08	0.03	0.02	0.01
Ho	0.00	bdl	0.00	0.01	0.01	0.01	0.01	0.01	0.00	0.00	0.00
Er	0.02	0.02	0.01	0.03	0.03	0.02	0.03	0.04	0.01	0.01	0.01
Tm	0.00	bdl	0.00	0.01	0.00	0.00	0.01	0.01	0.00	0.00	bdl
Yb	0.06	bdl	0.01	0.06	0.04	0.01	0.05	0.06	0.01	0.03	0.01
Lu	0.02	bdl	0.00	0.01	0.01	bdl	0.00	0.01	0.00	0.00	0.00
Total REE	13.70	12.25	14.41	2.45	1.46	2.18	2.89	2.68	1.94	2.53	2.62
Eu anomaly	12.86	10.95	12.24	15.24	12.87	24.21	20.18	13.19	38.32	48.71	26.38
Li	15.90	16.84	18.93	8.06	8.97	6.75	8.75	10.08	6.52	5.81	8.77
Sc	24.84	23.56	25.74	22.53	15.36	13.69	22.31	20.27	17.06	18.59	24.04
Ti	5975.91	7355.03	6138.17	5319.13	2442.20	3442.43	6044.43	6195.08	3551.63	3561.79	7372.29
V	222.75	136.75	175.56	193.72	157.79	154.32	181.10	185.08	180.55	164.08	134.55
Co	22.71	16.02	16.41	5.97	6.31	5.30	6.09	6.32	5.32	5.40	5.47
Ni	51.20	51.48	42.16	16.64	21.85	19.33	25.06	21.60	15.79	18.01	7.37
Zn	149.01	216.58	220.49	189.76	175.75	141.52	148.63	174.82	180.87	153.28	202.47
Rb	0.03	0.11	0.02	0.12	0.07	0.02	0.11	0.08	bdl	0.03	0.02
Sr	34.79	29.37	28.78	134.69	64.42	89.21	121.04	107.98	114.98	112.94	154.42
Y	0.15	0.12	0.08	0.31	0.59	0.13	0.31	0.29	0.08	0.10	0.05
Zr	31.60	1.26	0.08	3.00	3.71	3.39	4.96	3.75	0.60	7.44	0.29
Nb	0.14	0.32	0.25	0.15	0.05	0.03	0.14	0.11	0.04	0.03	0.17
Mo	0.09	0.06	0.08	0.17	0.23	0.13	0.21	0.38	0.09	0.16	0.15
Ag	0.05	0.25	0.01	0.03	bdl	0.02	0.02	0.03	0.02	0.02	0.04
Ba	0.28	5.26	0.27	1.62	0.64	0.55	1.34	1.43	0.49	0.98	0.93
Hf	0.72	0.03	0.00	0.06	0.08	0.13	0.12	0.07	0.01	0.24	0.01
Ta	0.04	0.24	0.13	0.01	0.01	0.00	0.01	0.01	0.00	0.00	0.01
W	bdl	0.04	0.01	0.12	0.05	0.02	0.17	0.13	0.03	0.04	0.06
Pb	9.06	11.39	10.98	13.04	8.90	11.46	12.47	10.94	13.39	16.73	14.52
Th	0.01	0.06	0.00	0.72	0.76	0.72	1.39	1.17	0.12	0.40	0.11
U	0.12	bdl	bdl	0.24	0.32	0.36	0.59	0.38	0.06	0.13	0.05

bdl: below detection limit

### 3.6 Summary

The tourmaline mineralisation occurred in north-east and north west of the Beldih mine within the muscovite schist and the quartz muscovite schist. Based on the morphology and relation with the host rock there are three different modes of occurrences of tourmaline (mode 1, mode 2 and mode 3). Within these modes of occurrences, there is two distinct generations of tourmalines observed. The first generation (Gen-I) of tourmaline occurred as laterally impersistent lenticular stringers, veins, laminations in quartz muscovite schist and alternate bands in quartz -tourmaline rock (mode 1 and mode 3). These tourmaline grains are fractured and aligned parallel the foliation plane ( $S_1$ ). Thus, first generation of tourmaline (Gen-I) is syn-tectonic to the regional deformation. Whereas, second generation (Gen-II) of tourmaline in muscovite schist occurs are coarse grained with prominent optical zoning and randomly oriented (mode 2). So second generation tourmaline formed in muscovite schist at post deformational of  $S_1$  and  $D_3/F_3$ . All the different generations (Gen-I and Gen-II) of the tourmaline are alkali rich and schorl to dravite in character. The core and the rim composition of Gen-I tourmaline is overlapping and straddle the boundary between schorl and dravite. Whereas Gen-II tourmaline core composition straddles the boundary between schorl and dravite but the rim composition is dravite. In the chondrite normalised REE diagram, Gen-I tourmalines show overall LREE enrichment with a strong positive Eu anomaly followed by flat to concave up HREE pattern. Whereas Gen-II tourmalines show negatively sloped LREE with notably positive Eu anomaly followed by flat to slightly concave up HREE pattern.  $REE_{total}$  content in Gen-I tourmaline is higher than the Gen-II of tourmaline.

# CHAPTER 4

## Tourmaline bearing rocks in and around Kutni

Kutni village is located 25 km south-east from Barabazar town in Purulia district, West Bengal. The position of the Kutni area is shown in the map of Fig 1.5a. Geologically, Kutni falls inside the SPSZ and situated southern part of SPSZ (Fig 1.5a). The detailed geological description of the area is dealt in the subsequent section.

### 4.1 Lithology and structure of the area

The major lithological distribution in and around Kutni area is shown in Fig 4.1.1. Like Haripaldih (Chapter 2) and Beldih (Chapter 3), the CGGC components of the SPSZ in this sector are represented by muscovite schist/ muscovite quartz schist in the north. Due to variation of quartz content alternate quartz rich and mica rich bandings of variable thickness are also seen in this area. A Prominent schistosity plane is developed due to presence of phyllosilicate mineral i.e. muscovite (Fig.4.1.2a). A laterally persistent mappable body of wide quartz vein (100-250m) intruded within the muscovite schist/ muscovite quartz schist and continuous along the E-W trending foliation plane. This quartz vein is suffered deformation and is weakly foliated in places. The Chandil formation of NSMB, exposed south of muscovite schist/quartz-muscovite schist is represented by phyllite, the dominant component, that contains discrete pods and lenses of diverse lithologies. Phyllite is very fine-grained, light to dark coloured and composed of phyllosilicates which define the prominent foliation plane (Fig 4.1.2b). The colour of the phyllite is varying due to the variation in abundance of the phyllosilicate minerals present. Phyllite content phyllosilicate minerals such as muscovite, biotite, chlorite with quartz and feldspar. Elliptical pods of nepheline-bearing syenite, apatite-magnetite rocks and mafic ultramafic rocks occurred as intrusive within phyllite. The Intrusive body such as mafic-ultramafic rocks and apatite-magnetite rich rocks form within phyllites and are similar to what is encountered in Beldih and Fatepur area towards central part of SPSZ. The foliation planes are not uniformly developed within the mafic –ultramafic rocks due to stress heterogeneity all along with the unit and appeared as granular, coarse grained and more

or less massive on outcrop scale (Fig 4.1.2c). In Sushina hill near Kutni there are most conspicuous intrusive rocks found which is grey coloured alkaline unit that forms a rounded to oblong mount extending in NW-SE direction. The major part of the Sushina hill is dominated by nepheline syenite. This rock unit is medium to coarse grained, leucocratic and composed of albite megacrysts with aegirine and nepheline grains (Fig 4.1.2d). Due to the stress heterogeneity, some part of the exposure occurs as massive which is characterized by the absence of significant stretching of albite megacrysts. Whereas, some part occurs as prominent banding due to have stretched albite megacrysts. This banding occurs due to alternate light coloured bands of extensively stretched feldspar megacrysts and dark coloured bands of aegirine (Fig 4.1.2d). The Nepheline syenite is deformed and foliated which is parallel to the regional foliation. Quartz veins are intruded on both the quartz-muscovite schists (CGGC) and the phyllite of NSMB (Chandil formation). In the northern part of the Dandudih village, near Dandudih school, there is also a large unit of quartz vein that occurs as an elliptical body (E-W trend) intruding within the phyllite. This large quartz vein appears as quartz reef. Width of the quartz reef is up to 200m and laterally pinch out towards east and west direction. Quartz reef is composed of fine to medium grained milky white colour quartz (Fig 4.1.2e). A crude foliation exhibits within the quartz reef defines by elongated quartz grains. Under hand lens, the rocks exhibit saccaroidal texture due to recrystallization (Fig 4.1.2e). The northern and the southern boundary of the quartz reef is sheared. Stretching lineation of quartz is present in sheared quartz reef (Fig 4.1.2f). The boundary of the quartz reef is parallel with the adjacent phyllite of Chandil formation. Within this quartz reef tourmaline mineralisation occurred which will be describe in the next segment.

There are no primary structures preserved in and around Kutni area. The rocks in this region suffered at least three phases of deformation. The first phase of deformation ( $D_1$ ), produces the  $F_1$  folds whose axial planar schistosity ( $S_1$ ) is the most prominent planar fabric occurring as the regional schistosity of the study area, irrespective of lithology. The second phase of deformation ( $D_2$ ) produces  $F_2$  folds defined by the folding of the  $S_1$  planes. The third phase of deformation ( $D_3$ ) produces the  $F_3$  folds defined by the large broad warps of the resistant lithounits.

The strike of the regional foliation ( $S_1$ ) shown by muscovite schist/quartz muscovite schist varies from  $80^\circ$ - $100^\circ$  and dipping steeply ( $65$ - $80^\circ$ ) towards north (Fig 4.1.2a). Most prominent planar structures present in the phyllite of Kutni area is the regional foliation ( $S_1$ ) having a general trend of  $80^\circ$ - $100^\circ$  and  $120^\circ$ - $140^\circ$  respectively (Fig 4.1.2b). The variations of the strike due to the regional scale folding of  $S_1$ . The dip amount varies greatly from ( $60^\circ$ - $85^\circ$ )

towards both north and south directions. The phyllite is itself a very friable lithounit and shows dislodgement in many places. Due to the overall steep dipping nature of the foliation plane within the phyllite, the apparent change in dip direction may be an artefact. First generation or  $F_1$  folds are defined by the cross-cutting quartz veins (Fig 4.1.2g) whose axial planes are parallel to the foliation( $S_1$ ) of the rocks.  $F_1$  are mostly asymmetric with thickened hinges and longer limb sometimes become parallel to the foliation. The  $F_1$  fold defined by quartz vein within phyllite plunges  $35^\circ \rightarrow 115^\circ$ . The attitude of  $F_1$  axial plane is  $110^\circ/80^\circ$  N. The  $F_1$  folds are thus steeply inclined moderately plunging tight folds. The  $F_2$  folds are defined by well-developed puckers in muscovite schist (Fig 4.1.2a) and folding of  $S_1$  in phyllite (Fig 4.1.2h). The  $F_2$  fold measured from the pucker axis in muscovite schist plunges  $30^\circ \rightarrow 100^\circ$ . The attitude of  $F_2$  axial plane in muscovite schists is  $95^\circ/85^\circ$  N. The  $F_2$  folds are steeply inclined moderate plunging tight folds. Therefore, the axial planes of  $F_1$  and  $F_2$  folds are almost parallel. So it is not clearly understood that the shear fabric which is parallel to the regional foliation in some strain localized area is the product of the late stage  $D_1$  deformation or the primary  $S_2$  surface. A third generation of open folds ( $F_3$ ), is defined by broad warps of the schistosity with in the muscovite schists and phyllite. These  $F_3$  folds axial plane is tending towards NE-SW direction. Therefore, in the study area  $F_1$  and  $F_2$  are coaxial and  $F_3$  occurs as cross fold. Locally, Quartz veins occurred along the axial plane of the  $F_3$  fold along NE-SW direction. Extensional structures are defined by the discordant and concordant (with respect to  $S_1$ ) quartz veins within in the phyllite observed in the area. Discordant and concordant quartz veins show boudinage and pinch-and-swell structures respectively.

Quartz reef exposed as isolated hillocks with longer axes trending E-W direction. Quartz reef is intruded parallel to the foliation plane ( $S_1$ ) define by phyllite. Quartz reef is deformed and weakly foliated. In places the quartz reef is highly sheared. The foliation showing E-W trend with steeply dipping towards north which is parallel to the regional foliation ( $S_1$ ) define by adjacent phyllite. Therefore, field features support the view that the protolith of the quartz reef was emplaced during or prior to the regional  $S_1$  fabric ( $D_1$  deformation).

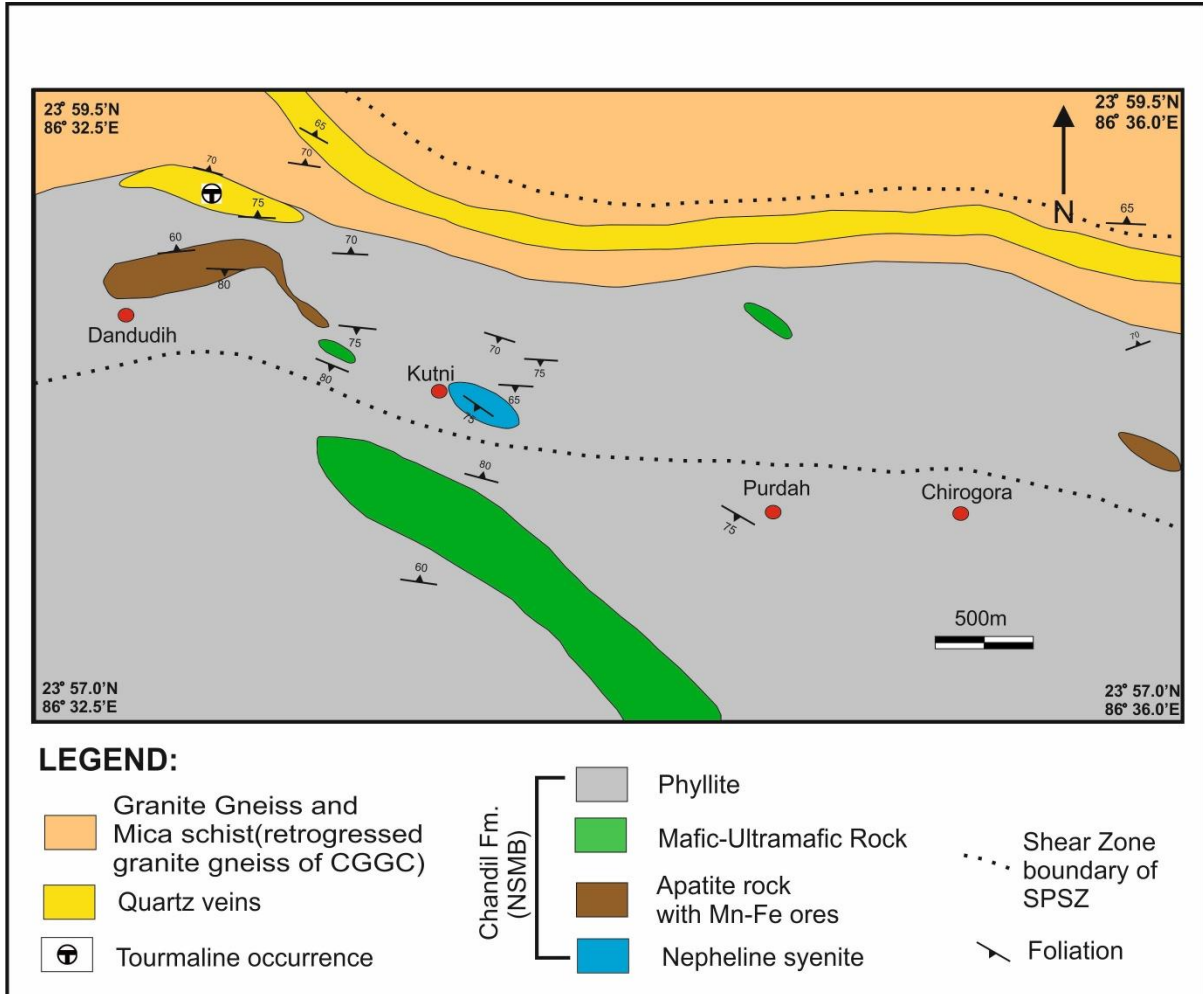


Fig 4.1.1: Lithological map of Kutni area, Purulia [ Modified after BRNS funded research project (Sanction no.2008/36/36-BRNS), entitled “Pressure-Temperature-fluid evolution in parts of SPSZ- Implication for boron metasomatism and U-Fe-Cu-P Mineralisation”, P.I Pulak Sengupta, 2014.]

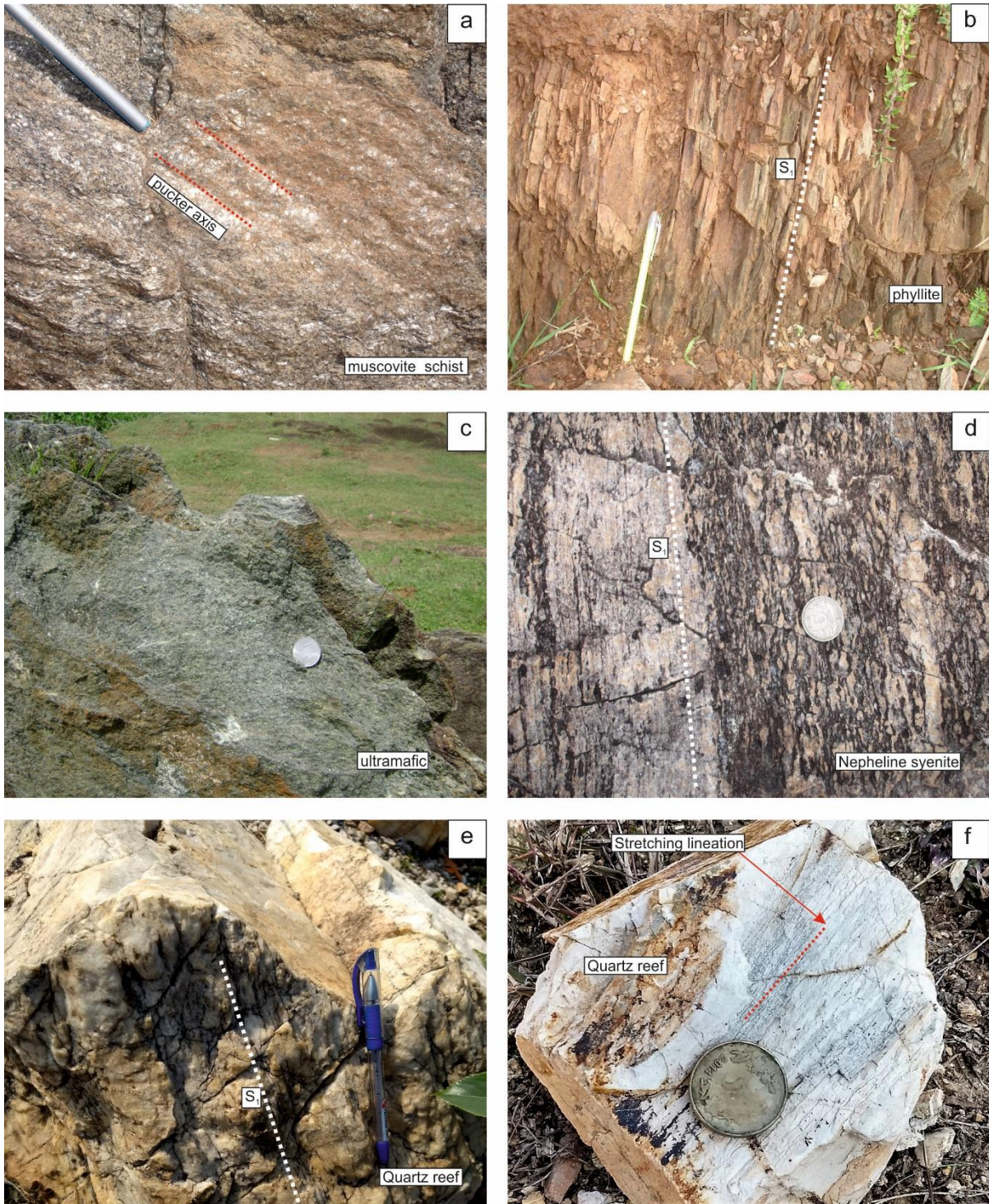


Fig 4.1.2a: Prominent schistosity plane( $S_1$ ) is develop in muscovite schist .The  $F_2$  folds are defined by well-developed puckers. Fig 4.1.2b: Phyllite is very fine grained, light to dark coloured and composed of phyllosilicates which define the prominent schistosity plane( $S_1$ ). Fig 4.1.2c:Ultramafic rocks are granular, coarse grained and more or less massive in outcrop scale. Fig 4.1.2d: Nepheline syenite is medium-coarse grained, leucocratic and composed of albite megacrysts with aegirine and nepheline grains. Fig 4.1.2e: Quartz reef is composed of fine to medium grained milky white colour quartz and weakly foliated. Fig 4.1.2f:Stretching lineation of quartz is present in sheared quartz reef.

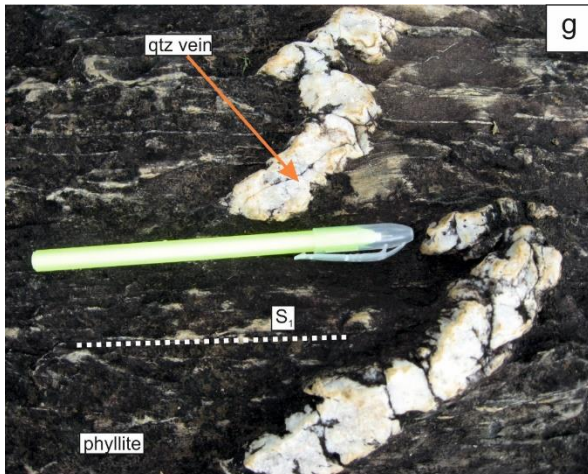


Fig 4.1.2g: First generation or  $F_1$  folds are defined by quartz veins whose axial planes are parallel to the schistosity ( $S_1$ ) of the rocks.  $F_1$  are mostly asymmetric with thickened hinges and longer limb sometimes become parallel to the foliation. Fig 4.1.2h:  $F_2$  fold is defined by the folding of  $S_1$  in phyllite.

## 4.2 Field features of tourmaline bearing rocks

Tourmaline bearing rocks are restricted in the quartz reef that is enclosed by the phyllite of the Chandil formation of NSMB. Based on the size and morphology of tourmaline and the relation of the tourmaline-bearing aggregates with the host rock, three distinct modes of occurrence are established.

In mode 1, millimetre thin laminae that are alternately rich in tourmaline and quartz occur as isolated pods within the quartz reef (Fig 4.2a, 4.2b and 4.2c). The thickness of alternate tourmaline and quartz rich laminae is varying from 1mm- 5mm (Fig 4.2a, 4.2b and 4.2c). The laminae are mainly discontinuous in nature and can be traceable up to to 1- 5cm laterally. At places these tourmaline rich laminae are laterally continuous. In tourmaline rich laminae, tourmalines are very fine grained (usually < 1 mm). The grains are so small that it is almost impossible to identify individual tourmaline grain in naked eye. These alternate tourmaline and quartz rich laminae are oriented parallel to the regional fabric ( $S_1$ ) (Fig 4.2a, 4.2b and 4.2c). Similar to the regional foliation ( $S_1$ ) this alternate tourmaline and quartz rich laminae are folded and showing  $F_2$  fold (Fig 4.2b). The host quartz reef sends veins within the thinly laminated tourmaline-quartz rock (Fig 4.2c). From the field feature supports the view that mode tourmalines are syn- tectonic regarding  $S_1/D_1$ .

In the second mode (mode 2), within the thinly banded quartz tourmaline rock, tourmaline aggregates occur as massive tourmaline rich bands alternate with quartz reef (Fig 4.2d). These tourmaline rich bands are 1-3 cm thick and made up of fine-grained tourmaline aggregates (usually < 1 mm) and less amount of quartz (<10 vol%). The quartz rich (>90 vol%) bands exhibit saccaroidal texture due to recrystallization. The tourmaline rich bands show trend  $100^\circ$ . The banded tourmaline-quartz rock is oriented parallel to the regional foliation ( $S_1$ ) (Fig 4.2d) which is defined by adjacent phyllite. Extensive layer parallel stretching causes detachment of thinly banded quartz-tourmaline rock is noted (Fig 4.2e). So, the tourmaline in banded quartz tourmaline rock is syn-tectonic with respect to regional  $S_1/D_1$ .

In third mode (mode 3), medium to coarse long prismatic grain of tourmaline occurs within quartz vein (Fig 4.2f). Tourmaline grains are randomly oriented with long acicular (2 to 3 cm along elongation) grains. (Fig 4.2f). These quartz veins cut across the  $S_1$  foliation of the host rock. These tourmaline grains remain unaffected by any regional deformation. So, they may have formed post  $F_3/D_3$ .

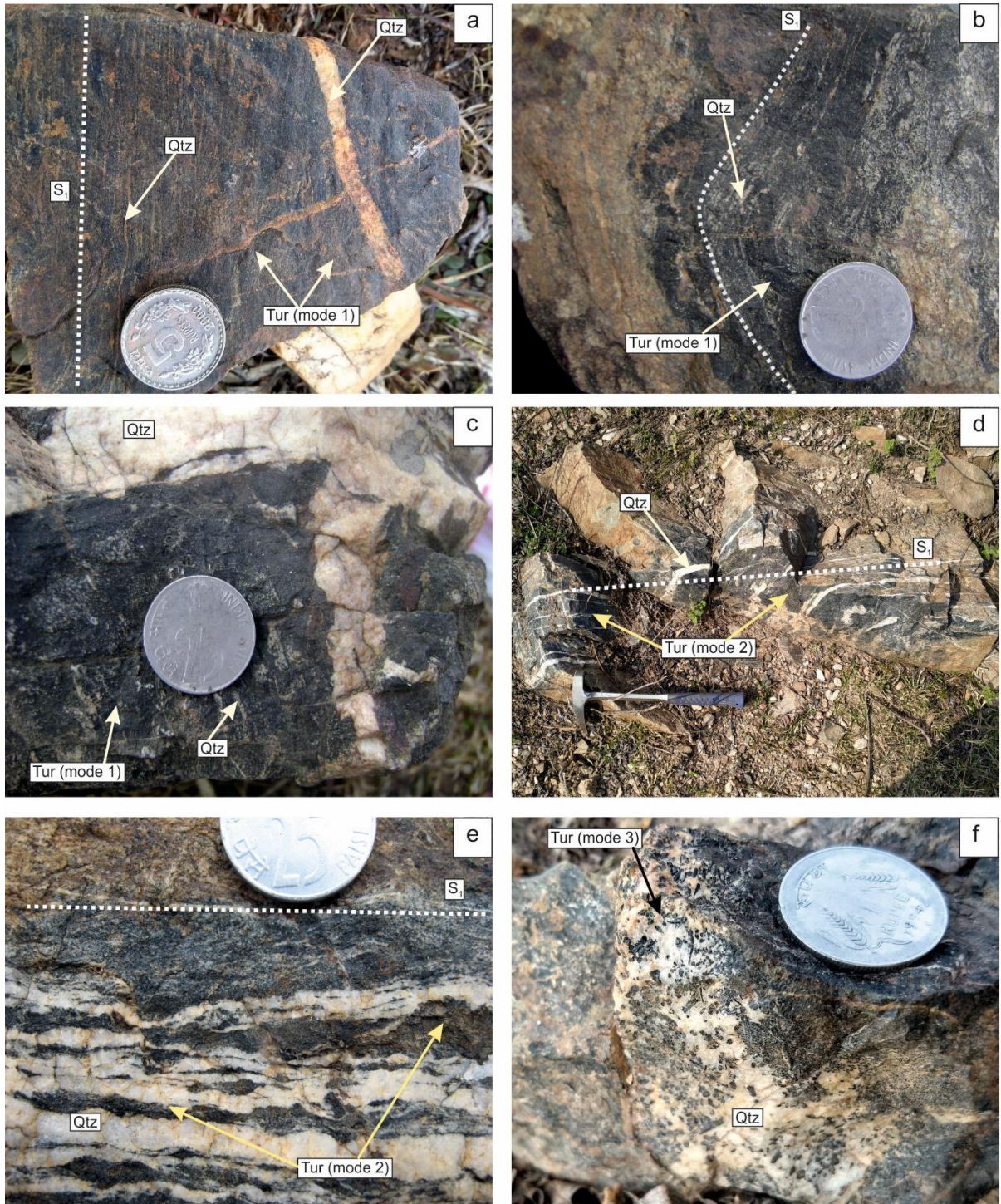


Fig 4.2a: In mode-1, millimetre thin laminae of alternately rich in tourmaline and quartz are occurred within laminated tourmaline-quartz rock. Fig 4.2b: Alternate tourmaline and quartz rich laminae are folded and showing  $F_2$  fold in mode 1 association. Fig 4.2c: The host quartz reef sends veins within the thinly laminated tourmaline-quartz rock. Fig 4.2d: In mode 2, the thinly banded tourmaline-quartz rock, locally quartz free, alternate with quartz reef. Banded tourmaline-quartz rock is oriented parallel to the  $S_1$ . Fig 4.2e: Extensive layer parallel stretching cause detachment of thinly banded quartz-tourmaline rock is noted. Fig 4.2f: In mode 3, medium to coarse long prismatic grain of tourmaline randomly oriented within quartz vein.

### 4.3 Petrographic description of tourmaline bearing rocks

The host sheared quartz reef consists of very fine grain (5-50  $\mu\text{m}$ ) quartz. The quartz grains are granular in shape and thoroughly recrystallized. The grains are mostly elliptical in shape. Quartz ribbons, although recrystallized are discernible at places (Fig 4.3a). The rocks show one set of prominent foliations which is defined by flattened quartz grains. The foliation plane is oriented parallel to the regional  $S_1$  fabric.

Tourmaline and quartz are the dominant minerals in the laminated/banded tourmaline quartz rock. Based on field and microscopic study there are three modes (mode 1, mode 2 and mode 3) of tourmaline occurrences. Considering all the modes there are two generations of tourmaline are being identified.

Laminated quartz tourmaline rock in mode I include alternating thin tourmaline-rich laminae (>80 modal vol% tourmaline) and quartz-rich laminae (>90 modal vol% quartz) (Fig 4.3b). Under microscope the laminated texture is prominent but the laminae are mostly discontinuous in nature. In places continuous tourmaline rich laminae (thickness of each laminae 0.2-0.5 mm) also found. Tourmaline rich laminae exhibits fine-grained (50-100 $\mu\text{m}$  along long axis) aggregates of needle, granule, prismatic shaped tourmaline. Tourmaline shows strong pleochroism in the shades of light green to dark greenish brown without prominent optical zoning (Fig 4.3d). Subhedral tourmaline grains long axis oriented parallel to the  $S_1$  fabric (Fig 4.3c). The major foliation is crenulated. Tourmaline grains are associated with elliptical quartz grains which are also aligned parallel to the  $S_1$  fabric (Fig 4.3c). Post crystalline deformational features such as sutured grain boundary, formation of sub-grains, undulose extinction common in quartz grains (Fig 4.3c). Within the quartz rich laminae tourmaline occurs as discrete or isolated prismatic fine grains with a preferred orientation along  $S_1$  (Fig 4.3d). In places, tourmaline grains are associated with ilmenite (Fig 4.3d). Cross fracture is very common in mode 1 tourmaline grains. S-C fabric is observed in laminated quartz tourmaline rock which indicates that the rock is sheared (Fig 4.3b). Therefore, tourmaline grains in mode 1 association are syn-tectonic to  $S_1$  and designated as Gen-I (first generation) tourmaline.

In mode 2, the banded tourmaline quartz rock shows alternate bands of tourmaline rich and quartz rich bands. Within the tourmaline rich (>90 modal vol% tourmaline) bands, tourmalines are fine to medium grained (50-200 $\mu\text{m}$  along long axis), prismatic and equant in shape. (Fig 4.3e). The quartz grains occur at the intergranular spaces between the tourmaline grain within the tourmaline rich band. The quartz grains are recrystallized. In tourmaline rich

bands, tourmaline grain occurs as clusters where long axis of the grains defines a linear fabric that is parallel to the  $S_1$  (Fig 4.3e). In places, tourmaline grains are associated with ilmenite (Fig 4.3e). Tourmaline grains show strong pleochroism in the shades of light green to dark greenish brown. At places, basal section of tourmaline grains shows poor optical zoning from light green core and greenish brown rim. Tourmaline grains within banded tourmaline rock are syn-tectonic to  $S_1$  because they are oriented parallel to  $S_1$ . Thus the tourmaline grains are designated as Gen-I (first generation) tourmaline.

In mode 3, tourmaline grains occur within the quartz vein. These tourmaline grains are coarse, prismatic (0.5-5 mm) and euhedral in shape (Fig 4.3f). Tourmaline grains are haphazardly oriented and also characterized by extremely variable grain sizes. Tourmaline grains are fractured. Tourmaline grains show strong pleochroism in the shades of light bluish green to dark greenish brown (in PPL). Basal sections of tourmaline grains show optical zoning with greenish blue core and dark green rim (Fig 4.3f). Therefore, these coarse haphazardly oriented tourmaline grains are supposed to be formed at post  $D_3/F_3$ . Thus, the tourmaline grains are designated as Gen-II (second generation).

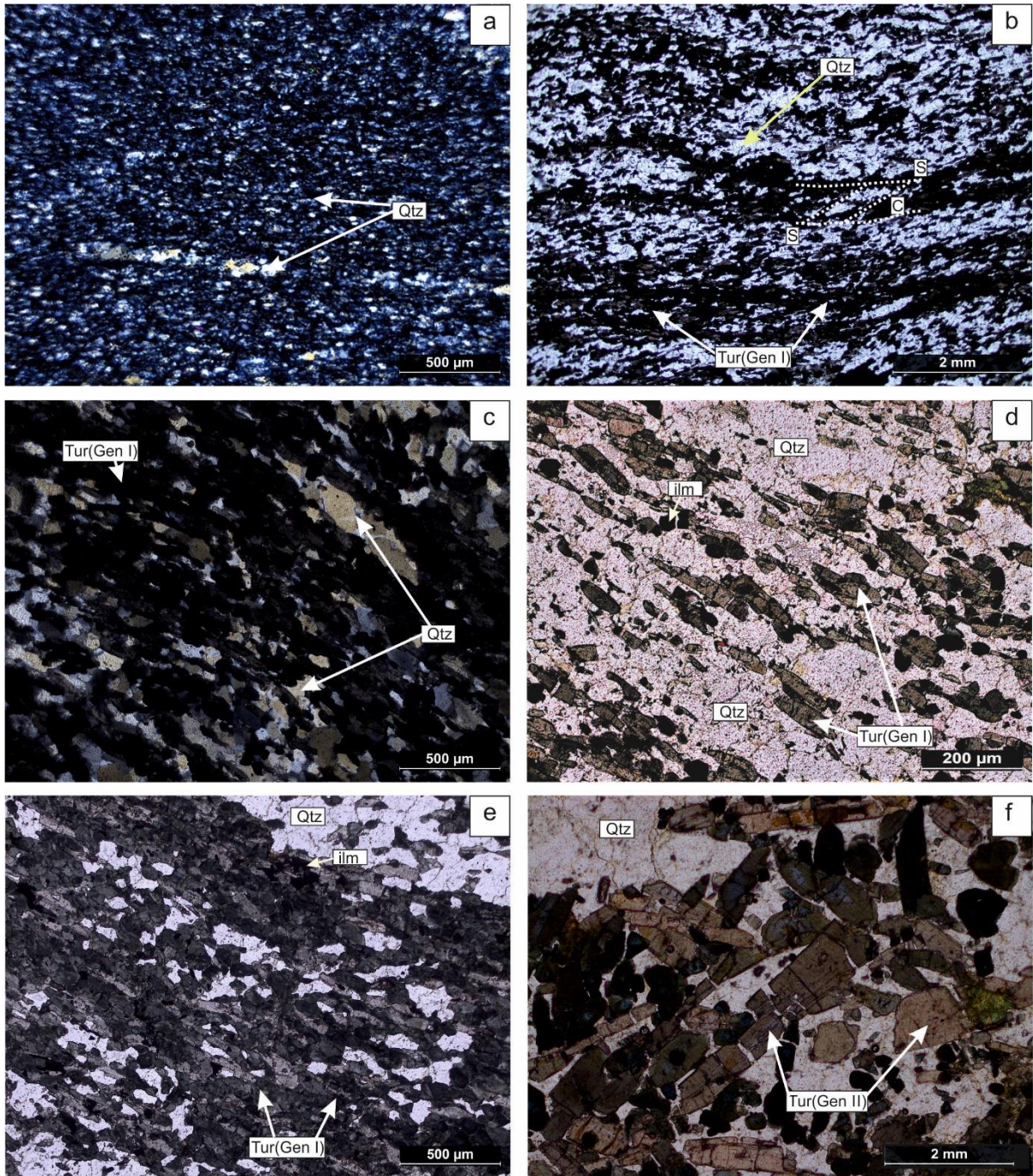


Fig 4.3a: The host sheared quartz reef consists of very fine, elliptical quartz grains which are thoroughly recrystallized and parallel to the  $S_1$  fabric. Fig 4.3b: Laminated quartz tourmaline rock in mode I include alternating thin Gen I tourmaline-rich laminae and quartz-rich laminae. S-C fabric is observed in laminated quartz tourmaline rock(mode1).Fig 4.3c: Gen I tourmaline rich laminae exhibits fine-grain aggregates of needle, granule, prismatic shaped tourmaline alternating with recrystallized quartz rich laminae in mode 1 association (under CPL). Fig 4.3d: Within the quartz rich laminae Gen I tourmaline occurs as discrete or isolated prismatic fine grains with a preferred orientation along  $S_1$  in mode 1 association. Fig 4.3e: Within the tourmaline rich bands, fine to medium grained, prismatic tourmaline grain oriented parallel to the  $S_1$  fabric in banded quartz tourmaline rock(mode 2). Fig 4.3f: The Gen II coarse, prismatic tourmaline grains are haphazardly oriented in mode 3 association.

## 4.4 Tourmaline mineral chemistry

The Standard analytical procedures of major elements analysis and normalization of tourmaline are given in the appendix I and II. Overall, T sites of tourmaline in the assemblage are nearly filled with Si ( $5.90 \pm 0.04$  apfu; Table 4.4.2a). The Z site of the tourmaline is completely filled up with Al. The Al in apfu of the tourmaline compositions exceeds 6 ( $6.35 \pm 0.11$  apfu) suggesting that some Al must be present in Y site. Within quartz reef there are two generation of tourmaline. First generation (Gen-I) Tourmaline is oriented parallel to  $S_1$  fabric and syn tectonic with respect to  $D_1$ . Whereas second generation tourmaline is coarse grained and haphazardly oriented. So, these tourmalines are formed after  $D_3/F_3$  and designated as second generation or Gen-II. The Al content is higher in Gen-I tourmaline ( $6.38 \pm 0.16$  apfu) than the Gen-II ( $6.31 \pm 0.03$  apfu) tourmaline. The Ti in tourmaline structure is higher in the Gen-I ( $0.07 \pm 0.02$  apfu) than the Gen-II ( $0.06 \pm 0.01$  apfu). X-site vacancy, estimated from the measured Na+ Ca + K contents is  $0.34 \pm 0.05$  apfu. The X-vacancy in tourmaline structure is higher in the Gen-I ( $0.35 \pm 0.05$  apfu) than the Gen-II ( $0.30 \pm 0.03$ apfu). There is significant content of Ca in tourmaline structure ( $0.28 \pm 0.05$  apfu). The Ca in tourmaline structure is higher in the Gen-I ( $0.29 \pm 0.05$  apfu) than the Gen-II ( $0.26 \pm 0.04$  apfu). In terms of the Ca-X vacancy-Na+K diagram (Fig 4.4.1a), all tourmaline grains in this assemblage straddle boundary between alkali and X-vacancy group and a few grains fall in the calcic group. Gen-I tourmaline core and rim composition overlap between alkali and X-vacancy group. One data each core and rim composition of Gen-I tourmaline fall in the calcic group. Gen-II tourmaline compositions are restricted within the alkali group. The rim of the Gen-II tourmalines is less X-vacancy than the core. Thus, the Gen-II tourmaline is more alkali and less calcic rich than the Gen-I tourmaline. In the  $X/(X + Na)$  vs.  $X_{Mg}$  ( $X_{Mg} = Mg/Fe^{2+} + Mg$ ) diagram (Fig 4.4.1b), tourmaline compositions both Gen-I and Gen-II are plotted near the junction point of all four classes of tourmaline i.e schorl, dravite, foitite and magnesio-foitite. The Gen-I tourmaline compositions straddle the boundary between dravite, foitite and magnesio-foitite. Whereas Gen-II tourmaline compositions are restricted only in dravite compositional field. There is compositional overlap between core and rim compositions in both Gen-I and Gen-II. The Gen-I tourmaline compositions are less magnesian and have more X- site vacancies relative to the Gen-II tourmaline compositions. The  $X_{Mg}$  in tourmaline structure is lower in the Gen-I ( $0.53 \pm 0.07$  apfu) than the Gen-II ( $0.66 \pm 0.03$  apfu). Representative microprobe analyses of tourmaline are given in Table 4.4.2a.

Tourmaline grains compositions show significant chemical substitution and are expressed by different exchange vectors. Within these assemblages the two generation of tourmaline (Gen-I and Gen-II) compositions shows strong substitution trend parallel to vector  $\text{MgFe}_{-1}$  ( $r^2=0.95$ ), but tourmaline compositions are below the line  $\text{Fe} + \text{Mg} = 3$  which indicates that the substitution of Al in the Y-site (Fig 4.4.1c). In  $\text{Al}_{\text{total}}$  vs X- vacancy diagram (Fig 4.4.1d), the spread of tourmaline compositions show that the chemical substitution occurred due to exchange vectors  $\text{AlO}[\text{R}(\text{OH})]_{-1}$  ( $r^2= 0.40$ ) where  $\text{R} = \text{Fe}^{2+} + \text{Mg}$ . In the  $[\text{R}_1 (= \text{Na} + \text{Ca}) + \text{R}_2 (= \text{Fe} + \text{Mg} + \text{Mn})]$  vs.  $[\text{R}_3 (= \text{Al} + 1.33 \times \text{Ti})]$  plot (Fig 4.4.1e), tourmaline compositions of all the generations fall within the upper half of the parallelogram formed by the lines joining the positions of the tourmaline species. Tourmaline compositions shows more affinity towards the exchange vector  $\text{AlO}[\text{R}(\text{OH})]_{-1}$ . In the  $\text{Al}_{\text{total}}$  vs.  $\text{Fe} + \text{Mg}$  (Fig 4.4.1f) diagram tourmaline compositions show that the chemical substitution was dominated and expressed by substitution occurs along the  $\text{AlO}[\text{R}(\text{OH})]_{-1}$  and  $\square\text{Al}(\text{NaR})_{-1}$  exchange vector ( $r^2=0.83$ ).

Ilmenite shows nearly end member composition and presented in Table 4.4.2b.

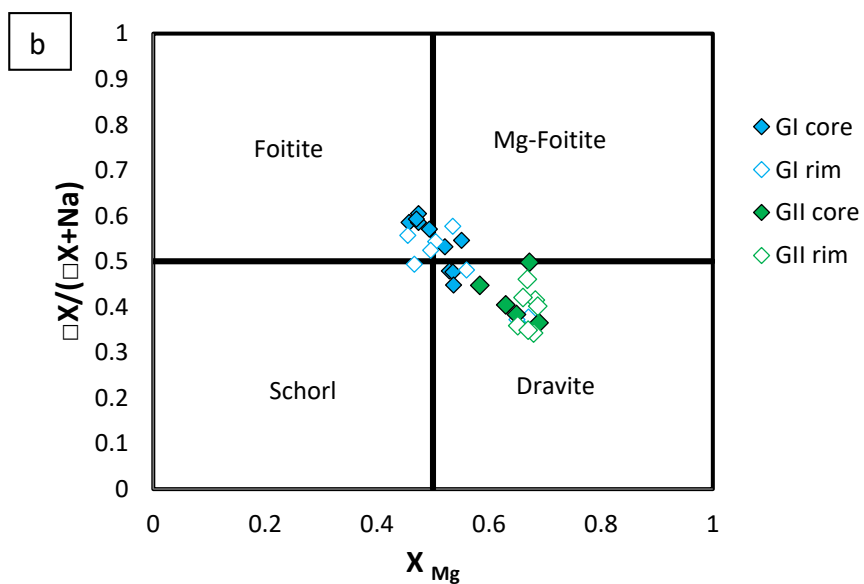
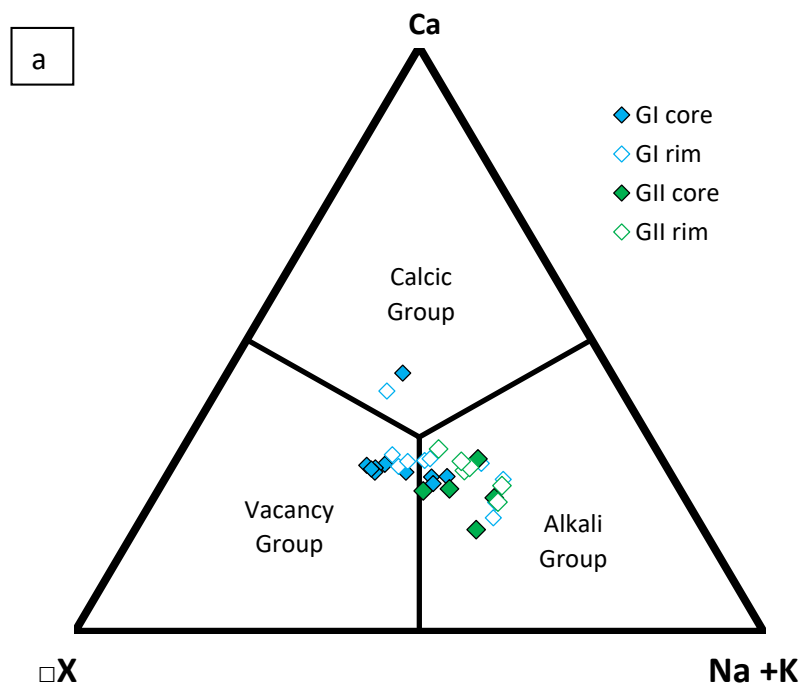


Fig 4.4.1a: Principal tourmaline groups based on the classification scheme of Hawthorne and Henry (1999). Fig 4.4.1b Nomenclature diagram of tourmaline based on X-site vacancy/(X-site vacancy + Na) vs. Mg/(Mg + Fe<sup>2+</sup>) plot after Henry et al. (2003).

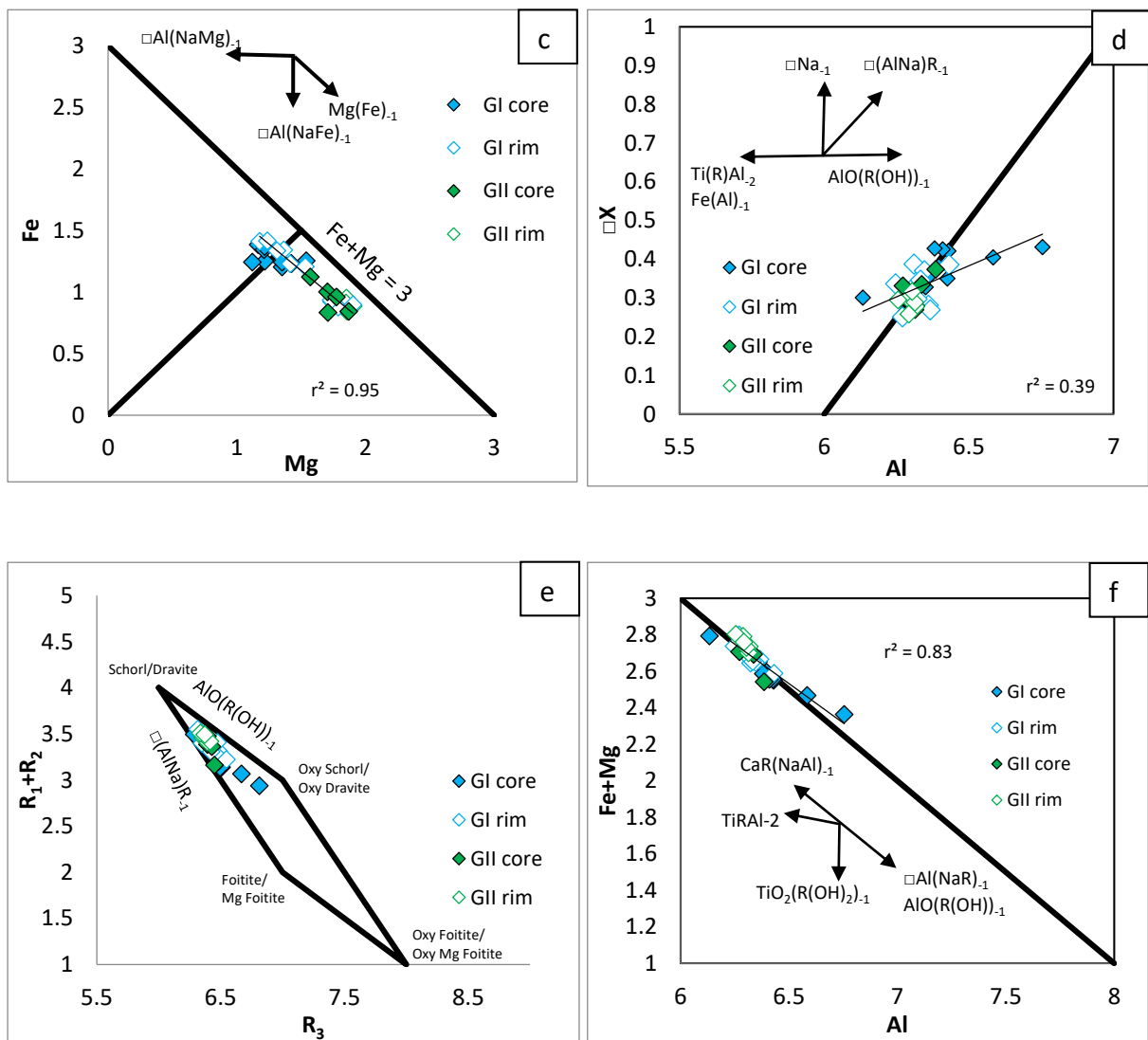


Fig 4.4.1c: In Fe vs Mg diagram a prominent Fe-Mg substitution occurs, showing strong substitution trend parallel to vector  $MgFe_{-1}$ . Fig 4.4.1d In  $Al_{total}$ -vs- X-site vacancy diagram, compositions of tourmaline show more affinity to the exchange vector of  $AlO[R(OH)]_{-1}$ . Fig 4.4.1e: In the  $[R_1 (=Na + Ca) + R_2 (=Fe + Mg + Mn)]$  vs.  $[R_3 (=Al + 1.33 \times Ti)]$  plot, tourmaline compositions fall within the upper half of the parallelogram formed by the lines joining the positions of the tourmaline species. Compositions show more affinity to the exchange vector  $AlO[R(OH)]_{-1}$ . Fig 4.4.1f: In Al vs Fe+Mg diagram, compositions of tourmaline show more affinity to the exchange vector  $Al(NaR)_{-1}$  and  $AlO[R(OH)]_{-1}$ .

Table 4.4.2a: Representative EPMA analysis of tourmaline

Generation	Gen I															
Sample no.	BR 29/A II															
Point	2 / 1	17 / 1	19 / 1	21 / 1	26 / 1	26 / 2	26 / 3	26 / 4	26 / 5	26 / 6	3 / 1	18 / 1	20 / 1	22 / 1	26 / 7	26 / 8
Core/Rim	core	rim	rim	rim	rim	rim	rim									
Al <sub>2</sub> O <sub>3</sub>	30.83	33.58	34.45	32.07	32.80	32.35	32.44	32.39	33.05	32.71	30.39	32.45	32.91	32.83	32.13	32.46
FeO	8.89	8.99	8.94	9.74	8.66	8.86	8.86	8.85	9.77	9.90	8.33	6.64	6.40	6.84	9.63	9.63
TiO <sub>2</sub>	0.90	0.50	0.35	0.46	0.43	0.50	0.72	0.53	0.52	0.45	0.91	0.50	0.66	0.35	0.59	0.67
SiO <sub>2</sub>	35.24	35.28	35.00	35.01	35.83	35.43	35.42	35.62	36.26	36.05	33.44	35.52	35.81	36.46	35.38	35.66
K <sub>2</sub> O	0.03	0.02	0.01	0.00	0.02	0.04	0.02	0.01	0.00	0.00	0.01	0.00	0.00	0.03	0.02	0.01
CaO	2.47	1.62	1.61	1.55	1.50	1.53	1.43	1.50	1.56	1.58	2.20	1.25	1.65	1.12	1.59	1.65
Na <sub>2</sub> O	0.77	0.95	0.88	0.91	1.19	1.04	1.21	1.26	0.95	0.92	0.73	1.55	1.40	1.59	1.01	1.05
Cr <sub>2</sub> O <sub>3</sub>	0.02	0.08	0.07	0.00	0.05	0.02	0.01	0.00	0.00	0.00	0.01	0.00	0.00	0.00	0.00	0.00
MnO	0.06	0.05	0.05	0.05	0.03	0.00	0.05	0.02	0.04	0.07	0.05	0.08	0.07	0.09	0.10	0.05
MgO	6.12	4.91	4.52	4.60	5.46	5.41	5.73	5.75	4.94	4.93	5.38	7.01	7.31	7.12	5.50	5.31
B <sub>2</sub> O <sub>3</sub> *	10.38	10.52	10.52	10.28	10.53	10.42	10.49	10.50	10.63	10.56	9.93	10.50	10.65	10.68	10.46	10.53
Total	95.71	96.50	96.40	94.67	96.50	95.60	96.38	96.43	97.72	97.17	91.38	95.50	96.86	97.11	96.41	97.02
Si(T)	5.95	5.87	5.82	5.95	5.95	5.94	5.89	5.92	5.97	5.97	5.90	5.91	5.88	5.96	5.89	5.91
Al(T)	0.05	0.13	0.18	0.05	0.05	0.06	0.11	0.08	0.03	0.03	0.10	0.09	0.12	0.04	0.11	0.09
B(T)	3.00	3.00	3.00	3.00	3.00	3.00	3.00	3.00	3.00	3.00	3.00	3.00	3.00	3.00	3.00	3.00
Al(Z)	6.00	6.00	6.00	6.00	6.00	6.00	6.00	6.00	6.00	6.00	6.00	6.00	6.00	6.00	6.00	6.00
Al(Y)	0.08	0.45	0.58	0.38	0.38	0.34	0.25	0.27	0.37	0.35	0.23	0.27	0.24	0.28	0.20	0.26
Ti(Y)	0.11	0.06	0.04	0.06	0.05	0.06	0.09	0.07	0.06	0.06	0.12	0.06	0.08	0.04	0.07	0.08
Cr(Y)	0.00	0.01	0.01	0.00	0.01	0.00	0.00	0.00	0.00	0.00	0.00	0.00	0.00	0.00	0.00	0.00
Fe(Y)	1.25	1.25	1.24	1.39	1.20	1.24	1.23	1.23	1.34	1.37	1.23	0.92	0.88	0.93	1.34	1.34
Mn(Y)	0.01	0.01	0.01	0.01	0.00	0.00	0.01	0.00	0.01	0.01	0.01	0.01	0.01	0.01	0.01	0.01
Mg(Y)	1.54	1.22	1.12	1.17	1.35	1.35	1.42	1.43	1.21	1.22	1.42	1.74	1.79	1.73	1.37	1.31
K(X)	0.01	0.00	0.00	0.00	0.00	0.01	0.00	0.00	0.00	0.00	0.00	0.00	0.00	0.01	0.00	0.00
Ca(X)	0.44	0.29	0.28	0.28	0.27	0.27	0.25	0.27	0.27	0.28	0.41	0.22	0.29	0.20	0.28	0.29
Na(X)	0.25	0.30	0.28	0.30	0.38	0.34	0.39	0.40	0.30	0.29	0.25	0.50	0.44	0.50	0.33	0.34
X vacancies	0.30	0.40	0.43	0.42	0.35	0.38	0.35	0.33	0.43	0.43	0.34	0.28	0.27	0.30	0.39	0.37
X <sub>Mg</sub>	0.55	0.49	0.47	0.46	0.53	0.52	0.54	0.54	0.47	0.47	0.54	0.65	0.67	0.65	0.50	0.50

Note: Atomic proportions based on  $\Sigma T+Z+Y$  cations = 15.  $X_{Mg} = Mg/(Fe^{2+} + Mg)$ .

\* B<sub>2</sub>O<sub>3</sub> calculated assuming B to be 3 atoms per formula unit.

Table 4.4.2a: Representative EPMA analysis of tourmaline (continued).

Generati on	Gen I	Gen I	Gen I	Gen I	Gen II										
Sample no.	BR 29/A II	BR 29/A II	BR 29/A II	BR 29/A II	BR29/A VI	BR29/A VI	BR29/A VI	BR29/A VI	BR29 /AVI	BR 29/A I	BR29/ AVI	BR29/A VI	BR29/ AVI	BR29/A VI	BR29/A VI
Point	26 / 9	26 / 10	26 / 11	26 / 12	29 / 1	31 / 1	33 / 1	35 / 1	37 / 1	26 / 13	28 / 1	32 / 1	34 / 1	36 / 1	38 / 1
Core/Rim	rim	rim	rim	rim	core	core	core	core	core	rim	rim	rim	rim	rim	rim
Al <sub>2</sub> O <sub>3</sub>	32.60	32.41	32.42	32.25	32.51	32.64	32.38	31.67	32.98	32.77	33.09	32.43	32.62	32.07	32.57
FeO	10.09	10.21	8.82	6.50	7.32	6.14	8.08	6.79	6.07	6.98	6.57	6.12	6.60	6.87	6.65
TiO <sub>2</sub>	0.69	0.54	0.62	0.27	0.74	0.51	0.55	0.47	0.39	0.24	0.49	0.48	0.67	0.49	0.48
SiO <sub>2</sub>	35.05	35.72	36.27	35.71	36.12	35.93	35.47	34.73	36.16	36.16	36.32	35.88	35.78	35.39	35.93
K <sub>2</sub> O	0.02	0.03	0.02	0.03	0.03	0.03	0.03	0.00	0.04	0.02	0.02	0.00	0.00	0.03	0.05
CaO	1.70	1.66	1.70	1.48	1.00	1.31	1.38	1.64	1.38	1.27	1.60	1.60	1.79	1.65	1.43
Na <sub>2</sub> O	0.95	1.11	1.15	1.51	1.54	1.53	1.29	1.33	1.19	1.57	1.35	1.35	1.17	1.27	1.52
Cr <sub>2</sub> O <sub>3</sub>	0.03	0.17	0.08	0.00	0.03	0.07	0.02	0.07	0.66	0.00	0.00	0.00	0.10	0.14	0.00
MnO	0.16	0.03	0.00	0.05	0.11	0.00	0.07	0.06	0.00	0.03	0.04	0.00	0.03	0.05	0.00
MgO	4.72	5.01	6.29	7.74	6.99	7.64	6.35	7.04	6.98	7.31	7.93	7.54	7.47	7.51	7.57
B <sub>2</sub> O <sub>3</sub> *	10.43	10.54	10.68	10.56	10.64	10.62	10.50	10.32	10.64	10.65	10.80	10.58	10.64	10.52	10.64
Total	96.44	97.43	98.05	96.10	97.03	96.42	96.12	94.12	96.49	97.00	98.21	95.98	96.87	95.99	96.84
Si(T)	5.87	5.92	5.93	5.89	5.91	5.90	5.89	5.87	5.94	5.91	5.86	5.93	5.87	5.86	5.89
Al(T)	0.13	0.08	0.07	0.11	0.09	0.10	0.11	0.13	0.06	0.09	0.14	0.07	0.13	0.14	0.11
B(T)	3.00	3.00	3.00	3.00	3.00	3.00	3.00	3.00	3.00	3.00	3.00	3.00	3.00	3.00	3.00
Al(Z)	6.00	6.00	6.00	6.00	6.00	6.00	6.00	6.00	6.00	6.00	6.00	6.00	6.00	6.00	6.00
Al(Y)	0.30	0.25	0.18	0.16	0.18	0.22	0.23	0.19	0.32	0.23	0.14	0.24	0.17	0.11	0.18
Ti(Y)	0.09	0.07	0.08	0.03	0.09	0.06	0.07	0.06	0.05	0.03	0.06	0.06	0.08	0.06	0.06
Cr(Y)	0.00	0.02	0.01	0.00	0.00	0.01	0.00	0.01	0.09	0.00	0.00	0.00	0.01	0.02	0.00
Fe(Y)	1.41	1.42	1.21	0.90	1.00	0.84	1.12	0.96	0.83	0.95	0.89	0.85	0.90	0.95	0.91
Mn(Y)	0.02	0.00	0.00	0.01	0.02	0.00	0.01	0.01	0.00	0.00	0.01	0.00	0.00	0.01	0.00
Mg(Y)	1.18	1.24	1.53	1.90	1.70	1.87	1.57	1.77	1.71	1.78	1.91	1.86	1.83	1.85	1.85
K(X)	0.00	0.01	0.00	0.01	0.01	0.01	0.01	0.00	0.01	0.00	0.00	0.00	0.00	0.01	0.01
Ca(X)	0.30	0.29	0.30	0.26	0.17	0.23	0.24	0.30	0.24	0.22	0.28	0.28	0.31	0.29	0.25
Na(X)	0.31	0.35	0.36	0.48	0.49	0.49	0.41	0.43	0.38	0.50	0.42	0.43	0.37	0.41	0.48
X vacancies	0.39	0.35	0.34	0.25	0.33	0.28	0.34	0.27	0.37	0.28	0.30	0.29	0.32	0.30	0.26
X <sub>Mg</sub>	0.45	0.47	0.56	0.68	0.63	0.69	0.58	0.65	0.67	0.65	0.68	0.69	0.67	0.66	0.67

Note: Atomic proportions based on  $\Sigma T+Z+Y$  cations = 15.  $X_{Mg} = Mg/(Fe^{2+} + Mg)$ .

\* B<sub>2</sub>O<sub>3</sub> calculated assuming B to be 3 atoms per formula unit.

Table 4.4.2b: Representative EPMA analysis of ilmenite.

Sample no	BR 29A
DataSet/ Point	68
Mineral	ilmeni te
SiO <sub>2</sub>	0.01
TiO <sub>2</sub>	52.13
Al <sub>2</sub> O <sub>3</sub>	0.00
Cr <sub>2</sub> O <sub>3</sub>	0.03
FeO	45.82
MnO	1.87
MgO	0.06
CaO	0.00
Na <sub>2</sub> O	0.00
K <sub>2</sub> O	0.00
P <sub>2</sub> O <sub>5</sub>	0.00
Total	99.97
Normaliza tion basis	3(O)
Si	0.00
Ti	0.99
Al	0.00
Cr	0.00
Fe	0.97
Mn	0.04
Mg	0.00
Ca	0.00
Na	0.00
K	0.00
P	0.00

## 4.5 Trace and REE concentrations of tourmaline

In chondrite normalized REE (McDonough and Sun, 1995) diagram, Gen-I tourmalines show LREE enrichment with sharp negative sloped pattern (Fig 4.5.1a). Concentration and enrichment patterns of LREE in core and rim are nearly equivalent except rims are slightly enriched. Both core and rim show prominent and near equal positive Eu anomalies ( $\text{Eu}/\text{Eu}^* = 2.67-10.89$ ) with  $(\text{La}/\text{Lu})_{\text{CN}} = 1.82-72.32$  ( $\text{La}/\text{Lu} > 1$ ). However, core and rim can be distinguished by their different HREE concentrations and patterns (Fig 4.5.1a). HREE in the core is depleted with respect to chondrite (between  $\sim 1-0.1$  X chondrite) while their pattern is slightly irregular and concave upward. The rims show progressive HREE enrichment with sharp positive slope and overall enrichment with respect to chondrite ( $\sim 1-10$  X chondrite). Both LREE and HREE enrichment show an overall concave up pattern in the rims (Fig 4.5.1a). The  $\text{REE}_{\text{total}}$  content at the core varies from 7.11 ppm to 8.51 ppm (average  $7.99 \pm 0.57$  ppm) and corresponding rim  $\text{REE}_{\text{total}}$  varies from 10.11 ppm to 22.03 ppm (average  $14.23 \pm 4.74$  ppm). So, the rim is higher  $\text{REE}_{\text{total}}$  than the core. In chondrite normalized REE (McDonough and Sun, 1995) pattern, Gen-II tourmalines show LREE enrichment with sharp negative sloped pattern both for the core and the rim (Fig 4.5.1b). It shows a strong positive Eu anomaly ( $\text{Eu}/\text{Eu}^* = 31.64-49.24$ ) with  $(\text{La}/\text{Lu})_{\text{CN}} = 4.06-16.22$  ( $\text{La}/\text{Lu} > 1$ ). HREE in the core is depleted with respect to chondrite (between  $\sim 1-0.01$  X chondrite) while their pattern is slightly irregular and concave upward (Fig 4.5.1b). The rim shows progressive HREE enrichment than the core. The core shows overall depleted but slightly positive sloped HREE pattern with slight depletion in Er. The  $\text{REE}_{\text{total}}$  content varies from 1.98 ppm to 2.95 ppm. The  $\text{REE}_{\text{total}}$  content is very low compared to Gen-I tourmaline.

In UCC normalized multielement plot (Rudnick and Gao, 2003) of Gen-I tourmaline, significant depletion in LIL elements such as Rb, Ba and minor depletion in Sr are observed (Fig 4.5.1c). Concentrations of Ni, Co and Pb are near crustal values. The core shows depleted but overall flat pattern in HREE and Y. The rim has slightly depleted to near crustal concentration ( $\sim 0.1-1$  X UCC). In the rim the HREE-Y concentration shows flat to slightly negative sloped which indicates progressive HREE enrichment. Both core and rim show dominant positive Eu anomaly and slightly positively sloped LREE pattern (Fig 4.5.1c). The LREE pattern and concentrations of core and rim are nearly similar. Among the HFSE, prominent positive anomaly of Ti is noted. The cores and rim show overall depleted but variable concentrations of Zr, Hf.

In UCC normalized multielement plot (Rudnick and Gao, 2003) of Gen-II tourmaline, significant depletion in LIL elements such as Rb, Ba is noted (Fig 4.5.1d). Concentrations of Ni, Co and Pb are near crustal values. The core and rim show depleted but overall negative slope in HREE and Y. Rim is HREE+Y enriched than the core. Both core and rim show dominant positive Eu anomaly and slightly positively sloped LREE patterns (Fig 4.5.1d). Within HFS elements, notable depletion such as Hf, Zr and Th is observed.

Representative LA-ICP-MS trace-element analyses (in ppm) of tourmalines are given in Table 4.5.2a.

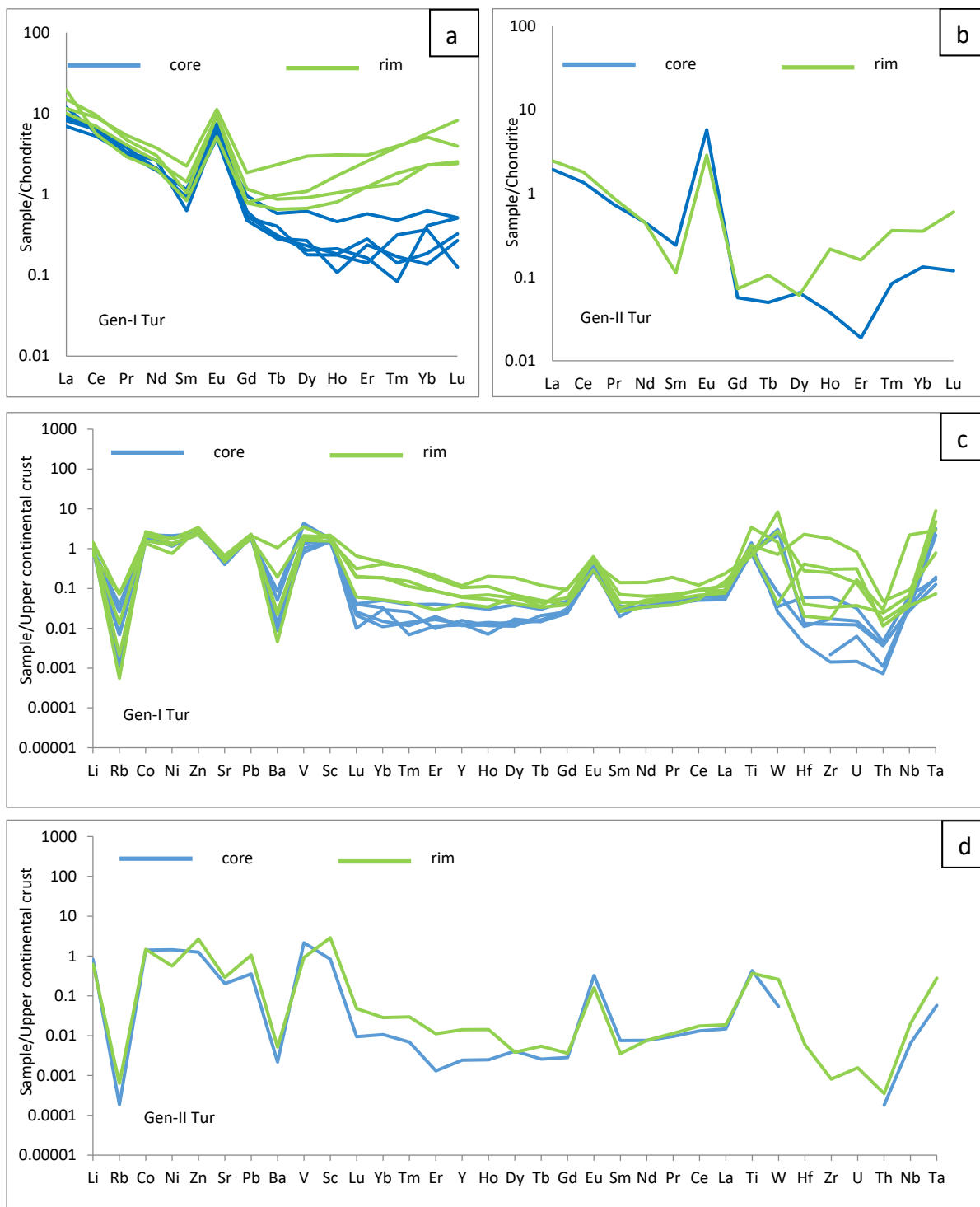


Fig 4.5.1a: Chondrite normalized (McDonough and Sun, 1995) trace elements diagram of Gen-I tourmaline (Blue –core: Green-rim) in quartz reef. Fig 4.5.1b: Chondrite normalized (McDonough and Sun, 1995) trace elements diagram of Gen-II tourmaline (Blue –core: Green-rim) in quartz reef. Fig 4.5.1c: Upper continental crust (UCC) normalized (Rudnick and Gao, 2003) multielement diagram for Gen-I tourmaline (Blue –core: Green-rim) in quartz reef. Fig 4.5.1d: Upper continental crust (UCC) normalized (Rudnick and Gao, 2003) multielement diagram for Gen-II tourmaline (Blue –core: Green-rim) in quartz reef.[The gaps in the spidergrams represent element concentrations that are below detection limit.]

Table 4.5.2a : Representative LA-ICPMS trace element analysis (in ppm) of tourmaline.

Sample no.	BK 29A I	BK 29A I	BK 29A I	BK 29A A	BK 29A A	BK 29A I	BK 29A I	BK 29A I	BK 29A A	BK 29A A	BK 29A IV	BK 29A IV
Mineral	Tourmaline											
Point	65	63	67	30	33	69	64	70	32	34	19	62
Generation	Gen I	Gen II	Gen II									
Core/Rim	core	core	core	core	core	rim	rim	rim	rim	rim	core	rim
La	2.16	2.82	1.93	2.06	1.64	4.62	7.28	3.56	2.73	2.37	0.46	0.58
Ce	4.01	3.49	3.89	4.22	3.19	3.40	7.59	5.84	5.48	4.24	0.83	1.10
Pr	0.35	0.29	0.29	0.31	0.30	0.27	1.35	0.44	0.50	0.38	0.07	0.08
Nd	0.94	0.90	0.96	1.20	0.95	0.94	3.81	1.38	1.71	1.18	0.21	0.21
Sm	0.13	0.17	0.13	0.09	0.13	0.12	0.66	0.15	0.33	0.21	0.04	0.02
Eu	0.42	0.40	0.28	0.35	0.30	0.29	0.45	0.53	0.63	0.53	0.32	0.16
Gd	0.10	0.12	0.10	0.11	0.19	0.16	0.40	0.16	0.37	0.23	0.01	0.01
Tb	0.01	0.01	0.01	0.01	0.02	0.02	0.02	0.04	0.08	0.03	0.00	0.00
Dy	0.04	0.07	0.06	0.05	0.15	0.17	0.24	0.27	0.73	0.22	0.02	0.01
Ho	0.01	0.01	0.01	0.01	0.03	0.04	0.03	0.09	0.17	0.06	0.00	0.01
Er	0.02	0.04	0.05	0.03	0.09	0.20	0.07	0.41	0.49	0.20	0.00	0.03
Tm	0.01	0.00	0.00	0.00	0.01	0.05	0.01	0.10	0.10	0.03	0.00	0.01
Yb	0.06	0.02	0.03	0.07	0.10	0.37	0.10	0.91	0.82	0.37	0.02	0.06
Lu	0.00	0.01	0.01	0.01	0.01	0.06	0.02	0.20	0.10	0.06	0.00	0.01
Total REE	8.28	8.35	7.74	8.52	7.11	10.71	22.03	14.07	14.23	10.12	1.98	2.30
Eu anomaly	10.90	8.43	7.60	10.58	5.70	6.36	2.67	10.36	5.49	7.28	49.24	31.65
Li	23.16	19.86	21.18	22.99	17.76	22.55	16.94	29.65	34.78	28.06	19.69	14.90
Sc	25.59	24.51	22.03	22.01	20.84	27.22	25.35	30.63	21.74	28.55	11.74	40.12
Ti	3025.42	3311.78	2918.28	5395.46	3153.15	2614.05	2529.61	4615.25	13084.90	3807.95	1645.84	1405.40
V	386.63	418.84	132.29	98.95	78.66	204.62	341.94	184.42	157.33	157.86	208.96	88.91
Co	33.34	35.55	35.13	27.91	38.64	36.13	38.09	27.68	23.26	45.88	24.29	25.39
Ni	57.24	54.14	98.31	57.78	99.20	84.45	63.65	57.35	35.22	82.15	67.23	26.38
Zn	158.85	158.74	150.83	185.12	160.84	162.63	150.89	180.78	214.10	227.73	84.08	178.79
Rb	3.10	0.58	0.57	0.09	2.15	1.08	6.01	0.18	5.82	0.05	0.02	0.05
Sr	196.88	188.17	156.13	127.49	166.92	166.95	180.51	174.20	149.16	214.59	64.50	92.46
Y	0.33	0.27	0.25	0.26	0.75	1.26	0.87	2.20	2.45	1.31	0.05	0.30
Zr	2.42	0.42	11.66	0.27	3.33	48.10	6.50	342.64	3.37	58.49	0.06	0.16
Nb	0.38	0.50	0.77	0.44	0.34	0.53	0.80	1.11	26.32	0.44	0.08	0.24
Mo	0.14	0.19	0.11	0.03	0.05	0.09	0.29	0.12	0.20	0.06	0.04	0.07
Ag	0.55	0.22	0.02	0.08	0.06	0.36	0.63	0.19	0.13	0.09	0.02	0.03
Ba	31.82	54.06	8.25	5.45	14.50	122.36	659.04	16.00	13.86	2.88	1.37	3.25
Hf	0.07	bdl	0.32	0.02	0.06	1.48	0.21	12.06	0.11	2.17	bdl	0.03
Ta	1.97	2.88	0.15	0.17	0.11	4.30	7.98	0.70	2.61	0.07	0.05	0.25
W	5.78	4.04	0.07	0.05	0.15	5.22	15.85	1.36	2.74	0.08	0.10	0.49
Pb	38.41	30.63	34.98	34.68	30.75	30.49	36.09	37.09	36.16	39.17	6.05	17.91
Th	0.04	0.01	0.05	0.01	0.04	0.17	0.25	0.50	0.31	0.12	0.00	0.00
U	0.03	0.02	0.09	0.00	0.04	0.37	0.10	2.23	0.45	0.84	bdl	0.00

bdl - below detection limit

## 4.6 Summary

The tourmaline mineralization is found north west of the Kutni village within the quartz reef. There are two generations of tourmaline that occurred within the quartz reef hosted by phyllite which is the part of Chandil formation (NSMB). Banded quartz tourmaline rock shows thick to thin laminae of alternatively rich in tourmaline and quartz. This rock is deformed and folded along with the regional foliation( $S_1$ ). Tourmalines are fine to medium grained and oriented parallel to the  $S_1$  fabric. So these tourmalines are syn-tectonic to the regional deformation ( $S_1/D_1$ ) and denoted as first generation (Gen-I) of tourmaline. There are another generation of tourmaline occurs within the quartz vein which cut across the  $S_1$  plane. These medium to coarse long prismatic tourmalines are randomly oriented. These tourmaline grains are denoted as second generation (Gen-II) and are supposed to be formed at post  $D_3/F_3$ . Tourmaline grain of second generation shows distinct optical zoning from greenish blue core to dark green rim. The Gen-I of tourmaline X-vacancy is rich and alkali poor than the Gen-II tourmaline. The Gen-I tourmaline is dravite, foitite and magnesio-foitite in composition. Whereas Gen-II of tourmaline is dravite in composition. In chondrite normalized REE diagram, Gen-I tourmaline grains show enrichment patterns of LREE for both core and rim with strong positive Eu anomaly. HREE in the core is depleted and shows flat pattern. Whereas the rim shows progressive enrichment of HREE. Gen-II tourmaline shows LREE enrichment with positive Eu anomaly. HREE shows concave up to flat spectra. The  $REE_{total}$  content in Gen-II is very low compared to Gen-I tourmaline.

# CHAPTER 5

## Tourmaline bearing rocks in and around Mukutmanipur

Mukutmanipur-Porapahar area is situated near the Mukutmanipur reservoir in Bankura district, West Bengal. The position of the Mukutmanipur area is shown in the map of Fig 1.5a. Geologically, Mukutmanipur falls inside the SPSZ and situated northern part of SPSZ (Fig 1.5a). The detailed geological description of the area is dealt in the subsequent section.

### 5.1 Lithology and structure of the area

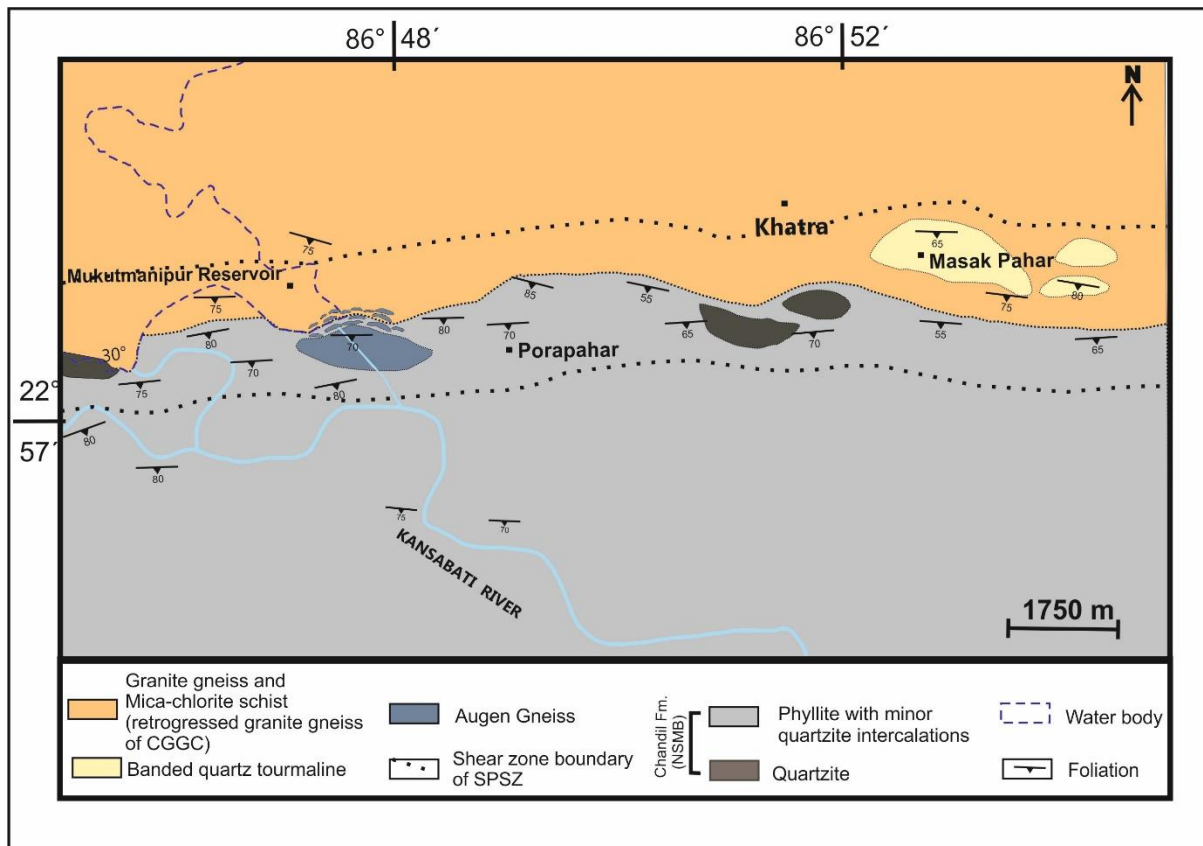
The major lithological distribution in and around Mukutmanipur area is shown in Fig 5.1.1. There are distinct two types of rock suites exposed. Southern block is represented by quartzite-phyllite intercalated unit of Chandil formation belonging to NSMB whereas northern block is represented by granite gneiss and their retrograded parts (schists) of CGGC. Quartzite-phyllite intercalated unit covers most of the parts of south. This lithology generally forms a low lying undulatory topography and east-west trending mounds south of the Khatra-Mukutmanipur Road. The deformed quartzite is massive in appearance, fine grained, grayish white in colour. In places, quartzite in the high strain zone is characterized by grain size refinement and development mylonitic foliation (Fig 5.1.2a). Flattened quartz grains in this rock define an E-W trending foliation plane. So, the quartzite bears the evidence of intense ductile deformation that is manifested by the development of mylonitic foliation. The quartzite is brecciated at places due to brittle deformation and the anastomosing widely opened fractures thus developed are filled up with ferruginous and siliceous materials (Fig 5.1.2b). The breccia zone mainly occurs as detached bands and cross cutting the mylonitic foliation. Angular clasts of sheeted quartzite are found within fine grained, dark brown coloured ferruginous material (Fig 5.1.2b). Intercalated phyllites are more foliated compared to the adjoining quartzite and characteristically form the valleys and plane lands. Phyllite is very fine grained, light to dark coloured and composed of phyllosilicates which define the

prominent foliation plane (Fig 5.1.2c). Phyllites are carbonaceous in places (Fig 5.1.2d). Locally, phyllite contains angular clasts of quartz and feldspar along with phyllosilicates minerals (chlorite+ muscovite + biotite ). Thus, they are tuffaceous in origin. The Chandil formation includes a vast area of tuffaceous phyllite intercalated with quartzites (Ray et al., 1996; Mazumder, 2005; Acharyya et al., 2006). Mylonitic foliation is developed within the phyllite which is parallel to the regional schistosity (E-W trending) in the high strain zone. The CGGC rocks are represented by various types of granitoid towards extreme north (Fig 5.1.2e). The most prominent exposure of this granitoid is found near the Mukutmanipur reservoir mainly within the river bed and the irrigation canals. Few detached outcrops of granitoid can also be seen along Khatra-Mukutmanipur road. The CGGC granitoids of the study area do not show well defined gneissic banding. Rare amphibole and/or biotite porphyroblasts are present in the rock. Elongated quartz and feldspar grains crudely define an E–W trending foliation (Fig 5.1.2e). This granitoid is locally intruded as homophanous aplites (Fig 5.1.2g). A porphyritic granite unit intruded both quartzite-phyllite intercalated rocks (Fig-5.1.2h) of the southern block (NSMB) as well as the homophanous aplites (CGGC) (Fig 5.1.2g) of the northern block, mainly along their contacts. Due to superimposed deformation the K-feldspar grains are flattened of the porphyritic granite and appeared as augen gneiss (Fig 5.1.2f). Both the granite in northern block as well as quartzite-phyllite unit of southern block are sheared along a high strain zone of variable width. Due to extreme ductile deformation that leads to remarkable grain size reduction and transforms the porphyritic granite to granite mylonite (Fig 5.1.2i, j). The porphyritic nature of the rock (Fig 5.1.2j) is found to be preserved only in the less deformed area due to strain localisation. The mylonitic foliation in granite mylonite is defined by feldspar augen and flattened quartz grains. The mylonitic foliation is E-W trending and parallel to the regional foliation. One of the characteristic feature is found in extremely deformed granite mylonite that the development of dark greenish black coloured bands (Fig 5.1.2i, 5.1.2j and 5.1.2l). These dark coloured bands are variable in dimension from few centimeter to few meter and parallel to the mylonitic foliation define by granite mylonite. These dark bands show profuse development of phyllosilicate minerals i.e chlorite, biotite, muscovite (Fig 5.1.2i). The phyllosilicates developed a distinct schistosity that oriented parallel to the mylonitic foliation (Fig 5.1.2i). The granite mylonite and the interlayered phyllosilicate bands are folded at places (Fig 5.1.2j). The schistosity defined by phyllosilicates mineral in darker bands show micro-folding or crenulation cleavage (Fig 5.1.2k). Biswas et al., 2013 and Acharjee et al., 2016, reported tourmaline mineralization near Mukutmanipur area, Bankura. An important

rock type found in this area is a banded tourmaline-quartz rock in Masak pahar region which is located 10 km east from the Mukutmanipur reservoir. This rock occurs as elongated lensoid bodies very close to the quartzite (of southern block) and granite (of northern block) contact. The detailed description of tourmaline mineralization in banded quartz tourmaline will be described in the next segment.

The effect of extreme crystal-plastic deformation has led to remarkable grain size reduction and formation of a mylonitic fabric in high strain zone. Mylonitic foliation which developed in granite mylonite, quartzite, phyllosilicate rich bands and phyllite are parallel to the regional schistosity of the pelitic rocks of the adjoining NSMB (Chandil formation). There are no primary structures preserved in and around Mukutmanipur area. The rocks in this region suffered at least three phases of deformation. The first phase of deformation ( $D_1$ ), produces the  $F_1$  folds whose axial planar schistosity ( $S_1$ ) is the most prominent planar fabric occurring as the regional schistosity of the study area, irrespective of lithology. The second phase of deformation ( $D_2$ ) produces  $F_2$  folds defined by the folding of the  $S_1$  planes. The third phase of deformation ( $D_3$ ) produces the  $F_3$  folds defined by the large broad warps of the resistant lithounits. The strike of regional foliation ( $S_1$ ) shown by phyllite varies from  $80^\circ$ - $100^\circ$  and dipping steeply ( $65$ - $80^\circ$ ) towards south. General strike of the mylonitic foliation ranges  $70$ - $100^\circ$  and dip  $55$ - $80^\circ$  towards S to SE ( $S_1$ ). There are different generations of quartz veins with variable thickness occurred within granite mylonite, phyllosilicate rich bands and phyllite. First generation or  $F_1$  folds are defined by quartz veins (Fig 5.1.2m) whose axial planes are parallel to the mylonitic foliation. ( $S_1$ ) in granite mylonite.  $F_1$  are mostly asymmetric with thickened hinges and longer limb sometimes become parallel to the foliation. The  $F_1$  fold of quartz vein within granite mylonite plunges  $35^\circ \rightarrow 260^\circ$ . The attitude of  $F_1$  axial plane is  $90^\circ/80^\circ$  S. The  $F_1$  folds are thus steeply inclined moderately plunging tight folds. The granite mylonite and the interlayered phyllosilicate bands are folded and showing  $F_2$  (Fig 5.1.2j). Locally, The  $F_2$  folds are defined by well-developed crenulation cleavage in thin layers of phyllosilicate-rich materials (Fig 5.1.2k). Some quartz veins show boudinage or pinch and swell type structure within the mylonitic foliation and also participated in the later crenulation development (Fig 5.1.2n). The  $F_2$  fold measured from crenulation cleavage in phyllosilicate-rich band plunges  $40^\circ \rightarrow 280^\circ$ . The attitude of  $F_2$  axial plane from crenulation cleavage in phyllosilicate-rich band is  $100^\circ/75^\circ$  S. The  $F_2$  folds are steeply inclined moderate plunging tight folds. Rarely, a N-S trending broad warp developed on the limbs of the  $F_2$ . Therefore, in the study area  $F_1$  and  $F_2$  are coaxial and  $F_3$  occurs as a cross fold. No pervasive planar structures are developed along  $F_3$ . Discordant and concordant quartz veins show boudinage and pinch-and-swell structures

respectively. Locally, brittle fracturing occurred along the axial plane of the  $F_3$  fold and filled up with ferruginous and siliceous materials. So it can be well argued that the study area around Mukutmanipur bears evidences of superposed ductile and brittle deformation. Evidence of stress heterogeneity in local scale is also observed along SPSZ. The attitude of the foliation planes in all the lithounits is similar which suggests that they have suffered similar deformational events. Mylonitization in the study area occurred during the  $F_1$  folding.



Map 5.1.1: Lithological map of Mukutmanipur area, Bankura [Modified after BRNS funded research project (Sanction no.2008/36/36-BRNS), entitled "Pressure-Temperature-fluid evolution in parts of SPSZ- Implication for boron metasomatism and U-Fe-Cu-P Mineralisation", P.I Pulak Sengupta, 2014]

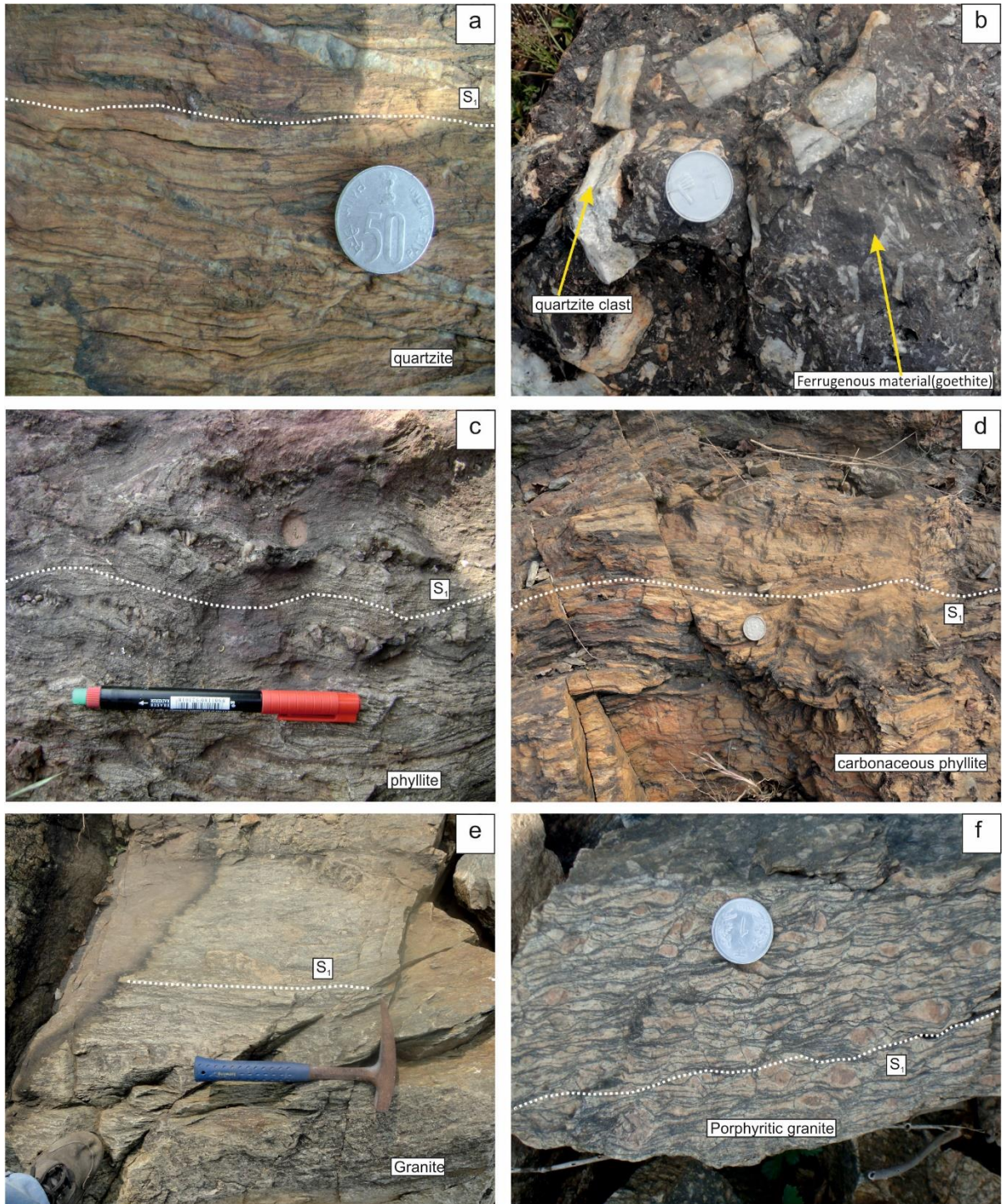


Fig 5.1.2a: Quartzite in the high strain zone is characterized by grain size refinement and development mylonitic foliation (S<sub>1</sub>). Fig 5.1.2b: Angular clasts of sheeted quartzite are found within fine grained, dark brown coloured ferruginous material. Fig 5.1.2c: Phyllite is very fine grained, light to dark coloured and composed of phyllosilicates which define the prominent foliation plane (S<sub>1</sub>). Fig 5.1.2d: Phyllites are carbonaceous in places. Fig 5.1.2e: Elongated quartz and feldspar grains in granite of CGGC define the foliation plane (S<sub>1</sub>). Fig 5.1.2e: Due to superimposed deformation, the K-feldspar grains are flattened of the porphyritic granite and appeared as augen gneiss.

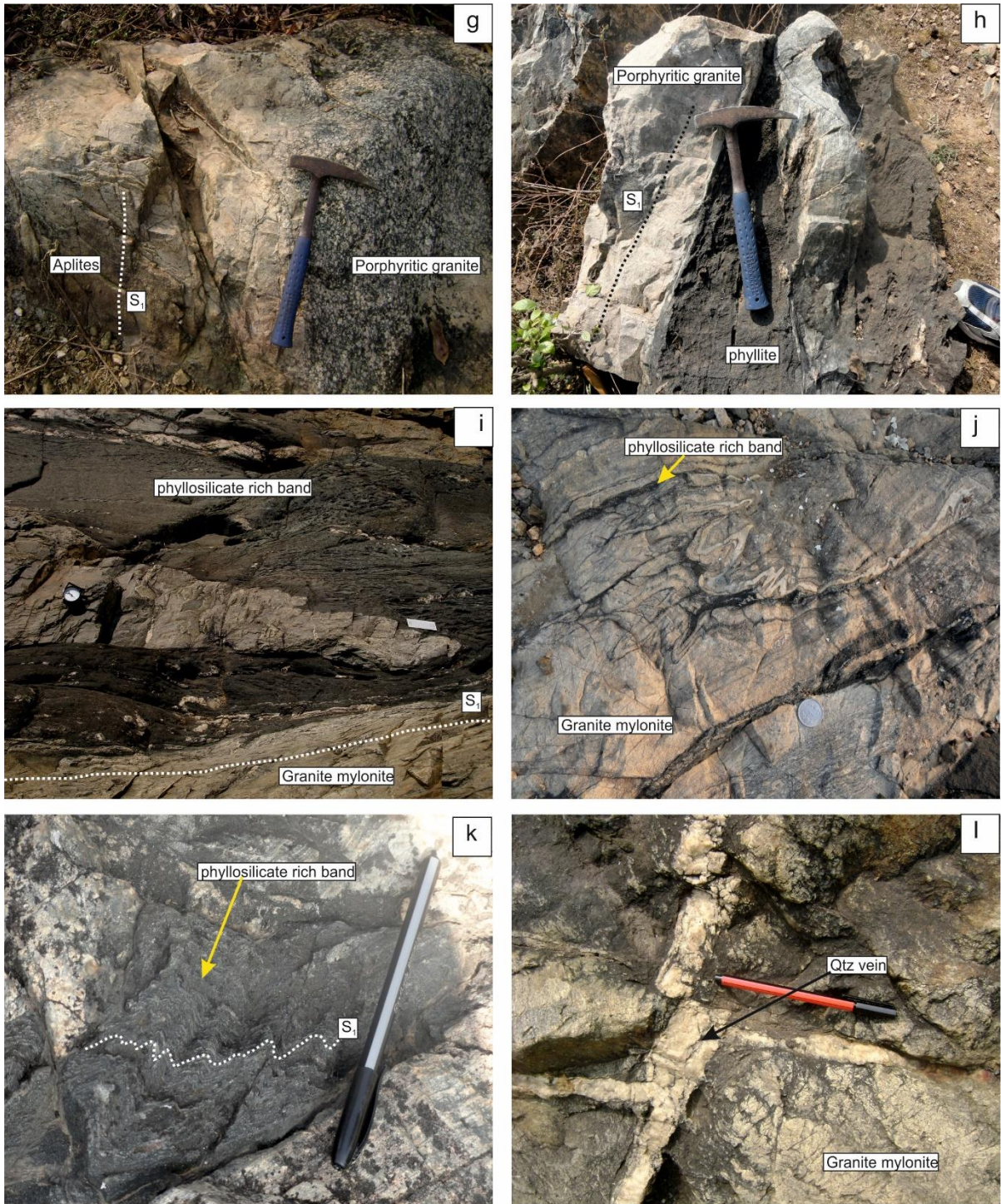


Fig 5.1.2g: Porphyritic granite unit intruded in homophanous aplites of CGGC .Fig 5.1.2h: Porphyritic granite unit intruded quartzite-phyllite intercalated rocks of NSMB. Fig 5.1.2i: phyllosilicate rich bands are variable in dimension and parallel to the mylonitic foliation ( $S_1$ ) define by granite mylonite Fig 5.1.2j: The granite mylonite and the interlayered phyllosilicate bands are folded and showing  $F_2$ . Fig 5.1.2k: The  $F_2$  folds are defined by well-developed crenulation cleavage in thin layers of phyllosilicate-rich materials in phyllosilicate rich bands. Fig 5.1.2l: Quartz veins cut across the mylonitic fabric( $S_1$ ) and detached due to brittle deformation.

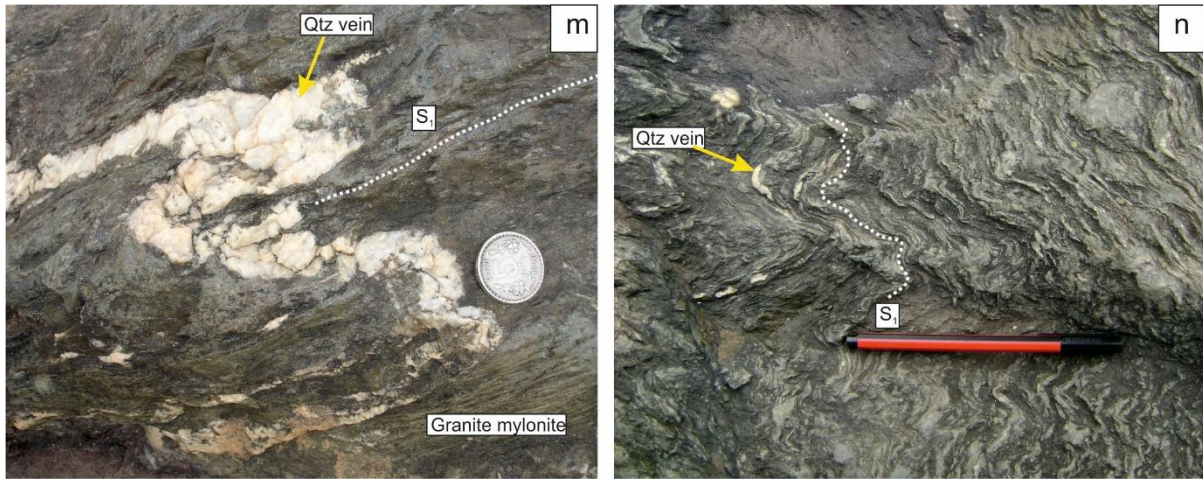


Fig 5.1.2m:  $F_1$  folds are defined by quartz veins whose axial planes are parallel to the mylonitic foliation ( $S_1$ ) in granite mylonite. Fig 5.1.2n: Some quartz veins show boudinage or pinch and swell type structure within the mylonitic foliation and also participated in the later granulation development.

## 5.2 Field features of tourmaline bearing rocks

Tourmaline is found in banded quartz tourmaline rock adjoining granite mylonite and quartz veins in Masak Pahar area, east of the Mukutmanipur. This banded quartz tourmaline rock occurs as elongated E-W trending lensoid body well within the SPSZ and surrounded by mica -chlorite schist (retrogressed granite of CGGC). Large to small bodies of banded quartz tourmaline rock occurs as pods and forms isolated mounds. Based on the size and morphology of tourmaline and the relation of the tourmaline-bearing aggregates with the host rock four distinct mode of occurrence are established.

**Mode 1:** In mode 1, banded quartz tourmaline rock shows laterally persistent alternate thin quartz-rich laminae and tourmaline- rich laminae (Fig 5.2a). The thickness of alternate tourmaline and quartz rich laminae is varying from 2mm- 5mm. The laminae are continuous in nature and can be traceable up to several meters. The tourmaline rich laminae define by very fine (usually < 1 mm), granular aggregates of tourmaline grains. The tourmaline grains are so fine grained that identification of individual grain under naked eye is very difficult. These alternate tourmaline and quartz rich laminae are oriented parallel to the E-W trending regional  $S_1$  fabric (Fig 5.2a). In banded quartz tourmaline rock, the alternate laminations of quartz and tourmaline are deformed and folded, defining tight to isoclinal  $F_2$  fold (Fig 5.2b). At places, curvature of the hinges of  $F_2$  fold produced eyed- fold (Fig 5.2d). Intense deformation produced pinch-and swell structure in quartz rich laminae (Fig 5.2c). From the field feature supports the view that mode 1 tourmalines are syn-tectonic with respect to  $S_1/D_1$ . These banded quartz-tourmaline rocks are brecciated by later brittle fracturing. The brittle fractures that are superposed on the ductile fabric are filled with goethite veins (Fig 5.2e).

**Mode 2:** In mode 2, within the banded quartz tourmaline rock, tourmaline aggregates occur as massive tourmaline rich bands (Fig 5.2f). The tourmaline rich bands are locally quartz free. The thickness of tourmaline rich bands varies from 1cm- 5cm. Tourmalines are fine grained (usually < 1 mm) and identification of individual grain is difficult under naked eye. These tourmaline rich bands are oriented parallel to the banded quartz tourmaline rock as well as to the  $S_1$  fabric which indicate that they are syn tectonic with respect to regional  $S_1/D_1$ .

**Mode 3:** In mode 3, millimetre thick bands/veins that are alternately rich in tourmaline and quartz occurs within the granite mylonite (Fig 5.2g). Tourmaline grains within in the tourmaline rich bands are very fine grained (usually < 1 mm) and glassy in appearance. Similar to the mylonitic foliation ( $S_1$ ) this alternate tourmaline and quartz rich bands are folded

showing  $F_2$  fold (Fig 4.2b). From the field feature supports the view that mode 3 tourmalines are syn-tectonic regarding  $S_1/D_1$ .

**Mode 4:** In this mode coarse, acicular tourmaline (1-5cm along long axis) grains occur within quartz veins (Fig 5.2h). These quartz veins cut across the  $S_1$  foliation of the host rock. These tourmaline grains are commonly haphazardly oriented but may also show rosette texture (Fig 5.2h) and also show no signs of ductile deformation. So, these tourmalines are formed after latest deformation i.e.  $F_3/D_3$ .

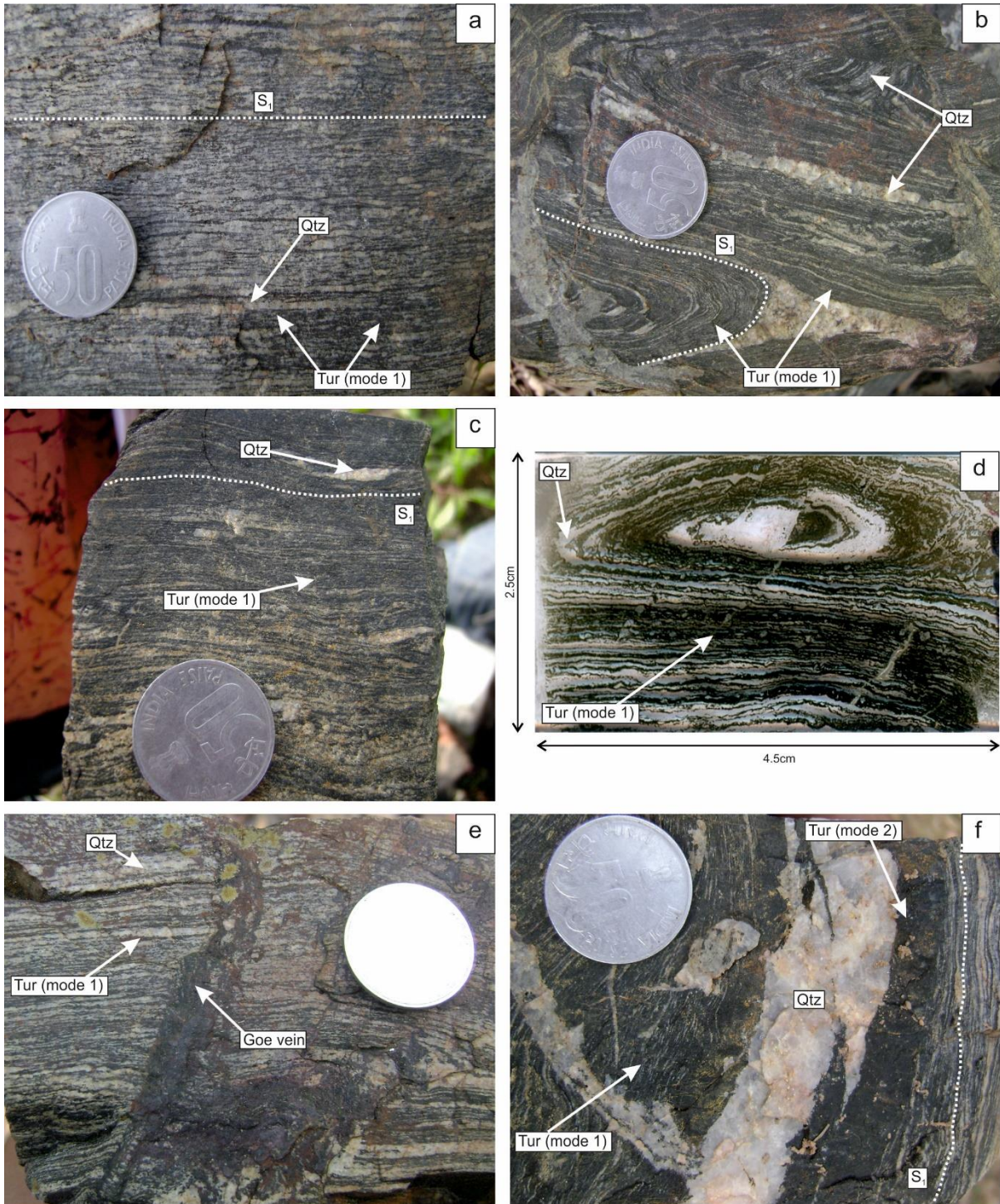


Fig 5.2a: In mode 1, banded quartz tourmaline rock alternate thin quartz-rich laminae and tourmaline-rich laminae. Fig 5.2b: Alternate tourmaline and quartz rich laminae are folded and showing  $F_2$  fold in mode 1 association. Fig 5.2c: Intense deformation produced pinch-and swell structure in quartz rich laminae in mode 1 association. Fig 5.2d: In mode 1, curvature of the hinges of  $F_2$  fold produced eye-fold in banded tourmaline-quartz rock(mode 1).Fig 5.2e: Banded quartz-tourmaline rock are brecciated by later brittle fracturing and filled with goethite veins. Fig 5.2f: In mode 2, within the banded quartz tourmaline rock, tourmaline aggregates occur as massive tourmaline rich bands.

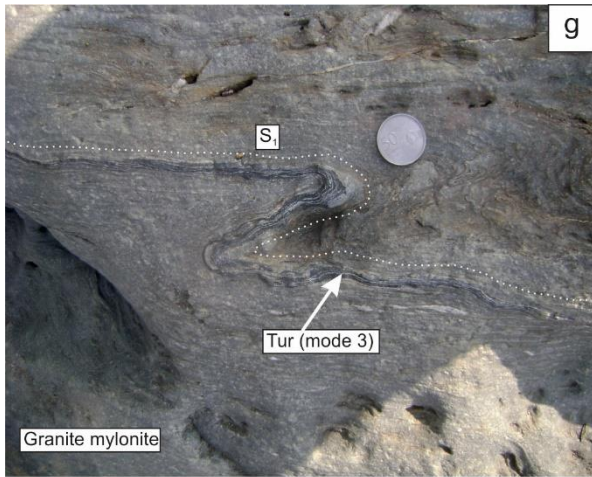


Fig 5.2g: In mode 3, millimetre thin bands that are alternately rich in tourmaline and quartz occurs within the granite mylonite and showing  $F_2$  fold. Fig 5.2h: In mode 4, coarse and acicular tourmaline grain occur haphazardly oriented but may also show rosette texture within the quartz vein.

### 5.3 Petrographic description of tourmaline bearing rocks

The exotic banded quartz tourmaline rock is hosted by mica-chlorite schist which is the retrogressed part of granite of CGGC. Mica-chlorite schist occurs as millimetre to centimetre thick layer with phyllosilicate rich bands alternate with phyllosilicate poor bands (Fig 5.3a). Phyllosilicate rich bands consist of muscovite, biotite and chlorite. The proportion of biotite is less than combined abundance of muscovite and chlorite (<20 molar vol% of biotite). The muscovite, biotite and chlorite are fine grained and show dynamic recrystallization. Mylonitic foliation defined by these phyllosilicate minerals is parallel to the regional foliation ( $S_1$ ) (Fig 5.3a). The phyllosilicate poor band consists of K-feldspar and quartz. Flattened and recrystallized quartz aggregates are oriented parallel to the  $S_1$  fabric defined by adjacent phyllosilicate rich bands.

Based on field and microscopic study there are four modes (mode 1, mode 2 mode 3 and mode 4) of tourmaline occurrences. Considering all the modes there are two generations of tourmaline are being identified.

In mode I, banded quartz tourmaline rock represents millimetre to decimetre thin alternate layer of tourmaline rich laminae (>90 modal vol% tourmaline) and quartz rich laminae (>90 modal vol% quartz) (Fig 5.3b). These laminae are continuous in nature and thickness varies from place to place (thickness of each lamina 0.5-1 mm). Tourmaline grains in tourmaline rich laminae are fine (10-50  $\mu\text{m}$  along long axis) and euhedral to subhedral in shape. It shows strong pleochroism in the shades of light green to dark green without prominent optical zoning (Fig 5.3b). Micro fracture observed in tourmaline grains. Equant to short prismatic tourmaline grains are oriented parallel to the  $S_1$  fabric (Fig 5.3b and 5.3c). The major foliation is crenulated (Fig 5.3b). Within the quartz rich laminae prismatic tourmaline occurs as discrete or isolated grains with a preferred orientation along  $S_1$ . Quartz grains are flattened and oriented parallel to the  $S_1$  (Fig 5.3c). They have sutured grain boundaries and partially recrystallized (Fig 5.3c). The banded quartz tourmaline rock is deformed and folded at places. The alternate tourmaline rich laminae and quartz rich laminae show tight  $F_2$  fold (Fig 5.3d). Therefore, tourmaline grains in mode 1 association are syn-tectonic with respect to  $S_1$  and designated as Gen-I (first generation) tourmaline.

In mode 2, fine to medium grained tourmaline aggregates formed massive tourmaline rich band (Fig 5.3e). Tourmaline grains in tourmaline rich band are fine to medium (20-100  $\mu\text{m}$  along long axis) and euhedral to subhedral in shape. Tourmaline grains are equant to

prismatic in habit (Fig 5.3e and 5.3f). Tourmaline grains are highly fractured. It shows strong pleochroism in the shades of light green to dark green (Fig 5.3f). At places, medium grained tourmaline in basal section shows prominent optical zoning with bluish green colour and brownish green colour rim (Fig 5.3f). Long axis of prismatic tourmaline grains are oriented parallel to the  $S_1$  fabric (Fig 5.3e and 5.3f). Islands of recrystallized quartz aggregates are present in the tourmaline-rich layers (Fig 5.3e). Recrystallized quartz ribbon was noted within the tourmaline rich band which is parallel to the  $S_1$  (Fig 5.3e). Therefore, tourmaline in tourmaline rich band in mode 2 association is syn-tectonic with respect to  $S_1/D_1$  and designated as Gen-I (first generation).

In mode 3, alternate tourmaline and quartz rich bands occur within the mylonitic granite (Fig 5.3g). The mylonitic granite consists of phyllosilicate rich layer along with quartz and feldspar. They are very fine grained and defining the mylonitic foliation which is parallel to the regional foliation ( $S_1$ ) (Fig 5.3g). Aggregates of tourmaline in tourmaline rich band are very fine grain (<50  $\mu\text{m}$ ). It is difficult to identify the individual grain boundary of tourmaline grains in the central part of the vein due to the overlapping of grains. Whereas in the boundary of the tourmaline rich band, fine prismatic tourmaline grains are observed. Discrete prismatic fine tourmaline grains grow over the phyllosilicate layer and are oriented parallel to the  $S_1$  fabric defined by phyllosilicate rich bands. Tourmaline grains show pleochroism in the shades of green to greenish brown without optical zoning. This tourmaline rich bands are oriented parallel to the  $S_1$  fabric defined by the adjacent granite mylonite (Fig 5.3g). Thus the tourmaline in tourmaline rich band are syn tectonic with respect to  $S_1/D_1$  and designated as Gen-I (first generation) tourmaline.

In mode 4, coarse (0.2-7mm) tourmaline grains occur in quartz vein. Prismatic tourmaline grains are randomly oriented and also characterized by extremely variable grain size (Fig 5.3h). These grains are highly fractured. Tourmaline grains show strong pleochroism in the shades of light green to dark greenish brown. Tourmaline grains show strong optical zoning with greenish blue core and dark green rim (Fig 5.3h). Therefore, these coarse randomly oriented tourmaline grains are supposed to be formed at post  $D_3/F_3$ . Thus, the tourmaline grains are designated as Gen-II (second generation).

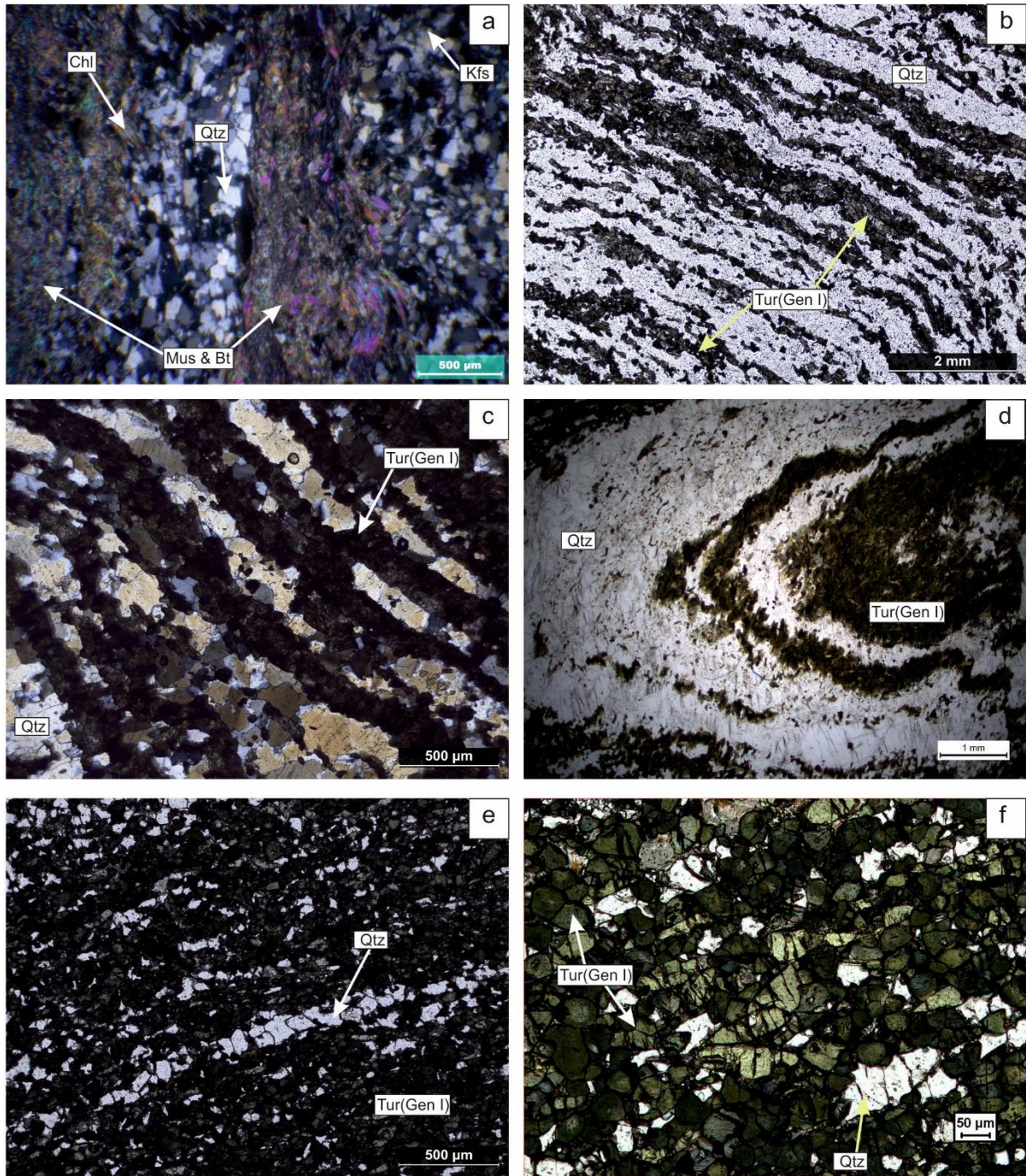


Fig 5.3a: Mica-chlorite schist occurs as millimetre to centimetre thick layer with phyllosilicate rich(muscovite + biotite + chlorite) bands alternate with phyllosilicate poor(quartz + feldspar) bands which are parallel to the  $S_1$  (under CPL). Fig 5.3b: Banded quartz tourmaline rock represents millimetre to decimetre thin alternate layer of Gen I tourmaline rich laminae and quartz rich laminae in mode 1 association. Fig 5.3c: Gen I tourmaline rich laminae alternating with recrystallized quartz rich laminae which are parallel to the  $S_1$  in mode 1 association (under CPL). Fig 5.3d: The alternate Gen I tourmaline rich laminae and quartz rich laminae shows tight  $F_2$  fold in mode 1 association. Fig 5.3e: Fine to medium grained Gen I tourmaline aggregates formed massive tourmaline rich band and oriented parallel to the  $S_1$  fabric in mode 2 association. Fig 5.3f: At places medium grained Gen I tourmaline in basal section shows prominent optical zoning with bluish green colour and brownish green colour rim in tourmaline rich band (mode 2 association).

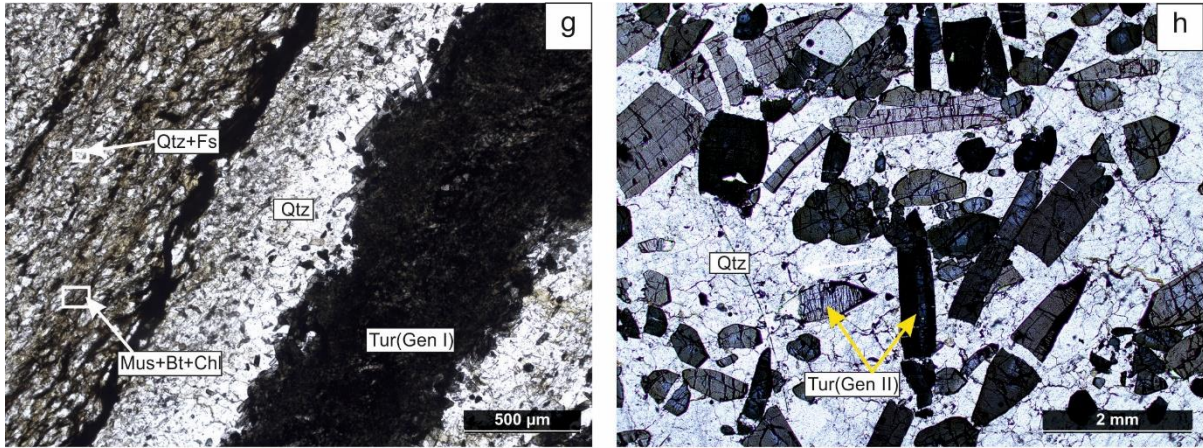


Fig 5.3g: In mode 3, alternate Gen I tourmaline and quartz rich bands occur within the mylonitic granite and oriented parallel to the regional  $S_1$ . Fig 5.3h: The Gen II coarse, prismatic tourmaline grains are randomly oriented in mode 4 association.

## 5.4 Tourmaline mineral chemistry

Standard analytical procedures of major and trace elements analysis and normalization of tourmalines are given in the appendix I and II. Based on field occurrence and microscopic there are two generations of tourmaline (Gen-I and Gen-II). First generation (Gen-I) tourmaline are oriented parallel to  $S_1$  fabric and syn tectonic regarding to  $S_1/D_1$ . Whereas second generation tourmaline is randomly oriented within the quartz vein. So, these tourmalines are formed after  $D_3/F_3$  and designated as second generation or Gen-II.

Overall T-sites of tourmaline in all the two generations of tourmaline are completely or nearly filled up with Si (Gen-I :  $6.00 \pm 0.03$  apfu, Gen-II :  $5.97 \pm 0.04$  apfu). The Z site of the tourmaline is completely filled up with Al. The Al in apfu of the tourmaline compositions exceeds 6 [Gen-I ( $6.07 \pm 0.08$  apfu) , Gen-II ( $6.09 \pm 0.19$  apfu)] suggesting that some Al must be present in Y site. The Al content in Gen-II tourmaline is higher than the Gen-I tourmaline Ti content in Gen-I ( $0.13 \pm 0.03$  apfu) and Gen-II ( $0.13 \pm 0.03$  apfu) are nearly the same. X-sites vacancy is estimated from the measured Na+Ca+K contents. In terms of the Ca-X-site vacancy-Na+K diagram (Fig 5.4.1.a), all tourmaline grains of different generations are plots in the “Alkali group”. The X-vacancy in tourmaline structure is higher in the Gen-II ( $0.15 \pm 0.05$  apfu) than the Gen-I ( $0.13 \pm 0.03$  apfu). The Ca contents of Gen-II tourmaline ( $0.20 \pm 0.05$  apfu) is higher than the Gen-I tourmaline ( $0.08 \pm 0.03$  apfu). Though there exists a compositional overlap between two generations of tourmaline (Gen-I and Gen-II), the Gen-I compositions are less calcic and alkali rich than the Gen-II compositions. In the  $X/(X + Na)$  vs.  $X_{Mg}$  (=  $Mg/(Mg+Fe^{2+})$ ). diagram (Fig 5.4.1.b), the tourmaline compositions of both generations are plotted in schorl and dravite field. Gen-I tourmaline grains straddle the boundary between schorl and dravite. However, Gen-I core is schorl in character and the rim composition straddles the boundary between schorl and dravite. So, the rim ( $0.48 \pm 0.02$  apfu) is more  $X_{Mg}$  rich than the core ( $0.35 \pm 0.05$  apfu). Gen-II tourmalines are more  $X_{Mg}$  rich ( $0.62 \pm 0.02$  apfu) than Gen-I and dravite in character. There is composition overlap between the core and the rim of Gen-II tourmaline. Acharjee et al., 2016, also reported tourmaline in Masak pahar area. According to Acharjee et al., 2016, the tourmaline compositions are alkali rich and schorl to dravite in character (Fig 5.4.1.a and Fig 5.4.1.b). Representative microprobe analyses of tourmaline are given in Table 5.4.3a.

Tourmaline show extensive substitution in the X-, Y-, Z-, T-, and W-sites (Hawthorne and Henry 1999). In Mukutmanipur area, tourmaline compositions define a dominate trend in Fe vs. Mg diagram (Fig 5.4.1.c). Gen-I and Gen-II tourmaline compositions show significant Fe-Mg

substitution and are expressed by the  $\text{MgFe}_{-1}$  exchange vectors ( $r^2=0.79$ ). Gen-I tourmaline compositions plot near or below the line of  $\text{Fe}^{2+} + \text{Mg} = 3$  which indicate tourmaline have Al in their Y sites. Whereas major compositions of Gen-II tourmaline on or below the line  $\text{Fe}^{2+} + \text{Mg} = 3$  but some are above the line which defines that some Gen-II compositions of tourmaline have no Al in their Y sites. There are systematic variations of Fe and Mg content in different generations of tourmaline. The Gen-I ( $1.55 \pm 0.22$  apfu) tourmaline Fe is higher than the Gen-II ( $1.06 \pm 0.10$  apfu). Whereas, Mg content in Gen-I ( $1.26 \pm 0.19$  apfu) is poorer than the Gen-II ( $1.73 \pm 0.12$  apfu) tourmaline. In X-site vacancy vs.  $\text{Al}_{\text{total}}$  diagram (Fig 5.4.1.d), spread of tourmaline compositions for Gen-I and Gen-II shows distinct substitution occur along  $\square\text{Al}(\text{NaR})_{-1}$  exchange vector ( $r^2=0.53$ ) where  $\text{R} = \text{Fe}^{2+} + \text{Mg}$  (Fig 5.4.1.d). In the  $[\text{R}_1(=\text{Na}+\text{Ca})+\text{R}_2(=\text{Fe}+\text{Mg}+\text{Mn})]$  vs.  $[\text{R}_3(=\text{Al}+1.33\times\text{Ti})]$ , most of the tourmaline compositions of all generations fall within the upper half of the parallelogram formed by the lines joining the positions of the tourmaline species. Gen-I and Gen-II tourmaline compositions trend are parallel to the  $\square\text{Al}(\text{NaR})_{-1}$  exchange vectors (Fig 5.4.1e). In Fe+Mg vs  $\text{Al}_{\text{total}}$  diagram (Fig 5.4.1f), the data array defines a distinct negative trend that is consistent with the chemical substitutions defined by the exchange vectors  $\square\text{Al}(\text{NaR})_{-1}$  and  $\text{AlO}(\text{R}(\text{OH}))_{-1}$  ( $r^2=0.98$ ) for both Gen-I and Gen-II.

Fig 5.4.2a is a line traverse that shows the compositional variation across optical zoning of a tourmaline grain. In a particular tourmaline grain of first generation (Gen-I) tourmaline having a bluish green colour core and brownish green colour rim, composition traverse has been taken with a difference of  $1.5\mu\text{m}$  gap between two points (Fig 5.4.2a). The core is enriched in Fe, Al, Na+K, Xvac than the rim and depleted in Mg,  $\text{X}_{\text{Mg}}$ , Ca than the rim portion. In Fe vs Mg diagram (Fig 5.4.2b) a prominent Fe-Mg substitution occurs, showing strong substitution trend parallel to vector  $\text{MgFe}_{-1}$  ( $r^2=0.96$ ). In  $\text{Al}_{\text{total}}$  vs X vac (Fig 5.4.2c), the spread of tourmaline compositions shows that the chemical substitution was dominated and expressed by the exchange vectors towards  $\square\text{Al}(\text{NaR})_{-1}$  ( $r^2=0.70$ ). The array of data in the Fe + Mg + Ti vs. total Al diagram (Fig 5.4.2e) shows a strong negative slope which also suggests that the bluish green cores to greenish brown rims tourmaline Al content became poorer and substitution occurs along  $\text{TiRAl}_{-2}$  exchange vector ( $r^2=0.98$ ) where  $\text{R} = \text{Fe}^{2+} + \text{Mg}$ .

Fig 5.4.2f is a line traverse that shows the compositional variation across optical zoning of a tourmaline grain. In second generation tourmaline (Gen-II) tourmaline grain displays strong optical zoning characterized by greenish blue core to dark green rim. The compositional traverse has been taken from core to rim. The core is distinctly enriched in  $\text{Fe}^{2+}$ , Na+K, and

rim is enriched in Mg, Ti, Ca, X<sub>vac</sub>. In Fe vs Mg diagram, a moderate Fe-Mg substitution occurs ( $r^2=0.51$ ) along MgFe<sub>-1</sub>(Fig 5.4.2g). In Al<sub>total</sub> vs X<sub>vac</sub>, the spread of Gen-II tourmaline compositions shows that the chemical substitution was dominated and expressed by the exchange vectors towards  $\square\text{Al}(\text{NaR})_{-1}$  ( $r^2 = 0.74$ ) (Fig 5.4.2h). In Fe + Mg + Ti vs. total Al diagram, strong substitution occurs along the AlO(R(OH))<sub>-1</sub> (Fig 5.4.2j) exchange vector ( $r^2=0.97$ ).

Muscovite, biotite, chlorite, quartz and K-feldspar are present throughout the host rock i.e mica chlorite schist. In Muscovite FeO<sub>t</sub> content varies from 3.67 to 3.86 wt%. Muscovite shows a significant amount of pyrophyllite component (~25 mol %). In biotite X<sub>Mg</sub> content varies from ~ 0.33 to 0.41. TiO<sub>2</sub> content of biotite varies from 1.30 to 2.39 wt%. In chlorite X<sub>Mg</sub> content is 0.61. The X<sub>Kfs</sub> value of the K-feldspar is 0.96. Compositions of muscovite, biotite, chlorite, and Kfeldspar are presented in Table 5.4.3b.

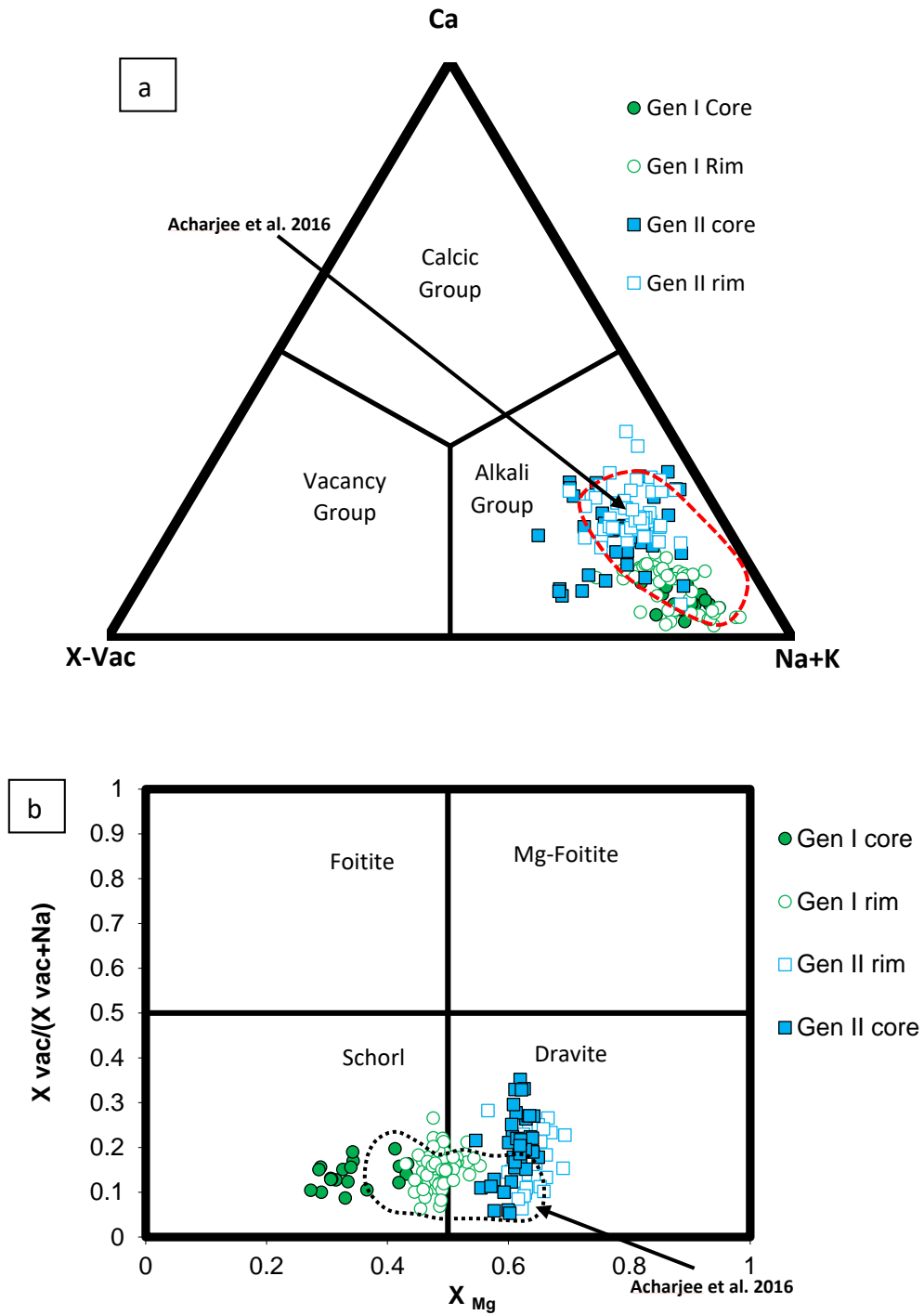


Fig 5.4.1.a: Principal tourmaline groups based on the classification scheme of Hawthorne and Henry (1999). Fig 5.4.1.b Nomenclature diagram of tourmaline based on X-site vacancy/(X-site vacancy + Na) vs. Mg/(Mg + Fe<sup>2+</sup>) plot after Henry et al. (2003).

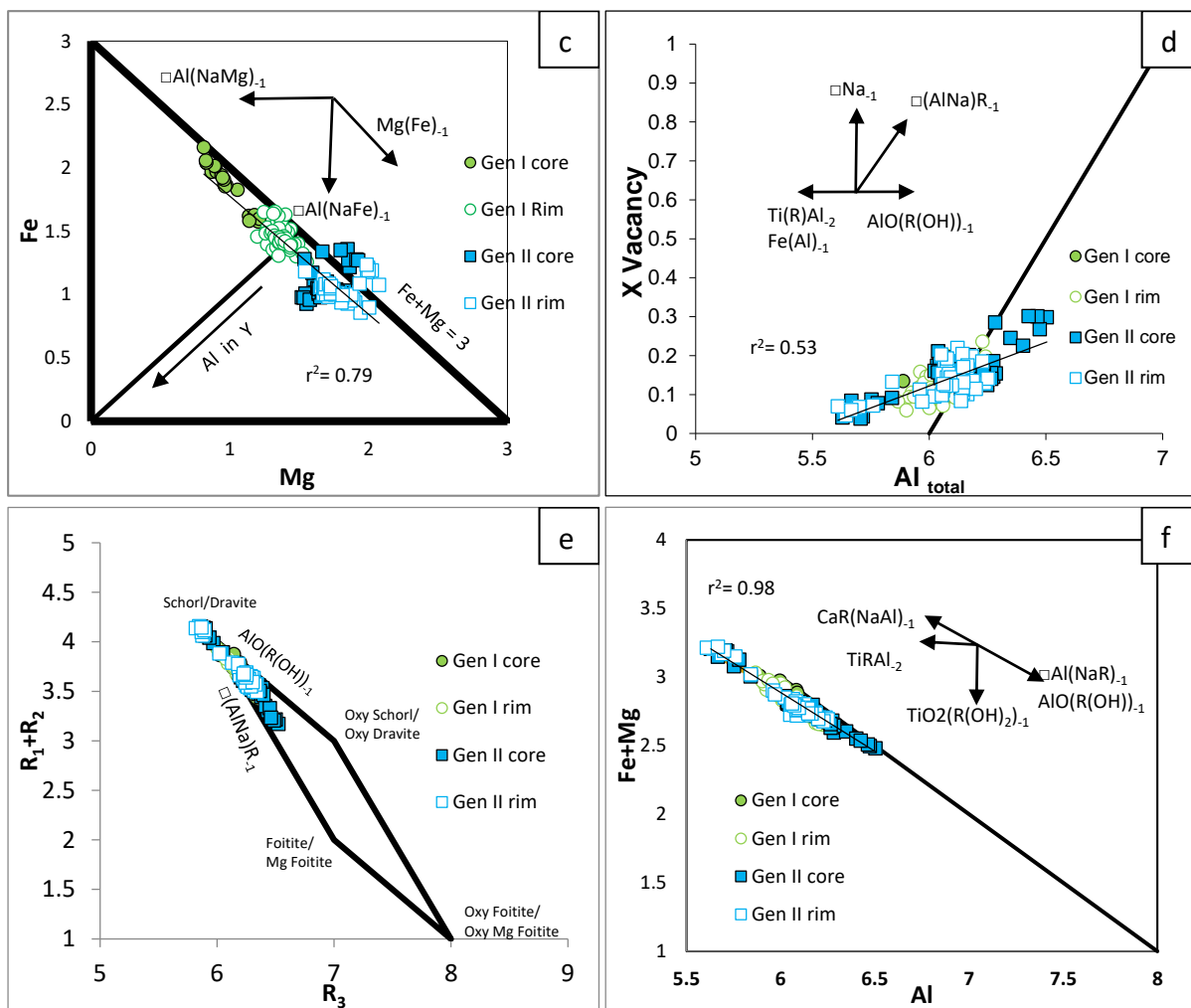


Fig 5.4.1.c: Tourmaline compositions define a negative trend in Fe vs. Mg diagram. Gen-I and Gen-II tourmaline show substitution occurs along  $MgFe_{-1}$  exchange vector. Fig 5.4.1.d: In  $Al_{total}$ -vs- X-site vacancy diagram compositions Gen-I and Gen-II tourmaline show distinct substitution occur along  $\square Al(NaR)_{-1}$  exchange vector where  $R = Fe^{2+} + Mg$ . Fig 5.4.1.e: In the  $[R_1(=Na+Ca)+R_2(=Fe+Mg+Mn)]$  vs.  $[R_3(=Al+1.33 \times Ti)]$ , most of the tourmaline compositions of Gen-I and Gen-II fall within the upper half of the parallelogram and substitution occur due to  $\square Al(NaR)_{-1}$  exchange vector. Fig 5.4.1.f: In the  $Fe+Mg$  vs  $Al_{total}$  diagram, the data array defines a distinct negative trend that is consistent with the chemical substitutions defined by the exchange vectors  $\square Al(NaR)_{-1}$  and  $AlO(R(OH))_{-1}$ .

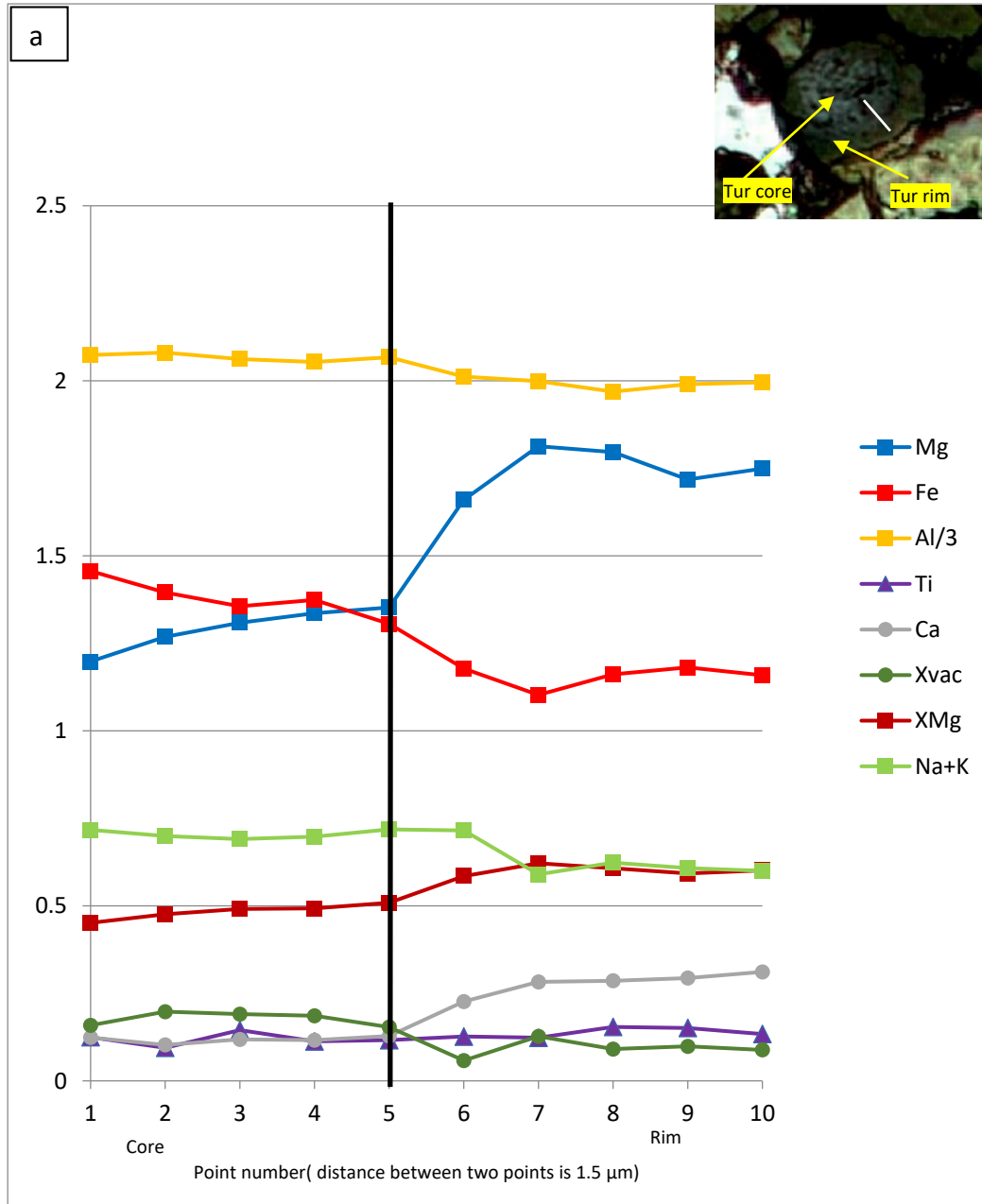


Fig 5.4.2a: Plot of compositional variations of Gen-I tourmaline from the bluish green core and brownish green rim of a single zoned tourmaline grain.  $X_{Mg} = Mg/(Fe^{2+} + Mg)$ . Zero on the X-axis represents the starting point of the compositional traverse from the bluish green colour core. Photomicrograph of the zoned tourmaline and the traverse path is shown by the solid line (plane polarized light)

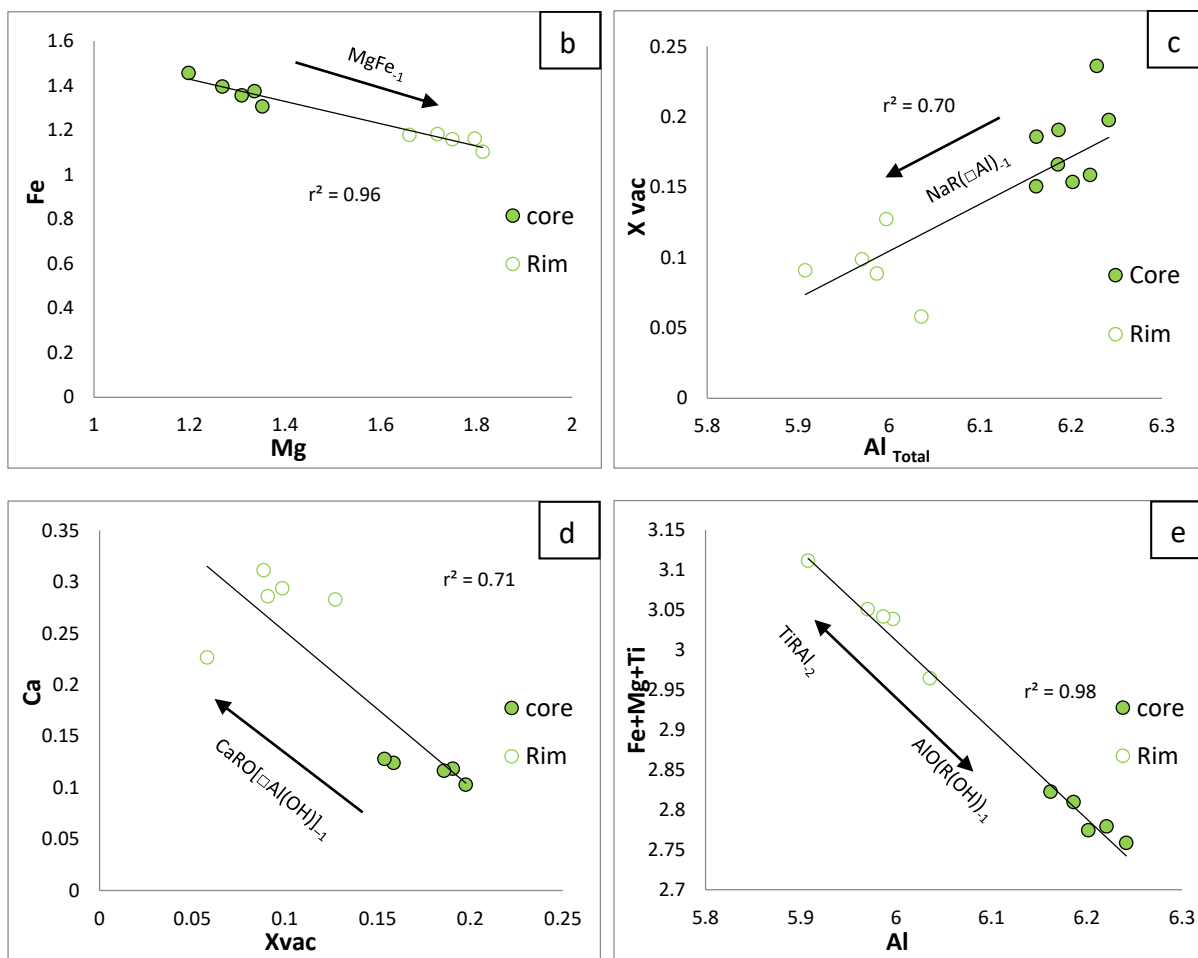


Fig 5.4.2b: Plot of data from the traverse of the zoned tourmaline grain in terms of Fe vs. Mg showing strong correlations. Fig 5.4.2c: Plot of data from the traverse of the zoned grain in terms of X-site vacancy vs. total Al showing positive correlations. Fig 5.4.2d: Plot of data from the traverse of the zoned grain in terms of Ca vs. X-vac showing least negative correlations. Fig 5.4.2e: Plot of data from the traverse of the zoned grain in terms of Fe+Mg+Ti vs.  $Al_{Total}$  showing strong negative correlations.

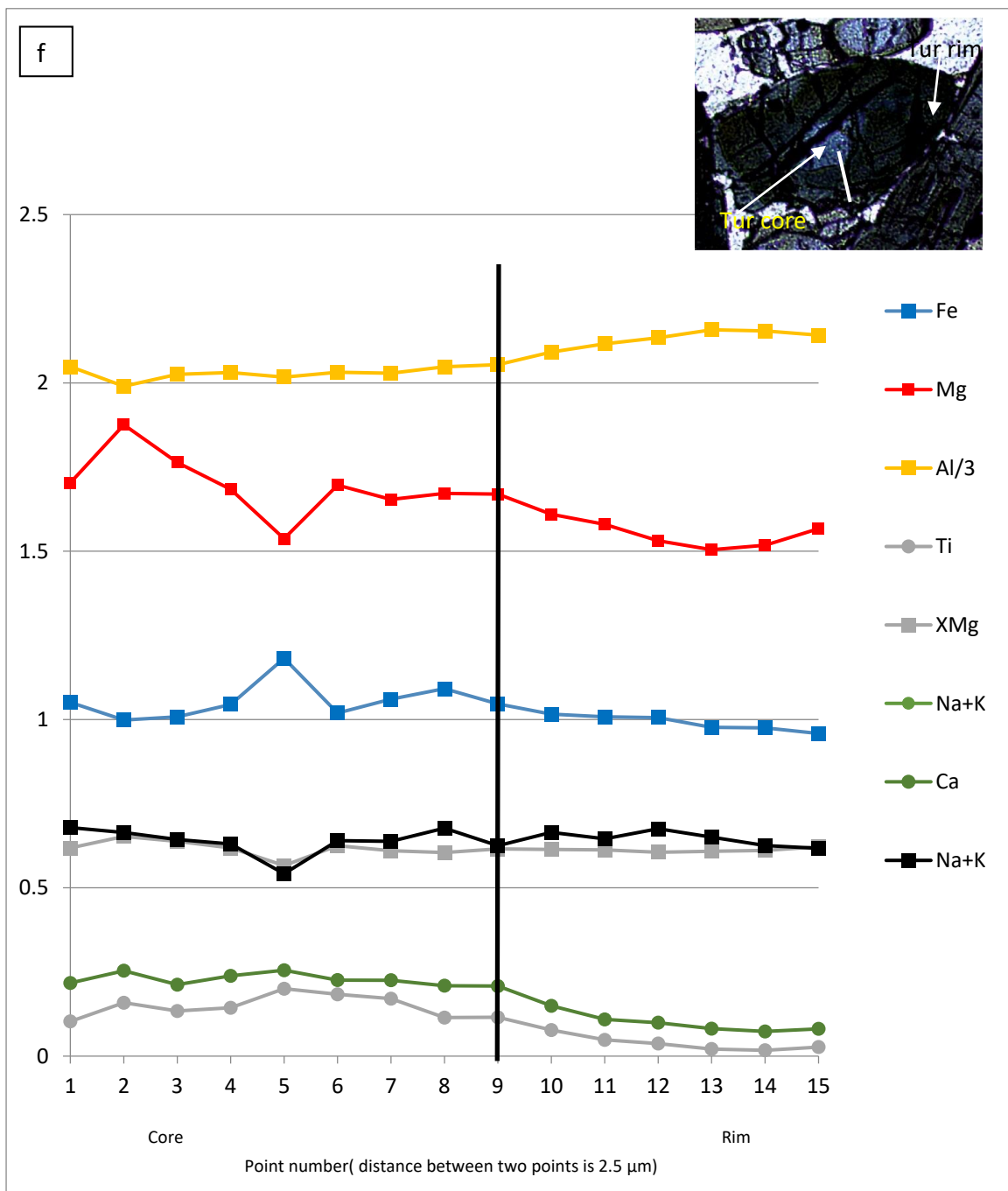


Fig 5.4.2f: Plot of compositional variations of Gen-II tourmaline from the greenish blue colour core and dark green colour rim of a single zoned tourmaline grain.  $X_{Mg} = Mg / (Fe^{2+} + Mg)$ . Zero on the X-axis represents the starting point of the compositional traverse from the inky blue colour core. Photomicrograph of the zoned tourmaline and the traverse path is shown by the solid line (plane polarized light). Al plotted as Al/3.

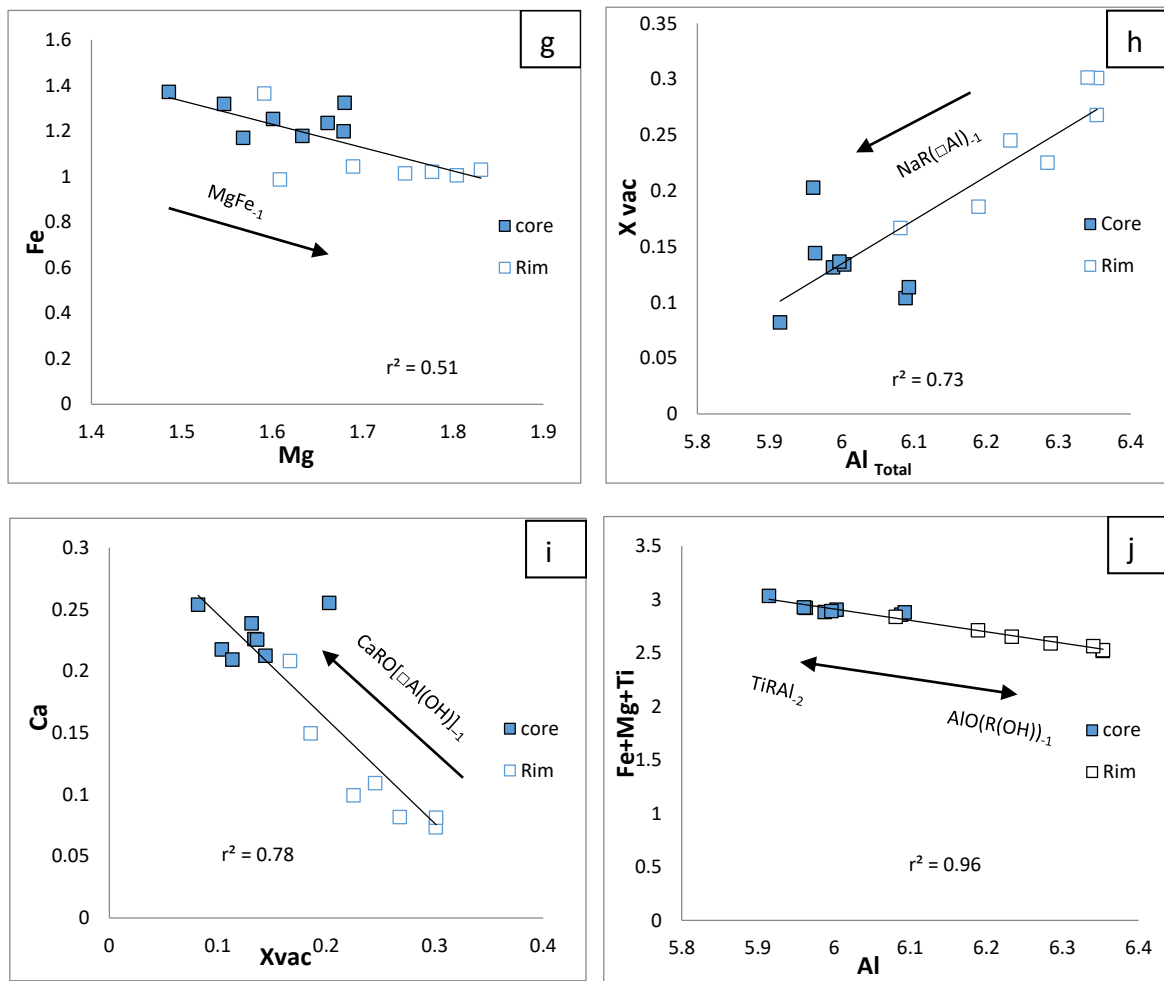


Fig 5.4.2g: Plot of data from the traverse of the zoned tourmaline grain in terms of Fe vs. Mg showing moderate correlations. Fig 2.5.4.2h: Plot of data from the traverse of the zoned grain in terms of X-site vacancy vs. total Al showing positive ( $r^2 = 0.74$ ) correlations. Fig 5.4.2i: Plot of data from the traverse of the zoned grain in terms of Ca vs. X-vac negative ( $r^2 = 0.78$ ) least correlations. Fig 5.4.2j: Plot of data from the traverse of the zoned grain in terms of Fe+Mg+Ti vs. Total Al negative ( $r^2 = 0.97$ ) strong correlations.

Table 5.4.3a: Representative EPMA analysis of tourmaline

Generati on	Gen I																				
Sample no.	PP 73a	PP73 c	PP73 c	PP73 c	PP73 c	PP73 c															
Point	35 / 1	36 / 1	37 / 1	39 / 1	41 / 1	1 / 8	1 / 9	1 / 10	2 / 13	2 / 14	2 / 15	2 / 16	2 / 17	2 / 18	2 / 19	2 / 20	1 / 1	5 / 1	8 / 8	8 / 9	8 / 10 <sup>#</sup>
Core/Rim	core																				
Al <sub>2</sub> O <sub>3</sub>	29.25	30.08	29.69	29.74	29.88	29.69	29.55	29.94	29.97	30.02	29.81	29.70	29.90	29.91	30.13	29.11	30.36	30.00	30.31	29.88	30.35
FeO	11.14	12.86	14.17	12.92	13.68	13.65	13.42	12.95	12.86	13.32	13.44	13.97	13.96	14.17	14.35	14.79	11.39	11.33	11.03	11.09	11.04
TiO <sub>2</sub>	0.79	0.69	0.78	0.90	0.80	0.54	0.66	0.66	0.59	0.76	0.81	0.70	0.66	0.73	0.63	0.85	1.11	0.90	0.91	0.85	1.07
SiO <sub>2</sub>	35.05	35.55	35.35	35.87	35.22	34.96	35.10	34.93	35.15	34.94	35.12	34.60	34.23	34.58	34.69	33.81	35.34	35.44	35.28	35.11	35.39
K <sub>2</sub> O	0.04	0.03	0.05	0.09	0.06	0.08	0.03	0.07	0.06	0.05	0.05	0.04	0.07	0.06	0.04	0.07	0.07	0.06	0.06	0.06	0.04
CaO	1.26	0.42	0.32	0.42	0.28	0.30	0.29	0.30	0.22	0.31	0.29	0.35	0.32	0.32	0.27	0.35	0.53	0.49	0.55	0.60	0.51
Na <sub>2</sub> O	1.90	2.51	2.54	2.29	2.46	2.43	2.40	2.36	2.31	2.47	2.59	2.42	2.41	2.35	2.41	2.43	2.18	2.30	2.26	2.28	2.41
Cr <sub>2</sub> O <sub>3</sub>	0.12	0.03	0.10	0.00	0.00	0.00	0.03	0.03	0.01	0.00	0.09	0.01	0.00	0.05	0.00	0.00	0.05	0.00	0.00	0.07	0.08
MnO	0.00	0.02	0.00	0.00	0.00	0.11	0.03	0.00	0.07	0.00	0.03	0.07	0.12	0.00	0.00	0.09	0.03	0.06	0.00	0.02	0.00
MgO	5.57	4.17	3.26	3.79	3.39	3.52	3.65	3.74	3.76	3.76	3.72	3.49	3.46	3.24	3.24	3.12	4.49	4.60	4.74	4.72	4.47
B <sub>2</sub> O <sub>3</sub> *	10.21	10.30	10.21	10.27	10.19	10.12	10.13	10.13	10.15	10.18	10.20	10.10	10.07	10.11	10.14	9.94	10.28	10.24	10.25	10.18	10.28
Total	95.33	96.66	96.47	96.29	95.96	95.40	95.29	95.11	95.15	95.81	96.15	95.45	95.20	95.52	95.90	94.56	95.83	95.42	95.39	94.86	95.64
Si(T)	5.99	6.00	6.00	6.00	6.00	6.00	6.00	6.00	6.00	5.98	6.00	5.96	5.91	5.95	5.95	5.91	6.00	6.00	6.00	6.00	6.00
Al(T)	0.01	0.00	0.00	0.00	0.00	0.00	0.00	0.00	0.00	0.02	0.00	0.04	0.09	0.05	0.05	0.09	0.00	0.00	0.00	0.00	0.00
B(T)	3.00	3.00	3.00	3.00	3.00	3.00	3.00	3.00	3.00	3.00	3.00	3.00	3.00	3.00	3.00	3.00	3.00	3.00	3.00	3.00	3.00
Al(Z)	5.83	5.98	5.95	5.93	6.00	6.00	5.98	6.00	6.00	6.00	5.96	5.97	5.99	6.00	6.00	5.90	6.00	6.00	6.00	6.00	6.00
Al(Y)	0.00	0.00	0.00	0.00	0.01	0.01	0.00	0.04	0.05	0.00	0.00	0.00	0.00	0.00	0.02	0.00	0.01	0.00	0.03	0.00	0.03
Ti(Y)	0.10	0.09	0.10	0.12	0.10	0.07	0.09	0.09	0.08	0.10	0.10	0.09	0.09	0.09	0.08	0.11	0.14	0.12	0.12	0.11	0.14
Cr(Y)	0.02	0.00	0.01	0.00	0.00	0.00	0.00	0.00	0.00	0.00	0.01	0.00	0.00	0.01	0.00	0.00	0.01	0.00	0.00	0.01	0.01
Fe(Y)	1.59	1.83	2.04	1.86	1.97	1.97	1.94	1.87	1.85	1.91	1.92	2.01	2.02	2.04	2.06	2.16	1.62	1.63	1.58	1.60	1.58
Mn(Y)	0.00	0.00	0.00	0.00	0.00	0.02	0.00	0.00	0.01	0.00	0.00	0.01	0.02	0.00	0.00	0.01	0.00	0.01	0.00	0.00	0.00
Mg(Y)	1.42	1.06	0.83	0.97	0.87	0.91	0.94	0.96	0.97	0.96	0.95	0.90	0.89	0.83	0.83	0.81	1.14	1.18	1.21	1.21	1.14
K(X)	0.01	0.01	0.01	0.02	0.01	0.02	0.01	0.02	0.01	0.01	0.01	0.01	0.02	0.01	0.01	0.02	0.02	0.01	0.01	0.01	0.01
Ca(X)	0.23	0.08	0.06	0.08	0.05	0.06	0.05	0.06	0.04	0.06	0.05	0.06	0.06	0.06	0.05	0.07	0.10	0.09	0.10	0.11	0.09
Na(X)	0.63	0.82	0.84	0.75	0.81	0.81	0.80	0.78	0.77	0.82	0.85	0.81	0.81	0.78	0.80	0.82	0.71	0.76	0.74	0.75	0.79
X vacancies	0.13	0.10	0.09	0.15	0.12	0.12	0.14	0.14	0.18	0.12	0.08	0.12	0.12	0.14	0.14	0.10	0.18	0.14	0.14	0.12	0.11
X <sub>Mg</sub>	0.47	0.37	0.29	0.34	0.31	0.31	0.33	0.34	0.34	0.33	0.33	0.31	0.31	0.29	0.29	0.27	0.41	0.42	0.43	0.43	0.42

Note: Atomic proportions based on ΣT+Z+Y cations = 15. X<sub>Mg</sub> = Mg/(Fe<sup>2+</sup> + Mg).

\* B<sub>2</sub>O<sub>3</sub> calculated assuming B to be 3 atoms per formula unit.

# composition used in C-space

Table 5.4.3a: Representative EPMA analysis of tourmaline(continued).

Generation	Gen I	Gen I																				
Sample no.	PP 73a	PP73c																				
Point	34 / 1	38 / 1	40 / 1	1 / 1	1 / 2	1 / 3	1 / 4	1 / 5	1 / 6	1 / 7	2 / 3	2 / 4	2 / 5	2 / 6	2 / 7	2 / 8	2 / 9	2 / 10	2 / 11	2 / 12	3 / 1	
Core/Rim	rim	rim	rim																			
Al <sub>2</sub> O <sub>3</sub>	30.21	29.51	30.06	30.97	30.92	30.53	29.98	30.25	30.34	29.97	30.35	30.14	29.79	29.72	29.70	29.58	29.07	29.54	29.56	29.81	30.71	
FeO	10.60	11.47	9.12	10.84	10.44	10.67	10.67	10.58	10.40	11.10	8.86	9.11	9.86	10.50	10.67	11.12	11.39	11.42	11.60	11.55	9.53	
TiO <sub>2</sub>	0.63	0.86	1.14	0.27	0.37	0.55	0.37	0.42	0.42	0.42	0.97	1.08	1.06	1.10	1.23	1.07	0.79	0.87	0.58	0.69	0.52	
SiO <sub>2</sub>	36.37	35.62	36.51	36.34	35.91	35.92	36.11	35.84	36.19	35.75	35.80	36.34	36.04	35.84	36.19	35.76	35.69	35.60	35.65	35.38	36.03	
K <sub>2</sub> O	0.05	0.02	0.09	0.06	0.06	0.04	0.05	0.00	0.02	0.03	0.07	0.04	0.03	0.03	0.04	0.10	0.08	0.07	0.04	0.02	0.07	
CaO	0.16	0.68	0.23	0.12	0.16	0.22	0.20	0.13	0.24	0.30	0.27	0.25	0.27	0.18	0.18	0.24	0.29	0.20	0.26	0.37	0.41	
Na <sub>2</sub> O	2.52	2.22	2.42	2.67	2.44	2.57	2.73	2.45	2.54	2.45	2.42	2.30	2.42	2.62	2.64	2.58	2.58	2.72	2.59	2.47	2.31	
Cr <sub>2</sub> O <sub>3</sub>	0.00	0.01	0.00	0.00	0.20	0.00	0.00	0.03	0.02	0.00	0.00	0.03	0.02	0.00	0.00	0.00	0.00	0.11	0.05	0.04	0.13	
MnO	0.02	0.03	0.03	0.07	0.00	0.10	0.00	0.02	0.00	0.00	0.00	0.04	0.05	0.00	0.07	0.00	0.00	0.01	0.04	0.00	0.00	
MgO	5.31	4.86	5.81	5.06	4.95	5.27	5.68	5.22	5.44	5.28	6.16	5.81	5.90	5.61	5.54	5.42	5.49	5.35	5.22	5.20	5.68	
B <sub>2</sub> O <sub>3</sub> *	10.39	10.24	10.41	10.44	10.35	10.37	10.36	10.28	10.37	10.28	10.35	10.38	10.36	10.34	10.40	10.32	10.25	10.30	10.27	10.26	10.38	
Total	96.26	95.52	95.82	96.84	95.80	96.24	96.15	95.22	95.98	95.58	95.25	95.52	95.80	95.94	96.66	96.19	95.63	96.19	95.86	95.79	95.77	
Si(T)	6.00	6.00	6.00	6.00	6.00	6.00	6.00	6.00	6.00	6.00	6.00	6.00	6.00	6.00	6.00	6.00	6.00	6.00	6.00	6.00	6.00	
Al(T)	0.00	0.00	0.00	0.00	0.00	0.00	0.00	0.00	0.00	0.00	0.00	0.00	0.00	0.00	0.00	0.00	0.00	0.00	0.00	0.00	0.00	
B(T)	3.00	3.00	3.00	3.00	3.00	3.00	3.00	3.00	3.00	3.00	3.00	3.00	3.00	3.00	3.00	3.00	3.00	3.00	3.00	3.00	3.00	
Al(Z)	5.95	5.90	5.91	6.00	6.00	6.00	5.93	6.00	5.99	5.97	6.00	5.94	5.89	5.89	5.85	5.87	5.81	5.87	5.90	5.94	6.00	
Al(Y)	0.00	0.00	0.00	0.07	0.12	0.03	0.00	0.03	0.00	0.00	0.00	0.00	0.00	0.00	0.00	0.00	0.00	0.00	0.00	0.00	0.06	
Ti(Y)	0.08	0.11	0.14	0.03	0.05	0.07	0.05	0.05	0.05	0.05	0.12	0.14	0.13	0.14	0.16	0.14	0.10	0.11	0.07	0.09	0.07	
Cr(Y)	0.00	0.00	0.00	0.00	0.03	0.00	0.00	0.00	0.00	0.00	0.00	0.00	0.00	0.00	0.00	0.00	0.00	0.01	0.01	0.01	0.02	
Fe(Y)	1.51	1.65	1.30	1.53	1.48	1.51	1.52	1.51	1.48	1.58	1.26	1.30	1.40	1.49	1.51	1.58	1.63	1.62	1.65	1.64	1.35	
Mn(Y)	0.00	0.00	0.00	0.01	0.00	0.01	0.00	0.00	0.00	0.00	0.00	0.01	0.01	0.00	0.01	0.00	0.00	0.00	0.01	0.00	0.00	
Mg(Y)	1.35	1.25	1.48	1.27	1.25	1.33	1.44	1.33	1.38	1.34	1.56	1.48	1.49	1.42	1.40	1.37	1.40	1.35	1.33	1.31	1.43	
K(X)	0.01	0.00	0.02	0.01	0.01	0.01	0.01	0.00	0.00	0.01	0.01	0.01	0.01	0.01	0.01	0.02	0.02	0.02	0.01	0.00	0.01	
Ca(X)	0.03	0.12	0.04	0.02	0.03	0.04	0.04	0.02	0.04	0.05	0.05	0.04	0.05	0.03	0.03	0.04	0.05	0.04	0.05	0.07	0.07	
Na(X)	0.82	0.73	0.78	0.86	0.79	0.83	0.89	0.80	0.83	0.80	0.79	0.75	0.79	0.85	0.85	0.84	0.85	0.89	0.85	0.81	0.75	
X vacancies	0.14	0.14	0.16	0.10	0.16	0.12	0.07	0.17	0.13	0.14	0.15	0.20	0.16	0.11	0.10	0.09	0.08	0.06	0.09	0.12	0.16	
X <sub>Mg</sub>	0.47	0.43	0.53	0.45	0.46	0.47	0.49	0.47	0.48	0.46	0.55	0.53	0.52	0.49	0.48	0.46	0.46	0.45	0.45	0.45	0.52	

Note: Atomic proportions based on ΣT+Z+Y cations = 15. X<sub>Mg</sub> = Mg/(Fe<sup>2+</sup> + Mg).

\* B<sub>2</sub>O<sub>3</sub> calculated assuming B to be 3 atoms per formula unit.

Table 5.4.3a: Representative EPMA analysis of tourmaline(continued).

Generation	Gen I	Gen I	Gen I	Gen I	Gen I	Gen I	Gen I	Gen I	Gen I	Gen I	Gen I	Gen I	Gen I	Gen I	Gen I	Gen I	Gen I	Gen I	Gen I	Gen I	Gen I
Sample no.	PP73c	PP73c	PP73c	PP73c	PP73c	PP73c	PP73c	PP73c	PP73c	PP73c	PP73c	PP73c	PP73c	PP73c	PP73c	PP73c	PP73c	PP73c	PP73c	PP73c	PP73c
Point	4 / 1	7 / 1	8 / 11	8 / 12	8 / 13	8 / 14	8 / 15	8 / 16	8 / 17	8 / 18	8 / 19	8 / 20	8 / 21	8 / 22	9 / 9	9 / 10	9 / 11	9 / 12	9 / 13	9 / 14	9 / 15
Core/Rim	rim	rim	rim	rim	rim	rim	rim	rim	rim	rim	rim	rim	rim	rim	rim	rim	rim	rim	rim	rim	rim
Al <sub>2</sub> O <sub>3</sub>	30.02	30.27	30.70	30.97	30.83	31.05	30.65	30.97	31.19	31.18	31.16	31.01	31.02	30.96	29.92	30.13	29.92	30.20	29.92	29.03	30.31
FeO	9.87	9.62	10.12	9.81	9.76	9.89	9.73	9.80	9.93	10.29	9.82	9.58	9.75	9.19	10.74	9.14	9.28	9.79	10.24	9.68	10.24
TiO <sub>2</sub>	1.02	0.84	0.99	0.64	0.63	0.69	0.89	0.84	0.69	0.98	0.74	1.14	0.89	0.91	1.04	1.19	1.12	0.83	0.95	0.85	0.96
SiO <sub>2</sub>	35.85	35.92	35.77	35.48	35.79	35.79	35.55	35.41	35.46	35.47	35.48	35.55	35.71	35.43	35.60	36.00	35.41	35.64	35.75	34.37	35.86
K <sub>2</sub> O	0.01	0.04	0.02	0.02	0.04	0.00	0.05	0.08	0.03	0.04	0.02	0.07	0.05	0.05	0.07	0.07	0.08	0.03	0.08	0.04	0.02
CaO	0.60	0.56	0.61	0.68	0.64	0.66	0.63	0.66	0.58	0.69	0.57	0.66	0.65	0.71	0.82	0.72	0.77	0.67	0.64	0.56	0.59
Na <sub>2</sub> O	2.29	2.29	2.28	2.18	2.11	2.25	2.22	2.14	2.00	2.18	2.13	2.08	2.12	2.17	2.17	2.18	2.22	2.27	2.32	2.28	2.18
Cr <sub>2</sub> O <sub>3</sub>	0.03	0.00	0.00	0.12	0.16	0.11	0.00	0.09	0.00	0.00	0.00	0.02	0.04	0.06	0.07	0.00	0.00	0.01	0.07	0.06	0.00
MnO	0.09	0.05	0.00	0.14	0.00	0.00	0.00	0.00	0.00	0.00	0.00	0.01	0.07	0.11	0.03	0.07	0.01	0.01	0.04	0.00	0.00
MgO	5.82	5.66	5.27	5.40	5.21	5.16	5.26	5.18	5.06	4.75	5.01	5.19	5.32	5.34	5.36	6.10	6.01	5.69	5.47	5.01	5.22
B <sub>2</sub> O <sub>3</sub> *	10.37	10.35	10.39	10.35	10.34	10.39	10.31	10.33	10.32	10.36	10.32	10.36	10.39	10.33	10.33	10.41	10.29	10.32	10.33	9.91	10.34
Total	95.97	95.60	96.15	95.79	95.51	95.99	95.29	95.50	95.26	95.94	95.25	95.67	96.01	95.26	96.15	96.01	95.11	95.46	95.81	91.79	95.72
Si(T)	6.00	6.00	6.00	5.98	6.00	6.00	6.00	6.00	6.00	6.00	6.00	6.00	6.00	6.00	6.00	6.00	6.00	6.00	6.00	6.00	6.00
Al(T)	0.00	0.00	0.00	0.02	0.00	0.00	0.00	0.00	0.00	0.00	0.00	0.00	0.00	0.00	0.00	0.00	0.00	0.00	0.00	0.00	0.00
B(T)	3.00	3.00	3.00	3.00	3.00	3.00	3.00	3.00	3.00	3.00	3.00	3.00	3.00	3.00	3.00	3.00	3.00	3.00	3.00	3.00	3.00
Al(Z)	5.93	5.99	6.00	6.00	6.00	6.00	6.00	6.00	6.00	6.00	6.00	6.00	6.00	6.00	5.91	5.93	5.93	5.99	5.93	6.00	6.00
Al(Y)	0.00	0.00	0.03	0.08	0.10	0.11	0.07	0.09	0.16	0.11	0.16	0.08	0.08	0.10	0.00	0.00	0.00	0.00	0.00	0.00	0.00
Ti(Y)	0.13	0.11	0.13	0.08	0.08	0.09	0.11	0.11	0.09	0.12	0.09	0.14	0.11	0.12	0.13	0.15	0.14	0.11	0.12	0.11	0.12
Cr(Y)	0.00	0.00	0.00	0.02	0.02	0.01	0.00	0.01	0.00	0.00	0.00	0.00	0.01	0.01	0.01	0.00	0.00	0.00	0.01	0.01	0.00
Fe(Y)	1.40	1.37	1.43	1.38	1.39	1.40	1.39	1.39	1.41	1.46	1.40	1.36	1.37	1.31	1.52	1.29	1.32	1.39	1.46	1.44	1.46
Mn(Y)	0.01	0.01	0.00	0.02	0.00	0.00	0.00	0.00	0.00	0.00	0.00	0.00	0.01	0.02	0.00	0.01	0.00	0.00	0.01	0.00	0.00
Mg(Y)	1.47	1.44	1.33	1.36	1.32	1.30	1.34	1.31	1.28	1.20	1.27	1.31	1.34	1.35	1.35	1.54	1.53	1.44	1.39	1.33	1.33
K(X)	0.00	0.01	0.00	0.00	0.01	0.00	0.01	0.02	0.01	0.01	0.00	0.01	0.01	0.01	0.02	0.01	0.02	0.01	0.02	0.01	0.00
Ca(X)	0.11	0.10	0.11	0.12	0.12	0.12	0.11	0.12	0.10	0.12	0.10	0.12	0.12	0.13	0.15	0.13	0.14	0.12	0.12	0.11	0.11
Na(X)	0.74	0.75	0.74	0.71	0.69	0.73	0.72	0.70	0.65	0.71	0.70	0.68	0.69	0.71	0.71	0.71	0.73	0.74	0.76	0.77	0.71
X vacancies	0.15	0.15	0.15	0.16	0.19	0.15	0.15	0.17	0.24	0.16	0.20	0.19	0.19	0.15	0.13	0.15	0.12	0.13	0.11	0.11	0.18
X <sub>Mg</sub>	0.51	0.51	0.48	0.50	0.49	0.48	0.49	0.49	0.48	0.45	0.48	0.49	0.49	0.51	0.47	0.54	0.54	0.51	0.49	0.48	0.48

Note: Atomic proportions based on  $\Sigma T+Z+Y$  cations = 15.  $X_{Mg} = Mg/(Fe^{2+} + Mg)$ .

\* B<sub>2</sub>O<sub>3</sub> calculated assuming B to be 3 atoms per formula unit.

Table 5.4.3a: Representative EPMA analysis of tourmaline(continued).

Generation	Gen I	Gen II																			
Sample no.	PP73c	PP 7																			
Point	9 / 16	9 / 17	9 / 18	9 / 19	9 / 20	9 / 21	9 / 22	9 / 23	9 / 24	9 / 25	9 / 26	9 / 27	9 / 28	9 / 29	32 / 3	32 / 4	32 / 5	32 / 7	32 / 8	33 / 2	33 / 3
Core/Rim	rim	core																			
Al <sub>2</sub> O <sub>3</sub>	30.67	30.01	30.05	30.24	30.64	30.21	30.88	30.00	30.21	30.25	30.27	30.17	29.76	30.10	30.47	31.27	30.77	30.59	30.66	30.65	30.93
FeO	10.43	10.30	10.48	10.26	10.04	10.01	9.99	9.89	10.18	9.85	9.82	10.12	9.93	9.92	7.05	7.02	7.47	7.31	7.87	7.39	7.19
TiO <sub>2</sub>	0.92	0.94	0.97	1.01	0.83	0.63	0.70	0.92	0.78	0.72	0.73	0.74	0.84	0.84	0.85	0.97	1.11	1.11	1.14	1.12	0.90
SiO <sub>2</sub>	35.68	35.77	35.48	35.75	35.42	35.92	35.70	35.89	35.81	35.59	36.17	36.04	35.58	35.78	36.17	35.84	36.13	36.08	35.99	35.80	35.68
K <sub>2</sub> O	0.10	0.09	0.05	0.07	0.06	0.04	0.05	0.05	0.05	0.07	0.07	0.07	0.08	0.06	0.05	0.02	0.03	0.03	0.01	0.05	0.03
CaO	0.61	0.61	0.57	0.65	0.62	0.54	0.62	0.67	0.60	0.61	0.57	0.45	0.64	0.60	1.07	1.10	1.09	1.22	1.12	1.47	1.52
Na <sub>2</sub> O	2.39	2.21	2.33	2.24	2.36	2.28	2.30	2.26	2.39	2.32	2.45	2.42	2.29	2.04	2.02	1.84	1.88	1.93	1.77	1.64	
Cr <sub>2</sub> O <sub>3</sub>	0.00	0.00	0.04	0.00	0.00	0.00	0.00	0.05	0.00	0.09	0.00	0.00	0.11	0.00	0.07	0.04	0.00	0.02	0.08	0.00	0.04
MnO	0.00	0.06	0.00	0.00	0.00	0.00	0.09	0.00	0.18	0.09	0.09	0.01	0.07	0.02	0.00	0.01	0.12	0.07	0.00	0.05	0.06
MgO	4.97	5.05	5.12	5.20	5.33	5.17	5.39	5.49	5.38	5.32	5.44	5.53	5.33	5.48	7.34	7.02	7.12	7.18	6.82	7.37	7.24
B <sub>2</sub> O <sub>3</sub> *	10.36	10.28	10.27	10.33	10.32	10.29	10.38	10.33	10.34	10.29	10.37	10.36	10.25	10.31	10.46	10.49	10.51	10.49	10.48	10.49	10.46
Total	96.13	95.32	95.36	95.75	95.62	95.09	96.10	95.55	95.92	95.27	95.85	95.94	95.01	95.40	95.57	95.80	96.19	95.98	96.10	96.16	95.69
Si(T)	6.00	6.00	6.00	6.00	6.00	6.00	6.00	6.00	6.00	6.00	6.00	6.00	6.00	6.00	6.00	5.99	6.00	6.00	6.00	5.97	5.97
Al(T)	0.00	0.00	0.00	0.00	0.00	0.00	0.00	0.00	0.00	0.00	0.00	0.00	0.00	0.00	0.00	0.01	0.00	0.00	0.00	0.03	0.03
B(T)	3.00	3.00	3.00	3.00	3.00	3.00	3.00	3.00	3.00	3.00	3.00	3.00	3.00	3.00	3.00	3.00	3.00	3.00	3.00	3.00	3.00
Al(Z)	6.00	5.98	5.99	5.99	6.00	6.00	6.00	5.95	5.98	6.00	5.98	5.96	5.95	5.98	5.96	6.00	5.96	5.95	5.96	5.91	5.98
Al(Y)	0.04	0.00	0.00	0.00	0.04	0.01	0.06	0.00	0.00	0.02	0.00	0.00	0.00	0.00	0.00	0.04	0.00	0.00	0.00	0.00	0.00
Ti(Y)	0.12	0.12	0.12	0.13	0.11	0.08	0.09	0.12	0.10	0.09	0.09	0.09	0.11	0.11	0.11	0.12	0.14	0.14	0.14	0.14	0.11
Cr(Y)	0.00	0.00	0.01	0.00	0.00	0.00	0.00	0.01	0.00	0.01	0.00	0.00	0.01	0.00	0.01	0.01	0.00	0.00	0.01	0.00	0.01
Fe(Y)	1.48	1.48	1.50	1.46	1.42	1.44	1.41	1.42	1.45	1.41	1.40	1.44	1.43	1.42	0.99	0.98	1.04	1.02	1.10	1.03	1.01
Mn(Y)	0.00	0.01	0.00	0.00	0.00	0.00	0.01	0.00	0.03	0.01	0.01	0.00	0.01	0.00	0.00	0.00	0.02	0.01	0.00	0.01	0.01
Mg(Y)	1.26	1.30	1.31	1.32	1.35	1.33	1.35	1.40	1.36	1.36	1.39	1.40	1.37	1.40	1.84	1.75	1.77	1.79	1.70	1.83	1.80
K(X)	0.02	0.02	0.01	0.02	0.01	0.01	0.01	0.01	0.01	0.02	0.01	0.01	0.02	0.01	0.01	0.00	0.01	0.01	0.00	0.01	0.01
Ca(X)	0.11	0.11	0.10	0.12	0.11	0.10	0.11	0.12	0.11	0.11	0.10	0.08	0.12	0.11	0.19	0.20	0.19	0.22	0.20	0.26	0.27
Na(X)	0.78	0.72	0.76	0.73	0.77	0.75	0.75	0.74	0.78	0.78	0.75	0.80	0.80	0.75	0.66	0.65	0.59	0.60	0.62	0.57	0.53
X vacancies	0.09	0.15	0.12	0.14	0.11	0.15	0.13	0.13	0.10	0.09	0.13	0.11	0.07	0.13	0.14	0.15	0.21	0.17	0.18	0.16	0.20
X <sub>Mg</sub>	0.46	0.47	0.47	0.47	0.49	0.48	0.49	0.50	0.49	0.49	0.50	0.49	0.49	0.50	0.65	0.64	0.63	0.64	0.61	0.64	0.64

Note: Atomic proportions based on  $\Sigma T+Z+Y$  cations = 15.  $X_{Mg} = Mg/(Fe^{2+} + Mg)$ .

\* B<sub>2</sub>O<sub>3</sub> calculated assuming B to be 3 atoms per formula unit.

Table 5.4.3a: Representative EPMA analysis of tourmaline(continued).

Generati on	Gen II	Gen II	Gen II	Gen II	Gen II	Gen II	Gen II	Gen II	Gen II	Gen II	Gen II											
Sample no.	PP 7	PP 7	PP 7	PP 7	PP 15	PP 15	PP 15	PP 15	PP 15	PP 15	PP 15	PP 15	PP 15	PP 15	PP 15							
Point	33 / 4	33 / 5	33 / 7	33 / 8	11 / 1	12 / 1	13 / 1	14 / 1	17 / 1	19 / 1	22 / 10	22 / 11	22 / 12	22 / 13	22 / 14	22 / 15	23 / 1	23 / 2	23 / 3	23 / 4	23 / 5	
Core/Rim	core	core	core	core	core	core	core	core	core	core	core	core										
Al <sub>2</sub> O <sub>3</sub>	31.22	31.48	31.80	31.93	30.17	30.93	30.32	31.88	32.07	33.40	31.99	32.70	32.79	33.24	33.06	33.38	31.86	32.13	31.95	31.78	31.91	
FeO	7.23	7.34	7.04	7.63	9.89	8.32	9.05	7.66	7.56	6.71	7.30	7.32	7.26	7.07	7.03	7.02	7.53	7.58	7.19	6.99	7.29	
TiO <sub>2</sub>	0.66	0.60	0.90	0.82	0.57	0.67	0.98	0.59	0.66	0.13	0.62	0.39	0.30	0.17	0.14	0.22	0.85	0.68	0.52	0.78	0.60	
SiO <sub>2</sub>	35.61	35.75	38.05	37.99	36.00	36.50	35.92	36.41	36.15	37.18	36.46	37.32	37.06	37.20	37.04	37.33	36.19	35.93	36.46	36.11	36.35	
K <sub>2</sub> O	0.02	0.05	0.06	0.03	0.07	0.04	0.01	0.08	0.03	0.06	0.03	0.03	0.02	0.06	0.06	0.01	0.05	0.06	0.07	0.06	0.08	
CaO	1.46	1.39	1.03	0.88	0.58	0.51	1.51	0.72	1.10	0.49	0.85	0.63	0.57	0.47	0.42	0.47	0.98	0.96	1.07	1.09	1.10	
Na <sub>2</sub> O	1.66	1.69	1.68	2.18	2.19	2.45	1.77	2.12	2.13	1.92	2.07	2.04	2.13	2.03	1.94	1.97	2.13	2.11	2.02	2.00	2.04	
Cr <sub>2</sub> O <sub>3</sub>	0.00	0.01	0.06	0.00	0.00	0.06	0.14	0.00	0.04	0.00	0.08	0.00	0.02	0.07	0.00	0.09	0.00	0.00	0.00	0.04	0.00	
MnO	0.08	0.08	0.00	0.06	0.01	0.03	0.02	0.00	0.02	0.00	0.03	0.00	0.05	0.00	0.08	0.00	0.03	0.05	0.03	0.00	0.02	
MgO	6.99	7.17	6.44	6.93	5.47	6.36	6.11	6.47	6.66	6.31	6.52	6.50	6.26	6.17	6.20	6.48	6.70	6.61	6.60	6.63	6.61	
B <sub>2</sub> O <sub>3</sub> *	10.43	10.50	10.78	10.88	10.31	10.51	10.43	10.56	10.60	10.71	10.58	10.74	10.68	10.71	10.66	10.78	10.60	10.57	10.58	10.53	10.58	
Total	95.36	96.06	97.84	99.33	95.26	96.38	96.26	96.49	97.02	96.91	96.53	97.67	97.14	97.19	96.63	97.75	96.92	96.68	96.49	96.01	96.58	
Si(T)	5.97	5.94	6.00	6.00	6.00	6.00	6.00	6.00	5.98	6.00	6.00	6.00	6.00	6.00	6.00	6.00	5.99	5.95	6.00	6.00	6.00	
Al(T)	0.03	0.06	0.00	0.00	0.00	0.00	0.00	0.00	0.02	0.00	0.00	0.00	0.00	0.00	0.00	0.00	0.01	0.05	0.00	0.00	0.00	
B(T)	3.00	3.00	3.00	3.00	3.00	3.00	3.00	3.00	3.00	3.00	3.00	3.00	3.00	3.00	3.00	3.00	3.00	3.00	3.00	3.00	3.00	
Al(Z)	6.00	6.00	6.00	6.00	5.99	6.00	5.93	6.00	6.00	6.00	6.00	6.00	6.00	6.00	6.00	6.00	6.00	6.00	6.00	6.00	6.00	
Al(Y)	0.06	0.05	0.04	0.01	0.00	0.03	0.00	0.17	0.11	0.39	0.17	0.23	0.28	0.35	0.35	0.34	0.09	0.13	0.17	0.14	0.15	
Ti(Y)	0.08	0.08	0.11	0.10	0.07	0.08	0.12	0.07	0.08	0.02	0.08	0.05	0.04	0.02	0.02	0.03	0.11	0.08	0.06	0.10	0.07	
Cr(Y)	0.00	0.00	0.01	0.00	0.00	0.01	0.02	0.00	0.01	0.00	0.01	0.00	0.00	0.01	0.00	0.01	0.00	0.00	0.00	0.01	0.00	
Fe(Y)	1.01	1.02	0.99	1.04	1.42	1.17	1.28	1.07	1.05	0.93	1.02	1.01	1.01	0.98	0.98	0.96	1.04	1.05	1.00	0.98	1.02	
Mn(Y)	0.01	0.01	0.00	0.01	0.00	0.00	0.00	0.00	0.00	0.00	0.00	0.00	0.01	0.00	0.01	0.00	0.00	0.01	0.00	0.00	0.00	
Mg(Y)	1.75	1.78	1.61	1.69	1.40	1.60	1.54	1.60	1.64	1.55	1.62	1.60	1.55	1.52	1.53	1.58	1.65	1.63	1.64	1.65	1.64	
K(X)	0.00	0.01	0.01	0.01	0.02	0.01	0.00	0.02	0.01	0.01	0.01	0.01	0.00	0.01	0.01	0.00	0.01	0.01	0.01	0.01	0.02	
Ca(X)	0.26	0.25	0.18	0.15	0.10	0.09	0.27	0.13	0.19	0.09	0.15	0.11	0.10	0.08	0.07	0.08	0.17	0.17	0.19	0.19	0.19	
Na(X)	0.54	0.54	0.53	0.67	0.72	0.79	0.57	0.68	0.68	0.60	0.66	0.64	0.67	0.64	0.61	0.62	0.68	0.67	0.64	0.64	0.65	
X vacancies	0.20	0.20	0.28	0.17	0.16	0.12	0.16	0.18	0.12	0.30	0.19	0.25	0.23	0.27	0.30	0.30	0.14	0.15	0.15	0.15	0.14	
X <sub>Mg</sub>	0.63	0.64	0.62	0.62	0.50	0.58	0.55	0.60	0.61	0.63	0.61	0.61	0.61	0.61	0.61	0.62	0.61	0.61	0.62	0.63	0.62	

Note: Atomic proportions based on ΣT+Z+Y cations = 15. X<sub>Mg</sub> = Mg/(Fe<sup>2+</sup> + Mg).

\* B<sub>2</sub>O<sub>3</sub> calculated assuming B to be 3 atoms per formula unit.

Table 5.4.3a: Representative EPMA analysis of tourmaline(continued).

Generation	Gen II	Gen II	Gen II	Gen II	Gen II	Gen II	Gen II	Gen II	Gen II	Gen II	Gen II	Gen II	Gen II	Gen II	Gen II	Gen II	Gen II				
Sample no.	PP 15	PP 15	PP60	PP 7	PP 7																
Point	23 / 6	23 / 7	23 / 8	23 / 9	23 / 10	23 / 11	32 / 1	33 / 1	45 / 1	48 / 1	50 / 1	54 / 1	58 / 1	26 / 1	28 / 1	29 / 1	30 / 1	31 / 1	33 / 1	33 / 18	33 / 19
Core/Rim	core	core	core	core	core	core	core	core	core	core	core	core	core	rim	rim						
Al <sub>2</sub> O <sub>3</sub>	31.54	31.85	31.60	31.45	31.69	30.86	28.45	29.23	29.52	28.86	29.80	29.12	28.44	30.74	30.95	31.09	30.79	31.10	30.58	30.34	31.03
FeO	7.32	7.45	7.25	7.42	7.32	7.16	9.67	8.71	9.16	9.08	9.62	9.13	9.55	6.68	6.96	6.18	6.95	6.65	6.75	6.44	7.02
TiO <sub>2</sub>	0.64	0.72	0.66	0.60	0.60	0.40	1.40	1.29	0.93	1.11	1.26	1.08	1.37	0.76	0.98	0.95	1.01	0.78	0.89	1.02	1.06
SiO <sub>2</sub>	36.43	36.14	36.30	36.01	36.22	35.69	35.59	35.92	35.99	35.39	36.05	35.83	35.74	36.74	36.92	36.66	36.21	36.14	35.44	36.18	36.34
K <sub>2</sub> O	0.02	0.06	0.01	0.05	0.02	0.09	0.06	0.05	0.04	0.07	0.11	0.09	0.05	0.01	0.05	0.03	0.08	0.00	0.05	0.05	0.01
CaO	0.94	1.06	0.91	1.00	0.99	1.05	1.61	1.58	1.20	1.44	0.83	1.45	1.36	1.40	1.58	1.39	1.50	0.98	1.60	1.45	1.30
Na <sub>2</sub> O	2.16	1.97	2.23	2.10	2.09	1.93	2.03	1.93	2.18	2.10	2.30	2.13	2.03	1.81	1.97	1.83	1.77	1.89	1.77	1.94	1.81
Cr <sub>2</sub> O <sub>3</sub>	0.00	0.00	0.04	0.00	0.00	0.17	0.12	0.04	0.00	0.03	0.00	0.03	0.00	0.00	0.04	0.03	0.14	0.00	0.05	0.01	0.05
MnO	0.00	0.05	0.05	0.01	0.03	0.00	0.00	0.03	0.00	0.04	0.02	0.03	0.07	0.00	0.00	0.03	0.00	0.02	0.00	0.07	0.00
MgO	6.71	6.83	6.91	6.55	6.69	6.54	7.39	7.49	7.49	7.64	6.73	7.77	7.14	7.63	7.68	7.86	7.36	7.43	7.44	8.07	7.31
B <sub>2</sub> O <sub>3</sub> *	10.55	10.58	10.57	10.47	10.53	10.32	10.39	10.46	10.48	10.36	10.49	10.47	10.35	10.58	10.70	10.63	10.54	10.49	10.39	10.53	10.57
Total	96.31	96.71	96.53	95.66	96.18	94.21	96.71	96.73	96.99	96.12	97.21	97.13	96.10	96.35	97.83	96.68	96.35	95.48	94.96	96.10	96.50
Si(T)	6.00	5.98	6.00	6.00	6.00	6.00	5.97	6.00	5.98	5.95	5.99	5.96	6.00	6.00	6.00	6.00	6.00	6.00	5.98	6.00	6.00
Al(T)	0.00	0.02	0.00	0.00	0.00	0.00	0.03	0.00	0.02	0.05	0.01	0.04	0.00	0.00	0.00	0.00	0.00	0.00	0.02	0.00	0.00
B(T)	3.00	3.00	3.00	3.00	3.00	3.00	3.00	3.00	3.00	3.00	3.00	3.00	3.00	3.00	3.00	3.00	3.00	3.00	3.00	3.00	3.00
Al(Z)	6.00	6.00	6.00	6.00	6.00	6.00	5.56	5.68	5.73	5.64	5.79	5.64	5.63	5.95	5.91	5.98	5.95	6.00	5.95	5.87	5.98
Al(Y)	0.12	0.10	0.09	0.13	0.13	0.12	0.00	0.00	0.00	0.00	0.00	0.00	0.00	0.00	0.00	0.00	0.00	0.05	0.00	0.00	0.00
Ti(Y)	0.08	0.09	0.08	0.08	0.08	0.05	0.18	0.16	0.12	0.14	0.16	0.14	0.17	0.09	0.12	0.12	0.13	0.10	0.11	0.13	0.13
Cr(Y)	0.00	0.00	0.01	0.00	0.00	0.02	0.02	0.01	0.00	0.00	0.00	0.00	0.00	0.00	0.01	0.00	0.02	0.00	0.01	0.00	0.01
Fe(Y)	1.02	1.03	1.01	1.04	1.02	1.03	1.36	1.22	1.27	1.28	1.34	1.27	1.35	0.94	0.96	0.86	0.97	0.93	0.95	0.90	0.98
Mn(Y)	0.00	0.01	0.01	0.00	0.00	0.00	0.00	0.00	0.00	0.01	0.00	0.00	0.01	0.00	0.00	0.00	0.00	0.00	0.00	0.01	0.00
Mg(Y)	1.67	1.68	1.71	1.64	1.66	1.67	1.85	1.86	1.85	1.91	1.67	1.92	1.80	1.90	1.89	1.94	1.83	1.85	1.87	2.00	1.81
K(X)	0.00	0.01	0.00	0.01	0.00	0.02	0.01	0.01	0.01	0.01	0.02	0.02	0.01	0.00	0.01	0.01	0.02	0.00	0.01	0.01	0.00
Ca(X)	0.17	0.19	0.16	0.18	0.17	0.19	0.29	0.28	0.21	0.26	0.15	0.26	0.24	0.25	0.27	0.24	0.26	0.17	0.29	0.26	0.23
Na(X)	0.69	0.63	0.71	0.68	0.67	0.63	0.66	0.62	0.70	0.68	0.74	0.68	0.66	0.58	0.62	0.58	0.57	0.61	0.57	0.62	0.58
X vacancies	0.14	0.17	0.13	0.14	0.15	0.16	0.04	0.09	0.08	0.04	0.09	0.04	0.08	0.18	0.10	0.17	0.15	0.22	0.13	0.11	0.19
X <sub>Mg</sub>	0.62	0.62	0.63	0.61	0.62	0.62	0.58	0.61	0.59	0.60	0.55	0.60	0.57	0.67	0.66	0.69	0.65	0.67	0.66	0.69	0.65

Note: Atomic proportions based on ΣT+Z+Y cations = 15. X<sub>Mg</sub> = Mg/(Fe<sup>2+</sup> + Mg).

\* B<sub>2</sub>O<sub>3</sub> calculated assuming B to be 3 atoms per formula unit.

Table 5.4.3a: Representative EPMA analysis of tourmaline(continued).

Generati on	Gen II	Gen II	Gen II	Gen II	Gen II	Gen II	Gen II	Gen II	Gen II	Gen II	Gen II	Gen II	Gen II	Gen II	Gen II	Gen II	Gen II	Gen II	Gen II	Gen II	Gen II	
Sample no.	PP 7	PP 15	PP 15	PP 15	PP 15	PP 15	PP 15															
Point	33 / 20	15 / 1	16 / 1	18 / 1	20 / 1	21 / 1	22 / 1	22 / 2	22 / 3	22 / 4	22 / 5	22 / 6	22 / 7	22 / 8	22 / 9	23 / 12	23 / 13	23 / 14	23 / 15	23 / 16	23 / 17	
Core/Rim	rim	rim	rim	rim	rim	rim	rim	rim	rim	rim	rim	rim	rim	rim	rim	rim	rim	rim	rim	rim	rim	rim
Al <sub>2</sub> O <sub>3</sub>	31.44	30.36	32.26	31.34	31.43	31.35	31.56	30.50	30.62	30.57	27.17	30.93	30.70	31.50	31.34	31.82	30.98	31.33	30.77	29.67	31.70	
FeO	6.72	7.55	7.29	7.51	7.40	7.27	7.61	7.19	7.16	7.39	7.48	7.29	7.54	7.89	7.50	7.04	7.57	7.19	7.97	7.30	7.20	
TiO <sub>2</sub>	0.60	0.99	0.46	0.71	0.90	0.97	0.83	1.27	1.06	1.13	1.41	1.46	1.35	0.92	0.92	0.42	0.71	0.76	0.87	0.61	0.67	
SiO <sub>2</sub>	36.22	36.33	36.59	35.93	35.92	35.89	36.26	36.12	36.39	35.98	32.05	36.17	35.97	36.07	36.29	36.29	36.11	36.55	36.48	34.68	36.30	
K <sub>2</sub> O	0.06	0.06	0.11	0.10	0.06	0.03	0.06	0.08	0.06	0.04	0.11	0.07	0.04	0.09	0.06	0.09	0.05	0.03	0.04	0.08	0.02	
CaO	0.95	1.14	1.01	1.14	1.09	1.33	1.24	1.44	1.20	1.34	1.28	1.28	1.27	1.19	1.18	1.11	0.88	0.96	0.33	0.89	1.07	
Na <sub>2</sub> O	1.94	2.10	2.13	2.05	2.17	1.93	2.10	2.03	1.97	1.93	1.43	1.96	1.96	2.07	1.92	2.02	1.95	2.09	2.49	2.19	1.95	
Cr <sub>2</sub> O <sub>3</sub>	0.00	0.12	0.00	0.09	0.01	0.03	0.06	0.00	0.00	0.19	0.08	0.00	0.06	0.00	0.00	0.00	0.04	0.00	0.03	0.00	0.04	
MnO	0.00	0.03	0.00	0.11	0.09	0.00	0.01	0.00	0.02	0.00	0.07	0.00	0.11	0.08	0.00	0.03	0.05	0.00	0.07	0.05	0.04	
MgO	7.26	6.84	6.97	7.04	6.88	7.26	6.92	7.58	7.09	6.72	5.48	6.83	6.62	6.78	6.74	6.89	6.74	7.10	6.70	6.52	6.74	
B <sub>2</sub> O <sub>3</sub> *	10.51	10.48	10.68	10.53	10.54	10.56	10.62	10.56	10.52	10.45	9.33	10.55	10.48	10.59	10.55	10.55	10.45	10.59	10.51	10.05	10.55	
Total	95.70	96.00	97.50	96.55	96.49	96.62	97.27	96.77	96.09	95.74	85.89	96.54	96.10	97.18	96.50	96.26	95.53	96.60	96.26	92.04	96.28	
Si(T)	6.00	6.00	6.00	5.97	5.97	5.95	5.99	6.00	6.00	6.00	6.00	6.00	6.00	5.97	6.00	6.00	6.00	6.00	6.00	6.00	6.00	
Al(T)	0.00	0.00	0.00	0.03	0.03	0.05	0.01	0.00	0.00	0.00	0.00	0.00	0.00	0.03	0.00	0.00	0.00	0.00	0.00	0.00	0.00	
B(T)	3.00	3.00	3.00	3.00	3.00	3.00	3.00	3.00	3.00	3.00	3.00	3.00	3.00	3.00	3.00	3.00	3.00	3.00	3.00	3.00	3.00	
Al(Z)	6.00	5.93	6.00	6.00	6.00	5.99	6.00	5.86	5.96	5.97	5.92	5.96	5.96	6.00	6.00	6.00	6.00	6.00	6.00	6.00	6.00	
Al(Y)	0.11	0.00	0.14	0.02	0.03	0.00	0.02	0.00	0.00	0.00	0.00	0.00	0.00	0.01	0.05	0.15	0.07	0.06	0.00	0.04	0.13	
Ti(Y)	0.08	0.12	0.06	0.09	0.11	0.12	0.10	0.16	0.13	0.14	0.20	0.18	0.17	0.11	0.12	0.05	0.09	0.09	0.11	0.08	0.08	
Cr(Y)	0.00	0.02	0.00	0.01	0.00	0.00	0.01	0.00	0.00	0.03	0.01	0.00	0.01	0.00	0.00	0.00	0.01	0.00	0.00	0.00	0.01	
Fe(Y)	0.94	1.07	1.00	1.04	1.03	1.01	1.05	1.00	1.01	1.04	1.18	1.02	1.06	1.09	1.05	0.98	1.06	1.00	1.12	1.07	1.00	
Mn(Y)	0.00	0.00	0.00	0.02	0.01	0.00	0.00	0.00	0.00	0.00	0.01	0.00	0.02	0.01	0.00	0.00	0.01	0.00	0.01	0.01	0.01	
Mg(Y)	1.80	1.73	1.70	1.74	1.71	1.79	1.70	1.88	1.78	1.69	1.54	1.70	1.66	1.67	1.68	1.71	1.69	1.76	1.67	1.70	1.67	
K(X)	0.01	0.01	0.02	0.02	0.01	0.01	0.01	0.02	0.01	0.01	0.03	0.01	0.01	0.02	0.01	0.02	0.01	0.01	0.01	0.02	0.00	
Ca(X)	0.17	0.20	0.18	0.20	0.19	0.23	0.22	0.25	0.21	0.24	0.26	0.23	0.23	0.21	0.21	0.20	0.16	0.17	0.06	0.16	0.19	
Na(X)	0.62	0.67	0.67	0.66	0.69	0.62	0.67	0.65	0.63	0.62	0.52	0.63	0.63	0.66	0.61	0.64	0.63	0.66	0.80	0.73	0.62	
X vacancies	0.20	0.11	0.13	0.12	0.10	0.14	0.10	0.08	0.14	0.13	0.20	0.13	0.14	0.11	0.17	0.14	0.20	0.16	0.14	0.08	0.18	
X <sub>Mg</sub>	0.66	0.62	0.63	0.63	0.62	0.64	0.62	0.65	0.64	0.62	0.57	0.63	0.61	0.60	0.62	0.64	0.61	0.64	0.60	0.61	0.63	

Note: Atomic proportions based on ΣT+Z+Y cations = 15. X<sub>Mg</sub> = Mg/(Fe<sup>2+</sup> + Mg).

\* B<sub>2</sub>O<sub>3</sub> calculated assuming B to be 3 atoms per formula unit.

Table 5.4.3a: Representative EPMA analysis of tourmaline(continued).

Generation	Gen II	Gen II	Gen II	Gen II	Gen II	Gen II	Gen II	Gen II												
Sample no.	PP 15	PP60																		
Point	23 / 18	23 / 19	23 / 20	23 / 21	23 / 22	23 / 23	23 / 24	23 / 25	23 / 26	23 / 27	23 / 28	23 / 29	23 / 30	23 / 1	24 / 1	46 / 1	51 / 1	52 / 1	53 / 1	55 / 1
Core/Rim	rim	rim	rim	rim	rim	rim	rim	rim												
Al <sub>2</sub> O <sub>3</sub>	31.31	31.69	31.10	30.79	30.58	31.07	31.04	30.80	30.98	30.83	30.69	30.89	30.77	28.91	29.73	28.65	28.59	30.07	29.23	28.68
FeO	7.51	7.21	7.57	7.49	7.49	7.44	7.69	7.77	7.49	7.11	7.43	7.63	7.12	8.74	7.82	8.36	8.55	7.87	8.62	8.81
TiO <sub>2</sub>	0.58	0.78	1.01	1.08	0.66	0.75	0.57	1.17	1.01	0.93	0.88	1.07	1.00	1.23	0.70	1.08	1.26	1.08	1.16	1.19
SiO <sub>2</sub>	36.12	36.34	36.40	36.23	36.27	36.18	36.45	36.57	36.09	36.43	36.17	35.90	36.29	36.09	36.45	36.22	36.09	36.65	36.03	35.52
K <sub>2</sub> O	0.09	0.06	0.10	0.02	0.07	0.04	0.08	0.05	0.02	0.05	0.06	0.09	0.04	0.04	0.08	0.06	0.05	0.03	0.04	0.08
CaO	1.06	0.95	1.06	1.08	1.17	1.09	1.08	1.11	1.19	1.15	1.12	1.17	1.26	1.45	1.59	1.87	2.02	1.00	1.44	1.53
Na <sub>2</sub> O	2.05	2.22	2.01	2.06	2.04	1.94	1.94	2.19	2.07	2.04	2.07	2.03	2.01	2.15	1.99	1.83	1.75	2.16	2.09	2.00
Cr <sub>2</sub> O <sub>3</sub>	0.01	0.06	0.02	0.00	0.00	0.06	0.05	0.00	0.00	0.00	0.12	0.00	0.00	0.12	0.10	0.00	0.12	0.03	0.03	0.07
MnO	0.03	0.00	0.21	0.06	0.00	0.00	0.04	0.00	0.03	0.00	0.00	0.09	0.04	0.03	0.00	0.06	0.03	0.00	0.00	0.00
MgO	6.73	6.85	6.90	6.84	6.71	6.72	6.75	6.90	7.04	6.86	6.88	6.96	7.28	8.09	8.47	7.93	8.16	7.88	8.11	7.95
B <sub>2</sub> O <sub>3</sub> *	10.49	10.59	10.58	10.51	10.43	10.48	10.52	10.60	10.53	10.51	10.48	10.50	10.54	10.52	10.60	10.45	10.49	10.61	10.52	10.38
Total	95.98	96.75	96.96	96.16	95.42	95.77	96.21	97.16	96.45	95.91	95.90	96.33	96.35	97.37	97.53	96.51	97.11	97.38	97.27	96.21
Si(T)	6.00	6.00	6.00	6.00	6.00	6.00	6.00	6.00	6.00	6.00	6.00	5.99	6.00	5.98	5.99	6.00	6.00	6.00	5.96	5.95
Al(T)	0.00	0.00	0.00	0.00	0.00	0.00	0.00	0.00	0.00	0.00	0.00	0.01	0.00	0.02	0.01	0.00	0.00	0.00	0.04	0.05
B(T)	3.00	3.00	3.00	3.00	3.00	3.00	3.00	3.00	3.00	3.00	3.00	3.00	3.00	3.00	3.00	3.00	3.00	3.00	3.00	3.00
Al(Z)	6.00	6.00	5.99	5.99	6.00	6.00	6.00	5.95	5.98	6.00	6.00	5.96	5.96	5.59	5.72	5.61	5.55	5.80	5.64	5.60
Al(Y)	0.09	0.09	0.00	0.00	0.00	0.07	0.05	0.00	0.00	0.01	0.00	0.00	0.00	0.00	0.00	0.00	0.00	0.00	0.00	0.00
Ti(Y)	0.07	0.10	0.13	0.14	0.08	0.09	0.07	0.15	0.13	0.12	0.11	0.13	0.13	0.15	0.09	0.14	0.16	0.13	0.14	0.15
Cr(Y)	0.00	0.01	0.00	0.00	0.00	0.01	0.01	0.00	0.00	0.00	0.02	0.00	0.00	0.02	0.01	0.00	0.02	0.00	0.00	0.01
Fe(Y)	1.05	1.00	1.05	1.05	1.07	1.05	1.08	1.08	1.04	1.01	1.05	1.06	0.99	1.21	1.07	1.18	1.19	1.08	1.19	1.23
Mn(Y)	0.00	0.00	0.03	0.01	0.00	0.00	0.01	0.00	0.00	0.00	0.00	0.01	0.01	0.00	0.00	0.01	0.00	0.00	0.00	0.00
Mg(Y)	1.68	1.69	1.71	1.71	1.70	1.69	1.69	1.71	1.75	1.73	1.73	1.73	1.81	2.00	2.07	1.99	2.02	1.94	2.00	1.99
K(X)	0.02	0.01	0.02	0.00	0.01	0.01	0.02	0.01	0.00	0.01	0.01	0.02	0.01	0.01	0.02	0.01	0.01	0.01	0.01	0.02
Ca(X)	0.19	0.17	0.19	0.19	0.21	0.19	0.19	0.19	0.21	0.20	0.20	0.21	0.22	0.26	0.28	0.33	0.36	0.18	0.25	0.27
Na(X)	0.66	0.71	0.64	0.66	0.66	0.62	0.62	0.70	0.66	0.65	0.67	0.65	0.64	0.69	0.63	0.59	0.56	0.69	0.67	0.65
X vacancies	0.13	0.11	0.15	0.14	0.12	0.17	0.17	0.10	0.12	0.13	0.12	0.12	0.13	0.05	0.07	0.06	0.07	0.13	0.07	0.06
X <sub>Mg</sub>	0.61	0.63	0.62	0.62	0.61	0.62	0.61	0.61	0.63	0.63	0.62	0.62	0.65	0.62	0.66	0.63	0.63	0.64	0.63	0.62

Note: Atomic proportions based on ΣT+Z+Y cations = 15. X<sub>Mg</sub> = Mg/(Fe<sup>2+</sup> + Mg).

\* B<sub>2</sub>O<sub>3</sub> calculated assuming B to be 3 atoms per formula unit.

Table 5.4.3b: Representative EPMA analysis of biotite, muscovite, chlorite and Kfeldspar .

Sample no	PP 38A	PP 38A	PP 38A	PP 38A	PP 38A	PP 38A	PP 38A	PP38	PP38
DataSet/ Point	8 / 1	10 / 1	13 / 1 <sup>#</sup>	16 / 1	7 / 1 <sup>#</sup>	9 / 1	15 / 1	27 / 1 <sup>#</sup>	45 / 1
Mineral	Biotite	Biotite	Biotite	Biotite	Muscovite	Muscovite	Muscovite	Chlorite	K-feldspar
SiO <sub>2</sub>	36.41	35.1	36.33	35.88	45.80	45.36	45.68	26.75	64.51
TiO <sub>2</sub>	1.3	2.39	0.1	1.59	0.29	0.11	0.4	0.00	0.02
Al <sub>2</sub> O <sub>3</sub>	16.47	15.85	17.25	16.51	31.62	32.25	31.15	21.70	19.16
Cr <sub>2</sub> O <sub>3</sub>	0.15	0.06	0.19	0	0.00	0.02	0	0.08	0
FeO	21.2	23.42	21.86	20.59	3.79	3.67	3.86	20.22	0
MnO	0.28	0.27	0.33	0.37	0.00	0.05	0.09	0.15	0
MgO	8.09	6.47	8.46	7.85	1.06	1.11	1.36	17.50	0.02
CaO	0.49	0.37	1.37	0.62	0.01	0.03	0.1	0.08	0
Na <sub>2</sub> O	0.18	0.18	0.26	0.24	0.25	0.3	0.28	0.09	0.44
K <sub>2</sub> O	7.02	8.36	1.69	7.45	11.19	11.25	11.2	0.19	16.19
P <sub>2</sub> O <sub>5</sub>	0	0	0	0	0.00	0	0	0.00	0
Total	91.76	92.48	87.84	91.11	94.01	94.15	94.12	86.77	100.34
Normalization basis	11(O)	11(O)	11(O)	11(O)	11(O)	11(O)	11(O)	28(O)	8(O)
Si	2.88	2.81	2.91	2.86	3.15	3.11	3.14	5.53	2.97
Ti	0.08	0.14	0.01	0.10	0.01	0.01	0.02	0.00	0.00
Al	1.53	1.50	1.63	1.55	2.56	2.61	2.53	5.29	1.04
Cr	0.01	0.00	0.01	0.00	0.00	0.00	0.00	0.01	0.00
Fe	1.40	1.57	1.46	1.37	0.22	0.21	0.22	3.50	0.00
Mn	0.02	0.02	0.02	0.02	0.00	0.00	0.01	0.03	0.00
Mg	0.95	0.77	1.01	0.93	0.11	0.11	0.14	5.39	0.00
Ca	0.04	0.03	0.12	0.05	0.00	0.00	0.01	0.02	0.00
Na	0.03	0.03	0.04	0.04	0.03	0.04	0.04	0.04	0.04
K	0.71	0.85	0.17	0.76	0.98	0.99	0.98	0.05	0.95
P	0.00	0.00	0.00	0.00	0.00	0.00	0.00	0.00	0.00
X <sub>Mg</sub>	0.40	0.33	0.41	0.40				0.61	
X <sub>kfs</sub>									0.96

<sup>#</sup> composition used in C-space

## 5.5. Trace and REE concentrations of tourmaline

In chondrite normalized REE (McDonough and Sun, 1995) diagram, Gen-I tourmalines show near chondritic to depleted LREE concentration with negative sloped pattern (Fig 5.5.1a). Concentration of LREE in core and rim is nearly equivalent. Both core and rim show prominent and near equal positive Eu anomalies ( $Eu/Eu^* = 8.02-58.14$ ) with  $(La/Lu)_{CN} = 3.43 - 18.84$  ( $La/Lu > 1$ ). The HREE concentration is subchondritic (0.1-1X chondrite). The HREE patterns are nearly flat except slight irregularities (Fig 5.5.1a). The rim is slightly enriched HREE than the core. The REE<sub>total</sub> content of Gen-I core varies from 1.03ppm-3.22ppm with an average of  $1.80 \pm 1.00$  ppm, whereas rim REE<sub>total</sub> content varies from 1.99ppm-2.53ppm with an average of  $2.30 \pm 0.28$  ppm. In Generation-I, the tourmaline rim is more REE<sub>total</sub> rich than the core. In chondrite normalized REE (McDonough and Sun, 1995) diagram, Gen-II tourmalines show subchondritic concentrations of LREE (1-0.1X chondrite), although they have a negatively slope similar to Gen-I (Fig 5.5.1b). Overall, LREE concentrations are lower than Gen-I. Both the core and the rim have prominent positive Eu anomalies ( $Eu/Eu^* = 7.44 - 29.16$ ) with  $(La/Lu)_{CN} = 0.60-10.45$ . The HREE pattern is flat to slightly positive sloped. The HREE concentrations of core and rim both vary with relatively wider range (Fig 5.5.1b). The core REE<sub>total</sub> content varies from 0.43ppm to 1.19 ppm at an average of  $0.84 \pm 0.29$  ppm, whereas the rim REE<sub>total</sub> contents varies from 0.78 ppm to 1.85 ppm at an average of  $1.16 \pm 0.36$  ppm. Thus, the rim is higher REE<sub>total</sub> than the core.

In UCC normalized multielement plot (Rudnick and Gao, 2003) of Gen I tourmaline, significant depletion in LIL elements such as Rb, Ba are observed (Fig 5.5.1c). Concentrations of Ni, Co and Pb are near to slightly depleted than UCC. HREE+Y concentrations are nearly flat and sub crustal values (0.1-0.01 X UCC). In HREE+Y, the rim concentrations is higher than the core. Prominent Eu anomaly is observed. LREE shows subcrustal value and overall concentrations is depleted. The LREE pattern and concentrations of core and rim are nearly similar. Among the HFSE, prominent positive anomaly of Ti is noted (Fig 5.5.1c). The cores and the show overall depleted of Zr, Hf. Ta is enriched than the Nb. In UCC normalised multielement plot (Rudnick and Gao, 2003) of Gen-II tourmaline shows significant negative anomaly in LIL elements such as Rb, Ba are observed like Gen-I (Fig 5.5.1d). HREE+Y concentrations show negative slightly negative slope with sub crustal values (0.1-0.01 X UCC). Prominent positive Eu anomaly noted. LREE shows subcrustal value and overall concentrations is depleted. LREE pattern is flat and rim is more enriched than the core (Fig

5.5.1d). Distinct positive Ti anomaly noted. The cores and rim show overall depleted but variable concentrations of Zr, Hf.

Representative LA-ICP-MS trace-element analyses (in ppm) of tourmaline is given in Table 5.5.2a.

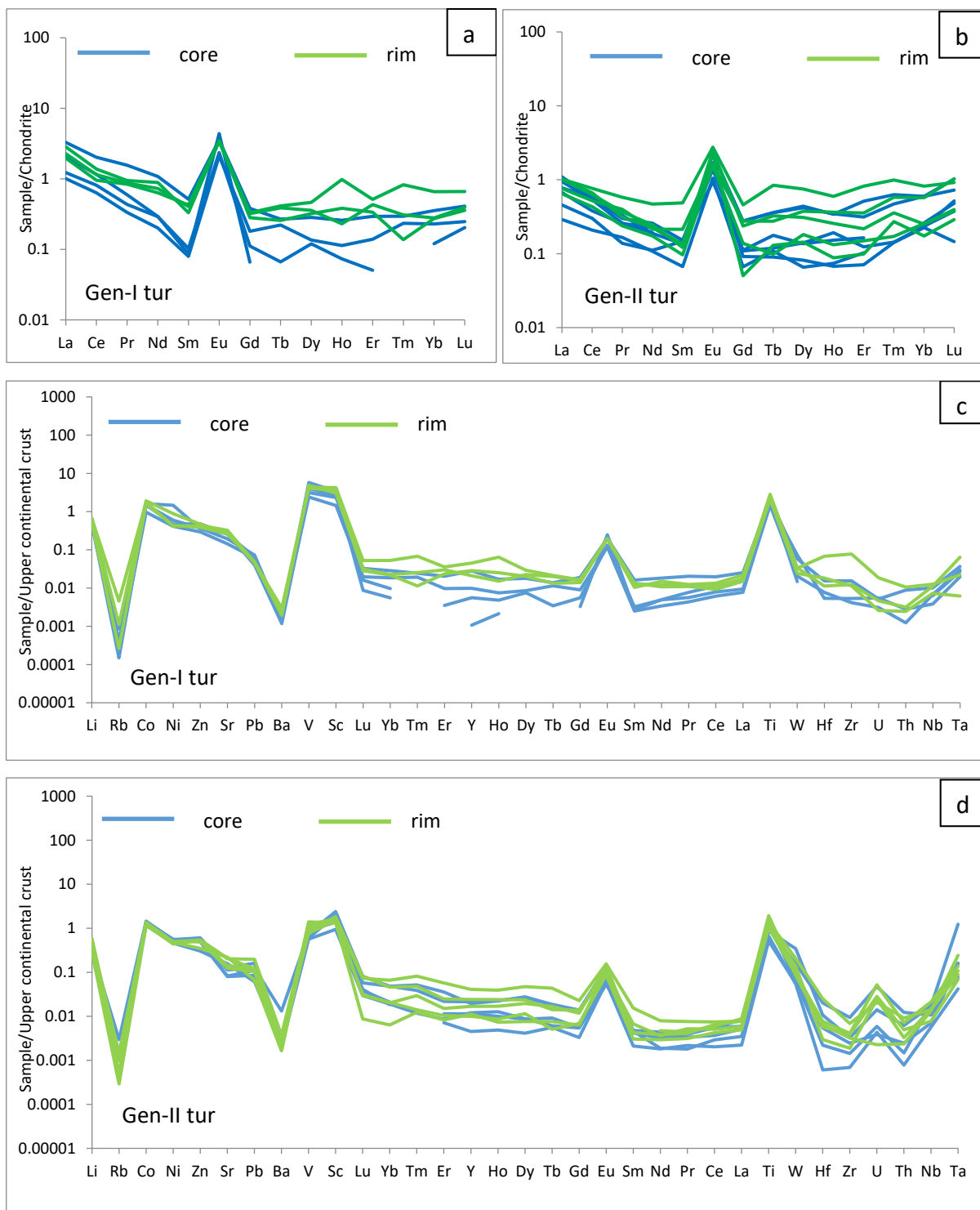


Fig 5.5.1a: Chondrite normalized (McDonough and Sun, 1995) REE spider diagram of Gen-I tourmaline (Blue – core : Green-rim). Fig 5.5.1b: Chondrite normalized (McDonough and Sun, 1995) REE spider diagram of Gen-II tourmaline (Blue –core : Green-rim). Fig 5.5.1c: Upper continental crust (UCC) normalized (Rudnick and Gao, 2003) multi-element diagram for Gen-I tourmaline (Blue –core: Green-rim). Fig 5.5.1d: Upper continental crust (UCC) normalized (Rudnick and Gao, 2003) multi-element diagram for Gen-II tourmaline (Blue –core: Green-rim).[The gaps in the spidergrams represent element concentrations that are below detection limit.]

Table 5.5.2a : Representative LA-ICPMS trace element analysis (in ppm) of tourmaline.

Sample no.	PP59A	PP15	PP15						
Mineral	Tourmaline								
Point	41	44	46	47	36	37	43	1	3
Generation	G-I	G-II	G-II						
Core/rim	Core	Core	Core	Core	Rim	Rim	Rim	Core	Core
La	0.78	0.29	0.24	0.49	0.68	0.54	0.47	0.11	0.07
Ce	1.24	0.50	0.39	0.71	0.85	0.70	0.59	0.18	0.13
Pr	0.15	0.04	0.03	0.06	0.09	0.08	0.08	0.01	0.02
Nd	0.49	0.13	0.09	0.13	0.41	0.33	0.29	0.05	0.05
Sm	0.08	0.02	0.01	0.01	0.05	0.06	0.06	0.02	0.01
Eu	0.20	0.13	0.12	0.25	0.20	0.19	0.20	0.05	0.06
Gd	0.08	0.02	0.04	0.01	0.06	0.07	0.06	0.02	0.01
Tb	0.01	0.00	0.01	bdl	0.01	0.01	0.01	0.00	0.00
Dy	0.07	0.03	0.03	bdl	0.08	0.11	0.09	0.03	0.02
Ho	0.01	0.00	0.01	0.00	0.02	0.05	0.01	0.01	0.00
Er	0.05	0.01	0.02	bdl	0.05	0.08	0.07	0.02	0.02
Tm	0.01	bdl	0.01	bdl	0.00	0.02	0.01	0.00	bdl
Yb	0.06	0.02	0.04	0.01	0.04	0.11	0.05	0.04	0.04
Lu	0.01	0.01	0.01	0.00	0.01	0.02	0.01	0.01	0.01
Total REE	3.23	1.20	1.04	1.73	2.53	2.38	1.99	0.57	0.44
Eu anomaly	8.02	22.07	17.60	58.14	11.41	9.20	9.41	7.45	15.73
Li	15.74	14.09	10.96	11.95	16.26	15.60	12.09	8.51	7.32
Sc	32.61	37.31	20.26	47.29	49.78	58.83	42.31	13.24	27.66
Ti	8133.02	5668.88	5932.73	8262.72	9319.75	10888.79	8060.77	2561.12	1975.73
V	305.85	381.93	233.33	560.08	394.93	425.93	469.79	54.78	57.89
Co	27.91	26.05	16.71	25.75	33.09	30.32	27.73	23.99	25.12
Ni	68.80	28.04	19.35	22.24	41.72	19.51	20.45	26.30	25.46
Zn	23.66	24.47	19.70	31.99	31.26	29.01	26.02	33.10	35.39
Rb	0.03	0.07	0.02	0.01	0.09	0.38	0.02	0.09	0.24
Sr	85.31	62.00	46.04	81.85	90.59	104.23	83.50	25.63	26.22
Y	0.59	0.12	0.21	0.02	0.60	0.95	0.44	0.25	0.10
Zr	2.99	0.80	1.03	0.21	2.40	14.95	2.22	0.13	0.47
Nb	0.12	0.08	0.05	0.08	0.14	0.15	0.09	0.07	0.08
Mo	0.05	0.03	0.02	bdl	bdl	0.05	bdl	0.06	0.04
Ag	0.03	0.19	0.06	0.09	0.13	0.05	0.01	0.01	bdl
Ba	0.74	0.96	0.98	1.04	1.64	1.87	1.22	1.32	1.49
Hf	0.08	0.04	0.03	bdl	0.06	0.36	0.10	0.00	0.03
Ta	0.03	0.03	0.02	0.02	0.06	0.02	0.01	0.04	0.15
W	0.11	0.04	0.14	0.03	0.06	0.06	0.05	0.10	0.11
Pb	0.68	1.24	1.04	1.11	0.83	0.79	0.78	1.45	1.88
Th	0.09	0.01	0.03	bdl	0.03	0.11	0.03	0.01	0.03
U	0.01	0.01	0.01	bdl	0.01	0.05	0.01	0.01	0.01

bdl- below detection limit

Table 5.5.2a : Representative LA-ICPMS trace element analysis (in ppm) of tourmaline(continued).

Sample no.	PP15									
Mineral	Tourmaline									
Point	6	10	16	17	2	5	7	13	14	15
Generation	G-II									
Core/rim	Core	Core	Core	Core	Rim	Rim	Rim	Rim	Rim	Rim
La	0.16	0.18	0.26	0.22	0.15	0.24	0.18	0.24	0.24	0.27
Ce	0.23	0.35	0.35	0.33	0.27	0.41	0.32	0.47	0.39	0.38
Pr	0.02	0.03	0.03	0.02	0.02	0.03	0.04	0.05	0.03	0.03
Nd	0.10	0.12	0.09	0.09	0.08	0.10	0.10	0.21	0.11	0.13
Sm	0.02	0.02	0.02	bdl	0.01	0.02	0.03	0.07	0.02	bdl
Eu	0.13	0.09	0.08	0.10	0.09	0.14	0.09	0.16	0.13	0.11
Gd	0.06	0.06	0.02	0.02	0.03	0.05	0.06	0.09	0.01	0.03
Tb	0.01	0.01	0.01	0.00	0.00	0.01	0.01	0.03	0.00	0.01
Dy	0.10	0.11	0.03	0.02	0.04	0.08	0.09	0.18	0.04	0.03
Ho	0.02	0.02	0.01	0.00	0.01	0.01	0.02	0.03	0.00	0.01
Er	0.05	0.08	0.03	0.01	0.02	0.03	0.06	0.13	0.02	0.02
Tm	0.01	0.02		0.00	0.00	0.01	0.01	0.02	0.01	0.00
Yb	0.10	0.10	0.04	0.04	0.04	0.04	0.09	0.13	0.03	0.01
Lu	0.03	0.02	0.01	0.00	0.01	0.01	0.03	0.02	0.01	0.00
Total REE	1.04	1.20	0.97	0.87	0.78	1.18	1.12	1.85	1.03	1.04
Eu anomaly	11.82	7.82	11.31	18.53	13.37	13.69	6.73	5.84	29.16	20.83
Li	9.30	10.70	6.15	7.29	11.91	12.62	10.19	13.94	12.56	6.85
Sc	33.38	24.84	19.21	16.93	21.04	18.72	25.64	23.01	17.79	19.29
Ti	3332.02	3657.00	4875.64	6070.12	4754.11	7398.29	3930.46	5325.56	6489.68	5968.40
V	73.67	83.28	86.16	134.64	75.13	135.41	82.39	117.60	124.40	103.87
Co	22.59	22.66	20.08	21.25	22.58	23.50	21.93	20.61	20.73	20.02
Ni	23.47	26.00	21.56	22.13	23.16	23.14	22.36	20.63	20.80	22.52
Zn	38.27	40.56	20.31	22.64	34.96	36.31	33.41	35.91	36.52	23.35
Rb	0.11	0.09	0.08	0.06	0.12	0.04	0.10	0.08	0.08	0.02
Sr	36.17	40.75	50.02	69.17	44.87	67.16	39.61	65.01	65.39	70.51
Y	0.45	0.41	0.24	0.19	0.21	0.35	0.51	0.86	0.17	0.24
Zr	0.63	1.81	0.28	0.17	0.36	0.75	0.79	1.32	0.36	0.62
Nb	0.21	0.13	0.23	0.13	0.18	0.09	0.26	0.17	0.11	0.16
Mo	0.06	0.08	0.05	0.04	0.06	0.03	0.04	0.03	0.03	0.06
Ag	0.04	0.01	bdl	bdl	0.00	0.01	0.02	0.01	0.01	bdl
Ba	8.26	1.70	1.42	1.41	1.84	1.06	1.39	2.32	2.38	1.03
Hf	0.06	0.11	0.01	0.02	0.02	0.03	0.04	0.13	0.04	0.03
Ta	1.11	0.14	0.07	0.04	0.10	0.06	0.12	0.08	0.13	0.22
W	0.65	0.30	0.13	0.08	0.26	0.16	0.17	0.39	0.28	0.19
Pb	2.11	2.72	1.04	0.98	2.12	2.03	1.77	3.34	2.58	1.12
Th	0.07	0.13	0.02	0.01	0.03	0.05	0.08	0.10	0.03	0.02
U	0.04	0.13	0.02	0.00	0.07	0.08	0.14	0.06	0.03	0.01

bdl- below detection limit

## 5.6 Summary

Banded quartz tourmaline rock that occurs in Masak pahar near Mukutmanipur area, is hosted by mica chlorite schist i.e retrogressed part of granitic component of CGGC. Chattopadhyay et al. (2016), previously worked in the particular rocks i.e the granite mylonite and the interlayered phyllosilicate bands in this area. From the stoichiometrically balanced reaction and textural modelling, they have shown that the formation of chlorite and muscovite from granite enhances the porosity (large negative volume change of the solid) of the rock which help to fluid to infiltrate to the host rock and metasomatised it. Whereas formation biotite from chlorite+albite, the reaction shows a positive volume change which lower the porosity of the rock and hinders the biotite growth. Due to infiltration of aqueous fluid during ductile shearing in SPSZ converted the mylonitic granite to mica -chlorite schist. Due to extremely channelized fluid flow the phyllosilicates band are restricted and occur as centimetre to decimetre thick band within the sheared granite. It is also evident from other parts of SPSZ i.e in Haripaldih, Beldih and Kutni area where preponderance presence of muscovite schist or quartz muscovite schist adjacent to the granitic rock of CGGC. This happened due to infiltration driven metamorphism during ductile shearing SPSZ.

From the field and petrography study, there are two different generations of tourmaline found. The first generation (Gen-I) of tourmaline is fine to medium grained and occurs as granular aggregates of laterally continuous bands alternate with quartz rich bands. Tourmaline grains within the banded quartz tourmaline rock are oriented parallel to the  $S_1$  fabric. This tourmaline bearing rock is deformed, folded and defining tight to isoclinal  $F_2$  fold similar to the adjacent host rock. From the field evidence and textural study, it can be inferred that the first generation (Gen-I) tourmaline is syn-tectonic regarding  $S_1/D_1$ . Another set of coarse long prismatic tourmaline was found within the quartz vein. This tourmaline bearing quartz vein cut across the  $S_1$  fabric at a high angle. These tourmalines are randomly oriented. Thus, the tourmaline grains are denoted as second generation (Gen-II) and are supposed to be formed at post  $D_3/F_3$ . All tourmaline grains of different generations are alkali rich in composition. Gen-I tourmaline is less calcic and alkali rich than the Gen-II compositions. Gen-I tourmaline core is schorl in character whereas rim straddles the boundary between schorl and dravite which inferred that the rim is more magnesium rich than the core. Gen-II tourmalines are more magnesium rich than the Gen-I tourmaline and dravite in character. Chondrite normalized REE pattern of Gen-I tourmaline shows near chondritic to depleted LREE concentration with negative sloped pattern. These tourmaline shows prominent positive Eu anomaly. The HREE

patterns is nearly flat. Gen-II tourmaline shows subchondritic LREE concentrations with negative slope similar to Gen-I. But overall LREE concentrations are lower than the Gen-I. Gen-II tourmaline also shows a prominent positive Eu anomaly. The HREE pattern is flat to slightly positive sloped for Gen-II tourmaline. The average REE<sub>total</sub> is higher in Gen-I tourmaline than Gen-II.

# CHAPTER 6

## Tourmaline bearing rocks in and around Ujainpur

The study area, Ujainpur is situated ~20 km west of the town Tatanagar (Fig.1.5b) in Jharkhand. Geologically, it is located in the western part of SSZ. There are several tourmaline-bearing rocks that are reported all along the SSZ (Sengupta et al., 2005; Pal et al. 2010; Sengupta et al., 2011; Patel et al., 2021). Unlike most other reported occurrences, tourmaline-bearing assemblages in the studied area is associated with dumortierite ( $[(Al, \square)Al_6BSi_3O_{16}(O, OH)_2]$ ). However, the emphasis of this study will be on the tourmaline-rich rocks. The study of tourmaline-bearing assemblages have included in this study for (1) unlike many other tourmaline occurrences in SSZ and SPSZ, tourmaline-bearing assemblages are reported from the kyanite-quartzite of Chaibasa formation, a prominent lithology that occurs all along the northern part of the North Singhbhum Mobile Belt (NSMB, Sengupta et al., 2005; Chakraborty et al., 2015) and (2) different generation of tourmaline veins are developed in the area and (3) the study of tourmaline bearing assemblages from this area can be compared with the tourmaline –bearing occurrences described from the SPSZ (Chapters 2, 3, 4 and 5) area. In this chapter, the distribution of tourmaline-bearing rock in kyanite-quartzite and kyanite-muscovite schist, their appearance in the field, nature of exposure and relationship with each other as identified in field study, petrography and mineral chemistry of tourmaline will be described in details.

### 6.1 Lithology and structure of the area

The study area, Ujainpur is located in the western flank of the SSZ (Fig 1.5b). Kyanite-quartzite(KQ) is the dominant lithology of the study area with variable amounts of kyanite, muscovite, pyrophyllite, quartz and boron rich mineral namely dumortierite and tourmaline. The Ujainpur area is marked by isolated hillocks of kyanite-quartzite surrounded by the mica schist of the NSMB (Fig 6.1.1). Intense tropical weathering led to extensive soil formation on the muscovite schist. A complete gradation from kyanite-quartzite (<10 vol % muscovite) ( Fig 6.1.2a) to kyanite-muscovite schist (Fig 6.1.2d) (> 60vol % muscovite) was found within a few

meters and kyanite gradually disappears and the rock becomes muscovite-schist (muscovite + pyrophyllite + quartz).

Kyanite-Quartzite (hereafter KQ) having alternate bands of kyanite- and quartz- rich segregations (1mm to 1cm thick) is the dominant country rock in the study area. The stretched grains of kyanite and elongated recrystallized quartz grain aggregate are parallel to the regional planar fabric of the SSZ ( $S_1$ ) (Fig 6.1.2.a). Locally the planar fabric of the KQ swerves around pods almost entirely made up of coarse (2cm-4cm) long, bladed and randomly oriented kyanite crystals (Fig.6.1.2b). The kyanite/quartz ratio in the KQ varies widely and in places the KQ grades to quartzite with only few scattered grains of kyanite (Fig.6.1.2c). This figure is consistent with the view that the deformation that was associated with the development of the regional planar fabric affected the massive kyanite and banded KQ. The kyanite that predates the  $S_1$  fabric is marked as  $ky_1$ . This early foliation ( $S_1$ ) is highly deformed and folded along the regional shear foliation( $S_2$ ). Commonly, KQ rock grades into kyanite-muscovite schists (Fig.6.1.2d) and occasionally occurs as an elongated pod within the kyanite mica schist (Fig 6.1.1). In places KQ is variably replaced with thin laminae of muscovite (Fig6.1.2d). Within the intensely sheared parts of the rock, i.e., in kyanite-muscovite schist, the trace of  $S_1$  is completely obliterated. The shear foliation( $S_2$ ) is more prominent within the kyanite muscovite schist where the foliation is defined by muscovite (Fig.6.1.2d). The schistosity ( $S_2$ ) of the kyanite-muscovite schist trends  $340-20^\circ$  and dips  $50-70^\circ$  towards east. In the south east of KQ and kyanite- mica schist is graded into mica schist and prominent shear foliation ( $S_2$ ) define by phyllosilicates mineral. Detached outcrop of mica schist is found within the soil cover of the area.

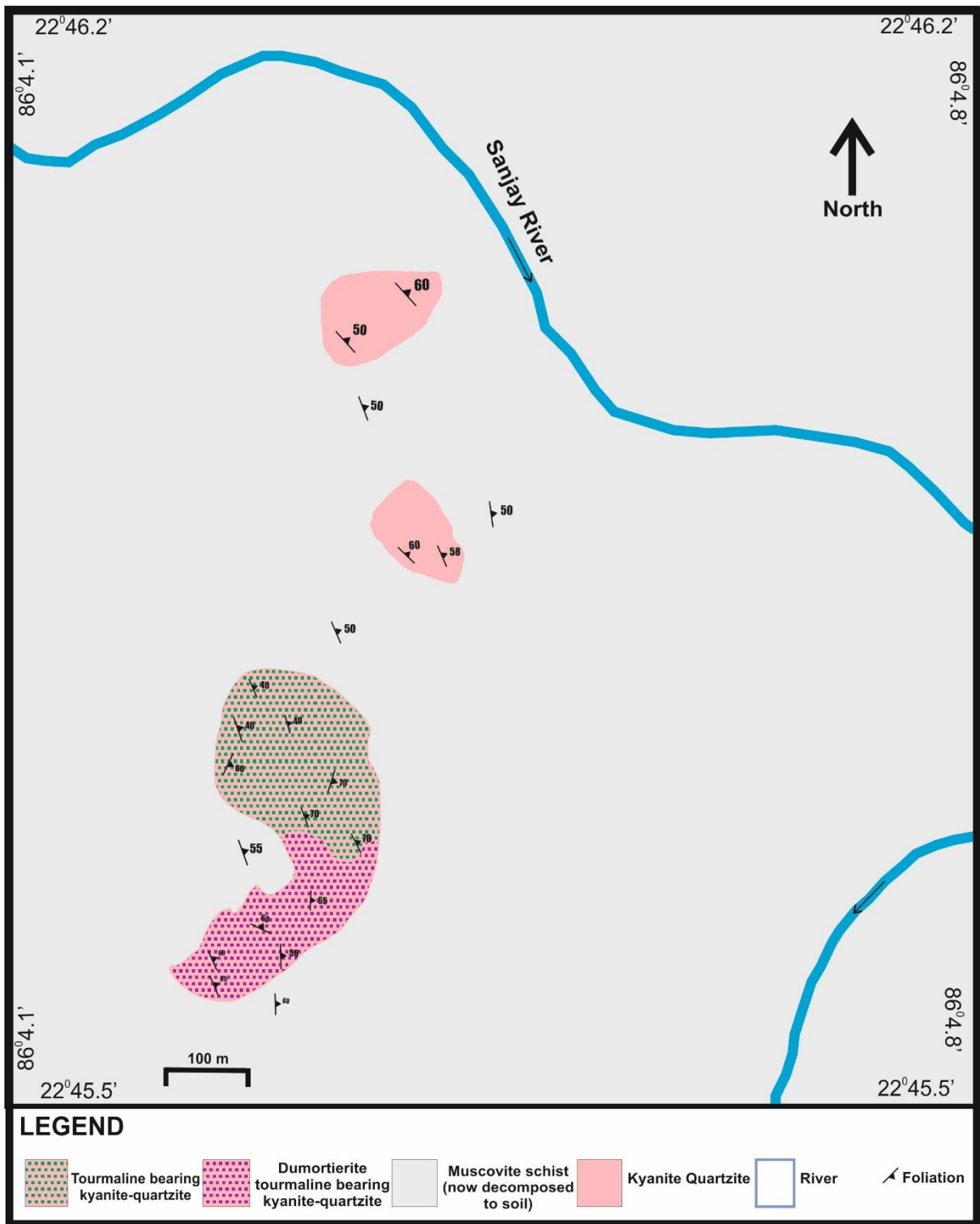


Fig 6.1.1: Detailed Lithological map of Ujainpur area.

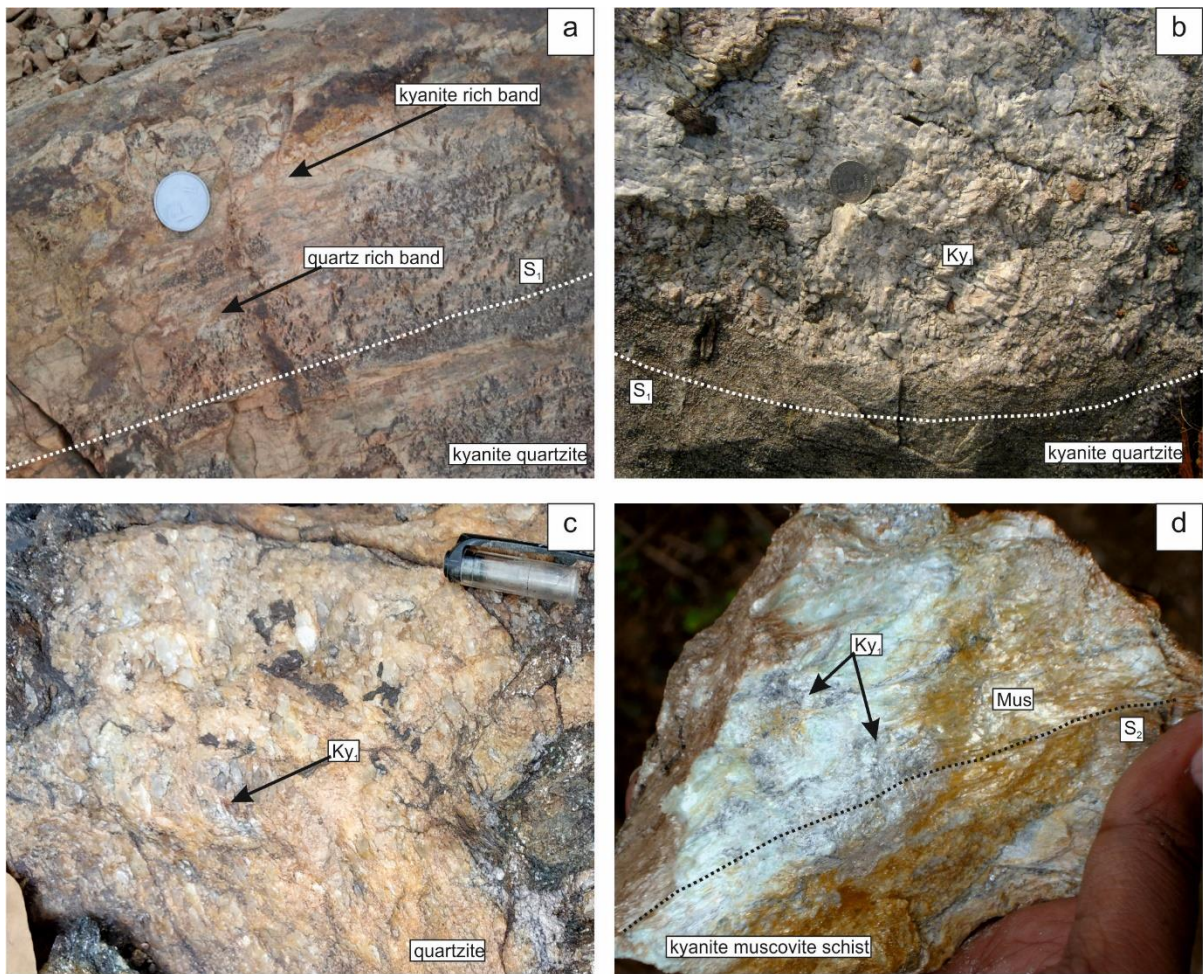


Fig 6.1.2a: KQ(kyanite quartzite) rock defined by alternating bands of kyanite and quartz-rich segregation. The stretched grains of kyanite and elongated aggregates of quartz grains are oriented parallel to the  $S_1$  fabric. Fig 6.1.2b: Kyanite rich pods are found within the KQ rock where the kyanite grains are coarse granular to prismatic (2cm-4cm long) in shape and randomly orientated. Fig 6.1.2c: The kyanite/quartz ratio in the KQ varies widely and in places the KQ grades to quartzite with a few scattered grains of kyanite. Fig 6.1.2d: The shear foliation( $S_2$ ) is prominent within the kyanite muscovite schist where the foliation defined by muscovite.

## 6.2 Field features of tourmaline bearing rocks

KQ are dissected by different generations of tourmaline ( $\pm$  dumortierite) veins/segregations. Based on the abundance of tourmaline and dumortierite, it has been classified the contour in two-part, northern part is tourmaline rich part than dumortierite (tourmaline  $>80$  vol%, dumortierite  $<20$  vol%) and southern part is dumortierite rich part than tourmaline (dumortierite  $>60$  vol%, tourmaline  $<40$  vol%) in host KQ rock (Fig 6.1.1).

The first generation (Gen-I) tourmaline veins/pods develop along the  $S_1$  fabric (Fig 6.2a, 6.2b and 6.2c). The tourmaline rich pods consist of coarse grain (0.5 cm to 1 cm in length) tourmaline (70 volumes % of tourmaline) and kyanite ( $ky_1$ ) (Fig 6.2b). Gen-I tourmaline vein shows pinch and swell structure along  $S_1$  fabric (Fig 6.2c). The field features are consistent with the view that (1) the tourmaline pods formed after massive kyanite ( $ky_1$ ) pods and (2) The Gen-I tourmaline may be syn-tectonic and formed during the formation of  $S_1$  foliation. The tourmaline layers (Gen-I) are folded by the tight to isoclinal  $F_2$  folds (Fig 6.2d). The second generation (Gen-II) tourmaline and dumortierite veins (Thickness of vein - 0.5cm to 2cm) cuts across the Gen-I tourmaline veins and develop along the axial plane of the  $F_2$  folds (Fig 6.2d). Locally, some of the Gen-II tourmaline veins contain significant amount of dumortierite. In view of this, the Gen-II are divided into Gen-IIA (without dumortierite) and Gen-IIB (with dumortierite). Gen-IIB tourmaline veins are mm to cm thick bands contains both tourmaline and dumortierite in widely varying proportions (Fig 6.2e). Stretching of Gen-II tourmaline and dumortierite layers supports the view that these layers are syn-tectonic with the shear foliation ( $S_2$ ) (Fig 6.2e). Gen-II tourmaline veins are folded by open to tight asymmetric folds ( $F_3$ ) (Fig 6.2e and Fig 6.2f). In outcrop scale, it is commonly observed that the KQ rock is extensively replaced by tourmaline and dumortierite veins oriented along  $S_2$  fabric. However, small relict patches of KQ rock still occasionally occur within this assemblage (Fig 6.2.g). The third generation (Gen-III) tourmaline occurs as thick ramifying tourmaline veins and dendritic aggregates. These Gen-III tourmaline veins are cut across to the high angle to the shear foliation ( $S_2$ ) as well as Gen-II tourmaline-dumortierite veins hosted by KQ rock (Fig 6.2i). In places, dumortierite layer are being replaced by Gen-III tourmaline (Fig 6.2h). Therefore, Gen-III tourmaline occurs after  $F_3$ . Late stage kyanite veins (Fig 6.2j) cut across KQ-dumortierite-tourmaline assemblage as well as the  $S_2$  plane. Kyanite veins occur as coarse bladed crystals of kyanite that develop perpendicular to the walls of the veins. Thus, this kyanite within kyanite veins is denoted as  $ky_2$ . Therefore these veins were emplaced after  $F_3$ .

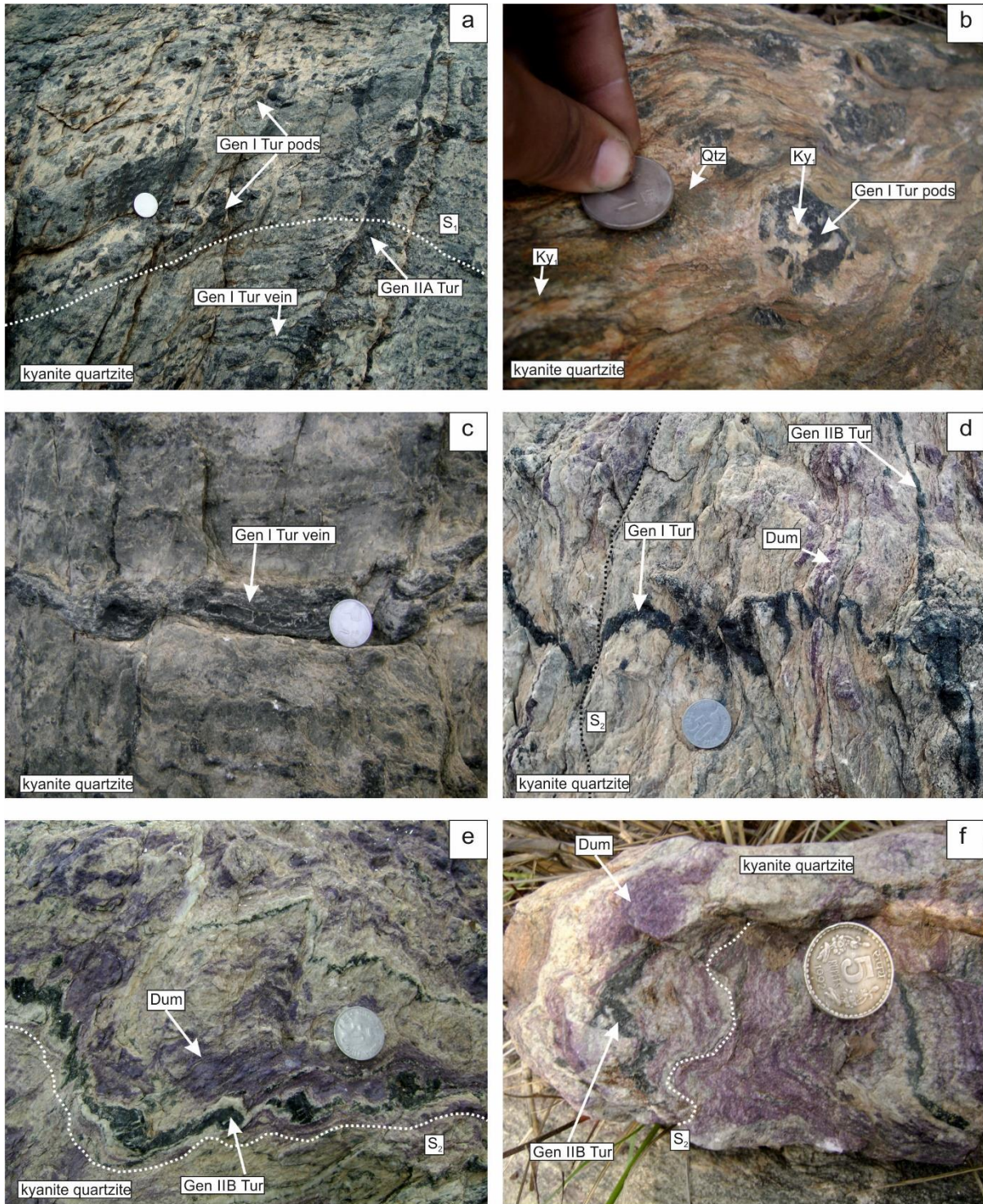


Fig 6.2a: The first generation (Gen I) tourmaline veins/pods develop along the  $S_1$  fabric. Gen II tourmaline veins cuts across the Gen I tourmaline veins. Fig 6.2b: The tourmaline rich pods (Gen I) oriented along the  $S_1$  fabric. Fig 6.2c: Gen I tourmaline vein shows pinch and swell structure along  $S_1$  fabric. Fig 6.2d: The second generation (Gen II) tourmaline and dumortierite veins(0.5cm to 2cm) cuts across the Gen I tourmaline veins and develop along the axial plane of the  $F_2$  folds .Fig 6.2e:Stretching of Gen II tourmaline-dumortierite layers supports the view that these layers are syn-tectonic with the shear foliation( $S_2$ ). Fig 6.2f: Gen-II tourmaline-dumortierite veins are folded by open to tight asymmetric folds ( $F_3$ ).

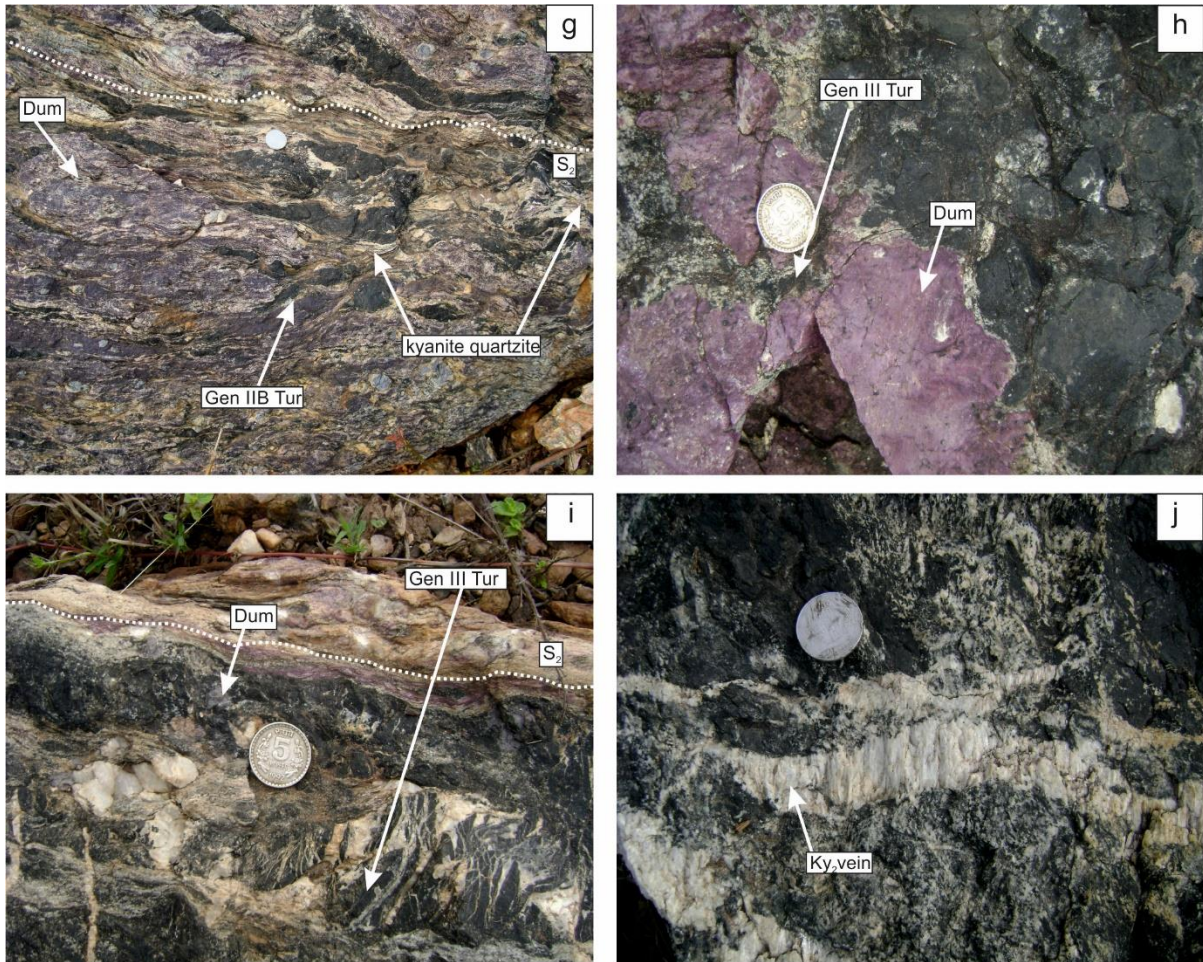


Fig 6.2g: The KQ rocks is extensively replaced by tourmaline and dumortierite veins oriented along  $S_2$  fabric. Fig 6.2h: dumortierite layer replace by Gen III tourmaline rich veins. Fig 6.2i: Gen-III tourmaline grains occur as thick ramifying tourmaline veins and dendritic aggregates cut across to the high angle to the shear foliation( $S_2$ ). Fig 6.2j: Kyanite veins occur as coarse bladed crystals of kyanite( $Ky_2$ ) that develop perpendicular to the walls of the veins.

### 6.3 Petrographic description of tourmaline bearing rocks

Textural relations among different minerals in the studied rocks show that kyanite ( $ky_1$ ), quartz and rutile constitute the earliest recognizable assemblage in the host KQ rock. Petrographic studies reveal that volumetric proportion of kyanite ( $ky_1$ ) within the KQ-rock varies widely, i.e. ~20-70 modal vol %. In the kyanite-rich end members (~60-70 modal vol% kyanite), kyanite forms the matrix of the rock where rutile and quartz occur at the interstitial places (Fig. 6.3a). Within isolated kyanite pods observed in the exposure of KQ-rocks (Fig.6.2b), the kyanite grains ( $ky_1$ ) are coarse and randomly oriented (Fig 6.3b).

Within the KQ-rock, the earliest foliation, i.e., the  $S_1$  fabric is rarely observed in the outcrop and under the microscope as it is pervasively transposed by the second-generation foliation, viz.  $S_2$ . Intense deformation and metamorphism that resulted the  $S_2$  fabric, developed a plethora of microstructures. Recrystallization of blades of kyanite ( $ky_1$ ) yielded polygonal aggregates of it (Fig 6.3a). Individual kyanite blades ( $ky_1$ ) show folding and development of multiple kinks (locally in conjugate sets) (Fig. 6.3c). Some places, kyanite ( $ky_1$ ) grains are boudinaged and exhibiting undulose extinction (Fig. 6.3d). Quartz grains show sutured and bulbous grain boundaries (Fig. 6.3e), undulose extinction, deformation bands and development of sub-grains. Marginal recrystallization in quartz grains develop a core-mantle structure. Kyanite ( $ky_1$ ) blades are extensively replaced by muscovite and pyrophyllite (Fig. 6.3f and 6.3g). Locally, the grains of phyllosilicates (pyrophyllite + muscovite) are oriented parallel to the prominent fabric ( $S_2$ ) (Fig. 6.3g and 6.3j). However, in some places, the grains of phyllosilicates (pyrophyllite + muscovite) do not show any orientation. This indicates that although replacement of kyanite may have started before or during the major deformation event ( $F_2$ ), their growth may have outlasted deformation (Fig 6.3d and 6.3f).

From the occurrences and textural relations observed during thin section study, the tourmaline grains are classified in three different generations. The first generation (Gen-I) tourmaline veins are bluish green in colour without notable zoning that occurs as aggregates of grains (Fig 6.3h and 6.3i). Gen-I tourmaline replaces the kyanite ( $ky_1$ ) grain within host KQ rock (Fig 6.3i).

Second generation tourmaline (Gen-II) that occurs as veins along the  $S_2$ -plane, are coarse to medium grained, granular in character (Fig 6.3h and 6.3i)) that commonly replace the Gen-I tourmaline (Fig 6.3h)

Second generation (Gen-II) tourmaline veins are mainly composed of granular aggregates along without (Gen-IIA) or with (Gen-IIB) dumortierite grains and both are parallel to the shear foliation ( $S_2$ ; Fig 6.3h and 6.3k). Gen-IIA tourmaline veins are solely composed medium to coarse, granular, prismatic aggregates of tourmaline grains. They exhibit brownish green core and light yellowish green rim under plane polarised light (PPL; Fig 6.3h). Gen-IIB tourmaline occurs as fine to medium, granular aggregates showing homogenous green body colour under PPL (Fig 6.3i and 6.3j). Locally, Gen-IIB tourmaline is oriented parallel to the shear foliation ( $S_2$ ) that is primarily defined by flakes of muscovite + pyrophyllite (Fig 6.3j).

It is commonly observed that both Gen-IIA and Gen-IIB tourmaline grains either cut across (Fig 6.3h) or replace the bluish green Gen-I tourmaline grains along the grain boundaries (Fig 6.3i). The dumortierite grains are pink-coloured, medium-grained, subhedral-granular that occur as aggregates along with Gen-IIB tourmalines following the  $S_2$ -foliation. The dumortierite grains replace the kyanite ( $ky_1$ ) and muscovite + pyrophyllite assemblage (Fig 6.3k and 6.3l). It is also observed that both kyanite ( $ky_1$ ) and dumortierite are replaced by the Gen-IIB tourmaline along the grain boundaries (Fig. 6.3m). Such replacement texture is defined by aggregates of Gen-IIB tourmaline around relict crystals of kyanite and dumortierite (Fig. 6.3m). Dumortierite aggregates are aligned along the  $S_2$  planes replacing both kyanite and muscovite + pyrophyllite oriented along  $S_2$  (Fig 6.3k). Again, the Gen-IIB tourmaline grains also grow preferably along the  $S_2$  planes suggesting that the growth of phyllosilicates (muscovite + pyrophyllite) replacing kyanite, dumortierite and Gen-IIB tourmaline all are syn-tectonic to the second phase of deformation forming  $S_2$ . However, replacement of dumortierite by Gen- IIB tourmaline suggests that dumortierite formed earlier than Gen-IIB tourmaline.

Third Generation of tourmaline (Gen-III) grains are mostly fine-grained, prismatic in shape and exhibit dark green to brown pleochroism (Fig 6.3n and 6.3o). They are either randomly oriented or show rosette texture (Fig 6.3n and 6.3o). Gen-III tourmaline grains replace the earlier tourmaline (Gen-IIB) -dumortierite, phyllosilicate and kyanite ( $ky_1$ ) assemblage (Fig 6.3n and 6.3o). Therefore, Gen-III tourmaline occurs after  $F_3$ . At places, coarse-grained kyanite ( $ky_2$ ) veins cut across the aforementioned tourmaline (Gen-II), dumortierite, kyanite( $ky_1$ ) and phyllosilicates (muscovite + pyrophyllite) assemblage (Fig 6.3p). Here, the kyanite ( $ky_2$ ) occurs as coarse, bladed crystals growing perpendicularly to the vein walls (Fig 6.3p).  $Ky_2$  exclusively occurs as coarse-grained, monominerallic kyanite veins and is distinctly different from  $ky_1$ , which occurs along with quartz in the host KQ-rock.

The successive mineralisation events and their corresponding textural characters in the study area are summarized below:

1. The modal abundance ratio of kyanite and quartz in the quartz-kyanite host rock of tourmaline mineralization varies widely starting from ~20-30 molar vol % to up to molar vol 70% kyanite. These kyanite ( $ky_1$ ) grains are replaced by an assemblage of muscovite and pyrophyllite that are aligned along the  $S_2$ .
2. The Gen-I bluish green tourmalines occur as fine-grained aggregates, preferentially along the  $S_1$  fabric.
3. Both kyanite ( $ky_1$ )-quartz and Gen-I tourmaline grains are replaced by, medium to coarse grained, green Gen-II tourmaline that preferentially grows along the  $S_2$  foliation planes. Gen-II tourmalines occur without (Gen-IIA) or with (Gen-IIB) association of dumortierite that also occur preferentially along the  $S_2$  foliation. Gen-IIB tourmalines are commonly seen to replace dumortierite along grain margins. Therefore, although both dumortierite and Gen-IIB tourmaline are syntectonic regarding  $S_2$  to  $F_3$  (i.e. both occur preferentially along the  $S_2$ ) the former must have crystallized earlier than the latter.
4. The dark green to brown, Gen-III tourmalines occur as aggregate of prismatic grains showing random to rosette orientation. They grow over the earlier assemblage of kyanite ( $ky_1$ )-quartz and Gen-II tourmaline-dumortierite. Therefore, Gen-III tourmaline occurs after  $F_3$ .
5. Coarse-grained kyanite veins ( $ky_2$ ) cut across the earlier assemblage of kyanite ( $ky_1$ )-quartz and Gen II tourmaline-dumortierite. This kyanite ( $ky_2$ ) specifically occurs as veins that cut across older fabrics and are distinguishable from  $ky_1$  by their distinctly coarser grain size and near monomineralic composition.

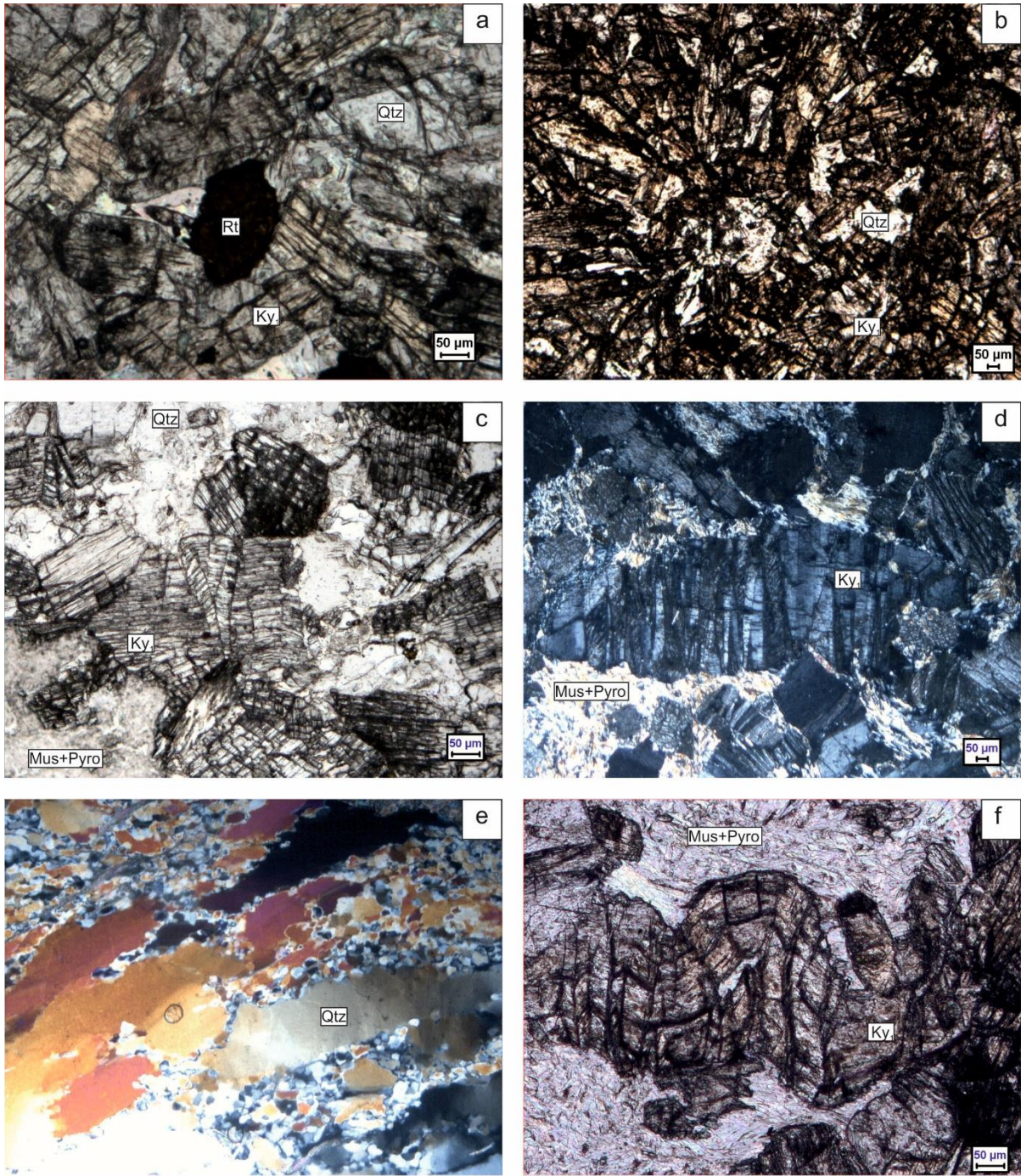


Fig 6.3a: The host KQ rocks consist of kyanite ( $ky_1$ ) (> 80 vol%) with rutile and quartz. Fig 6.3b: kyanite ( $ky_1$ ) occurs as a pods, shows randomly oriented blades of kyanite( $ky_1$ ). Fig 6.3c: kyanite ( $ky_1$ ) grains shows folding of individual blades and development of multiple kinks (locally in conjugate sets) in kyanite ( $ky_1$ ) crystals. Fig 6.3d: kyanite ( $ky_1$ ) grains are boudinaged and presence of undulatory extinction(under CPL). Fig 6.3e: Quartz grains show ductile deformation that is manifested by formation of ribbons, development of deformation bands, sub-grains, undulatory extinction, marginal and are stretched along  $S_2$ (under CPL). Fig 6.3f: Kink bands of kyanite ( $ky_1$ ) are extensively replaced by muscovite and pyrophyllite.

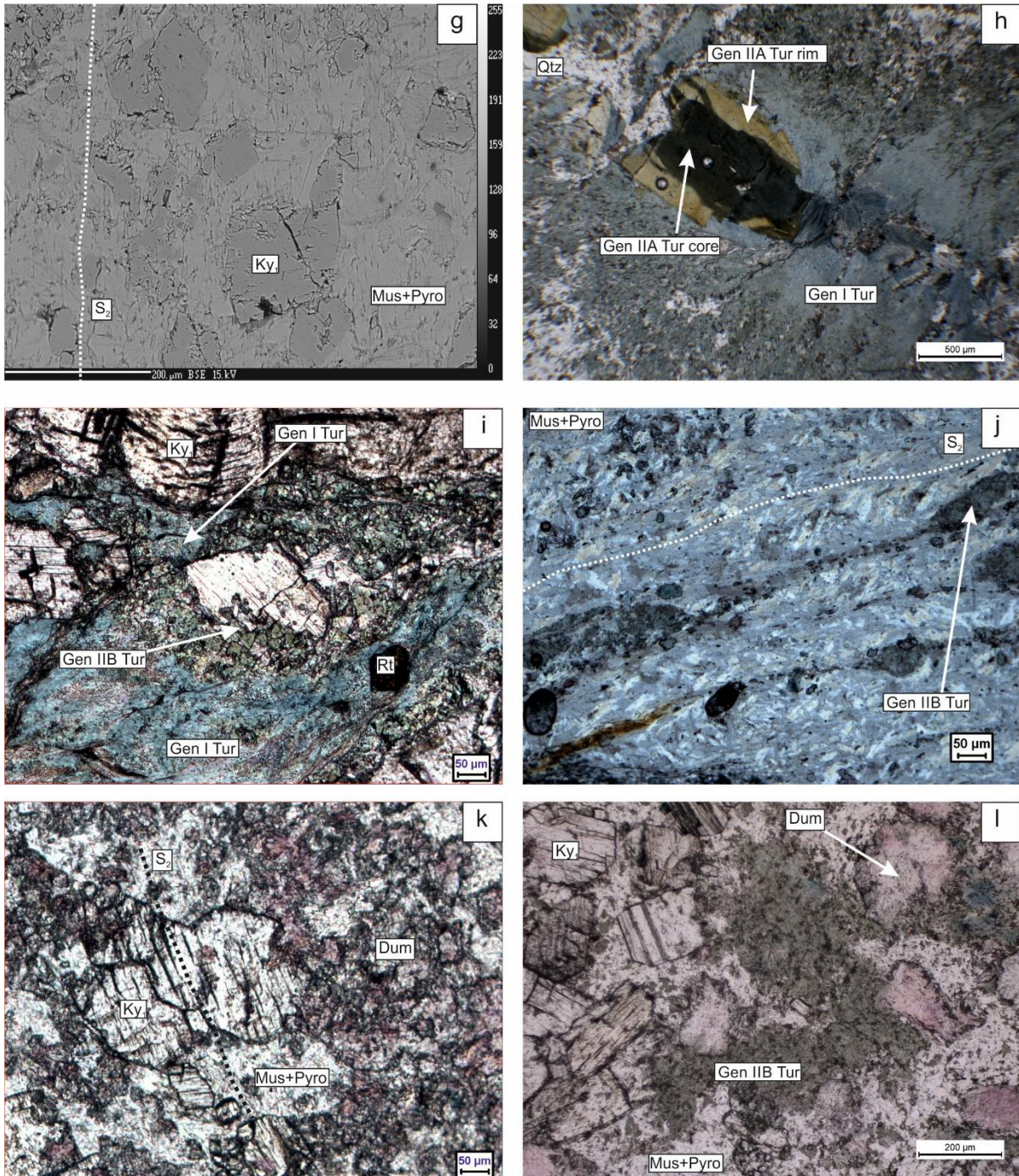


Fig 6.3g: BSE image of KQ rock where kyanite( $ky_1$ ) are extensively replaced by muscovite and oriented parallel to  $S_2$ (BSE image). Fig 6.3h: Gen I tourmaline veins is bluish green in colour with lack of zoning and occurs as aggregates of grains which is cut across by zoned Gen IIA tourmaline vein. Fig 6.3i: Gen IIB green tourmaline replace the kyanite( $ky_1$ ) grains as well as Gen I bluish green tourmaline. Fig 6.3j: Grains of phyllosilicates (pyrophyllite+muscovite) are oriented parallel to the prominent the shear fabric ( $S_2$ ). Gen IIB tourmaline formed along  $S_2$  fabric. Fig 6.3k: Dumortierite rich aggregates along  $S_2$ , replace the both kyanite( $ky_1$ ) and muscovite + pyrophyllite. Fig 6.3l: The Gen IIB tourmaline veins extensively replaced the kyanite ( $ky_1$ ) grains as well as phyllosilicates (muscovite+pyrophyllite).

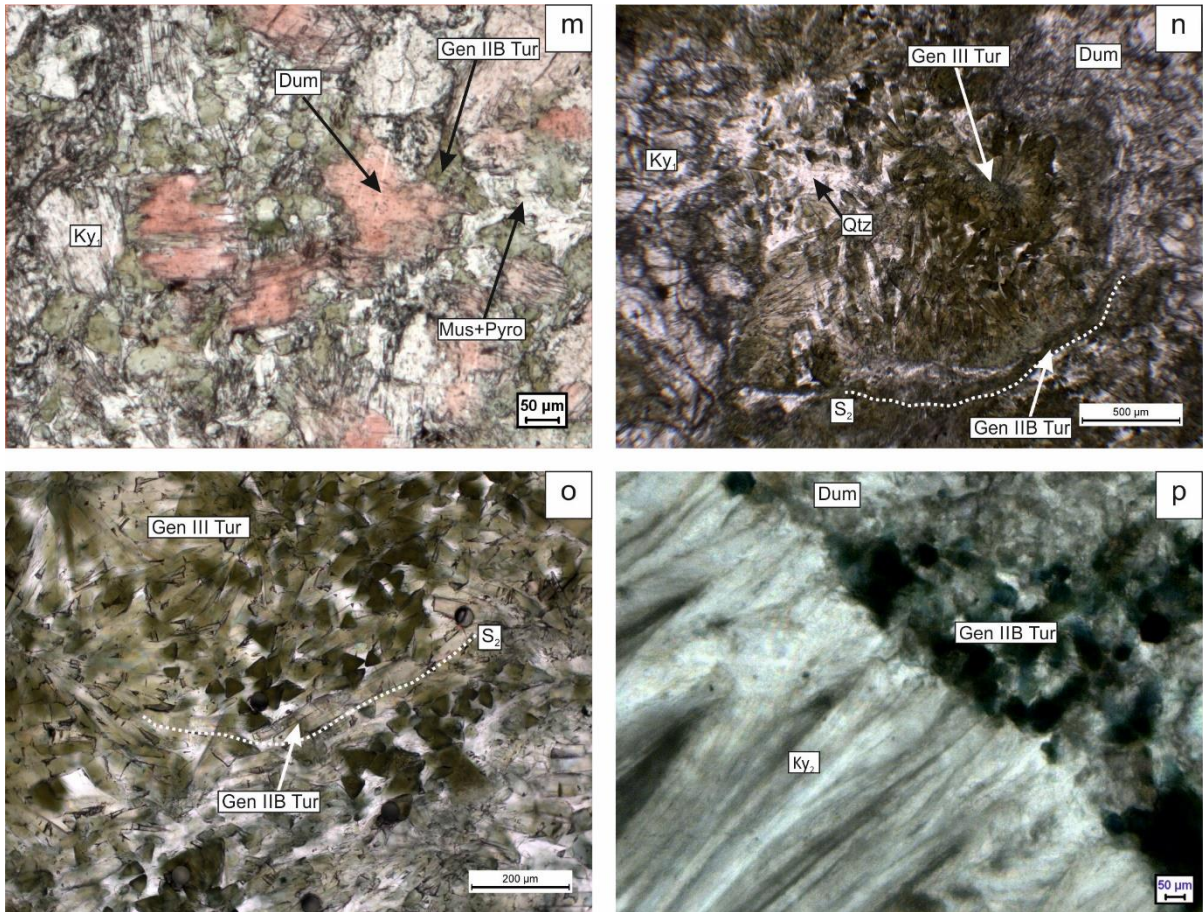


Fig 6.3m: Gen IIB green tourmaline replace dumortierite grains parallel to shear foliation( $S_2$ ). Fig 6.3n: Gen III tourmaline is extensively replacing the aggregates of tourmaline (Gen IIB), dumortierite, phyllosilicates and kyanite ( $ky_1$ ). Fig 6.3o: Gen IIB tourmaline cut across by Gen III tourmaline aggregates. Fig 6.3p: kyanite ( $ky_2$ ) veins occurs as coarse bladed crystals of kyanite( $ky_2$ ) that develop perpendicular to the walls of the vein.

## 6.4 Tourmaline mineral chemistry

Standard analytical procedure of major element analysis of some representative samples from the borosilicate-bearing veins and host kyanite-quartzite with associated minerals are given in appendix I. Procedure of normalization of tourmaline and dumortierite are also given in appendix II. Overall, T-sites of tourmaline in all the tourmaline veins (Gen-I, -IIA, -IIB and -III) are nearly filled with Si (Gen-I:  $5.92 \pm 0.03$  apfu; Gen-IIA:  $5.86 \pm 0.14$  apfu; Gen-IIB:  $5.94 \pm 0.05$  apfu; Gen-III:  $5.89 \pm 0.08$  apfu). The Z site of the tourmaline is completely filled up with Al for Gen-I, Gen-IIB and Gen-III. The Al in apfu of the tourmaline compositions exceeds 6 suggesting that some Al must be present in Y site. Al-content of tourmaline varies viz. Gen-I:  $6.96 \pm 0.12$  apfu; Gen-IIA:  $6.24 \pm 0.72$  apfu; Gen-IIB:  $7.09 \pm 0.13$  apfu; Gen-III:  $7.14 \pm 0.21$  apfu respectively. However, Gen-IIA tourmaline core ( $5.59 \pm 0.18$  apfu) is low aluminous than the rim ( $6.97 \pm 0.11$  apfu). Thus, the Gen-II tourmaline core Z site is not completely filled up Al and no Al is present in Y site. Al content in some of the tourmaline grains of Gen-IIB and Gen-III are very high (Gen-IIB: 6.95 - 7.35 apfu and Gen-III: 6.72 - 7.58 apfu) than the Gen-I and Gen-IIA. Therefore, tourmaline compositions of Gen-I, Gen-IIA rim, Gen-IIB and Gen-III are aluminous (Al>6 apfu) in nature but Gen-IIA core is Al deficient (Al<6 apfu). Ti content of tourmaline structure is varies viz. Gen-I:  $0.01 \pm 0.01$  apfu; Gen-IIA:  $0.10 \pm 0.03$  apfu; Gen-IIB:  $0.02 \pm 0.01$  apfu; Gen-III:  $0.03 \pm 0.02$  apfu respectively. X site vacancy, estimated from the measured Na+Ca+K content, shows a corresponding systematic variation, viz. Gen-I ( $0.43 \pm 0.06$  apfu); Gen-IIA ( $0.17 \pm 0.11$  apfu); Gen-IIB ( $0.57 \pm 0.11$  apfu); Gen-III ( $0.59 \pm 0.08$  a.p.f.u). Gen-I tourmaline composition straddles the boundary between alkali group and X vacancy group (Figure 6.4.1a). Gen-IIA tourmaline grains are plotted in the alkali group. There is major X-vacancies difference between the core and rim of the Gen-IIA tourmaline grain. The core is very low X-vacancies ( $0.07 \pm 0.03$  apfu) than the rim ( $0.28 \pm 0.02$  apfu). The tourmaline grains of the Gen-IIB and -III veins plot in the vacancy group (Figure 6.4.1a). Average Ca contents of tourmaline corresponding to different generations varies viz. Gen-I:  $0.05 \pm 0.02$  apfu; Gen-IIA:  $0.25 \pm 0.10$  apfu; Gen-IIB:  $0.03 \pm 0.02$  apfu; Gen-III:  $0.05 \pm 0.02$  apfu. So, the Gen-IIA is more calcic the Gen-I, -IIB and -III. Moreover, Gen-IIA core ( $0.34 \pm 0.07$  apfu) is more calcic than the corresponding rim ( $0.16 \pm 0.03$  apfu). For classification purposes, compositions have been plotted in the X-vac/ (X -vac+ Na) vs.  $X_{Mg}$  diagram where  $X_{Mg} = Mg+Fe$  (Figure 6.4.1b). Gen-I tourmaline is distinctly magnesium rich in comparison with the tourmaline in Gen-IIA, Gen-IIB and Gen-III. They straddle in boundary between dravite (or “oxy-dravite”) and magnesiofoitite (or “oxy-magnesio-foitite”). Gen-IIA

tourmaline grain shows distinctly magnesium rich and X-vacancy poor and plotted in the field of dravite (or “oxy-dravite”). Gen-IIB tourmaline are magnesium rich and X-vacancy plotted in the boundary between foitite (or “oxy-foitite”) and magnesio-foitite (or “oxy-magnesio-foitite”). The Gen-III tourmaline grains are plotted in the field of foitite (or “oxy-foitite”) (Figure 6.4.1b). From the diagram it shows that Gen-III and Gen-IIB veins have higher X-site vacancy ( $\square$ ) than Gen-I and Gen-IIA. The  $Mg/(Mg + Fe^{2+})$  or  $X_{Mg}$  shows a corresponding systematic variation viz. Gen-I ( $0.82 \pm 0.08$  apfu); Gen-IIA ( $0.67 \pm 0.04$  apfu); Gen-IIB ( $0.55 \pm 0.10$  apfu); Gen-III ( $0.40 \pm 0.09$  apfu). The  $X_{Mg}$  content in the core ( $0.64 \pm 0.02$  apfu) is lower than the rim ( $0.71 \pm 0.01$  apfu) of Gen-IIA tourmaline. Sengupta et al., 2011, also reported tourmaline in the same area. According to Sengupta et al., 2011, there are three generations of tourmaline which are vacancy to alkali rich in composition (Figure 6.4.1a). The tourmaline are dravite (+“oxy-dravite”) to Mg foitite (+“oxy-magnesio-foitite”) to foitite (+“oxy-foitite”) in character (Figure 6.4.1b). Pal et al., 2010, reported tourmaline in different host rock like quartz vein, biotite schist, chlorite schist, quartz tourmaline rock near Jaduguda of SSZ. According to Pal et al., 2010, tourmaline compositions are mainly alkali rich and dravitic in composition (Figure 6.4.1a). Recently, Patel et al., 2021 reported tourmaline mineralization in Mohuldih and Bagjada area within quartz-chlorite-sericite-schist and quartz-biotite-chlorite-muscovite schists of SSZ. Tourmalines are schorlitic to dravitic in composition ((Figure 6.4.1b). Representative different generations of tourmaline compositions are presented in Table 6.4.3a.

Tourmalines show extensive substitution in the X-, Y-, Z-, T-, and W-sites (Hawthorne and Henry, 1999). The different types of substitutions in the cation and anion sites of natural tourmalines have been reviewed in several publications (Henry and Dutrow, 1996; Slack, 1996; Henry et al., 2002). In Gen-I, -IIA, -IIB and -III tourmaline grain Fe contents shows a corresponding systematic variation viz. Gen-I ( $1.10 \pm 0.20$  apfu); Gen-IIA ( $0.92 \pm 0.30$  apfu); Gen-IIB ( $0.85 \pm 0.24$  apfu); Gen-III ( $0.35 \pm 0.18$  apfu) and the Mg contents viz. Gen-I ( $0.75 \pm 0.19$  apfu); Gen-IIA ( $1.82 \pm 0.31$  apfu); Gen-IIB ( $1.03 \pm 0.11$  apfu); Gen-III ( $1.67 \pm 0.17$  apfu). In Fe vs Mg diagrams (Figure 6.4.1c) tourmaline grains from Gen-IIA core show very high Fe and Mg value than the Gen-I, -IIA rim, -IIB and -III. In Gen-IIA core  $Fe^{2+} = 1.19 \pm 0.10$  apfu and  $Mg = 2.09 \pm 0.14$  apfu, whereas in rim  $Fe^{2+} = 0.62 \pm 0.03$  apfu and  $Mg = 1.52 \pm 0.06$  apfu. In Gen-IIA tourmaline core shows a strong trend parallel to the substitution vector  $MgFe_{-1}$ . Gen-IIA core tourmaline compositions plot above line  $Fe^{2+} + Mg = 3$  which indicates no Al in Y sites. Tourmaline grains from Gen-I, Gen-IIA rim, -IIB and -III show a strong trend parallel to the substitution vector  $MgFe_{-1}$  and tourmaline compositions are plot much below the line

$Fe+Mg=3$  which indicates substitution of Al in Y sites. In  $Al_{total}$  vs Si diagram (Figure 6.4.1d) Gen-I, -IIB and -III shows a poor negative correlation ( $r^2 = 0.47$ ) and minor substitution occur along the  $Al_2(R)_{-1}(Si)_{-1}$  exchange vector. But Gen-IIA core and rim data occur as cluster and no correlations found between them. In  $Al^{(Z)} + Al^{(Y)}$  vs  $Fe + Mg + Mn$  diagram, also strong negative correlation ( $r^2 = 0.99$ ) noted which indicates that chemical substitution is dominated and expressed by the exchange vectors towards  $\square Al(NaR)_{-1}$  and  $AlO[R(OH)]_{-1}$  where  $R = Fe^{2+} + Mg$  (Figure 6.4.1e). In the  $[R_1(=Na + Ca) + R_2(=Fe + Mg + Mn)]$  vs.  $[R_3(=Al + 1.33 \times Ti)]$  plot, most of the tourmaline compositions fall within the lower half of the parallelogram formed by the lines joining the positions of the tourmaline species (Figure 6.4.1f). Although the array of data in this plot suggests operation of both exchange vectors  $AlO[R(OH)]_{-1}$  and  $\square Al(NaR)_{-1}$ , most of the tourmaline compositions concentrate within the triangular area defined by the foitite, “oxy-foitite” and “oxy-dravite” end-members and is consistent with the presence of significant amounts of  $O_{-2}$  replacing  $(OH)_{-1}$  in the W-site of this tourmaline. But the Gen-IIA tourmaline core is plotted outside the parallelogram near the field of schorl/dravite and indicates that absence of Al in Y sites. This can further be tested by plotting the data in terms of excess charge vs.  $Fe + Mg + X$ -site vacancy diagram (Figure 6.4.1g). Excess charge is the sum of cation charges exceeding 49 for the tourmaline compositions normalized to  $T + Z + Y = 15$  (Henry and Dutrow, 1996). Despite significant uncertainty, the amount of excess charge provides an estimate of replacement of  $(OH)_{-1}$  by  $O_{-2}$ . The tourmaline grains of Gen-IIA core composition shows excess charge nearly 0 or  $<0$ , which indicates stronger influence from the substitution  $AlO[R(OH)]_{-1}$ . Tourmaline with  $>0.5$  excess charge is considered to be of the “oxy” variety (Arif et al., 2010). Therefore  $\sim 60\%$  of the total analysed tourmaline of Gen-I, -IIA rim, -IIB and -III of the study area belongs to the “oxy” species. Tourmaline from Gen-I veins is either dravite, magnesio-foitite or their corresponding “oxy” species, because of their lower value of X-site vacancy, higher  $X_{Mg}$  value and excess charge. Gen-IIA core tourmaline is not considered as “oxy” variety cause the composition with nearly 0 excess charge and dravite in composition but Gen-II rim is “oxy-dravite” due to presence of  $>0.5$  excess charge. The tourmaline from Gen-IIB and -III veins is either “oxy-foitite” or foitite because of their higher value of X- site vacancy, excess charge and lower  $X_{Mg}$  value. Furthermore, to understand the effect of substitutions other than  $AlO[R(OH)]_{-1}$ , the data are plotted in an X-site vacancy vs. total Al diagram (Figure 6.4.1h). In Gen-I tourmaline can also be explained by the alkali exchange vector  $\square Na_{-1}$ . On this plot, distribution of the compositions for tourmaline in Gen-IIA can also be explained by resultant of two exchange vector  $\square Al(NaR)_{-1}$  and  $AlO[R(OH)]_{-1}$ . Gen-IIB suggests chemical substitutions defined by the exchange vectors

$\square\text{Na}_{-1}$  and  $\square\text{Al}(\text{NaR})_{-1}$ . Substitution via the  $\text{AlO}[\text{R}(\text{OH})]_{-1}$  and  $\square\text{Al}(\text{NaR})_{-1}$  exchange vector is dominant in Gen-III tourmaline compositions.

Figure 6.4.2a is a line traverse that shows the compositional variation across optical zoning of a Gen-IIA tourmaline grain. The optical zoning coincides with significant compositional zoning. Gen-IIA tourmaline grain displays strong optical zoning characterized by deep brownish green colour cores and yellowish green in colour rims. Tourmaline grain core is enriched with Ca, Ti whereas the rim is enriched in  $X_{\text{vac}}$ , Al,  $X_{\text{Mg}}$  with Mg and Fe decreases towards the rim (Figure 6.4.2a). To clarify the chemical substitutions, the compositional data have been plotted in several different diagrams. In Fe vs Mg diagram prominent Fe-Mg substitution occurs (core is highly Fe and Mg rich than the rim), showing a strong substitution trend parallel to  $\text{MgFe}_{-1}$  ( $r^2=0.97$ ) (Figure 6.4.2b). In  $\text{Al}_{\text{total}}$ -vs- X-site vacancy diagram (Figure 6.4.2c), the spread of tourmaline compositions show that the chemical substitution was dominated and expressed by the exchange vectors towards  $\square\text{Al}(\text{NaR})_{-1}$  ( $r^2=0.98$ ) where  $\text{R} = \text{Fe} + \text{Mg}$ . The array of data in the  $\text{Fe} + \text{Mg} + \text{Ti}$  vs. total Al diagram suggests that chemical substitution was dominated and expressed by the exchange vectors  $\text{AlO}[\text{R}(\text{OH})]_{-1}$  ( $r^2=0.99$ ) (Figure 6.4.2d). In  $X_{\text{vac}}$  vs Ca diagram its shows that  $\text{CaRO}[\square\text{Al}(\text{OH})]_{-1}$  exchange vector is responsible for the core to rim substitution. (Figure 6.4.2e).

Muscovite shows a significant amount of pyrophyllite component (~32 mol %). The muscovite associated with dumortierite (and very less tourmaline) has higher magnesium values ( $X_{\text{Mg}} = \text{Mg}/\text{Mg} + \text{Fe}^{2+}$  varies from 0.38 to 0.70) while muscovite associated with tourmaline has moderate to low magnesium values ( $X_{\text{Mg}}$  varies from 0.11 to 0.41). Pyrophyllite, kyanite and rutile are almost end-member compositions. The dumortierite grains contain small amount of Fe and Mg (upto 0.05 apfu) and significant titanium (0.75-0.85wt%  $\text{TiO}_2$  that correspond to ~0.05apfu). The structural formula of the dumortierite calculated from EPMA analysis is  $(\text{Al}_{6.67}\text{Mg}_{0.05}\text{Ti}_{0.05}\text{Cr}_{0.01}\text{Fe}_{0.01}\square_{0.21})\Sigma_{7.00}\text{B}(\text{Si}_{2.86}\text{Al}_{0.13}\text{P}_{0.01})\Sigma_{3.00}\text{O}_{17.25}\text{OH}_{0.75}$ . Compositions of muscovite, pyrophyllite, kyanite, dumortierite and rutile are presented in Table 6.4.3b.

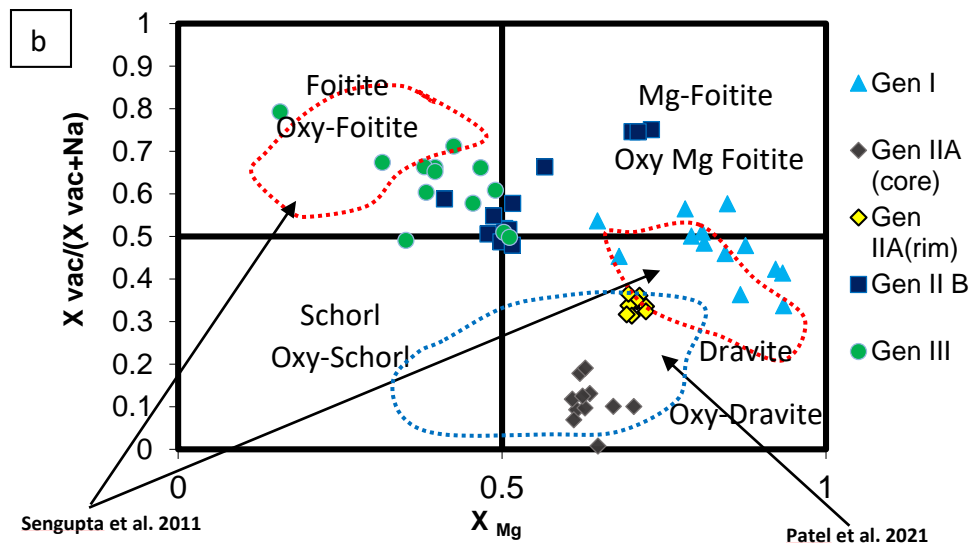
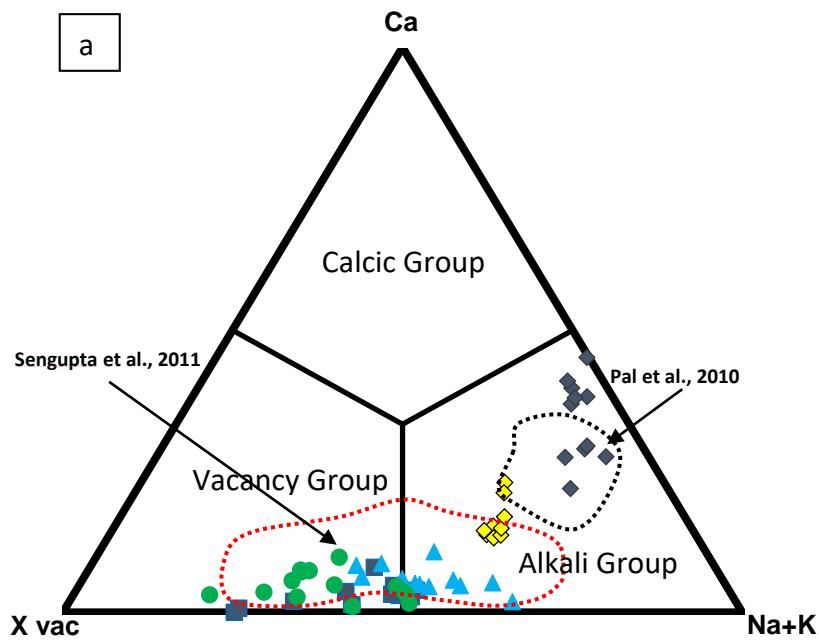


Figure 6.4.1a: Principal tourmaline groups based on the classification scheme of Hawthorne and Henry (1999). Figure 6.4.1b Nomenclature diagram of tourmaline based on X-site vacancy/(X-site vacancy + Na) vs. Mg/(Mg + Fe<sup>2+</sup>) plot after Henry et al. (2003).

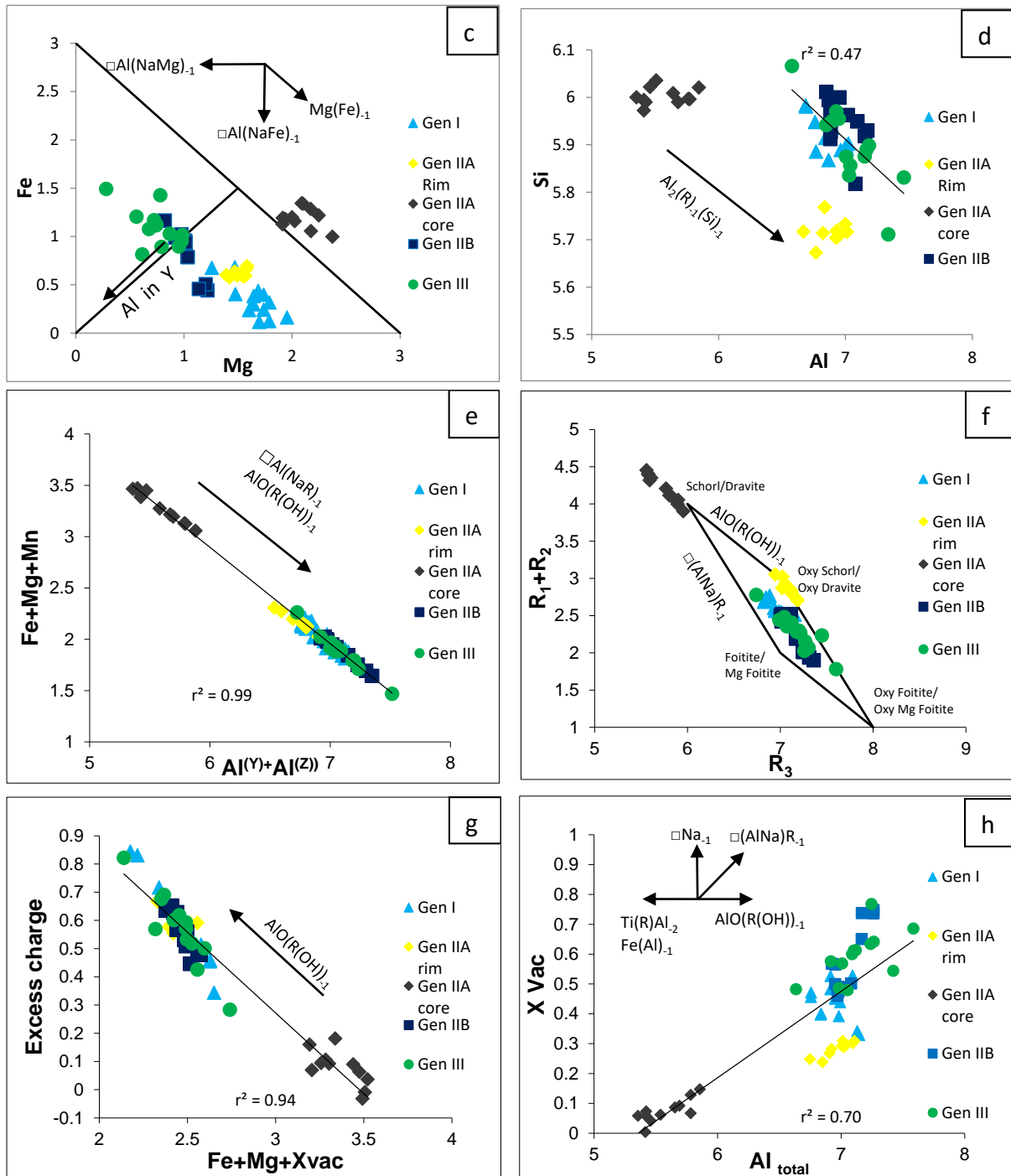


Figure 6.4.1c: Mg vs. Fe plot for tourmaline of different generations. Figure 6.4.1d:  $\text{Al}_{\text{total}}$  vs. Si plot shows moderate correlation along the  $\text{Al}_2(\text{R})_{-1}(\text{Si})_{-1}$  exchange vector. Figure 6.4.1e:  $(\text{ZAl} + \text{YAl})$  vs.  $(\text{Fe} + \text{Mg} + \text{Mn})$  plot shows a strong negative correlation ( $r^2 = 0.99$ ). Directions of exchange vectors are shown for reference. Figure 6.4.1f: Lines that join the positions of the tourmaline end-members in the  $(\text{R}_1 + \text{R}_2)$  vs.  $\text{R}_3$  plot define a parallelogram. Most of the tourmaline compositions plot in the lower half of the parallelogram because of their aluminous nature ( $\text{R}_1 = \text{Na} + \text{Ca}$ ;  $\text{R}_2 = \text{Fe}^{+2} + \text{Mg} + \text{Mn}$ ;  $\text{R}_3 = \text{totalAl} + 1.33 \times \text{Ti}$ ), whereas only Gen-IIA core compositions are plotted outside the upper part of parallelogram because of low Al in nature. Figure 6.4.1g: Excess charge vs.  $(\text{Fe} + \text{Mg} + \text{X-site vacancy})$  plot of all tourmaline compositions. strong correlation ( $r^2 = 0.94$ ) with a negative slope. Figure 6.4.1h: X-site vacancy vs.  $\text{Al}_{\text{total}}$  diagram of all different generations of tourmaline compositions. Directions of exchange vectors are shown for reference.

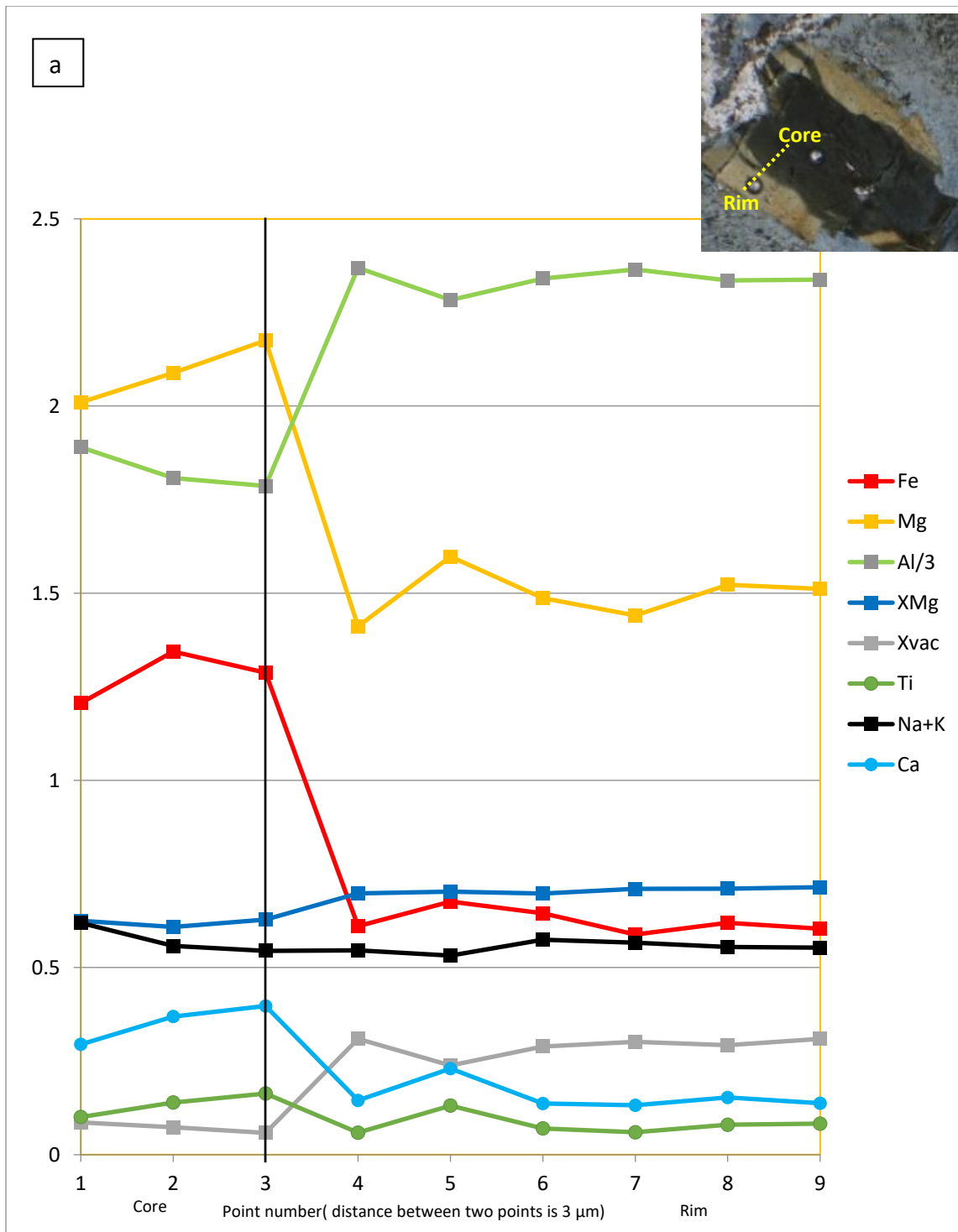


Figure 6.4.2a: Plot of compositional variations from the deep brownish green colour core and yellowish green in colour rim of a single zoned Gen-IIA tourmaline grain.  $X_{Mg} = Mg/(Fe^{2+} + Mg)$ . Zero on the X-axis represents the starting point of the compositional traverse from the deep brownish green colour core. Photomicrograph of the zoned tourmaline and the traverse path is shown by the solid line (plane polarized light). Al Plotted as Al/3

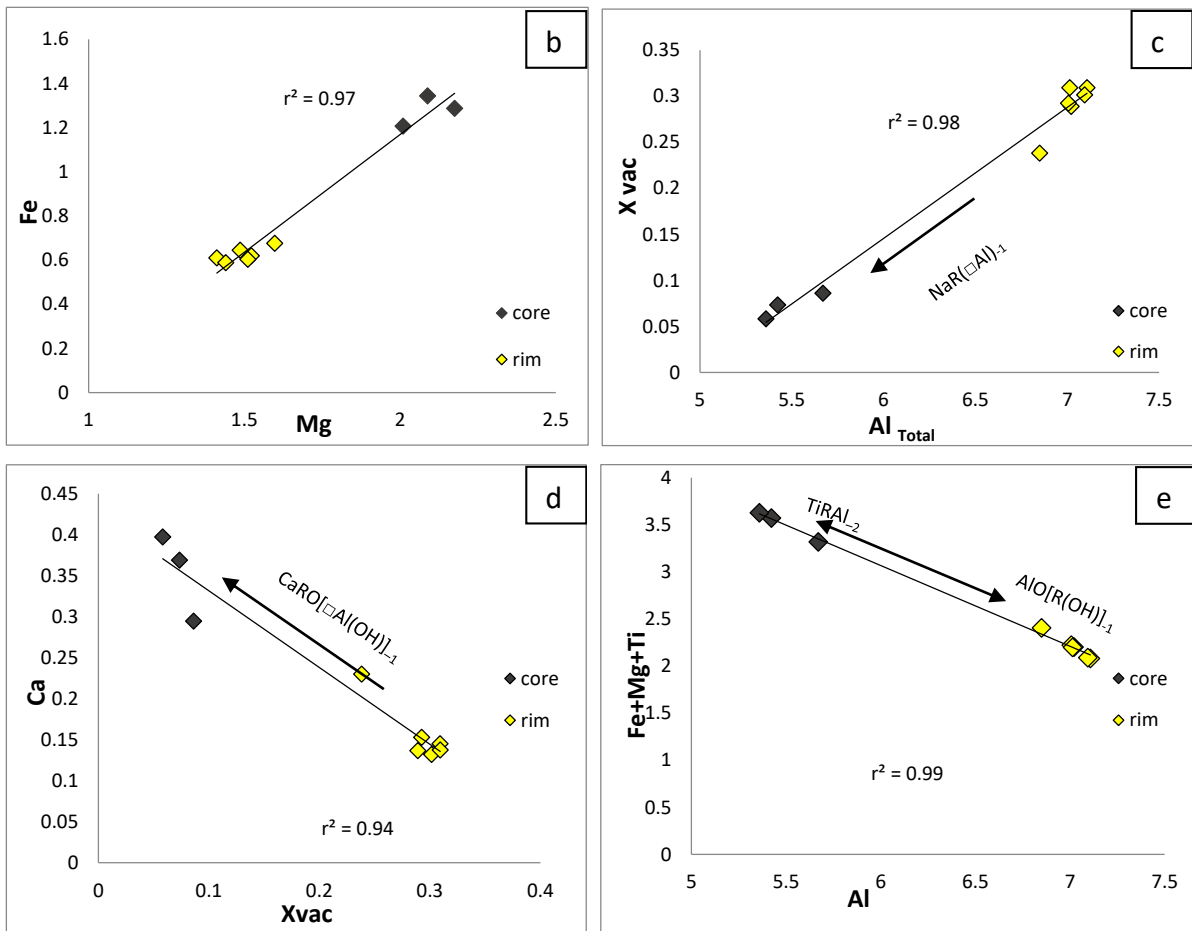


Figure 6.4.2b: Plot of data from the traverse of the zoned Gen-IIA tourmaline grain in terms of Fe vs. Mg showing positive ( $r^2 = 0.97$ ) strong correlations. Figure 6.4.2c: Plot of data from the traverse of the zoned grain in terms of X-site vacancy vs.  $Al_{total}$  showing positive ( $r^2 = 0.98$ ) strong correlations. Figure 6.4.2d: Plot of data from the traverse of the zoned grain in terms of Ca vs. X-vac negative ( $r^2 = 0.95$ ) strong correlations. Figure 6.4.2e: Plot of data from the traverse of the zoned grain in terms of Fe+Mg+Ti vs.  $Al_{Total}$  negative ( $r^2 = 0.99$ ) strong correlations.

Table 6.4.3a : Representative EPMA analysis of tourmaline.

Generation	Gen I	Gen I	Gen I	Gen I	Gen I	Gen I	Gen I	Gen I	GenIIA												
Sample no.	S 30A	S 30A	S 30A	S 30A	S 30A	S 30A	S 30A	S 30A	S 30D												
Point	23 / 4	23 / 5	23 / 6	23 / 7	23 / 8	23 / 9	23 / 10	23 / 11	23 / 12	23 / 13	23 / 14	23 / 15	28 / 1	19 / 1	1 / 1	2 / 1	7 / 1	8 / 8	8 / 9	8 / 10	
Core/Rim														core							
Al <sub>2</sub> O <sub>3</sub>	37.74	36.22	36.36	37.18	35.89	32.91	37.22	36.05	37.61	38.92	38.01	37.64	36.83	29.13	29.68	27.84	29.05	27.06	27.66	27.94	
FeO	0.98	3.04	3.35	2.95	2.35	2.68	5.11	5.13	1.88	0.91	1.84	2.30	1.25	8.50	8.58	9.64	8.36	9.17	9.66	8.38	
TiO <sub>2</sub>	0.07	0.25	0.23	0.18	0.11	0.12	0.16	0.29	0.05	0.01	0.01	0.09	0.01	0.61	0.63	0.63	0.83	1.29	1.11	0.78	
SiO <sub>2</sub>	38.34	38.21	38.34	37.89	36.17	32.67	37.12	36.96	38.49	38.57	37.67	38.19	38.21	35.75	36.35	36.20	36.12	35.77	36.01	35.09	
K <sub>2</sub> O	0.03	0.03	0.00	0.03	0.02	0.01	0.02	0.04	0.05	0.03	0.03	0.00	0.02	0.03	0.02	0.06	0.03	0.01	0.04	0.07	
CaO	0.29	0.31	0.36	0.29	0.48	0.32	0.51	0.63	0.30	0.12	0.31	0.27	0.34	1.53	1.55	2.14	1.63	2.21	2.07	1.61	
Na <sub>2</sub> O	1.85	1.60	1.55	1.53	1.23	1.16	1.37	1.57	1.64	2.18	1.98	1.71	1.80	2.01	1.85	1.75	1.90	1.67	1.71	1.82	
Cr <sub>2</sub> O <sub>3</sub>	0.41	0.08	0.20	0.28	0.21	0.07	0.05	0.02	0.04	0.00	0.00	0.09	0.07	0.00	0.02	0.00	0.05	0.09	0.13	0.10	
MnO	0.00	0.00	0.00	0.03	0.08	0.03	0.00	0.00	0.00	0.00	0.00	0.00	0.02	0.01	0.00	0.00	0.02	0.02	0.00	0.00	
MgO	7.76	7.45	7.26	7.07	7.41	5.48	5.32	6.20	7.54	7.44	6.88	7.10	8.42	7.66	7.88	8.48	8.19	8.69	8.43	7.84	
B <sub>2</sub> O <sub>3</sub> *	11.24	11.09	11.14	11.13	10.71	9.62	10.95	10.91	11.23	11.35	11.10	11.17	11.16	10.35	10.53	10.44	10.48	10.35	10.44	10.14	
Total	98.70	98.27	98.79	98.55	94.65	85.08	97.81	97.79	98.81	99.53	97.83	98.56	98.14	95.56	97.09	97.18	96.67	96.32	97.24	93.76	
Si(T)	6.00	6.00	6.00	5.98	5.91	5.97	5.96	5.95	6.00	6.00	5.99	6.00	6.00	6.00	6.00	6.00	6.00	6.00	6.00	5.99	6.00
Al(T)	0.07	0.02	0.02	0.09	0.13	0.10	0.11	0.11	0.04	0.10	0.11	0.06	0.05	0.00	0.00	0.00	0.01	0.00	0.01	0.00	
B(T)	3.00	3.00	3.00	3.00	3.00	3.00	3.00	3.00	3.00	3.00	3.00	3.00	3.00	3.00	3.00	3.00	3.00	3.00	3.00	3.00	
Al(Z)	6.00	6.00	6.00	6.00	6.00	6.00	6.00	6.00	6.00	6.00	6.00	6.00	6.00	5.76	5.77	5.46	5.67	5.35	5.41	5.64	
Al(Y)	0.80	0.67	0.67	0.76	0.73	0.90	0.85	0.65	0.82	0.93	0.90	0.83	0.71	0.00	0.00	0.00	0.00	0.00	0.00	0.00	
Ti(Y)	0.01	0.03	0.03	0.02	0.01	0.02	0.02	0.04	0.01	0.00	0.00	0.01	0.00	0.08	0.08	0.08	0.10	0.16	0.14	0.10	
Cr(Y)	0.05	0.01	0.03	0.04	0.03	0.01	0.01	0.00	0.00	0.00	0.00	0.01	0.01	0.00	0.00	0.00	0.01	0.01	0.02	0.01	
Fe(Y)	0.13	0.40	0.44	0.39	0.32	0.41	0.69	0.69	0.25	0.12	0.24	0.30	0.17	1.20	1.19	1.34	1.16	1.29	1.34	1.21	
Mn(Y)	0.00	0.00	0.00	0.00	0.01	0.00	0.00	0.00	0.00	0.00	0.00	0.00	0.00	0.00	0.00	0.00	0.00	0.00	0.00	0.00	
Mg(Y)	1.82	1.77	1.71	1.66	1.80	1.49	1.27	1.49	1.77	1.73	1.63	1.67	1.98	1.93	1.94	2.11	2.03	2.18	2.09	2.01	
K(X)	0.01	0.01	0.00	0.01	0.00	0.00	0.00	0.01	0.01	0.01	0.01	0.00	0.00	0.01	0.00	0.01	0.01	0.00	0.01	0.01	
Ca(X)	0.05	0.05	0.06	0.05	0.08	0.06	0.09	0.11	0.05	0.02	0.05	0.05	0.06	0.28	0.27	0.38	0.29	0.40	0.37	0.29	
Na(X)	0.55	0.49	0.47	0.46	0.39	0.41	0.42	0.48	0.49	0.65	0.60	0.52	0.54	0.65	0.59	0.56	0.61	0.54	0.55	0.60	
X vacancies	0.39	0.46	0.47	0.48	0.53	0.53	0.49	0.40	0.45	0.33	0.34	0.44	0.40	0.07	0.13	0.04	0.09	0.06	0.07	0.09	
X <sub>Mg</sub>	0.93	0.81	0.79	0.81	0.85	0.78	0.65	0.68	0.88	0.94	0.87	0.85	0.92	0.62	0.62	0.61	0.64	0.63	0.61	0.62	

Note: Atomic proportions based on ΣT+Z+Y cations = 15. X<sub>Mg</sub> = Mg/(Fe<sup>2+</sup> + Mg).

\* B<sub>2</sub>O<sub>3</sub> calculated assuming B to be 3 atoms per formula unit.

Table 6.4.3a: Representative EPMA analysis of tourmaline(continued).

Generation	Gen IIA	Gen IIB																		
Sample no.	S 30D	S 30A																		
Point	11 / 1	13 / 1	16 / 1	17 / 1	6 / 1	8 / 2	8 / 3	8 / 4	8 / 5	8 / 6	8 / 7	10 / 1	14 / 1	15 / 1	23 / 1	23 / 2	23 / 3	27 / 1	29 / 1	32 / 1
Core/Rim	core	core	core	core	rim															
Al <sub>2</sub> O <sub>3</sub>	28.30	27.31	27.86	30.35	37.06	36.75	36.62	37.23	37.02	35.47	35.82	35.84	36.20	35.19	38.84	38.38	38.47	36.31	37.25	36.63
FeO	7.66	8.68	7.25	8.26	4.64	4.46	4.57	4.35	4.79	4.94	4.34	4.34	4.46	5.17	3.39	3.88	3.47	8.67	7.06	7.09
TiO <sub>2</sub>	1.10	0.84	1.01	0.45	0.54	0.68	0.66	0.49	0.58	1.07	0.46	0.59	0.88	1.21	0.07	0.10	0.07	0.37	0.15	0.24
SiO <sub>2</sub>	36.56	35.54	36.39	36.87	35.95	35.75	35.56	35.96	35.88	35.05	34.43	35.66	35.74	35.58	38.11	38.35	38.12	36.75	37.44	37.79
K <sub>2</sub> O	0.03	0.05	0.04	0.04	0.05	0.03	0.03	0.03	0.03	0.05	0.04	0.04	0.02	0.02	0.02	0.02	0.03	0.01	0.04	0.02
CaO	2.15	2.51	2.32	1.25	0.85	0.80	0.89	0.77	0.80	1.33	0.82	0.86	0.99	1.23	0.00	0.05	0.04	0.21	0.28	0.08
Na <sub>2</sub> O	1.73	1.64	1.64	1.98	1.81	1.77	1.77	1.82	1.84	1.66	1.67	1.78	1.81	1.72	0.82	0.83	0.82	1.27	1.48	1.35
Cr <sub>2</sub> O <sub>3</sub>	0.02	0.20	0.49	0.05	0.00	0.01	0.00	0.00	0.00	0.03	0.12	0.00	0.03	0.07	0.00	0.06	0.00	0.18	0.05	0.00
MnO	0.00	0.00	0.04	0.00	0.15	0.00	0.00	0.04	0.03	0.00	0.00	0.00	0.04	0.00	0.02	0.05	0.02	0.00	0.00	0.04
MgO	8.84	8.97	9.67	7.85	6.18	6.26	6.29	5.98	6.20	6.54	5.63	6.42	6.59	6.62	5.22	5.15	4.84	3.43	4.08	4.29
B <sub>2</sub> O <sub>3</sub> *	10.52	10.34	10.54	10.64	10.93	10.86	10.83	10.89	10.92	10.73	10.46	10.74	10.87	10.81	11.09	11.10	11.01	10.80	10.97	10.95
Total	96.91	96.06	97.23	97.74	98.14	97.36	97.21	97.55	98.10	96.86	93.79	96.28	97.62	97.62	97.58	97.96	96.89	97.99	98.79	98.47
Si(T)	6.00	5.98	6.00	6.00	5.78	5.79	5.77	5.81	5.77	5.74	5.80	5.84	5.78	5.79	6.00	6.00	6.00	5.97	6.00	6.00
Al(T)	0.00	0.03	0.01	0.00	0.29	0.28	0.30	0.27	0.29	0.33	0.28	0.23	0.29	0.28	0.03	0.00	0.00	0.09	0.07	0.01
B(T)	3.00	3.00	3.00	3.00	3.00	3.00	3.00	3.00	3.00	3.00	3.00	3.00	3.00	3.00	3.00	3.00	3.00	3.00	3.00	3.00
Al(Z)	5.51	5.38	5.40	5.84	6.00	6.00	6.00	6.00	6.00	6.00	6.00	6.00	6.00	6.00	6.00	6.00	6.00	6.00	6.00	6.00
Al(Y)	0.00	0.00	0.00	0.00	0.66	0.65	0.63	0.73	0.65	0.44	0.73	0.60	0.54	0.38	1.14	1.08	1.15	0.80	0.88	0.84
Ti(Y)	0.14	0.11	0.12	0.06	0.07	0.08	0.08	0.06	0.07	0.13	0.06	0.07	0.11	0.15	0.01	0.01	0.01	0.04	0.02	0.03
Cr(Y)	0.00	0.03	0.06	0.01	0.00	0.00	0.00	0.00	0.00	0.00	0.02	0.00	0.00	0.01	0.00	0.01	0.00	0.02	0.01	0.00
Fe(Y)	1.07	1.22	1.00	1.13	0.62	0.60	0.62	0.59	0.64	0.68	0.61	0.60	0.60	0.70	0.45	0.52	0.47	1.18	0.95	0.96
Mn(Y)	0.00	0.00	0.01	0.00	0.02	0.00	0.00	0.00	0.00	0.00	0.00	0.00	0.01	0.00	0.00	0.01	0.00	0.00	0.00	0.01
Mg(Y)	2.20	2.25	2.38	1.92	1.48	1.51	1.52	1.44	1.49	1.60	1.41	1.57	1.59	1.60	1.24	1.23	1.17	0.83	0.98	1.03
K(X)	0.01	0.01	0.01	0.01	0.01	0.01	0.01	0.01	0.01	0.01	0.01	0.01	0.00	0.00	0.00	0.00	0.01	0.00	0.01	0.00
Ca(X)	0.38	0.45	0.41	0.22	0.14	0.14	0.15	0.13	0.14	0.23	0.14	0.15	0.17	0.21	0.00	0.01	0.01	0.04	0.05	0.01
Na(X)	0.55	0.53	0.52	0.63	0.56	0.55	0.55	0.56	0.57	0.52	0.54	0.56	0.56	0.54	0.25	0.25	0.25	0.40	0.45	0.42
X vacancies	0.06	0.00	0.06	0.15	0.29	0.31	0.29	0.30	0.29	0.24	0.31	0.28	0.27	0.25	0.75	0.74	0.74	0.56	0.49	0.57
X <sub>Mg</sub>	0.67	0.65	0.70	0.63	0.70	0.71	0.71	0.71	0.70	0.70	0.70	0.72	0.72	0.69	0.73	0.70	0.71	0.41	0.51	0.52

Note: Atomic proportions based on ΣT+Z+Y cations = 15. X<sub>Mg</sub> = Mg/(Fe<sup>2+</sup> + Mg).

\* B<sub>2</sub>O<sub>3</sub> calculated assuming B to be 3 atoms per formula unit.

Table 6.4.3a: Representative EPMA analysis of tourmaline(continued).

Generation	Gen IIB	Gen III																	
Sample no.	S 30A	S 30A	S 30A	S 30A	S 30D	S 30D	S 30A	S 30D	S 30D	S 30C									
Point	32 / 2	32 / 3	32 / 4	32 / 5	8 / 1	12 / 1	6 / 1	7 / 1	9 / 1	15 / 1	16 / 1	32 / 6	32 / 7	32 / 8	32 / 9	32 / 10	5 / 1	18 / 1	14 / 1
Core/Rim																			
Al <sub>2</sub> O <sub>3</sub>	36.97	36.90	37.01	36.91	36.76	37.94	37.83	36.44	36.93	38.25	40.15	37.09	37.20	37.33	37.42	37.25	38.78	34.80	38.04
FeO	7.49	7.19	7.28	7.11	7.53	5.93	11.08	7.62	7.73	6.73	6.19	7.26	6.77	8.34	8.78	8.41	8.03	10.65	9.04
TiO <sub>2</sub>	0.29	0.18	0.21	0.26	0.17	0.01	0.07	0.43	0.17	0.25	0.09	0.22	0.19	0.58	0.60	0.53	0.15	0.10	0.18
SiO <sub>2</sub>	37.80	37.68	37.79	37.50	35.93	37.32	36.62	37.28	37.53	37.07	37.00	37.76	37.60	36.62	36.63	36.83	35.58	37.84	36.84
K <sub>2</sub> O	0.00	0.00	0.00	0.01	0.02	0.00	0.00	0.03	0.03	0.01	0.01	0.00	0.01	0.01	0.02	0.03	0.01	0.00	0.02
CaO	0.18	0.16	0.19	0.23	0.46	0.12	0.18	0.29	0.06	0.16	0.21	0.27	0.20	0.42	0.44	0.43	0.57	0.10	0.33
Na <sub>2</sub> O	1.57	1.63	1.53	1.63	1.32	1.07	0.64	1.20	1.35	1.07	0.91	1.53	1.58	1.01	1.00	1.03	1.15	1.61	0.99
Cr <sub>2</sub> O <sub>3</sub>	0.01	0.10	0.06	0.09	0.02	0.07	0.00	0.04	0.05	0.19	0.04	0.00	0.00	0.01	0.10	0.06	0.00	0.01	0.00
MnO	0.00	0.02	0.00	0.00	0.08	0.01	0.05	0.02	0.02	0.00	0.11	0.00	0.00	0.04	0.00	0.00	0.05	0.03	0.02
MgO	3.91	4.06	4.31	4.30	4.05	4.38	1.17	4.15	3.66	3.35	2.62	4.17	4.04	3.11	3.05	3.14	2.83	3.27	2.36
B <sub>2</sub> O <sub>3</sub> *	11.00	10.98	11.03	10.98	10.73	10.95	10.78	10.90	10.92	10.93	11.02	11.02	10.97	10.86	10.90	10.89	10.82	10.83	10.89
Total	99.22	98.90	99.42	99.01	97.06	97.80	98.42	98.37	98.45	98.00	98.35	99.33	98.56	98.33	98.95	98.61	97.96	99.22	98.70
Si(T)	6.00	6.00	6.00	6.00	5.87	5.98	5.95	6.00	6.00	5.97	5.93	6.00	6.00	5.92	5.90	5.95	5.78	6.00	5.95
Al(T)	0.03	0.04	0.05	0.07	0.18	0.08	0.10	0.06	0.03	0.11	0.17	0.05	0.05	0.14	0.16	0.13	0.29	0.00	0.12
B(T)	3.00	3.00	3.00	3.00	3.00	3.00	3.00	3.00	3.00	3.00	3.00	3.00	3.00	3.00	3.00	3.00	3.00	3.00	3.00
Al(Z)	6.00	6.00	6.00	6.00	6.00	6.00	6.00	6.00	6.00	6.00	6.00	6.00	6.00	6.00	6.00	6.00	6.00	6.00	6.00
Al(Y)	0.85	0.85	0.82	0.81	0.84	1.01	1.08	0.79	0.90	1.06	1.29	0.84	0.90	0.89	0.86	0.88	1.05	0.58	1.03
Ti(Y)	0.03	0.02	0.03	0.03	0.02	0.00	0.01	0.05	0.02	0.03	0.01	0.03	0.02	0.07	0.07	0.06	0.02	0.01	0.02
Cr(Y)	0.00	0.01	0.01	0.01	0.00	0.01	0.00	0.00	0.01	0.02	0.01	0.00	0.00	0.00	0.01	0.01	0.00	0.00	0.00
Fe(Y)	1.01	0.97	0.97	0.95	1.03	0.79	1.51	1.03	1.05	0.91	0.83	0.97	0.92	1.13	1.18	1.14	1.09	1.46	1.22
Mn(Y)	0.00	0.00	0.00	0.00	0.01	0.00	0.01	0.00	0.00	0.00	0.01	0.00	0.00	0.00	0.00	0.00	0.01	0.00	0.00
Mg(Y)	0.94	0.98	1.03	1.03	0.99	1.05	0.28	1.00	0.88	0.80	0.62	1.00	0.97	0.75	0.73	0.76	0.68	0.80	0.57
K(X)	0.00	0.00	0.00	0.00	0.00	0.00	0.00	0.01	0.01	0.00	0.00	0.00	0.00	0.00	0.00	0.01	0.00	0.00	0.00
Ca(X)	0.03	0.03	0.03	0.04	0.08	0.02	0.03	0.05	0.01	0.03	0.04	0.05	0.03	0.07	0.07	0.07	0.10	0.02	0.06
Na(X)	0.48	0.50	0.47	0.50	0.41	0.33	0.20	0.37	0.42	0.33	0.28	0.47	0.48	0.31	0.31	0.32	0.36	0.50	0.31
X vacancies	0.49	0.47	0.50	0.46	0.50	0.65	0.77	0.58	0.57	0.64	0.69	0.49	0.48	0.61	0.61	0.60	0.54	0.48	0.63
X <sub>Mg</sub>	0.48	0.50	0.51	0.52	0.49	0.57	0.16	0.49	0.46	0.47	0.43	0.51	0.52	0.40	0.38	0.40	0.39	0.35	0.32

Note: Atomic proportions based on ΣT+Z+Y cations = 15. X<sub>Mg</sub> = Mg/(Fe<sup>2+</sup> + Mg).

\* B<sub>2</sub>O<sub>3</sub> calculated assuming B to be 3 atoms per formula unit.

Table 6.4.3b : Representative EPMA analysis of muscovite, pyrophyllite, rutile, kyanite and dumortierite.

Sample no	S 30A	S 30A	S 30A	S 30A	S 30C				
DataSet/ Point	1 / 1	3 / 1	12 / 1	13 / 1	7 / 1	9 / 1	12 / 1	17 / 1	19 / 1
Mineral	Muscovite								
SiO <sub>2</sub>	48.287	48.74	49.588	47.781	47.936	49.098	47.605	48.693	47.944
TiO <sub>2</sub>	0.039	0.088	0.012	0.04	0.075	0	0	0.041	0.029
Al <sub>2</sub> O <sub>3</sub>	40.258	40.993	40.114	40.041	40.006	40.41	39.718	40.989	40.925
Cr <sub>2</sub> O <sub>3</sub>	0	0	0	0	0	0	0	0	0
FeO	0.368	0.067	0.121	0.128	0.206	0.203	0.132	0.275	0.207
MnO	0.014	0.052	0.103	0	0.013	0	0.007	0	0
MgO	0.074	0.09	0.095	0.054	0.014	0.026	0.052	0.032	0.002
CaO	0.011	0	0	0	0	0.022	0	0	0.012
Na <sub>2</sub> O	0.756	0.868	0.946	0.881	1.413	1.726	1.596	1.88	1.684
K <sub>2</sub> O	7.366	7.725	7.169	7.625	6.427	6.402	6.563	6.759	6.853
Total	97.173	98.623	98.148	96.55	96.09	97.887	95.673	98.669	97.656
Normalization basis	11(O)								
Si	3.06	3.04	3.10	3.05	3.06	3.07	3.06	3.04	3.02
Ti	0.00	0.00	0.00	0.00	0.00	0.00	0.00	0.00	0.00
Al	3.01	3.02	2.96	3.01	3.01	2.98	3.01	3.01	3.04
Cr	0.00	0.00	0.00	0.00	0.00	0.00	0.00	0.00	0.00
Fe	0.02	0.00	0.01	0.01	0.01	0.01	0.01	0.01	0.01
Mn	0.00	0.00	0.01	0.00	0.00	0.00	0.00	0.00	0.00
Mg	0.01	0.01	0.01	0.01	0.00	0.00	0.00	0.00	0.00
Ca	0.00	0.00	0.00	0.00	0.00	0.00	0.00	0.00	0.00
Na	0.09	0.11	0.11	0.11	0.17	0.21	0.20	0.23	0.21
K	0.60	0.62	0.57	0.62	0.52	0.51	0.54	0.54	0.55

Table 6.4.3b : Representative EPMA analysis of muscovite, pyrophyllite, rutile, kyanite and dumortierite (continued).

Sample no	S 30C	S 30D	S30 c	S30 c	S 30D	S 30C	S 30D	Sample no	S30D	S30D	S30D
DataSet/ Point	20 / 1	25 / 1	28	29	3 / 1	1 / 1	9 / 1	DataSet/ Point	22 / 1	28 / 1	29 / 1
Mineral	Musco vite	pyrophy llite	pyroph yllite	pyrop hyllite	Rutile	Kyanite in KQ(Ky1 )	Kyanite in Vein(Ky2 )	Mineral	Dumorti erite	Dumorti erite	Dumorti erite
SiO <sub>2</sub>	47.838	68.698	62.88	62	0.00	37.03	37.13	Al <sub>2</sub> O <sub>3</sub>	60.78	62.58	59.13
TiO <sub>2</sub>	0.017	0.046	0	0	98.90	0.00	0.01	FeO	0.17	0.24	0.17
Al <sub>2</sub> O <sub>3</sub>	40.806	30.439	30.81	30.01	0.02	63.31	62.50	TiO <sub>2</sub>	0.75	0.74	0.85
Cr <sub>2</sub> O <sub>3</sub>	0	0.036	0.02	0	0.03	0.08	0.16	SiO <sub>2</sub>	30.20	29.03	31.14
FeO	0.09	0.246	0.14	0.16	0.41	0.00	0.12	K <sub>2</sub> O	0.03	0.07	0.83
MnO	0	0	0	0	0.00	0.02	0.00	CaO	0.00	0.02	0.02
MgO	0.028	0.009	0.03	0.02	0.02	0.02	0.00	Na <sub>2</sub> O	0.00	0.04	0.10
CaO	0.02	0.065	0.04	0.04	0.04	0.00	0.02	Cr <sub>2</sub> O <sub>3</sub>	0.09	0.11	0.21
Na <sub>2</sub> O	1.357	0.051	0.54	0.5	0.01	0.00	0.00	MnO	0.00	0.00	0.00
K <sub>2</sub> O	6.51	0	0.9	0.92	0.00	0.00	0.01	MgO	0.38	0.26	0.35
Total	96.666	99.59	95.36	93.65	99.43	100.45	99.95	P <sub>2</sub> O <sub>5</sub>	0.07	0.10	0.07
Normaliza tion basis	11(O)	11(O)	11(O)	11(O)	2(O)	5(O)	5(O)	H <sub>2</sub> O*	1.18	1.19	1.18
Si	3.03	3.94	3.81	3.82	0.00	1.00	1.00	B <sub>2</sub> O <sub>3</sub> *	6.11	6.14	6.10
Ti	0.00	0.00	0.00	0.00	1.00	0.00	0.00	Total	99.69	100.42	100.08
Al	3.05	2.06	2.20	2.18	0.00	1.99	2.00	Normaliza tion basis	16.125(O )	16.125(O )	16.125(O )
Cr	0.00	0.00	0.00	0.00	0.00	0.00	0.00	Al	6.80	6.96	6.62
Fe	0.00	0.01	0.01	0.01	0.01	0.00	0.00	Fe	0.01	0.02	0.01
Mn	0.00	0.00	0.00	0.00	0.00	0.00	0.00	Ti	0.05	0.05	0.06
Mg	0.00	0.00	0.00	0.00	0.00	0.00	0.00	Si	2.86	2.74	2.96
Ca	0.00	0.00	0.00	0.00	0.00	0.00	0.00	K	0.00	0.01	0.10
Na	0.17	0.01	0.06	0.06	0.00	0.00	0.00	Ca	0.00	0.00	0.00
K	0.53	0.00	0.07	0.07	0.00	0.00	0.00	Na	0.00	0.01	0.02
								Cr	0.01	0.01	0.02
								Mn	0.00	0.00	0.00
								Mg	0.05	0.04	0.05
								P	0.01	0.01	0.01
								B	1.00	1.00	1.00
								OH	0.75	0.75	0.75
								Al <sup>iv</sup>	0.13	0.25	0.04
								Al <sup>vi</sup>	6.67	6.71	6.58
								Vacancy	0.21	0.17	0.28
								XMg	0.80	0.66	0.79

\* B<sub>2</sub>O<sub>3</sub> and H<sub>2</sub>O calculated assuming 1 B and 0.75(OH) apfu for dumortierite after Moore and Araki (1978).

## 6.5: Trace and REE concentrations of tourmaline

In chondrite normalized REE (McDonough and Sun, 1995) spectra, majority of Gen-I tourmalines show concave upward pattern (Fig 6.5.1a) without any Eu anomaly ( $\text{Eu}/\text{Eu}^*=1.02-1.13$ ). Enrichment of LREE and HREE is moderate (~ maximum 10X chondrite). MREE values are near chondrite. These tourmaline  $\text{REE}_{\text{total}}$  content is low (6.15-15.20 ppm). However, two data show high  $\text{REE}_{\text{total}}$  (78.2-1028.71 ppm) content with flat or negatively sloped pattern (LREE enrichment with respect to HREE) with distinct negative Eu anomaly ( $\text{Eu}/\text{Eu}^*=0.28-0.52$ ). HREE shows a nearly flat pattern.

In chondrite normalized (McDonough and Sun, 1995) REE diagram (Fig 6.5.1f) Gen-IIA tourmaline shows overall negative REE pattern (LREE enriched than HREE) (Fig 6.5.1b) with a prominent positive Eu anomaly. Core and rim are nearly indistinguishable and they show progressive LREE enrichment. Core of Gen IIA tourmaline shows a positive Eu anomaly ( $\text{Eu}/\text{Eu}^*=3.56-5.40$ ) with  $(\text{La}/\text{Lu})_{\text{CN}} = 34.57 - 86.09$  ( $\text{La}/\text{Lu} > 1$ ) and the rim shows a positive Eu anomaly ( $\text{Eu}/\text{Eu}^*=1.37-1.94$ ) with  $(\text{La}/\text{Lu})_{\text{CN}} = 189.76-875.95$  ( $\text{La}/\text{Lu} > 1$ ). Eu anomaly of the core is more prominent than the rim. HREE shows concave upward and depleted pattern (except one data that shows flat HREE pattern). In the core portion shows a positive Eu anomaly ( $\text{Eu}/\text{Eu}^*=3.56-5.40$ ) with  $(\text{La}/\text{Lu})_{\text{CN}} = 34.57 - 86.09$  ( $\text{La}/\text{Lu} > 1$ ) and the rim portions shows a positive Eu anomaly ( $\text{Eu}/\text{Eu}^*=1.37-1.94$ ) with  $(\text{La}/\text{Lu})_{\text{CN}} = 189.76-875.95$  ( $\text{La}/\text{Lu} > 1$ ). In Gen-IIA tourmaline the core (brownish green)  $\text{REE}_{\text{total}}$  content varies from 1.28ppm to 3.60 ppm and the rim(yellowish green)  $\text{REE}_{\text{total}}$  content varies from 2.14ppm to 4.12ppm.

In chondrite normalized REE (McDonough and Sun, 1995) diagram, Gen-IIB tourmalines show overall concave upward pattern (Fig 6.5.1c) with  $\text{La}/\text{Lu}_{\text{CN}} = 1.82-9.18$  ( $\text{La}/\text{Lu} > 1$ ). Positive Eu anomaly ( $\text{Eu}/\text{Eu}^*=1.89-3.74$ ) is noted. They show both LREE and HREE progressive enrichment. Enrichment of LREE is moderate (1-10X chondrite) to high (10-100X chondrite). A similar enrichment patterns is also observed in HREE. The REE contents of tourmaline varies from 10.69 ppm to 59.67 ppm with an average of 37.95 ppm.

In chondrite normalized REE (McDonough and Sun, 1995) diagram, Gen-III tourmaline (Fig 6.5.1d) shows overall concave upwards REE pattern and positive Eu anomaly ( $\text{Eu}/\text{Eu}^*=3.60-4.03$ ) with  $(\text{La}/\text{Lu})_{\text{CN}} = 2.27-3.81$ . LREE pattern shows smooth negative slope followed by positive Eu anomaly and followed by progressive enrichment of HREE. In Gen-III tourmaline  $\text{REE}_{\text{total}}$  content varies from 1.59ppm to 3.06 ppm at an average of 2.32 ppm.

The REE<sub>total</sub> content in Gen-III tourmaline is very low than the Gen-I and Gen-II. Dumortierite occurs along with the Gen-IIA tourmaline.

In chondrite normalized REE diagram dumortierite grain (Fig 6.5.1e) shows LREE enrichment pattern and negative Eu anomaly ( $Eu/Eu^* = 0.48 - 0.64$ ) with  $(La/Lu)_{CN} = 16.60 - 21.64$ . HREE shows a nearly flat pattern. Dumortierite grain REE<sub>total</sub> contents varies from 3.62 to 4.11 ppm at an average of 3.87 ppm.

UCC normalized multielement plot (Rudnick and Gao, 2003) (Fig 6.5.1f) of Gen-I tourmaline shows prominent depletion in LIL elements such as Rb and moderate depletion in Ba. Co, Ni, Zn, V, Sc concentration is near to upper crustal condition (0.1-10X UCC). This tourmaline grain shows flat REE pattern without significant Eu anomaly. Majority of the grains show overall REE concentration slightly depleted with respect to UCC (0.1 X UCC). While two grains show near or slightly enriched in REE concentration with respect to UCC (1-10 X UCC). Gen-I tourmaline also shows variable enrichment of HFSE such as Ti, W, Th. No relative enrichment or depletion is noted between Nb and Ta.

In UCC normalized multielement plot (Rudnick and Gao, 2003) (Fig 6.5.1g) of Gen-IIA tourmaline shows significant depletion of LILE such as Rb and Ba with minor Sr. Co, Ni, Zn, V, Sc are near crustal value. Concentration of these elements between core and rim are nearly consistent except Sr and Sc. HREE+Y shows overall concave up pattern. Both core and the rim of Gen-IIA tourmaline shows moderate positive Eu anomaly. Progressive enrichment of LREE is noted in both core and rim composition. Positive Ti anomaly is observed in the spectra. The core shows negative Th anomaly while the rim shows positive Th anomaly. The core exhibits progressive enrichment of Nb, Ta with respect to Th while the rim shows depleted in Nb with respect to Th and Ta.

UCC normalized multielement plot (Rudnick and Gao, 2003) (Fig 6.5.1h) of Gen-IIB tourmaline shows moderate depletion in LILE such as Rb and Ba. Compatible elements such as Co, Ni, Sr, V, Sc are near to crustal value. No significant fractionation between the REE is observed. Thus, the overall REE pattern is flat and near crustal value with moderate Eu anomaly. There is no significant Ti anomaly noted in Gen-IIB tourmaline. Variable depletion i.e. Hf and Zr is noted but Th concentration is near crustal value. Relative enrichment of Ta with respect to Nb is also observed.

UCC normalized multielement plot (Rudnick and Gao, 2003) (Fig 6.5.1i) of Gen-III tourmaline shows also depletion of Rb and Ba like other generations of tourmaline. Minor

depletion of Sr is noted. Compatible elements like Co, Ni, V, Sc are near crustal values. Overall REE pattern is slightly concave up i.e., depletion of MREE (except Eu) with respect to LREE and HREE. Eu shows moderate positive anomaly. Ti concentration is near crustal value. Depletion of U, Th is noted. Relative enrichment of Ta with respect to Nb is also observed. UCC normalized multielement plot (Rudnick and Gao, 2003) of dumortierite which occurred along with Gen IIB tourmaline, shows no significant depletion of LILE such as Rb and Ba is noted, unlike different generations of tourmaline (Fig 6.5.1j). The REE concentration is near crustal value with no Eu anomaly. REE shows nearly flat pattern. Ti enrichment is noted (10X UCC). Moderate depletion of Hf, Zr and enrichment of Th is observed. No relative enrichment between Nb and Ta seen.

Representative LA-ICP-MS trace-element analyses (in ppm) of different generations of tourmaline are given in Table 6.5.2a.

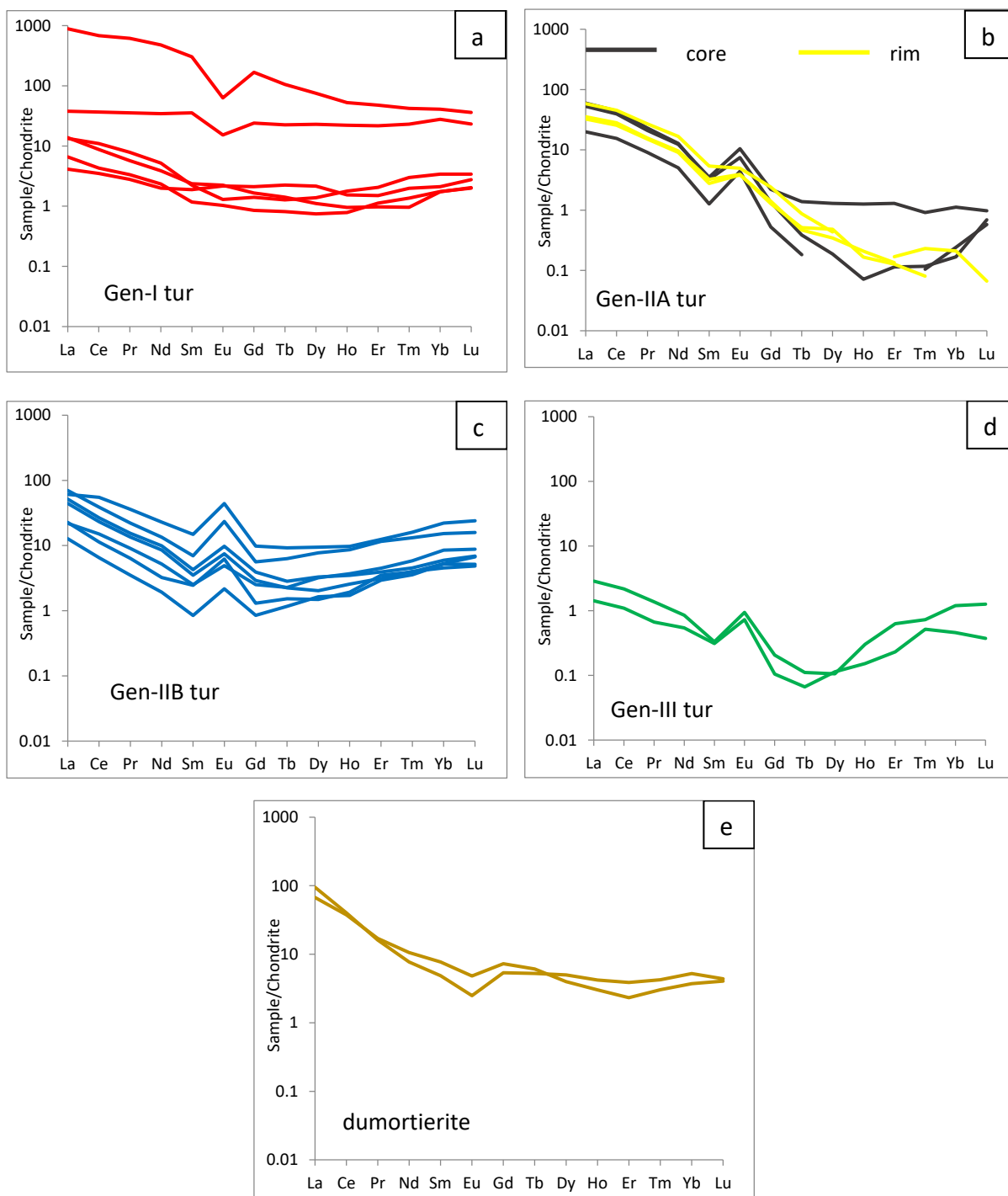


Fig 6.5.1a: Chondrite normalized (McDonough and Sun, 1995) REE spider diagram of Gen-I tourmaline. Fig 6.5.1b: Chondrite normalized (McDonough and Sun, 1995) REE spider diagram of Gen-IIA tourmaline (Black – core: Yellow-rim). Fig 6.5.1c: Chondrite normalized (McDonough and Sun, 1995) REE spider diagram of Gen IIB tourmaline. Fig 6.5.1d: Chondrite normalized ((McDonough and Sun, 1995) REE spider diagram of Gen III tourmaline. Fig 6.5.1e: Chondrite normalized (McDonough and Sun, 1995) REE spider diagram of dumortierite. [The gaps in the spidergrams represent element concentrations that are below detection limit.]

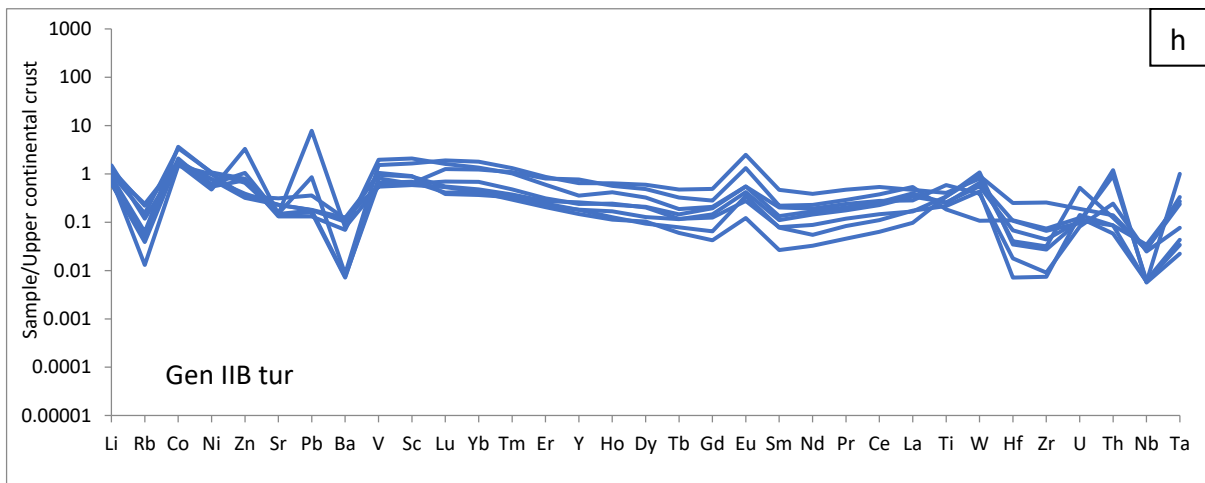
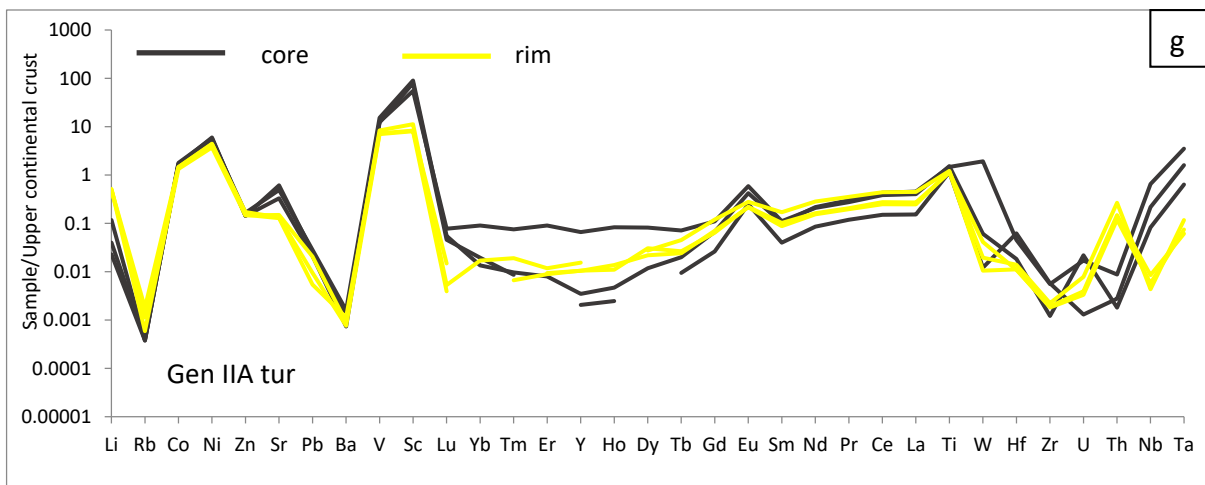
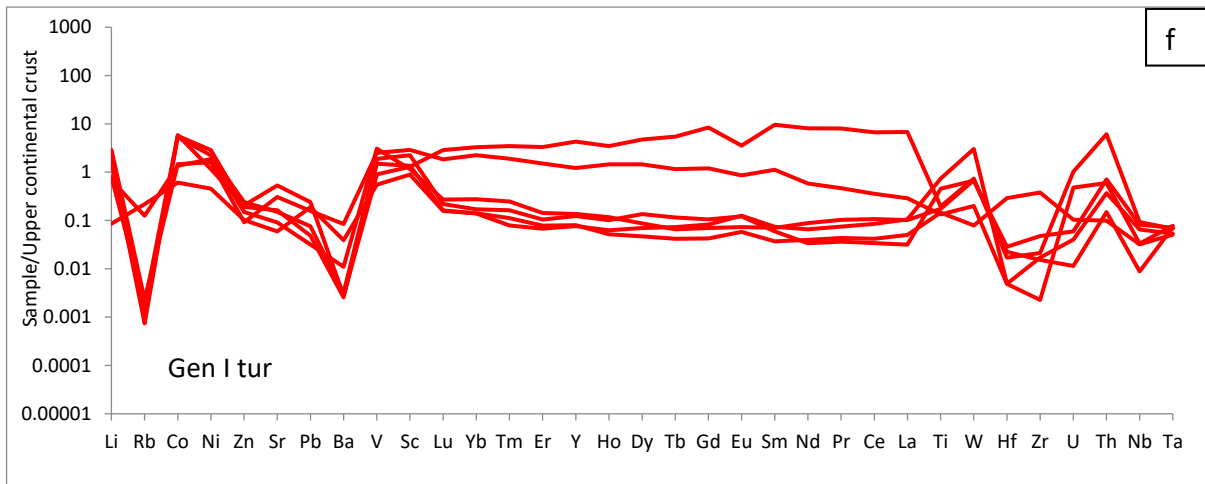


Fig 6.5.1f: Upper continental crust (UCC) normalized multi-element diagram for Gen-I tourmaline. Fig 6.5.1g: Upper continental crust (UCC) normalized multi-element diagram for Gen-IIA tourmaline. Fig 6.5.1h: Upper continental crust (UCC) normalized multi-element diagram for Gen-IIB tourmaline. [The gaps in the spidergrams represent element concentrations that are below detection limit.]

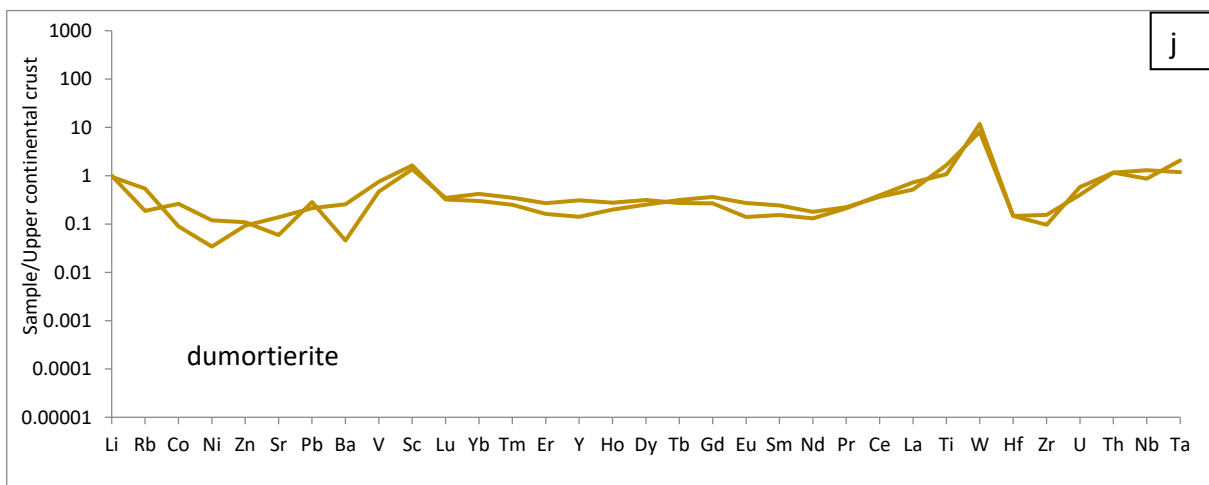
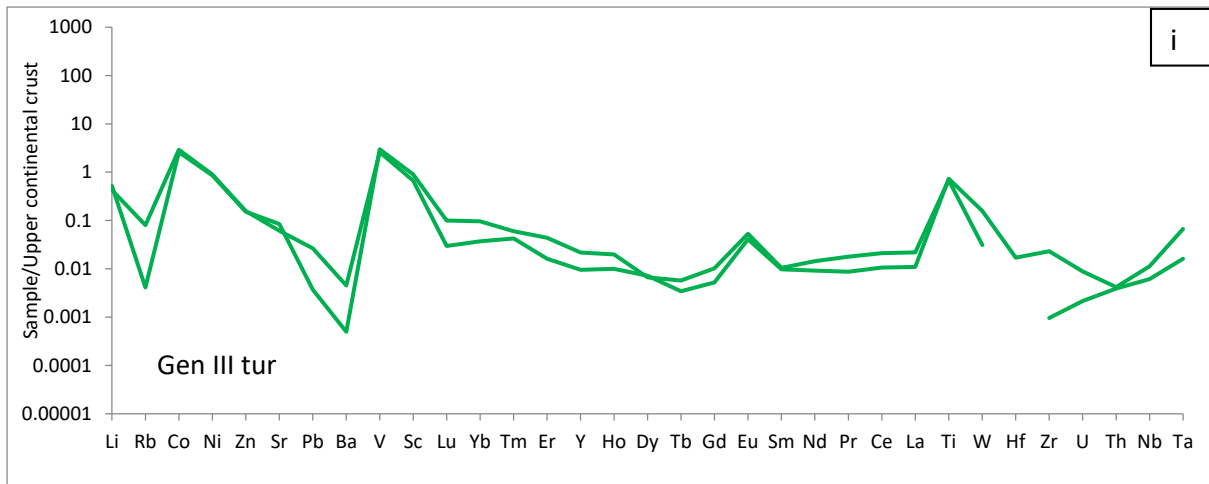


Fig 6.5.1i: Upper continental crust (UCC) normalized multi-element diagram for Gen-III tourmaline. Fig 6.5.1j: Upper continental crust (UCC) normalized multi-element diagram for dumortierite. [The gaps in the spidergrams represent element concentrations that are below detection limit.]

Table 6.5.2a : Representative LA-ICPMS trace element analysis (in ppm) of tourmaline.

Sample no.	S 30 b2	S 30 b2	S30d1	S 30 b2	S 30a3	S 30 c2	S30d1	S30d1	S30d1
Mineral	tourmaline								
Point	74	79	63	77	61	37	60	65	67
Generation	Gen I	Gen IIA	Gen IIA	Gen IIA					
Core/Rim							core	core	core
La	0.98	210.56	8.96	3.27	3.17	1.56	4.73	14.10	12.46
Ce	2.15	419.17	22.48	5.38	6.72	2.64	9.48	27.15	24.23
Pr	0.26	57.07	3.31	0.53	0.73	0.31	0.84	2.13	1.95
Nd	0.91	218.78	15.76	1.77	2.38	1.07	2.31	5.84	5.63
Sm	0.28	44.84	5.26	0.35	0.33	0.17	0.19	0.48	0.52
Eu	0.12	3.55	0.86	0.13	0.07	0.06	0.25	0.42	0.59
Gd	0.42	33.45	4.79	0.33	0.28	0.17	0.11	0.27	0.44
Tb	0.08	3.81	0.81	0.05	0.05	0.03	0.01	0.01	0.05
Dy	0.53	18.46	5.66	0.27	0.34	0.18	bdl	0.05	0.32
Ho	0.08	2.88	1.21	0.05	0.10	0.04	0.00	0.00	0.07
Er	0.24	7.62	3.48	0.16	0.33	0.18	bdl	0.02	0.21
Tm	0.05	1.04	0.57	0.02	0.07	0.03	0.00	0.00	0.02
Yb	0.34	6.59	4.48	0.28	0.55	0.28	0.04	0.03	0.18
Lu	0.07	0.89	0.57	0.05	0.08	0.05	0.01	0.02	0.02
Total REE	6.51	1028.71	78.20	12.64	15.20	6.78	17.97	50.52	46.69
Eu anomaly	1.09	0.28	0.52	1.13	0.73	1.03	5.40	3.56	3.76
Li	38.28	44.08	69.28	19.03	16.28	2.06	0.96	2.80	0.55
Sc	31.43	18.14	40.35	18.92	16.19	12.52	1107.56	1264.69	773.34
Ti	1741.70	747.51	513.13	2816.17	669.20	555.92	4379.40	5655.62	5877.11
V	182.69	87.38	244.08	145.16	298.10	53.66	1190.18	1483.48	1214.34
Co	91.99	101.14	25.32	97.57	23.52	10.51	28.79	29.20	30.87
Ni	105.00	54.13	75.64	135.02	87.78	21.48	280.53	254.36	268.51
Zn	16.04	13.83	6.16	12.78	10.06	6.83	9.53	11.02	9.61
Rb	0.08	0.06	0.19	0.15	10.33	17.86	0.03	0.03	0.03
Sr	48.36	169.60	98.05	52.10	29.14	19.01	105.40	156.63	196.43
Y	2.59	89.76	25.51	1.61	2.87	1.68	0.04	0.07	1.39
Zr	9.23	4.10	0.44	3.28	2.95	73.14	1.11	1.07	0.23
Nb	0.98	1.11	0.40	0.78	0.11	0.39	2.61	7.83	0.99
Mo	bdl	bdl	0.02	0.03	0.03	0.06	bdl	0.25	0.02
Ag	0.03	0.01	0.02	0.01	0.13	0.29	0.01	0.00	0.01
Ba	1.99	1.75	52.98	1.61	6.93	24.59	0.46	1.00	0.74
Hf	0.15	0.09	0.03	0.03	0.12	1.54	0.33	0.24	0.10
Ta	0.06	0.06	0.07	0.05	0.07	0.05	1.44	3.15	0.57
W	1.27	1.40	0.38	5.74	1.30	0.15	0.02	3.66	0.12
Pb	1.29	4.08	2.69	0.82	0.54	3.20	0.36	0.48	0.43
Th	7.43	63.90	6.26	3.86	1.57	1.04	0.03	0.09	0.02
U	0.16	2.77	1.30	0.11	0.03	0.28	0.00	0.05	0.06

bdl- below detection limit

Table 6.5.2a : Representative LA-ICPMS trace element analysis (in ppm) of tourmaline(continued).

Sample no.	S30d1	S30d1	S30d1	S30a2	S30c1	S30c1	S30a2	S30a2	S30a2
Mineral	tourmaline								
Point	66	68	61	54	96	97	48	49	51
Generation	Gen IIA	Gen IIA	Gen IIA	Gen IIB					
Core/Rim	rim	rim	rim						
La	8.41	7.68	13.84	8.78	12.25	10.53	14.48	5.37	3.02
Ce	17.27	15.73	27.86	17.42	16.32	14.25	33.67	6.95	3.99
Pr	1.46	1.40	2.51	1.70	1.43	1.25	3.34	0.59	0.33
Nd	4.38	4.14	7.64	5.18	4.53	3.90	10.46	1.48	0.88
Sm	0.48	0.41	0.80	0.95	0.63	0.52	2.20	0.36	0.13
Eu	0.22	0.22	0.28	0.55	0.55	0.42	2.48	0.35	0.12
Gd	0.26	0.28	0.48	0.83	0.78	0.58	1.95	0.26	0.17
Tb	0.02	0.02	0.03	0.13	0.10	0.08	0.33	0.06	0.04
Dy	0.12	0.09	0.11	1.26	0.81	0.50	2.32	0.37	0.40
Ho	0.01	0.01	bdl	0.35	0.19	0.14	0.53	0.11	0.09
Er	0.02	0.02	0.03	1.37	0.63	0.50	1.99	0.56	0.47
Tm	0.00	bdl	0.01	0.31	0.11	0.10	0.40	0.10	0.09
Yb	bdl	bdl	0.03	2.70	0.96	0.73	3.57	0.85	0.84
Lu	0.00	0.00	0.00	0.50	0.17	0.12	0.59	0.17	0.13
Total REE	32.65	29.99	53.62	42.02	39.47	33.62	78.31	17.56	10.69
Eu anomaly	1.92	1.94	1.38	1.89	2.39	2.33	3.65	3.48	2.56
Li	12.09	11.74	12.28	24.10	26.10	30.33	20.88	35.92	15.11
Sc	116.66	113.10	157.57	29.24	12.34	12.59	23.05	8.20	9.64
Ti	4338.00	4501.54	4647.23	2251.88	955.37	991.88	1556.55	828.88	1297.55
V	705.57	679.91	813.10	190.81	92.93	101.55	147.69	52.65	62.85
Co	25.28	25.05	23.13	58.79	31.28	28.64	62.68	27.51	33.02
Ni	208.18	203.68	174.87	50.35	36.93	35.97	49.69	22.34	28.90
Zn	10.08	11.49	9.77	53.13	26.16	21.35	43.80	221.26	70.36
Rb	0.09	0.15	0.05	12.46	19.64	18.06	5.16	9.71	3.20
Sr	41.16	42.50	47.90	42.27	73.26	73.78	48.36	47.36	47.33
Y	0.22	0.22	0.32	7.46	5.42	3.82	13.49	3.79	3.11
Zr	0.37	0.35	0.43	1.75	12.80	8.50	6.09	1.43	5.26
Nb	0.10	0.07	0.05	0.30	0.07	0.08	0.32	0.07	0.41
Mo	0.01	0.01	bdl	bdl	bdl	bdl	bdl	0.20	0.06
Ag	0.01	0.02	0.04	0.33	0.23	0.26	3.31	120.79	0.52
Ba	0.71	0.48	0.57	43.72	77.04	64.22	5.36	49.20	4.70
Hf	0.06	0.06	0.07	0.10	0.57	0.36	0.21	0.04	0.18
Ta	0.06	0.07	0.11	0.07	0.02	0.04	0.30	0.90	0.24
W	0.08	0.02	0.04	0.74	1.24	1.06	1.51	0.82	2.04
Pb	0.09	0.16	0.35	2.24	3.07	3.01	14.53	132.36	2.96
Th	1.56	1.26	2.79	2.55	12.54	9.62	1.30	0.90	0.90
U	0.01	0.01	0.02	0.22	0.26	0.29	1.39	0.38	0.29

bdl- below detection limit

Table 6.5.2a : Representative LA-ICPMS trace element analysis (in ppm) of tourmaline(continued).

Sample no.	S30a2	S 30 c2	S 30b	S 30b	S30a2	S30c1
Mineral	tourmaline	tourmaline	tourmaline	tourmaline	dumortierite	dumortierite
Point	52	46	66	67	56	92
Generation	Gen IIB	Gen IIB	Gen III	Gen III		
Core/Rim						
La	5.19	16.57	0.68	0.34	15.99	22.52
Ce	9.21	23.81	1.33	0.67	23.02	24.70
Pr	0.84	2.05	0.13	0.06	1.58	1.50
Nd	2.38	6.15	0.39	0.25	4.83	3.53
Sm	0.37	1.03	0.05	0.05	1.14	0.72
Eu	0.28	1.32	0.05	0.04	0.27	0.14
Gd	0.50	1.12	0.04	0.02	1.45	1.07
Tb	0.08	0.23	0.00	0.00	0.22	0.19
Dy	0.79	1.90	0.03	0.03	0.98	1.23
Ho	0.20	0.47	0.02	0.01	0.17	0.23
Er	0.72	1.85	0.10	0.04	0.37	0.62
Tm	0.14	0.33	0.02	0.01	0.08	0.11
Yb	1.37	2.46	0.19	0.07	0.60	0.84
Lu	0.22	0.39	0.03	0.01	0.10	0.11
Total REE	22.29	59.67	3.06	1.60	3.63	4.11
Eu anomaly	1.96	3.75	3.60	4.03	0.64	0.49
Li	14.85	18.71	12.44	10.18	22.72	23.97
Sc	8.73	8.96	12.60	9.34	22.77	18.96
Ti	1298.42	708.35	2617.35	2813.96	6357.76	4111.42
V	78.61	56.75	287.86	250.89	72.50	45.18
Co	36.08	25.54	44.99	50.22	1.55	4.52
Ni	25.54	46.50	40.34	42.11	1.61	5.63
Zn	49.59	23.20	10.15	10.52	6.23	7.31
Rb	4.07	1.07	0.34	6.57	44.38	15.30
Sr	46.86	99.67	27.06	19.63	44.07	18.91
Y	5.01	16.10	0.46	0.20	2.97	6.52
Zr	49.20	14.20	0.19	4.47	18.55	29.77
Nb	0.34	0.07	0.07	0.14	10.39	15.53
Mo	0.01	0.04	0.02	bdl	0.02	bdl
Ag	0.30	0.47	bdl	0.01	0.21	0.22
Ba	4.48	74.27	0.31	2.83	161.13	28.66
Hf	1.33	0.58	bdl	0.09	0.78	0.78
Ta	0.21	0.03	0.01	0.06	1.86	1.07
W	1.74	0.20	0.06	0.30	15.35	22.44
Pb	2.71	6.07	0.06	0.45	3.62	4.85
Th	1.46	0.61	0.04	0.04	12.16	12.12
U	0.51	0.33	0.01	0.02	1.58	1.08

bdl- below detection limit

## 5.6 Summary

KQ rocks is the host of the tourmaline-dumortierite rich boron bearing segregations. There are mainly three generations of tourmaline veins found in the Ujainpur area. The first generation (Gen-I) of tourmaline occurs as fine-grained aggregates, pinkish blue to bluish green in colour under petrographic microscope and preferentially along the  $S_1$  fabric. Gen-I tourmaline grains are cut across and replaced by medium to coarse grained aggregates Gen-II tourmaline as well as kyanite-quartz assemblage of KQ rock and preferentially grows along the  $S_2$  shear foliation. Gen-II tourmalines occur without (Gen-IIA) or with (Gen-IIB) association of dumortierite. Medium to coarse grained granular aggregates of Gen-IIA exhibits distinct brownish green core and light yellowish green rim under PPL. Gen-IIB tourmaline occurs as fine to medium, granular aggregates showing homogenous green body colour under PPL. From the field feature and petrographic study, it is evident that Gen-IIB tourmaline and dumortierite are syntectonic with respect to  $S_2$  but dumortierite formed earlier than the Gen-IIB tourmaline. The dark green to brown, Gen-III tourmalines occur as aggregate of prismatic grains showing random orientation. These tourmaline veins cut across the  $S_2$  plane and grow over the earlier assemblage of kyanite –quartz in KQ rock and Gen-II tourmaline-dumortierite veins. Therefore, Gen-III tourmaline occur after  $F_3$ . Tourmaline grains of Gen-I, -IIB and -III are more aluminous and Ca, alkali-deficient in nature than Gen-IIA. Gen-IIA tourmaline core is Al deficient ( $Al < 6$  apfu) and more calcic than the rim. Gen-I tourmaline composition straddles the boundary between alkali group and X vacancy group with low Ca content. Gen-IIA tourmaline grains are alkali rich with significant Ca in their structure. The tourmaline grains of the Gen-IIB and -III X vacancy rich than Gen-I and Gen-IIA. Gen-I tourmaline is magnesium rich than Gen-IIA, Gen-IIB, Gen-III tourmaline and dravite (or “oxy-dravite”) to magnesiofoitite (or “oxy-magnesio-foitite”) in character. Gen-IIA tourmaline is X vacancy deficient than Gen-I, Gen-IIB, Gen-III tourmaline and dravite (or “oxy-dravite”) in composition. Gen-IIB tourmaline is foitite (or “oxy-foitite”) to magnesio-foitite (or “oxy-magnesio-foitite”) in composition with significant amount of X- vacancies. The Gen-III tourmaline foitite (or “oxy-foitite”) in character with significant amount of X vacancies in their structure. In chondrite normalized REE, Gen-I tourmaline shows two distinct patterns. Tourmaline with low  $REE_{total}$  content shows concave up REE pattern i.e. progressive enrichment of LREE and HREE. These tourmaline grains show no Eu anomaly. While tourmaline grain with high  $REE_{total}$  content shows negative slope LREE pattern (LREE enriched than HREE) with negative Eu anomaly followed by flat HREE. Gen-IIA shows

overall negative REE pattern (LREE enriched than HREE) with a prominent positive Eu anomaly. HREE shows concave upward and depleted pattern. Core and rim are showing the same pattern except for Eu anomaly which is more prominent in the core than the rim. Gen-IIB tourmaline shows overall concave upward pattern with positive Eu anomaly. Gen-III tourmaline also shows a concave upwards REE pattern and positive Eu anomaly. The  $REE_{total}$  content in Gen III tourmaline is very low than the Gen-I, Gen-IIA, Gen-IIB tourmaline. Whereas,  $REE_{total}$  content is maximum in Gen-I tourmaline.

# CHAPTER 7

## Discussion

From combined field features, petrography, and mineral chemistry study, it is seen that the tourmaline bearing rocks of both the SPSZ and the SSZ show polyphase boron mineralization that accompanied regional deformation including shearing (Chapters 2, 3, 4, 5 and 6). In this chapter, the study of tourmaline of different generations from parts of the SPSZ and SSZ will be compared and discussed elaborately. Characteristics of tourmaline and a comparison between tourmaline mineralization corresponding to different generations from different areas along the SPSZ and the SSZ are presented in the Table 7.1.

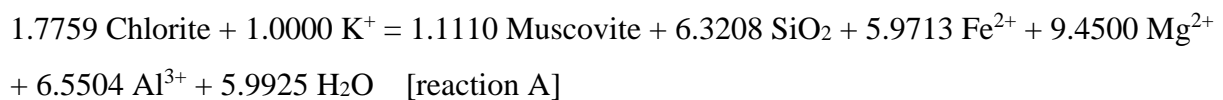
### 7.1 Summary of the tourmaline occurrences and the metasomatic reactions

In the following section the salient features of the different generations of tourmaline mineralization are presented. Along the SPSZ tourmaline mineralization occurred within three distinct rock types. In the Haripaldih area (dealt in Chapter 2) tourmaline is hosted by pegmatite veins within muscovite/quartz- muscovite schist (Table7.1). Whereas, in Beldih and Mukutmanipur region (dealt in Chapters 3 and 5) tourmaline is hosted by muscovite/quartz- muscovite schist and mica- chlorite schist (Table7.1) which are presumed to be the retrograded part of the CGGC rocks. Within the retrograded granite gneiss (part of the CGGC), centimeter to decimeter thick phyllosilicate rich bands are noted in the Mukutmanipur region. According to Chattopadhyay et al. 2016, Infiltration-driven metamorphism due to ductile shearing in the SPSZ converted the granite to mica-chlorite schist (Chapter 5). In the Kutni (dealt in Chapter 4) area tourmaline is hosted by phyllite (Table7.1) which is part of the Chandil formation of NSMB. It is evident from previous descriptions that there are two generations of tourmaline mineralization occurred along the SPSZ. The earliest stage of tourmaline (First Generation: Gen-I) formation is represented by banded or laminated quartz tourmaline rock in Beldih, Kutni, and Mukutmanipur areas (Fig 3.2a,4.2a,4.2e,5.2a, 5.2f and 5.2g). The Gen-I tourmalines are oriented parallel to the  $S_1$  regional fabric. From the structural and textural relations, it can be inferred that the Gen-I tourmalines are syn tectonic with respect to the regional deformation ( $D_1$ ) (Table7.1). Another set of tourmaline mineralization was noted, characterized by coarse, haphazardly

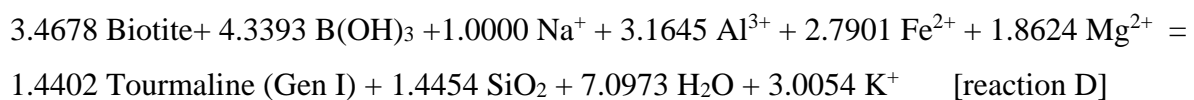
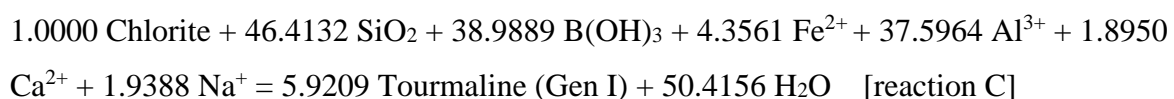
oriented tourmaline grain without any prior deformational features within the schistose rock and quartz vein. Therefore, these tourmaline grains are supposed to be formed at post D<sub>3</sub>/F<sub>3</sub> (Table 7.1). Thus, the tourmaline grains are designated as Gen-II (second generation) (Fig 3.2c, 4.2f and 5.2h). The formation of tourmaline in the schistose rock and phyllitic rock of the SPSZ result from the interaction of the host rock with boron-bearing fluid, synchronous with deformation and shearing along the SPSZ. Tourmaline-bearing rocks contain >50 vol% of tourmaline and strong oscillatory zoned tourmaline grains suggest that they were formed due to infiltration of boron rich hydrothermal fluid (Sengupta et al., 2005). Since no robust tourmaline-bearing thermobarometers are yet to be calibrated, an attempt has been made to infer the physical condition of metamorphism from the associated metamorphic minerals. The lack of suitable thermobarometers has been a major hindrance to the estimation of P-T conditions. Nevertheless, stability of biotite and lack of the assemblage in sheared granite and phyllite, it may be presumed that the thermal boundary of chlorite + K-feldspar was crossed. Temperature between 300-400°C seems to be the temperature of metamorphism. In the retrograded gneiss of the CGGC component, kyanite is sporadically present within the muscovite schist (Chapter 2). At the temperature of 300-400°C, the presence of kyanite suggest a pressure of 3-4 kbar (Fig 2.1.2d). Notwithstanding the uncertainties of P-T estimates, it can be suggested that 400°C (max) and 3-4 kbar were the metamorphic conditions of the studied area during the tourmaline-rich rocks were formed syn-tectonically (Chapter 3, 4 and 5). Chattopadhyay et al., 2016, reported that the shearing associated with metasomatic alteration in the granite of the CGGC occurred at  $470 \pm 50$  °C and 4 kbar (~15 km depth). The P-T conditions represent upper greenschist facies conditions and are characterized by intense dehydration of pelitic assemblages. The composition of tourmaline is controlled by the composition of hydrothermal fluid depending upon the fluid/rock ratio as well as interaction with the host rock (Henry and Guidotti, 1985; Slack and Trumbull, 2011; van Hinsberg et al., 2011). The concentration B in metasediments is very low (3-30ppm) (Leeman and Sisson 1996). Boron concentration in S-type granite is 1 to 12 ppm (Sauerer and Troll 1990). Average boron concentration in felsic intrusive varies from 10-30ppm (Cerny and Meintzer, 1988; Cerny, 1991). Therefore, boron released from the country rock is not sufficient to form huge tourmaline deposits. Thus, the tourmaline mineralization in the SPSZ should be the product of a large fluid influx of externally derived boron-bearing hydrothermal fluid. The Gen-I tourmalines in Beldih and Mukutmanipur region are alkali rich and most of them are schorl ( $X_{Mg}=0.43-0.57$ ) in character (Table 3.4.3a, and 5.4.3a). But Gen-I tourmaline from Kutni area is Alkali to X-vacancy rich and foitite to

Mg-foitite( $X_{Mg}=0.46-0.58$ ) in character (Table 4.4.2a). Therefore, the variation of tourmaline composition of the same generation (Gen-I) is due to the host rock lithology. Strong MgFe<sub>1</sub> substitution in Gen-I tourmaline structure hosted by muscovite/quartz-muscovite/mica chlorite schist and phyllite, suggests that infiltrated fluid was progressively rich in magnesium and depleted in Fe. Whereas Gen-II tourmalines in Beldih, Kutni and Mukutmanipur area are more Mg-rich than Gen-I tourmaline (Table 3.4.3a, 4.4.2a and 5.4.3a). Gen-II tourmaline grains are dravite ( $X_{Mg} = 0.55-0.69$ ) (Table 3.4.3a, 4.4.2a and 5.4.3a). The muscovitization and tourmaline mineralization observed in this area, indicate that metasomatic exchange between the host rocks and the hydrothermal fluid has taken place. However, for this study the four reactions that are proposed by Lecumberri-Sanchez et al., 2017, are balanced using the measured phase compositions. The stoichiometric reactions as calculated by the computer program C-Space (Torres-Roldan et al., 2000) are:

Muscovitization:



Tourmaline mineralization:



From these reactions, it can be inferred that a significant amount of B(OH)<sub>3</sub> is required for tourmaline crystallization. Thus, the externally buffered hydrothermal fluid was responsible for tourmaline mineralization in the study area. It is to be noted the Al in all the reactions are shown to be mobile species. Hydrothermal fluids in the natural metasomatic reactions may or may not makes the Al mobile (Dutta et al., 2011, Talukdar et al. 2017). The Fe and Mg content

of tourmalines is controlled by both Mg/Fe of hydrothermal fluids and Fe/Mg of the host rock as well as the salinity of the fluid (Patel et al., 2021). In highly saline fluid, Fe complex with Cl and therefore Mg-rich tourmaline will be crystallized from that fluid (Orlando et al., 2017). Whereas, for low salinity of the fluid Fe rich tourmaline will be crystallized. Thus, Fe/Mg variation of tourmaline crystal structure reflects the variations (and compositions) of salinity of the hydrothermal fluids. The composition of the fluid is controlled by externally derived fluid and internally metamorphogenic (during dehydration of the progressive metamorphism) hydrothermal fluids or mixing both of them. In an orogenic belt, meteoric fluid can percolate up to 10 km (Sibson, 1992; Barker et al., 2000). In the SPSZ metamorphism took place at 4 kbar i.e. ~15 km depth. Thus, the meteoric fluid is not the possible source of the external hydrothermal fluid. However, destabilization of mica, a sink of boron (Bebout et al., 1992), could enhance the B concentration and decreases the salinity in the hydrothermal fluids (Bebout et al., 1993; Bebout and Nakamura, 2003). In study area Gen-I tourmalines are more Fe- rich and Mg- poor than Gen-II. Therefore, the hydrothermal fluid which is responsible for Gen-I tourmaline precipitation is dominated by metamorphogenic fluids i.e. low saline fluids. However, Gen-II tourmaline precipitates from more saline hydrothermal fluid dominated by externally derived hydrothermal fluid. It is likely that the boron bearing fluids could be derived from granitic magma that is commonly rich in B (Sengupta et al., 2005, 2011).

Another type of tourmaline mineralization is found within the pegmatite vein hosted by muscovite/quartz muscovite schist in Haripaldih area (dealt in Chapter 2) of the SPSZ (Table 7.1). Pegmatite veins are co-deformed with the regional foliation i.e., the  $S_1$  fabric. The field feature and textural study support the view that, tourmaline mineralization in the pegmatite after the  $S_1/D_1$  but before and during the onset of  $D_2$  deformation (Fig 2.2a, Fig 2.2d of Chapter 2). There are distinct compositional variations observed between the core and the rim. The core is more alkali, Fe, Al, Ca rich than the rim (Table 2.4.3a). The tourmaline composition of the core is schorl ( $X_{Mg} = 0.40-0.44$ ) in character while the rim composition straddles the boundary between schorl and dravite ( $X_{Mg} = 0.48-0.52$ ). Thus, it can be inferred that the boron-rich low saline hydrothermal fluid is responsible for the tourmaline mineralization.

From the field and petrographic study, it is evident that tourmaline-bearing rocks in the Ujainpur area (NSMB) of the SSZ show polyphase boron mineralization within the host kyanite-quartzite and kyanite mica schist (Chapter 6). There are mainly three generations of tourmaline-bearing veins developed (Table 7.1). In the earliest stage which is the first

generation (Gen-I) tourmaline veins (Fig 6.2a, 6.2d, 6.3h and 6.3i) are formed along the  $S_1$ . The textural relations demonstrate that the second stage (Gen-II) of tourmaline (Fig 6.2e, 6.2f, 6.3j, 6.3l and 6.3m) mineralization occurs along the mylonitic foliation ( $S_2$ ) which is during the main phase of shearing. The third generation (Gen-III) of tourmaline (Fig 6.2i, 6.3n and 6.3o) is post tectonic in respect to the main phase of shearing ( $S_2$ ). In the studied area of Ujainpur (SSZ), the assemblage muscovite + pyrophyllite + kyanite + quartz is associated with tourmaline. This suggests that the peak metamorphism during the tourmaline mineralization is close to  $\sim 400^\circ\text{C}$ . The published isochore from fluid inclusions cuts the reaction pyrophyllite + quartz between 4-5 kbar. So  $\sim 400^\circ\text{C}$  and  $\sim 4-5$  kbar seem to be the metamorphic conditions in the studied area (Sengupta et al., 2011). This is consistent with the sporadic P-T estimates from different parts of the SSZ (Sengupta et al., 2005; Sengupta, 2012; Sengupta et al., 2011; Pal et al., 2010; Chakraborty et al., 2015). The inferred P-T values suggest that the studied area was buried at  $\sim 15-20$  km crustal depth and B-rich fluids metasomatized the host rock to produce tourmaline veins. From the textural study, it can be deciphered that B-rich fluid interacted with the kyanite-quartzite to form tourmaline. A significant amount of Al is required to crystallize tourmaline (Table 6.4.3a) which is assumed to be derived from kyanite in the host rock (Medaris et al., 2003; Henry and de Brodtkorb, 2009). Gen-I tourmalines compositionally Mg, alkali to X-vacancy rich. They are Dravite to Mg-Foitite ( $X_{\text{Mg}}=0.72-0.90$ ) in character (Table 6.4.3a). The fluid is highly saline because in saline fluid Fe complex with Cl and therefore Mg-rich tourmaline may be crystallized from that fluid (Orlando et al., 2017). Second generation (Gen-II) tourmaline veins occurred along without (Gen-IIA) or with (Gen-IIB) dumortierite grains and both are parallel to the shear foliation ( $S_2$ ). However, the relationship between the Gen-IIA and Gen-IIB tourmaline cannot be determined directly in micro-domain. Gen-IIA tourmaline grains exhibit a distinct brownish green core and light yellowish green rim under plane polarised light. These tourmaline grains are alkali rich and dravite ( $X_{\text{Mg}}=0.62-0.71$ ) in character (Table 6.4.3a). Whereas, the core is less aluminous and has higher Ca than the rim (Table 6.4.3a). So, the fluid becomes more aluminous and Ca poor for progressive crystallization of Gen-IIA. Thus, high Mg content in tourmaline structure indicates that Gen-IIA tourmalines crystallized from a saline fluid. Gen-IIB tourmaline occurred along with dumortierite parallel to  $S_2$ . Compositionally, these tourmaline grains are X-vacancy rich and foitite to Mg-foitite ( $X_{\text{Mg}}=0.48-0.61$ ) in character (Table 6.4.3a). Thus, the fluid responsible for Gen-IIB tourmaline crystallization is moderate saline fluid. Gen-III tourmaline is compositionally less Mg and more X vacancy rich than the rest of tourmaline (Gen-I and Gen-II) and foitite in character ( $X_{\text{Mg}}=0.35-0.45$ ) (Table 6.4.3a). Therefore, Gen-III tourmaline is

formed from a less saline hydrothermal fluid. From this study, it can be inferred that the Gen-I and Gen-II tourmaline are formed in more saline hydrothermal fluid than Gen-III.

Extensive work has been done on the major element composition and their variation in tourmaline depending on their crystallization environment but little work was done on trace element studies (Harris et al., 1992; Ward et al., 1992; Griffin et al., 1996; Jiang et al., 1999; Yavuz et al., 1999; Jiang et al., 2002, Jiang et al., 2004; Galbraith et al., 2009; Yavuz et al., 2011; Novák et al., 2011; Klemme et al., 2011; Gadas et al., 2012; Bačík et al., 2012; Roda-Robles et al., 2012; Marks et al., 2013; Drivenes et al., 2015; Hazarika et al., 2015, Hazarika et al., 2016, Harlaux et al., 2019; Hazarika et al., 2019, Patel et al. 2021; Hazarika et al., 2021; Ghosh et al., 2021). The incorporation of trace elements in tourmaline structure is poorly understood. Some work has been done by van Hinsberg and Marschall, 2007; van Hinsberg, 2011; Henry and Dutrow, 2011; Marks et al., 2013; Hazarika et al., 2015; Yang et al., 2015; Hazarika et al., 2016; Hazarika et al., 2019; Hazarika et al., 2021. These studies also discussed about the relationship between the incorporation of at least some trace elements depending on the major element composition. There is limited work done on trace element partitioning between tourmaline-associate mineral, tourmaline-melt, and tourmaline-fluid (Henry and Dutrow, 1996; Klemme et al., 2011; van Hinsberg, 2011; von Goerne et al., 2011; Ghosh et al., 2021). From the previous study, it can be inferred that major element compositions of tourmaline reflect dominantly those of the host rocks and mineralizing fluids (e.g., Henry and Guidotti, 1985; Slack et al., 1993; Henry and Dutrow, 1996; van Hinsberg et al., 2011). Whereas, the incorporation of trace elements in tourmaline structure is controlled by melt/fluid composition, local fluid-rock interactions, and crystal-chemical effects (van Hinsberg, 2011; Marks et al., 2013; Hazarika et al., 2015, Yang et al., 2015; Kalliomiäki et al., 2017; Hazarika et al., 2019; Hazarika et al., 2021).

Table 7.1 Characteristics of tourmaline and comparison between tourmaline mineralization corresponding to different generations from different areas along the SPSZ and SSZ, studied in the present work

Lineament	Area	Host rock	Generation of tourmaline mineralization and host rock fabric	Tourmaline chemical composition	REE pattern of tourmaline
SPSZ	Haripaldih	Pegmatite	Post tectonic w.r.t $S_1/D_1$ and pre to syn-tectonic w.r.t $F_2/D_2$	<ul style="list-style-type: none"> <li>Alkali group</li> <li>Core is schorl in composition whereas rim straddle the boundary between schorl-dravite</li> </ul>	<ul style="list-style-type: none"> <li>LREE enrichment with negative slope</li> <li>Positive Eu anomaly</li> <li>HREE depletion with negative slope</li> </ul>
			Beldih	Muscovite schist/quartz-muscovite schist	Gen-I (syn-tectonic w.r.t $S_1/D_1$ )
	Gen II (post-tectonic w.r.t $S_1/D_1$ and $D_3/F_3$ )	<ul style="list-style-type: none"> <li>Alkali group</li> <li>Core straddle the boundary between schorl-dravite whereas rim is dravite</li> </ul>			<ul style="list-style-type: none"> <li>LREE enrichment with negative slope</li> <li>Positive Eu anomaly</li> <li>Flat HREE pattern</li> </ul>
	Kutni	Quartz reef within phyllite	Gen-I (syn-tectonic w.r.t $S_1/D_1$ )	<ul style="list-style-type: none"> <li>Alkali to X-vacancy group</li> <li>Dravite, foitite to magnesio-foitite in composition for both core and rim</li> </ul>	<ul style="list-style-type: none"> <li>LREE enrichment with negative slope</li> <li>Positive Eu anomaly</li> <li>Flat to concave up HREE pattern</li> </ul>
			Gen II (post-tectonic w.r.t $S_1/D_1$ and $D_3/F_3$ )	<ul style="list-style-type: none"> <li>Alkali group</li> <li>Dravite in composition for both core and rim</li> </ul>	<ul style="list-style-type: none"> <li>LREE enrichment with negative slope</li> <li>Positive Eu anomaly</li> <li>Flat to concave up HREE pattern</li> </ul>
	Mukutmanipur	Mica-chlorite schist	Gen-I (syn-tectonic w.r.t $S_1/D_1$ )	<ul style="list-style-type: none"> <li>Alkali group</li> <li>Core is schorl in composition whereas rim straddle the boundary between schorl and dravite</li> </ul>	<ul style="list-style-type: none"> <li>Depleted LREE concentration with negative sloped</li> <li>Positive Eu anomaly</li> <li>Flat to concave up HREE pattern</li> </ul>
			Gen II (post-tectonic w.r.t $S_1/D_1$ and $D_3/F_3$ )	<ul style="list-style-type: none"> <li>Alkali group</li> <li>Dravite in composition for both core and rim</li> </ul>	<ul style="list-style-type: none"> <li>Depleted LREE concentration with negative sloped</li> <li>Positive Eu anomaly</li> <li>Flat to concave up HREE pattern</li> </ul>
	SSZ	Ujainpur	Kyanite quartzite/kyanite muscovite schist	Gen I(syn-tectonic w.r.t $S_1/D_1$ )	<ul style="list-style-type: none"> <li>Alkali to X-vacancy group</li> <li>Dravite to Mg foitite in composition</li> </ul>
Gen IIA (without dumortierite) – syn-tectonic w.r.t $S_2/D_2$				<ul style="list-style-type: none"> <li>Alkali group</li> <li>Dravite in composition</li> </ul>	<ul style="list-style-type: none"> <li>LREE enrichment with negative slope</li> <li>Positive Eu anomaly</li> <li>HREE depletion with negative slope</li> </ul>
Gen IIB (with dumortierite) – syn-tectonic w.r.t $S_2/D_2$				<ul style="list-style-type: none"> <li>X-vacancy group</li> <li>Foitite to Mg foitite in composition</li> </ul>	<ul style="list-style-type: none"> <li>LREE enrichment with negative slope</li> <li>Positive Eu anomaly</li> <li>Concave up HREE pattern</li> </ul>
Gen III(post tectonic w.r.t $D_3/F_3$ )				<ul style="list-style-type: none"> <li>X-vacancy group</li> <li>Foitite in composition</li> </ul>	<ul style="list-style-type: none"> <li>LREE enrichment with negative slope</li> <li>positive Eu anomaly</li> <li>Concave up HREE pattern</li> </ul>

## 7.2 REE characteristics of the tourmalines of the studied rocks

REE patterns of tourmaline is sporadically reported by Torres-Ruiz et al., 2003; Jiang et al., 2004; Pesquera et al., 2005; Garda et al. 2010; Marks et al., 2013; Hazarika et al., 2015, Yang et al., 2015; Kalliomäki et al., 2017; Hazarika et al., 2019; Hazarika et al., 2021, Patel et al., 2021. In this study, REE of different generations of tourmaline from the studied areas are presented (Chapters 2, 3, 4, 5 and 6) (Table 7.1). In Fig.7.2.1a to 7.2.1g and 7.2.2a to 7.2.2e, we have compared the published data of REE of tourmaline with the REE data that are generated in this study for different generations of tourmaline. The total REE and the chondrite normalized REE patterns of the studied tourmaline grains vary with the tourmaline generations and the host rock compositions (Fig.7.2.1a to 7.2.1g and 7.2.2a to 7.2.2e). Tourmaline from the kyanite-rich rocks of NSMB show distinctly higher REE concentrations (up to 1029 ppm; Table 6.5.2a) than the tourmalines from the SPSZ (up to 15ppm; Table 2.5.2a, Table 3.5.2a, Table 4.5.2a and Table 5.5.2a). Barring a few tourmaline grains from the kyanite-rich rocks of the NSMB, all other tourmaline grains, irrespective of their generation and host rock, show distinctly positive Eu anomaly (Fig 7.2.2c, 7.2.2d and 7.2.2e). The odd samples show weak negative to flat Eu anomaly (Fig 7.2.2a and 7.2.2b). The positive Eu- anomaly of tourmaline has been reported in different, albeit a few areas (Jiang et al., 2004; Pesquera et al., 2005; Garda et al. 2010; Marks et al., 2013; Hazarika et al., 2015, Yang et al., 2015; Kalliomäki et al., 2017; Hazarika et al., 2019; Hazarika et al., 2021, Patel et al., 2021). Similar to the published REE pattern of tourmaline grains, tourmaline in the SPSZ, shows moderate enrichment in LREE ( $La_N/Yb_N = 10-150$ ) (Table 2.5.2a, 3.5.2a, 4.5.2a and 5.5.2a), flat to marginally convex upward HREE patterns (Fig 7.2.1a to 7.2.1g). The REE data of tourmaline as reported by Hazarika et al., 2015; Pesquera et al., 2005; Garda et al., 2010 are similar to the REE patterns of the tourmaline in the SPSZ. However, relative to the REE pattern of tourmaline, reported by Garda et al. 2010, most of the REE, particularly the HREE show subchondritic values (Fig 7.2.1d, 7.2.1e, 7.2.1f and 7.2.1g). There is no significant difference, in terms of the REE patterns between Gen I and Gen II (Fig 7.2.1b, 7.2.1c, 7.2.1d, 7.2.1e, 7.2.1f and 7.2.1g). In contrast with the tourmaline from the SPSZ, the chondrite normalized REE pattern of the Kyanite-rich rock of the NSMB, by and large, shows flat REE pattern without much depletion of the HREE (relative to the LREE) (Fig 7.2.2a, 7.2.2b, 7.2.2d and 7.2.2e). The REE data of tourmaline as reported by Torres-Ruiz et al., 2003; Pesquera et al., 2005; Garda et al., 2010 are similar to the REE patterns of the tourmaline within the kyanite-quartzite of NSMB (Fig 7.2.2a, 7.2.2b, 7.2.2d and 7.2.2e). However, Gen IIA tourmaline shows LREE enrichment ( $La_N/Yb_N = 80-270$ )

(Table 6.5.2a), distinct positive Eu anomaly, and HREE depletion is noted and which shows similar REE pattern reported by Torres-Ruiz et al., 2003 (Fig 7.3c).

Studies have shown that REE prefers melt relative to coexisting aqueous fluids (Flynn and Burnham, 1978; Jolliff and Papike, 1987). In view of these studies, it is likely that the ingredients of low REE bearing tourmaline in the SPSZ was sourced from a metamorphogenic fluid source. The ingredients of the high REE tourmaline in the kyanite-quartzite of NSMB, on the other hand, could have formed from a granitic melt. Owing to the paucity of the exposures, it is not clear in the tourmaline mineralization in the kyanite-quartzite of NSMB was linked with coeval granitic/pegmatitic melt. Behaviour of REE in the metasomatic zones is a subject of debate. According to some studies REE remains immobile during hydrothermal and metamorphic processes (Hellman et al., 1979; Fleet, 1984; Bence and Taylor, 1985; Maclean, 1988). Other studies suggested that Eu and LREE preferentially fractionate into hydrothermal fluids (Michard and Albarede, 1986; Whitford et al., 1988; Plimer et al., 1991; Slack et al., 1993; Slack, 1996; Jiang et al., 2004) which is particularly true for the high-temperature fluid (>250 °C; Sverjensky, 1984; Bau, 1991; Bau and Möller, 1992). Decoupling of Eu from the other REE is manifested by the development of Eu anomalies, either negative or positive, in chondrite-normalized REE patterns (Bau, 1991; Bau and Möller, 1992). This occurs due to a change in Eu valence state (Eu can be in +2 or +3) due to changes in redox conditions of hydrothermal or metamorphic fluids (Bau 1991; Jiang et al., 2004). Based on theoretical calculation, Sverjensky 1984 referred that divalent Eu is predominant at temperatures >250° C in a hydrothermal and metamorphic environment. Therefore, in a reducing environment, Eu can occur in the divalent oxidation state (Bau, 1991). Tourmalines have a positive Eu anomaly due to the preferred incorporation of  $\text{Eu}^{2+}$  in their structure (van Hinsberg, 2011). The incorporation of REE in the tourmaline structure is controlled by its mineral chemistry (van Hinsberg, 2011; Marks et al., 2013; Hazarika et al., 2015). Tourmaline can accommodate  $\text{REE}^{3+}$  into the Y sites whereas,  $\text{Eu}^{2+}$  can accommodate in the X site of tourmaline structure (van Hinsberg, 2011; Marks et al., 2013; Hazarika et al., 2015).  $\text{Ca}^{2+}$  cations at the X site prefer LREE with larger ionic radii rather than HREE and Y in the tourmaline structure (Marks et al., 2013; Hazarika et al., 2015). The ionic radius of nine-fold coordinated  $\text{Ca}^{2+}$  (1.18 Å) is similar with those of LREEs in nine-fold coordination (1.21–1.13 Å) (Marks et al., 2013; Hazarika et al., 2015). HREEs although they are in same coordination but the ionic radius decreases down to 1.07–1.03 Å (Shannon, 1976; Marks et al., 2013; Hazarika et al., 2015). It was observed that substitution of LREEs in place of Ca in the X-site from the positive correlation between Ca and

LREEs (Marks et al., 2013; Hazarika et al., 2016; Harlaux et al., 2019). Thus, tourmaline with sufficient amount of Ca in its structure can accommodate LREEs. During fluid rock interaction, in the fluid the fractionation of LREEs than the HREEs is prominent (Jiang et al., 2004; Marks et al., 2013; Hazarika et al., 2015; Yang et al., 2015; Kalliomäki et al., 2017). An experimental study by Migdisov et al., 2018, inferred that the LREEs are more stable and mobile than the HREEs in chloride-bearing aqueous solutions. Tourmaline shows LREE enrichment and HREE depleted pattern relative to their host rock which indicates that LREE fractionates than HREE in tourmaline structure (Ruiz et al., 2003).

In this study both the generations of tourmaline along the SPSZ have a significant amount of Ca (0.10 to 0.35 apfu) (Table 2.4.3a, 3.4.3a, 4.4.3a and 5.4.3a) in their structure so it can be inferred that tourmaline can accumulate LREE than HREE in their structure. Thus, in the SPSZ region tourmalines are LREE enriched than HREE (Fig 7.2.1a to 7.2.1g). The positive Eu anomalies tourmalines due the substitution of  $\text{Eu}^{2+}$  for  $\text{Ca}^{2+}$  on the X-site in a reducing environment. Low REE contents, LREE incorporation in tourmaline structure than HREE and strong Positive Eu anomaly imply that tourmaline is formed due to hydrothermal fluid with high fluid/rock ratios under reducing conditions. However, some of the tourmaline grains along the SPSZ show enrichment of HREE. HREE enrichment due to plagioclase dissolution which releases more HREE in the fluid (Möller et al., 1997; Shibata et al., 2006) or greater availability of complexing agents like  $\text{F}^-$ ,  $\text{CO}_3^{2-}$ , or  $\text{OH}^-$  (Bau 1991). If the fluid/ rock ratio is high enough, fluid-rock interaction will lead to the preferential removal of HREE from the rock (Bau 1991). The host rocks in the study area contain < 10 vol % of plagioclase feldspar. Thus, HREE enrichment in tourmaline structure due to the presence of complexing agent in a high fluid/rock ratio conditions. Different generations (Gen- I, Gen-IIB and Gen-III) of tourmaline in host kyanite-quartzite of the NSMB are less calcic (0.02-0.07apfu) (Table 6.4.3a) than the tourmaline of the SPSZ. Thus, it shows flat REE pattern without much depletion of the HREE (relative to the LREE) (Fig 7.2.2a, 7.2.2b, 7.2.2d, 7.2.2e). However, Gen-IIA tourmaline shows a significant amount of Ca (15-35 apfu) (Table 6.4.3a) in their structure. Therefore, it shows LREE enrichment with a positive Eu anomaly (Fig 7.2.2c).

### **7.3 Significance of the trace element concentrations in the studied tourmaline bearing rocks**

The fluid- melt partitioning in the granitic system, suggest that Sr (along with REEs) strongly partitioned into the melt than the hydrothermal fluids (Marks et al., 2013; Drivenes et al., 2015). Thus, tourmaline that crystallized from granitic/ pegmatitic melts has higher concentrations of Sr (and REEs) than the tourmaline that crystallized from hydrothermal fluids. Li, Pb, Zn and Cu are typically fractionated into the hydrous fluids (London et al., 1988; Audetat and Pettke, 2003; Audetat et al., 2008; Zajacz et al., 2008; Borchert et al., 2010; Marks et al., 2013). According to Ghosh et al., 2021, high Li concentration of the fluid is derived from the granitic source. Higher Sr and REE concentrations and low Ni contents indicate that they may have crystallized from late-stage granite-derived melts (Marks et al., 2013). Tourmaline formed from late-stage fractionates of granitic magmas i.e pegmatitic melts rich in incompatible elements such as the REEs, Zr, Y, Sr and Pb whereas tourmaline formed from aqueous hydrothermal fluids is low in the high-field-strength elements (HFSEs) such as REEs, Zr and Y due to much lower solubility (Hazarika et al., 2015). Enrichment of Li and Be content in tourmaline might be an indicator that boron-rich hydrothermal fluids have a magmatic source (Slack et al., 1996). High Li, Mn, Zn, and Sn in tourmaline structure indicate relatively saline fluid derived from granitic sources (Codeco et al., 2020). LILE like Ba and Rb partitioned strongly into cogenetic minerals such as mica whereas Sr, Pb and the rare earth elements (REE) partition into tourmaline (due to partition coefficients slightly greater than 1) (Garda et al., 2010; Klemme et al., 2011; Ghosh et al., 2021). Other HFSE, such as Nb and Ta, are strongly partitioned into mica, whereas the tetravalent Zr, Hf, U and Th are partitioned into the coexisting tourmaline (Klemme et al., 2011; Ghosh et al., 2021).

In this study, different generations of tourmaline in the SPSZ, overall show low concentration of Li (10- 25ppm) (Table- 2.5.2a, 3.5.2a, 4.5.2a and 5.5.2a). In UCC multielement plot,(Fig 2.5.1a, 3.5.1c, 3.5.1d, 4.5.1c, 4.5.1d, 5.5.1c and 5.5.1d) of tourmaline shows prominent depletion in LILE such as Rb and Ba. Sr shows moderate depletion to near crustal values. Compatible and metal elements such as Ni, Co, Zn and V, Sc concentrations are consistent and closer to UCC values. Within HFS elements, overall notable depletion such as Y, Hf, Zr but variable concentrations are observed. Gen-II tourmaline shows lower concentration of Li (up to 15ppm) than Gen-I. Due to the low concentration of Li, Sr and notable depletion (with respect to UCC) of HFSE content, it can be suggested that hydrothermal fluid is dominated

by metamorphogenic fluids. A similar conclusion was also drawn from the REE pattern (discussed above). Prominent depletion in LILE such as Rb and Ba can be explained by co-precipitation of muscovite and tourmaline. But Gen-II tourmaline which occurs within quartz veins also shows depletion of Rb and Ba. So, it can be inferred that tourmaline itself did not fractionate Rb and Ba in their structure. The tourmaline in host kyanite quartzite of the NSMB of different generations shows higher Li concentration (15-45ppm) (Table-6.5.2a) than the SPSZ except Gen IIA(Li concentration is upto 3ppm) which indicates that the fluid may be derived from the granitic sources. In UCC multielement plot (6.5.1f, 6.5.1g, 6.5.1h, 6.5.1i and 6.5.1j) of tourmaline shows prominent depletion in LILE such as Rb and Ba. Sr shows moderate depletion to near crustal values. Compatible and metal elements such as Ni, Co, V, Sc concentrations are near to upper crustal values. Within HFS elements, overall notable depletion such as Hf, Zr but variable concentrations is observed. However, in Gen I tourmaline shows prominent enrichment Y compared to upper crustal value which indicates fluids are derived from the granitic magma. From the REE and trace element study it can be inferred that magmatic-hydrothermal fluid is not solely responsible for tourmaline mineralization along SSZ. The externally granite derived fluid mixed with internal metamorphogenic fluids is responsible for the different generations of tourmaline formation in Ujainpur area.

#### **7.4 Timing of tourmaline mineralization**

There is no robust geochronological data to confirm the actual age of ductile shearing in the SPSZ. The ~0.93 Ma old Sushina alkaline complex has intruded (Reddy et al., 2009 and Chatterjee et al., 2013) and shared the same deformation and metamorphism with the enclosing rocks. These deformed alkaline rocks are highly sheared, are interpreted to have formed in an extensional regime and was subsequently closed during deformation (Acharyya et al., 2006; Ray et al., 2012; Talukdar et al., 2012, Ray, 2016). This closure of the rift can be considered as the age of shearing. The shear deformation and development of the regional plane fabric i.e  $S_1$  is younger than ~0.93 Ga. This then follows that the Gen-I tourmaline which is syntectonic to  $S_1$ , is younger than ~0.93 Ga. The Gen-II tourmaline is much younger than the Gen-I. However, Tourmaline within the pegmatite are post tectonic regarding  $S_1/D_1$  and pre to syntectonic to  $D_2$ . Pegmatite veins are co-deformed with the regional foliation i.e.,  $S_1$  fabric. On the basis of the age of Sushina alkaline complex and continuation of  $S_1$  fabric in the Harpaldih region, the timing of tourmaline mineralization is poorly constrained as <0.93 Ga.

Tourmaline mineralization in the kyanite-rich rocks in the NSMB appears to be distinctly older. This is because of the fact that tourmaline mineralization in kyanite-quartzite of the NSMB are associated with the Cu-U mineralization (Pal et al., 2010; Sengupta et al., 2005; Sengupta et al., 2011; Pal and Rhede, 2013; Patel et al., 2021). According to Pal and Rhede, 2013, hydrothermal alteration and primary uranium mineralization occurred at ca. 1.88 Ga. At 1.65 Ga another hydrothermal event took place which is responsible for the remobilized of the early uranium and REE, Ca, and Fe metasomatism. The latest hydrothermal event affected the SSZ at ~1.0 Ga. The available information does not precisely date the tourmaline mineralization in the Ujainpur kyanite-rich rock. Nevertheless, studies of Sengupta et al., (2015, 2011), Pal et al., 2010, support the view that the Cu-U mineralized zones share the same deformation and metamorphism of the host rock. In view of this, tourmaline mineralization in kyanite-quartzite of the NSMB appear to be older than 1.0 Ga.

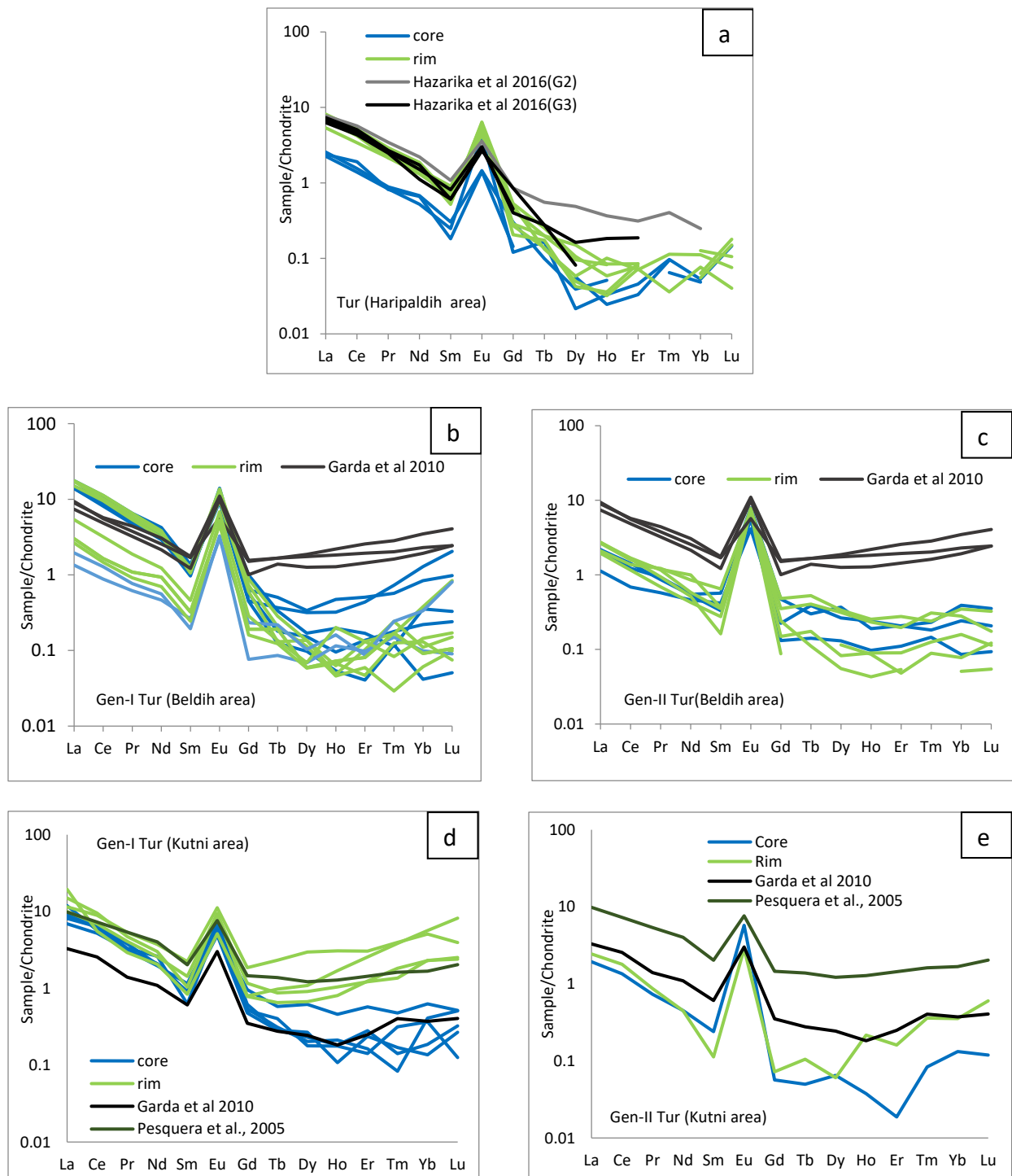


Fig 7.2.1a: Chondrite normalized REE pattern of tourmaline in Haripaldih (study area) and tourmaline from Bihar mica belt, India (Hazarika et al., 2015). Fig 7.2.1b: Chondrite normalized REE pattern of Gen-I tourmaline in Beldih (study area) and tourmaline from São José do Barreiro Area, NE Ribeira Belt, Southern Brazil (Garda et al., 2010). Fig 7.2.1c: Chondrite normalized REE pattern of Gen-II tourmaline in Beldih (study area) and tourmaline from São José do Barreiro Area, NE Ribeira Belt, Southern Brazil (Garda et al., 2010). Fig 7.2.1d: The chondrite normalized REE pattern of Gen-I tourmaline in Kutni (study area), tourmaline from Central Iberian Zone, Salamanca, Spain (Pesquera et al., 2005) and São José do Barreiro Area, NE Ribeira Belt, Southern Brazil (Garda et al., 2010). Fig 7.2.1e: The chondrite normalized REE pattern of Gen-II tourmaline in Kutni (study area), tourmaline from Central Iberian Zone, Salamanca, Spain (Pesquera et al., 2005) and São José do Barreiro Area, NE Ribeira Belt, Southern Brazil (Garda et al., 2010).

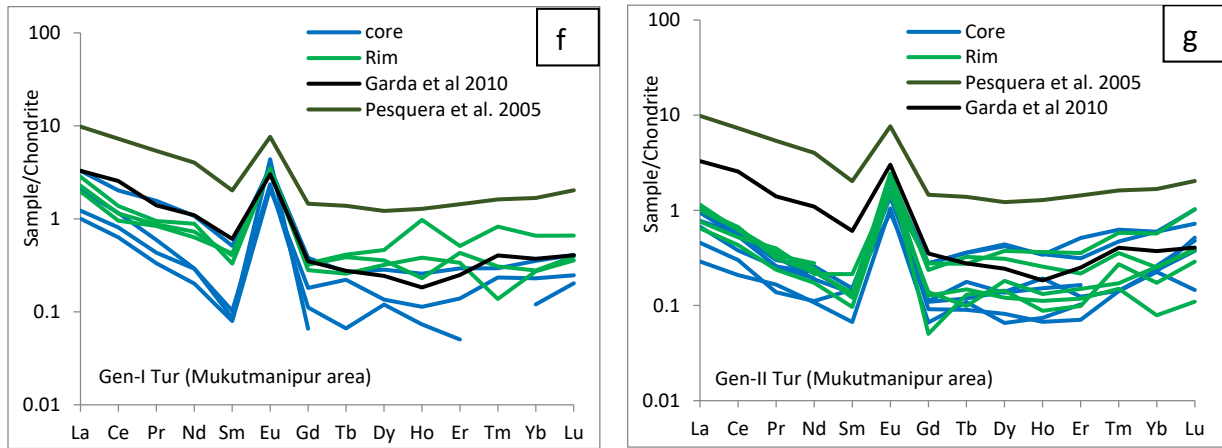


Fig 7.2.1f: The chondrite normalized REE pattern of Gen-I tourmaline in Mukutmanipur (study area), tourmaline from Central Iberian Zone, Salamanca, Spain (Pesquera et al., 2005) and São José do Barreiro Area, NE Ribeira Belt, Southern Brazil (Garda et al., 2010). Fig 7.2.1g: The chondrite normalized REE pattern of Gen-II tourmaline in Mukutmanipur (study area), tourmaline from Central Iberian Zone, Salamanca, Spain (Pesquera et al., 2005) and São José do Barreiro Area, NE Ribeira Belt, Southern Brazil (Garda et al., 2010).

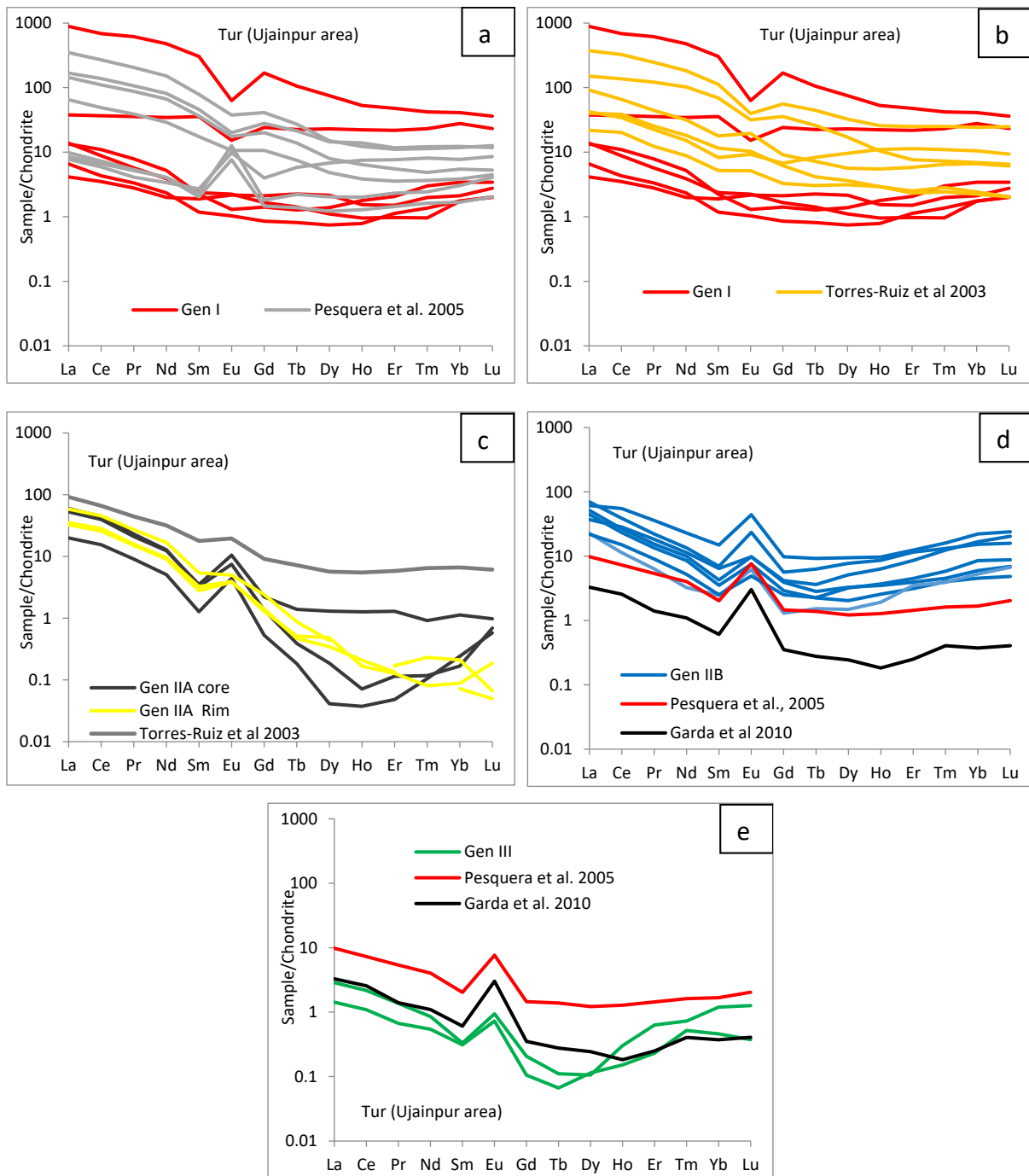


Fig 7.2.2a: The chondrite normalized REE pattern of Gen-I tourmaline in Ujainpur (study area) and tourmaline from Central Iberian Zone, Salamanca, Spain (Pesquera et al., 2005). Fig 7.2.2b The chondrite normalized REE pattern of Gen-I tourmaline in Ujainpur (study area) and tourmaline from Sierra Nevada, Betic Cordillera, southeastern Spain (Torres-Ruiz et al., 2003). Fig 7.2.2c: The chondrite normalized REE pattern of Gen-IIA tourmaline in Ujainpur (study area) and tourmaline from Sierra Nevada, Betic Cordillera, southeastern Spain (Torres-Ruiz et al., 2003). Fig 7.2.2d: The chondrite normalized REE pattern of Gen-IIB tourmaline in Ujainpur (study area), tourmaline from Central Iberian Zone, Salamanca, Spain (Pesquera et al., 2005) and São José do Barreiro Area, NE Ribeira Belt, Southern Brazil (Garda et al., 2010). Fig 7.2.2e: The chondrite normalized REE pattern of Gen-III tourmaline in Ujainpur (study area), tourmaline from Central Iberian Zone, Salamanca, Spain (Pesquera et al., 2005) and São José do Barreiro Area, NE Ribeira Belt, Southern Brazil (Garda et al., 2010).

## References

Acharjee, S., Ray, J., Dey, P., Bhattacharyya, D., Banerjee, M., Chattopadhyay, B., Sengupta, S., Bhatt, A. K., Chowdhury, D., Dwivedi, A. K., Mahato, S. 2016. Mineral chemistry of tourmaline from Mashak pahar, South Purulia Shear Zone (SPSZ), Eastern Indian Shield. *Journal of Earth System Science*, **125**, 1681-1696.

Acharyya, S. K. 1993. Greenstones from Singhbhum craton, their Archaean character, oceanic crustal affinity and tectonics. *Proceedings National Academy of Science India Section A*, **63**, 211-222.

Acharyya, S. K. 2003a. The Nature of Mesoproterozoic Central Indian Tectonic Zone with Exhumed and Reworked Older Granulites. *Gondwana Research*, **6**, 197–214.

Acharyya, S. K. 2003b. A plate tectonic model for Proterozoic crustal evolution of Central Indian Tectonic Zone. *Gondwana Geological Magazine*, **7**, 9-31.

Acharyya, A., Roy, S., Chaudhuri, B. K., Basu, S. K., Bhaduri, S. K., Sanyal, S. K. 2006. Proterozoic rock suites along south Purulia shear zone, eastern India: Evidence for rift related setting. *Journal of Geological Society of India*, **68**, 1069–1086.

Acharyya, S. K., Gupta, A., Orihashi, Y. 2010a. New U–Pb zircon ages from Paleo-Mesoarchean TTG gneisses of the Singhbhum Craton, eastern India. *Geochemical Journal*, **44**, 81–88.

Acharyya, S. K., Gupta, A., Orihashi, Y. 2010b. Neoproterozoic-Palaeoproterozoic stratigraphy of the Dhanjori basin, Singhbhum Craton, Eastern India: And recording of a few U- Pb zircon dates from its basal part. *Journal of Asian Earth Science*, **39**, 527-536, doi: 10.1016/j.jseas.2010.04.023.

Agrosi, G., Bosi, F., Lucchesi, S., Melchiorre, G., and Scandale, E. 2006. Mn tourmaline crystals from island of Elba (Italy): growth history and growth marks. *American Mineralogist*, **91**, 944–952.

Arif, M., Henry, D. J., and Moon, C. J. 2010. Cr-bearing tourmaline associated with emerald deposits from Swat, NW Pakistan: Genesis and its exploration significance. *American Mineralogist*, **95**, 799–809.

Audetat, A., Pettke, T., 2003. The magmatic–hydrothermal evolution of two barren granites: a melt and fluid inclusion study of Rito del Medio and Canada Pinabete plutons in northern New Mexico (USA). *Geochimica et Cosmochimica Acta*, **67**, 97–121.

Audetat, A., Pettke, T., Heinrich, C. A., Bodnar, R. J., 2008. The composition of magmatic–hydrothermal fluids in barren and mineralized intrusions. *Economic Geology*, **103**, 877–908.

Bačík, P., Uher, P., Ertl, A., Jonsson, E., Nysten, P., Kanický, V. Vaculovič, T. 2012. Zoned Ree Enriched Dravite from a Granitic Pegmatite in Forshammar Bergslagen Province, Sweden an Empa Xrd and La–Icp–Ms Study. *The Canadian Mineralogist*, **50**, 825–841.

Ball, V. 1881. The geology of Singhbhum and Manbhum. *Memoir, Geological Survey of India*, **18**, 554.

Bandyopadhyay, N. 2003. Metamorphic history of the rocks in the southeastern sector of the Proterozoic Singhbhum shear zone and its environs, Ph.D. Thesis, *University of Calcutta, Calcutta, India*.

Banerjee, P. K. 1982. Stratigraphy, petrology and geochemistry of some Precambrian basic volcanic and associated rocks of Singhbhum district, Bihar and Mayurbhanj and Keonjhar districts, Orissa. *Geological Survey of India*, **111**, 1–54.

Banerjee, A. K. 1985. On the nature of a part of the boundary between Chhotanagpur plateau and Singhbhum orogenic belt and its role in mineralization. *Bulletin of Geological Mineralogical Metallurgical Society of India*, **53**, 171 – 180.

Banerji, A. K., Talapatra, A. 1966. Soda-granites from south of Tatanagar, Bihar, India. *Geological Magazine*, **103**, 340–351.

Banerji, A. K. 1977. On the Precambrian banded iron formations and the manganese ores of the Singhbhum region, eastern India. *Economic Geology*, **72**, 90-98.

Banerji, A. K. 1991. Geology of the Chhotonagpur region. *Indian Journal Geology*, **63**, 275-282.

Barker, A.J., Bennet, D.G., Boyce, A.J., and Fallick, A.E. 2000. Retrogression by deep infiltration of meteoric fluids into thrust zones during late orogenic rapid unroofing. *Journal of Metamorphic Geology*, **18**, 307–318.

Bau, M. 1991. Rare-earth element mobility during hydrothermal and metamorphic fluid–rock interaction and the significance of the oxidation state of europium. *Chemical Geology*, **93**, 219–230.

Bau, M., Moeller, P. 1992. Rare earth element fractionation in metamorphogenic hydrothermal calcite, magnesite and siderite. *Mineralogy and Petrology*, **45**, 231-246.

Beaty, D. W., Hahn, G. A., Threlkeld, W. E. 1988. Field, isotopic, and chemical studies of tourmaline-bearing rocks in the Belt-Purcell Supergroup: genetic constraints and exploration significance for Sullivan type ore deposits. *Canadian Journal of Earth Sciences*, **25**, 392-402.

Bebout, G.E., Graham, C.M., Leeman, W.P., Sisson, V.B., 1992. Trace element distribution and mobility during prograde metamorphism of sediments: ion-microprobe study of the Pelona Schist, California. *EOS 73*, **327** (Spring Mtg. Amer. Geophys. Union).

Bebout, G.E., Nakamura, E., 2003. Record in metamorphic tourmalines of subduction-zone devolatilization and boron cycling. *Geology*, **31**, 407–410.

Bebout, G.E., Ryan, J.G., Leeman, W.P., 1993. B–Be systematics in subduction related metamorphic rocks: characteristics of the subducted component. *Geochimica et Cosmochimica Acta*, **57**, 2227–2237.

Bence, A.E., Taylor, B.E. 1985. Rare earth element systematics of West Shasta metavolcanic rocks: Petrogenesis and hydrothermal alteration. *Economic Geology*, **8**, 2164-2176.

Beurlen, H., de Moura, O. J. M., Soares, D. R., Da Silva, M. R. R., Rhede, D. 2011. Geochemical and geological controls on the genesis of gem-quality "Paraíba tourmaline" in granitic pegmatites from northeastern Brazil. *Canadian Mineralogist*, **49**, 277-300.

Bhattacharya, B. P. 1976. Metamorphism of the Precambrian rocks of the central part of Santhal Parganas district, Bihar. *The Quarterly Journal of the Geological, Mining, and Metallurgical Society of India*, **48**, 183-196.

Bhattacharya, B. P. 1982. Tectono-metamorphic environment of granite and pegmatite emplacement in the Precambrians of Bihar mica belt. In: Proceedings of Symposium on Mettallogeny of the Precambrian. *Geological Survey of India*, 45-56.

Bhattacharya, S. 1989. Ductile Shear Zone in Purulia. *Indian Journal of Geology*, **61**, 172-178.

Bhattacharya, S. 1992. Evolution of Singhbhum mobile belt by continental rifting and implications of the geochemistry of Purulia amphibolites. *Indian Journal of Earth Sciences*, **19**, 9-17.

Bhattacharjee, S., Mulder, J.A., Roy, S., Chowdhury, P., Cawood, P.A., Nebel, O., 2021. Unravelling depositional setting, age and provenance of the Simlipal volcano-sedimentary complex, Singhbhum craton: evidence for Hadean crust and Mesoarchean marginal marine sedimentation. *Precambrian Research*. **354**, 106038.

Biswas, S., Sengupta, N., Ray, R., Chakraborty, S., Sanyal, S., Sengupta, P. 2013. Repeated boron infiltration at continental suture zone: An example from South Purulia Shear Zone, West Bengal, India. 3rd Precambrian Continental Growth and Tectonism Abstract Volume, *IAGR Conference Series*, No **16**, 36-37.

Borchert, M., Wilke, M., Schmidt, C., Rickers, K., 2010a. Rb and Sr partitioning between haplogranitic melts and aqueous solutions. *Geochimica et Cosmochimica Acta*, **74**, 1057–1076.

Borchert, M., Wilke, M., Schmidt, C., Cauzid, J., Tucoulou, R., 2010b. Partitioning of Ba, La, Yb and Y between haplogranitic melts and aqueous solutions: an experimental study. *Chemical Geology*, **276**, 225–240.

Bose, M. K., Chakraborti, M. K. 1981. Fossil marginal basin from the Indian shield: A model for evolution of Singhbhum Precambrian belt, Eastern India. *Geologische Rundschau*, **70**, 504-518.

Bose, M. K. 1994. Sedimentation pattern and tectonic evolution of the Proterozoic Singhbhum basin in the Eastern Indian Shield. *Tectonophysics*, **231**, 325-346.

Bosi, F., Lucchesi, S. 2007. Crystal chemistry in the tourmaline group: structural constraints on chemical variability. *American Mineralogist*, **92**, 1054-1063.

Bragg, W. L. 1937. Atomic Structure of Minerals. *Cornell University Press*, Ithaca, NY, 292.

Cerny, P., 1991. Fertile granites of Precambrian rare-element pegmatite fields: is geochemistry controlled by tectonic setting or source lithologies? *Precambrian Research*. **51**,429-468.

Cerny, P., Meintzer, R. E., 1988. Fertile granites in the Archean and Proterozoic fields of rare-element pegmatites: crustal environment, geochemistry, and petrogenetic relationships. In: Taylor RP, Strong DF (eds) Recent Advances in the Geology of Granite-Related Mineral Deposits. *Canadian Institute of Mining and Metallurgy, Special Volume*, **39**,170-207.

Chakrabarty, A., Sen, A. K. 2010. Enigmatic association of the carbonatite and alkali-pyroxenite along the Northern Shear Zone: A saga of primary magmatic carbonatites. *Journal of the Geological Society of India*, **74**, 403-413.

Chakraborty, K.L., Majumder, T., 2002. Some important aspects of the banded iron formation (BIF) of Eastern Indian Shield (Jharkhand and Orissa). *Indian Journal of Geology*, **74**, 37–47.

Chakraborty, M., Sengupta, N., Biswas, S., Sengupta, P. 2015 Phosphate minerals as a recorder of P-T-fluid regimes of metamorphic belts: example from the Palaeoproterozoic Singhbhum

Shear Zone of the East Indian shield. *International Geology Review*, **57**, 1619-1632, doi: 10.1080/00206814.2014.982216.

Changkakoti, A., Gray, A., Morton, R. D., Sarkar, S. N. 1987. The Mosabani Copper Deposit, India – A preliminary study on the Nature and genesis of ore fluids. *Economic Geology*, **82**, 1619–1625.

Chatterjee, N., Banerjee, M., Bhattacharya, A., Maji, A. K. 2010. Monazite chronology, metamorphism–anatexis and tectonic relevance of the mid-Neoproterozoic Eastern Indian Tectonic Zone. *Precambrian Research*, **179**, 99-120.

Chatterjee, N. Ghose, N. C. 2011. Extensive Early Neoproterozoic high-grade metamorphism in North Chotanagpur Gneissic Complex of the Central Indian Tectonic Zone. *Gondwana Research*, **20**, 362–379.

Chatterjee, P., De, S., Ranaivoson, M., Mazumder, R., Arima, M. 2013. A review of the ~1600 Ma sedimentation, volcanism, and tectono-thermal events in the Singhbhum craton, Eastern India. *Geoscience Frontiers*, **4**, 277-287.

Chatterjee, S. C. 1936: The Anorthosites of Bengal. *Calcutta University Press*, 46.

Chattopadhyay, N., Ray, S., Sanyal, S., Sengupta, P., 2016. Mineralogical, textural and chemical reconstitution of granitic rock in ductile shear zone: a study from a part of the South Purulia Shear Zone, West Bengal, India. *Ductile Shear Zones from micro-to macro-scales Wiley, Chichester*, pp 141–163.

Chaudhuri, T., Wan, Y., Mazumder, R., Ma, M., Liu, D., 2018. Evidence of enriched, Hadean mantle reservoir from 4.2-4.0 Ga zircon xenocrysts from Paleoarchean TTGs of the Singhbhum Craton, Eastern India. *Scientific Reports*, **8**, 7069.

Clarke, D. B., Reardon, N. C., Chatterjee, A. K., Gregoire, D. C. 1989. Tourmaline composition as a guide to mineral exploration; a reconnaissance study from Nova Scotia using discriminant function analysis. *Economic Geology*, **84**, 1921- 1935.

Codeço, M.S., Weis, P., Trumbull, R.B., Van Hinsberg, V., Pinto, F., Lecumberri- Sanchez, P., Schleicher, A.M., 2020. The imprint of hydrothermal fluids on trace-element element

contents in white mica and tourmaline from the Panasqueira W-Sn-Cu deposit, Portugal. *Mineralium Deposita*. <https://doi.org/10.1007/s00126-020-00984-8>.

De, S., Mallik, L., Mazumder, R., Chatterjee, P., Ohta, T., Saito, S., Chiarenzelli, J. 2016. Sedimentation history of the Paleoproterozoic Singhbhum Group of rocks, eastern India and its implications. *Earth Science Reviews*, **163**, 141-161. doi: 10.1016/j.earscirev.2016.10.001

De, S., Mazumder, R., Ohta, T., Hegner, E., Yamada, K., Chiarenzelli, J., Altermann, W., Bhattacharyya, T., Arima, M. 2015. Geochemistry and Nd isotopic characteristics of the Paleoproterozoic metasedimentary rocks of the Singhbhum craton and their implications for provenance, paleoclimate and paleo weathering. *Precambrian Research*, **256**, 62-78.

Deb, M., Tiwari, A., Palmer, M. R., 1997. Tourmaline in Proterozoic massive sulphide deposits from Rajasthan, India. *Mineralium Deposita*, **32**, 94–99.

Dey, S., Topno, A., Liu, Y., Zong, K.Q. 2017a. Generation and evolution of Palaeoarchaeon continental crust in the central part of the Singhbhum Craton, eastern India. *Precambrian Research*, **298**, 268–291.

Dey, A., Mukherjee, S., Sanyal, S., Ibanez-Mejia, M., Sengupta, P. 2017b. Provenance and timing of sedimentation from a suite of metapelites from the Chotanagpur Granite Gneissic Complex, India: implications for Proterozoic tectonics in the East-Central part of the Indian shield. In: Majumdar, R. (Ed.) Influences on Compositional Change from Source to Sink. *Sediment Provenance*, Amsterdam, 453–486.

Dietrich, R. V. 1985. The Tourmaline Group, 1st edition. *Van Nostrand Reinhold Company*, New York, 300.

Drivenes, K., Larsen, R. B., Müller, A., Sørensen, B. E., Wiedenbeck, M., Raanes, M. P. 2015. Late-magmatic immiscibility during batholith formation: assessment of B isotopes and trace elements in tourmaline from the Land's End granite, SW England. *Contributions to Mineralogy and Petrology*, **169**, 1–27.

Duan, Z., Møller, N., Weare, J. H. 1995. Equation of state for the NaCl-H<sub>2</sub>O-CO<sub>2</sub> system: prediction of phase equilibria and volumetric properties. *Geochimica et Cosmochimica Acta*, **59**, 2869–2882.

Dunn, J. A., Dey, A. K. 1942. The geology and petrology of eastern Singhbhum and surrounding areas. *Memoir, Geological Survey of India*, **69**, 281–450.

Dutta, U., Bhui, U. K., Sengupta, P., Sanyal, S., & Mukhopadhyay, D. 2011. Magmatic and metamorphic imprints in 2.9 Ga chromitites from the Sittampundi Layered Complex, Tamil Nadu, India. *Ore Geology Reviews*, **40**, 90–107.

Dutrow, B.L., Holdaway, M.J., and Hinton, R.W. 1986. Lithium in staurolite and its petrologic significance. *Contributions to Mineralogy and Petrology*, **94**, 496–506.

Dutrow, B. L., Foster, C. T., Jr., Henry, D. J. 1999. Tourmaline-rich pseudomorphs in sillimanite zone metapelites: Demarcation of an infiltration front. *American Mineralogist*, **84**, 794-805.

Dutrow, B. L., Henry, D. J. 2000. Complexly zoned fibrous tourmaline, Cruzeiro Mine, Minas Gerais, Brazil: A record of evolving magmatic and hydrothermal fluids. *The Canadian Mineralogist*, **38**, 131-143.

Fareeduddin, Gupta, S., Golani, P., R., Kirmani, I., R., Chander, S. 2010. Tourmaline as metallogenic Indicator: Examples from Paleo-Proterozoic Pb–Zn and Cu–Au deposits of Rajasthan. *Journal of Geological Society of India*, **76**, 215–243.

Fleet, A. J., 1984. Aqueous and sedimentary geochemistry of the rare earth elements. In: Henderson, P. (Ed.) *Rare Earth Elements Geochemistry*, Elsevier, Amsterdam, 343-373.

Flynn, R. T., Burnham, C. W. 1978. An experimental determination of rare earth partition coefficients between a chloride containing vapor phase and silicate melts. *Geochimica et Cosmochimica Acta*, **42**, 685-701.

Foit, F. F., Rosenberg, P. E. 1977. Coupled substitutions in the tourmaline group. *Contributions to Mineralogy and Petrology*, **62**, 109–127. <https://doi.org/10.1007/BF00372871>.

Ford, W. E., Dana, E. S. 1932. A textbook of mineralogy, Fourth Edition, *John Wiley and Sons, New York*, 851.

Gadas, P., Novák, M., Staněk, J., Filip, J., Galiová, M.V. 2012. Compositional evolution of zoned tourmaline crystals from pockets in common pegmatites of the Moldanubian Zone, Czech Republic. *Canadian Mineralogist*, **50**, 895-912.

Galbraith, C. G., Clarke, D. B., Trumbull, R. B., Wiedenbeck, M. 2009. Assessment of tourmaline compositions as an indicator of emerald mineralization at the Tsa da Glisza prospect, Yukon Territory, Canada. *Economic Geology*, **104**, 713.

Garda, G. M., Beljavskis, P., D'Agostino, L. Z. Wiedenbeck, M. 2010. Tourmaline and rutile as indicators of a magmatic–hydrothermal origin for tourmalinite layers in the São José do Barreiro area, NE Ribeira Belt, southern Brazil. *Geologia USP Série Científica, São Paulo*, **10**, 97-117.

Ghose, N. C. 1983. Geology, Tectonics and evolution of the Chhotanagpur Granite Gneiss Complex, Eastern India. In: Recent Researches in Geology. *Hindustan Publishing, New Delhi*, **10**, 211-247.

Ghose, N. C, Mall, A. P., Mukherjee, D., Singh, R. N. 1990. A tectono-magmatic evolution of granite types of Chhotanagpur Massif. *Bulletin Geology, Mineralogy, Metallurgical Society of India*, **56**, 14–15.

Ghosh, A. K. 1972. Trace element geochemistry and genesis of the copper ore deposits of the Singhbhum shear zone, Eastern India. *Mineralium Deposita*, **7**, 292–313.

Ghosh, D., Sarkar, S. N., Saha, A.K., Ray, S. L. 1996. New insights on the early Achaean crustal evolution in eastern India: re-evaluation of lead-lead, samarium-neodymium and rubidium-strontium geochronology. *Indian Minerals*, **50**, 175-188.

Ghosh, G., Mukhopadhyay, J. 2007. Reappraisal of the structure of the Western Iron Ore Group, Singhbhum Craton, eastern India: implications for the exploration of BIF-hosted iron ore deposits. *Gondwana Research*, **12**, 525–532.

Ghosh, S. K., Sengupta, S. 1987. Progressive development of structures in a ductile shear zone. *Journal of Structural Geology*, **9**, 277–287.

Ghosh, S. K., Sengupta, S. 1990. Singhbhum shear zone: structural transition and kinematic model. *Proceedings of the Indian Academy of Sciences (Earth and Planetary Sciences)*, **99**, 229–247.

Ghosh, S. K., Sengupta, S. 1999. Boudinage and composite boudinage in superposed deformations and syntectonic migmatization. *Journal of Structural Geology*, **21**, 97-110.

Ghosh, U., Upadhyay, D., Abhinay, K., Mishra, B. 2021. Nature of the mineralizing fluids in the Balda and Motiya W-prospects, western India: Constraints from chemical and B-isotope composition of tourmaline. *Chemical Geology*, **582**, 120439.

Ghosh Roy, A. K., Sengupta, P. R. 1993. Alkalic-carbonatitic magmatism and associated mineralization along the Tamar-Porapahar lineament in the Proterozoics of Purulia district, West Bengal. *Indian Journal of Earth Sciences*, **20**, 193-200.

Goswami, J. N., Mishra, S., Wiedenbeck, M., Ray, S. L., Saha, A. K. 1995.  $^{207}\text{Pb}/^{206}\text{Pb}$  ages from the OMG, the oldest recognized rock unit from Singhbhum-Orissa Iron Ore craton, Eastern India. *Current Science, Bangalore*, **69**, 1008-1012.

Griffin, W. L., Slack, J. F., Ramsden, A. R., Win, T. T., Ryan, C. G. 1996. Trace elements in tourmalines from massive sulfide deposits and tourmalinites: Geochemical controls and exploration applications. *Economic Geology*, **91**, 657-675.

Griffin, W. L., Powell, W. J., Pearson, N. J., O'Reilly, S. Y. 2008. GLITTER: data reduction software for laser ablation ICP-MS. In: Sylvester, P. (Ed.) *Laser Ablation-ICP-MS in the Earth Sciences: Current Practices and Outstanding Issues. Mineralogical Association of Canada*, **40**, 308-311.

Guidotti, C.V., Grew, E.S., Yates, M.G., Dyar, M.D., Francis, C.A., Fowler, G., Husler, J., Shearer, C.K., and Wiedenbeck, M. 2000. Lithium in coexisting micas and tourmaline from western Maine. *Geological Society of America Abstracts with Programs*, **32(7)**, A-53.

Gupta, A., Basu, A., Ghosh, P. K. 1980: The Proterozoic ultramafic and mafic lavas and tuffs of the Dalma greenstone belt, Singhbhum, Eastern India. *Canadian Journal of Earth Science*, **17**, 210–231.

Gupta, A., Basu, A. 1991. Evolutionary trend of the mafic-ultramafic volcanism in the Proterozoic North Singhbhum mobile belt. *Indian Minerals*, **45**, 273-288.

Gupta, A., Basu, A. 2000. North Singhbhum Proterozoic mobile belt, Eastern India-a review. *Geological Survey of India, Special Publication*, **55**, 195-226.

Gupta. S., Jayananda, M., Fareeduddin. 2014. Tourmaline from the Archean G.R.Halli gold deposit, Chitradurga greenstone belt, Dharwar craton (India): Implications for the gold metallogeny. *Geoscience Frontiers*, **5**, 877- 892.

Harris, N. B. W., Gravestock, P., Inger, S. 1992. Ion-microprobe determinations of Trace element concentrations in garnets from anatectic assemblages. *Chemical Geology*, **100**, 41–49.

Harlaux, M., Mercadier, J., Marignac, C., Villeneuve, J., Mouthier, B., Cuney, M., 2019. Origin of the atypical Puyles- Vignes W breccia pipe Massif Central., France. constrained by trace element and boron isotopic composition of tourmaline. *Ore Geology Reviews* ,**114**, 103132.

Hawthorne, F. C., Henry, D. J. 1999. Classification of minerals of the tourmaline group. *European Journal of Mineralogy*, **11**, 201-215.

Hazarika, P., Mishra, B., and Pruseth, K. L., 2015a. Diverse tourmaline compositions from orogenic gold deposits in the Hutti-Maski greenstone belt, India: implications for sources of ore-forming fluids. *Economic Geology*, **110**, 337–353.

Hazarika, P., Pruseth K. L., Mishra B., 2015b. Neoproterozoic greenstone metamorphism in the eastern Dharwar Craton, India: constraints from Monazite U-Th-Pb total ages and PT pseudosection calculations. *Journal of Geology*, **123**, 429–461.

Hazarika, P., Mishra, B., Pruseth, K. L., 2016. Scheelite, apatite, calcite and tourmaline compositions from the late Archean Hutti orogenic gold deposit: implications for analogous two stage ore fluids. *Ore Geology Reviews*. **72**, 989–1003.

Hazarika, P., Bhuyan N., Upadhyay, D., Abhinay, K., Singh, N.N., 2019. The nature and sources of ore-forming fluids in the Bhukia gold deposit, Western India: constraints from chemical and boron isotopic composition of tourmaline. *Lithos*, **350**, 105227.

Hazarika, P., Upadhyay, D., Mishra, B., Borah, B., Abhinay K. 2021. Modelling B-release and isotopic fractionation during metamorphic dehydration of basalt and pelite: Implications for the source of mineralizing fluid in greenstone-hosted orogenic gold deposits. *Geochimica et Cosmochimica Acta*, **304**, 83–100

Hellman, P.L., Smith, R.E., Henderson, P. 1979. The mobility of the rare earth elements: evidence and implications from selected terrains affected by burial metamorphism. *Contributions to Mineralogy and Petrology*, **71**, 23—44.

Henry, D. J., Guidotti, C. V. 1985. Tourmaline as a petrogenetic indicator mineral: an example from the staurolite-grade metapelites of NW Maine. *American Mineralogist*, **70**, 1-15.

Henry, D. J., Dutrow, B. L. 1996. Metamorphic tourmaline and its petrogenetic applications. In: Grew, E., Anovitz, L. M (Eds.) Boron: Mineralogy Petrology, and Geochemistry, *Reviews in Mineralogy and Geochemistry, Mineralogical Society of America*, Washington DC, **33**, 503-557.

Henry, D.J., Dutrow, B.L., and Selverstone, J. 2003. Compositional asymmetry in replacement tourmaline—an example from the Tauern Window, Eastern Alps. *American Mineralogist*, **88**, 1399.

Henry, D. J., Dutrow, B. L., Selverstone, J. 2002. Compositional polarity in replacement tourmaline – an example from the Tauern Window, Eastern Alps. *Geological Materials Research*, **4**, 1-18.

Henry, D. J., Dutrow, B. L. 2011. The incorporation of fluorine in tourmaline: internal crystallographic controls or external environmental influence? *Canadian Mineralogist*, **49**, 41-56.

Henry, D. J., Kirkland, B. L., Kirkland, D. W. 1999. Sector-zoned tourmaline from the cap rock of a salt dome. *European Journal of Mineralogy*, **11**, 263-280.

Henry, D. J., Dutrow, B. L., Selverstone, J. 2002. Compositional polarity in replacement tourmaline – an example from the Tauern Window, Eastern Alps. *Geological Materials Research*, **4**, 1-18.

Henry, D. J., de Brodtkorb, M. K. 2009. Mineral chemistry and chemical zoning in tourmalines, Pampa del Tamboreo, San Luis, Argentina. *Journal of South American Earth Sciences*, **28**, 132–141.

Henry, D. J., Novák, M., Hawthorne, F. C., Ertl, A., Dutrow, B. L., Uher, P., Pezzotta, F. 2011. Nomenclature of the tourmaline supergroup minerals. *American Mineralogist*, **96**, 895–913.

Hiiller, W., Gandhi, S., M. 1997. Origin of tourmaline and oxide minerals from the metamorphosed Rampura Agucha Zn-Pb-(Ag) deposit, Rajasthan, India. *Mineralogy and Petrology*, **60**, 99-119.

Holtz, F., Johannes, W 1991. Effect of tourmaline on melt fraction and composition of first melts in quartzofeldspathic gneiss. *European Journal of Mineralogy*, **3**, 527-536.

Iyengar, S. V. P., Murthy, Y. G. K. 1982. The evolution of the Archaean-Proterozoic crust in parts of Bihar and Orissa, Eastern India. *Records, Geological Survey of India*, **112**, 1–5.

Jiang, S. Y. 1998. Stable and radiogenic isotope studies of tourmaline: an overview. *Journal of the Czech Geological Society*, **43**, 75–90.

Jiang, S. Y, Han, F., Shen, J. Z., Palmer, M. R. 1999a. Chemical and Rb–Sr, Sm–Nd isotopic systematics of tourmaline from the Dachang Sn–polymetallic ore deposit, Guangxi Province, P.R. China. *Chemical Geology*, **157**, 49–67.

Jiang, S. Y., Palmer, M. R., Slack, J. F., Shaw, D. R. 1999b. Boron isotope systematics of tourmaline formation in the Sullivan Pb–Zn–Ag deposit, British Columbia, Canada. *Chemical Geology*, **158**, 131–144. [https://doi.org/10.1016/S0009-2541\(99\)00023-6](https://doi.org/10.1016/S0009-2541(99)00023-6)

Jiang, S. Y., Palmer, M. R., Christopher, J. Y. 2002. Chemical and boron isotopic compositions of tourmaline from the Archean Big Bell and Mount Gibson gold deposits, Murchison Province, Yilgarn Craton, Western Australia. *Chemical Geology*, **188**, 229–247.

Jiang, S. Y., Yu, J. M., Lu, J. J. 2004. Trace and rare-earth element geochemistry in tourmaline and cassiterite from the Yunlog tin deposit, Yunnan, China: implication for migmatite–hydrothermal fluid evolution and ore genesis. *Chemical Geology*, **209**, 193–213.

Jolliff, B. L., Papike, J. J. 1987. Mineral recorders of Pegmatite internal evolution: REE contents of Tourmaline from the Bob Ingersoll pegmatite, South Dakota. *Geochimica et Cosmochimica Acta*, **51**, 2225–2232.

Jowhar, T. N. 2010. Chemistry of Tourmalines from the Gangotri Granite, Garhwal Higher Himalaya. *Earth Science India*, **3**.

Kalliomäki, H., Wagner, T., Fusswinkel, T., Sakellaris, G. 2017. Major and trace element geochemistry of tourmalines from Archean orogenic gold deposits: Proxies for the origin of gold mineralizing fluids? *Ore Geology Reviews*, **91**, 906–927.

Klemme, S., Marschall, H. R., Jacob, D. E., Prowatke, S., Ludwig, T. 2011. Trace-element partitioning and boron isotope fractionation between white mica and tourmaline. *The Canadian Mineralogist*, **49**, 165–76.

Krienitz, M. S., Trumbull, R. B., Hellmann, A., Kolb, J., Meyer, F. M., Wiedenbeck, M. 2008. Hydrothermal gold mineralization at the Hira-Buddini gold mine, India: constraints on fluid evolution and fluid sources from boron isotopic compositions of tourmaline. *Mineralium Deposita*, **43**, 421–434.

Kretz, R. 1983. Symbols for rock-forming minerals. *American Mineralogist*, **68**, 277–279.

Krosse, S. 1995. Hochdrucksynthese, Stabilität und Eigenschaften der Borsilikate Dravit und Kornerupin, sowie Darstellung und Stabilitätsverhalten eines neuen Mg-Al-borates. Thesis, *Ruhr-Universität Bochum*.

Kumar, M. N., Das, N., Dasgupta, S. 1978. Geology and mineralisation along the Northern Shear Zone, Purulia District, West Bengal— an up-to-date appraisal. *Records, Geological Survey of India*, **133**, 25–31.

Lang, S. B. 1974. Sourcebook of Pyroelectricity (Ferroelectricity and Related Phenomena). *Gordon & Breach Science, London, U.K.*

Lang, S.B. 2005. Pyroelectricity: from ancient curiosity to modern imaging tool. *Physics Today*, **58**, 31-36.

Lecumberri-Sanchez, P., Vieira, R., Heinrich, C.A., Pinto, F., Walle, M., 2017. Fluid-rock interaction is decisive for the formation of tungsten deposits. *Geology* **45**, 579–582. <https://doi.org/10.1130/G38974.1>.

Leeman, W. P., Sisson, V. B. 1996. Geochemistry of boron and its implications for crustal and mantle processes. In: Grew, E. S., Anovitz, L. M. (Eds) Boron: Mineralogy, Petrology and Geochemistry. *Reviews in Mineralogy*, **33**, 645-707.

London, D., Hervig, R. L., Morgan, G. B., 1988. Melt-vapor solubilities and elemental partitioning in peraluminous granite–pegmatite systems: experimental results with Macusani glass at 200 MPa. *Contributions to Mineralogy and Petrology*, **99**, 360–373.

London, D., Morgan, G. B., Wolf, D. 1996. Boron in granitic rocks and their contact aureoles. In: Grew, E. S., Anovitz, L. M., (Eds.) Boron. Mineralogy, petrology and geochemistry. The Mineralogical Society of America, *Reviews in Mineralogy and Geochemistry*, Washington, DC, **33**, 299–330.

London, D. 2011. Experimental synthesis and stability of tourmaline: a historical overview. *Canadian Mineralogist*, **49**, 117–136.

MacLean, W.H., 1988. Rare earth element mobility at constant inter-REE ratios in the alteration zone at the Phelps Dodge massive sulfide deposit, Matagami, Quebec. *Mineralium Deposita*, **23**, 231-238.

Mahadevan, T. M. 1992a. Geological evolution of the Chhotanagpur Gneissic Complex in a part of Purulia district, West Bengal. *Indian Journal of Geology*, **64**, 1–22.

Mahadevan, T. M. 1992b. Geology of Bihar and Jharkhand. *Geological Survey of India*, Bangalore, 563.

Mahadevan, T. M. 2002. Text Book Series 14: Geology of Bihar and Jharkhand. *Geological Society of India*, **60**, 380-380.

Mahato, S., Goon, S., Bhattacharya, A., Mishra, B., Bernhardt, H. J. 2008. Thermotectonic evolution of the North Singhbhum Mobile Belt (Eastern India): a view from the western part of the belt. *Precambrian Research*, **162**, 102-127.

Maji, A. K., Goon, S., Bhattacharya, A., Mishra, B., Mahato, S., Bernhardt, H. J. 2008. Proterozoic polyphase metamorphism in the Chhotanagpur Gneissic Complex (India), and implication for trans-continental Gondwanaland correlation. *Precambrian Research*, **162**, 385–402.

Manning, C.E. 2006. Mobilizing aluminum in crustal and mantle fluids. *Journal of Geochemical Exploration*, **89**, 251–253.

Marks, M. A., Marschall, H. R., Schühle, P., Guth, A., Wenzel, T., Jacob, D. E., Markl, G. 2013. Trace element systematics of tourmaline in pegmatitic and hydrothermal systems from the Variscan Schwarzwald (Germany): the importance of major element composition, sector zoning, and fluid or melt composition. *Chemical Geology*, **344**, 73–90.

Marocchi, M., Marschall, H.R., Konzett, J., Tropper, P., Ludwig T., Mair, V., Bargossi, G. M. 2011. Metasomatic tourmaline in hybrid contact bands between gneiss and peridotite in the Ulten Zone (Eastern Italian Alps): geochemistry and boron isotopic composition determined by SIMS. *Canadian Mineralogist*, **49**, 245–261.

Marschall, H. R., Ludwig, T., Altherr, R., Kalt, A., Tonarini, S. 2006. Syros metasomatic tourmaline: evidence for very high-d11B fluids in subduction zones. *Journal of Petrology*, **47**, 1915–1942.

Marschall, H. R., Korsakov, A. V., Luvizotta, G. L., Nasdala, L., Ludwig, T. 2009. On the occurrence and boron isotopic composition of tourmaline in (ultra) highpressure metamorphic rocks. *Journal Geological Society of London*, **166**, 811-823.

Mazumder, R., Sarkar, S. 2004. Sedimentation history of the Palaeoproterozoic Dhanjori Formation, Singhbhum, India and its implications. *Precambrian Research*, **130**, 267-287.

Mazumder, R. 2005. Proterozoic sedimentation and volcanism in the Singhbhum crustal province, India and their implications. *Sedimentary Geology*, **176**, 167-193.

Mazumder, R., Van Loon, A. J. 2012. Depositional history of diamictites from the Late Paleoproterozoic Dalma Formation (E India). *Sedimentary Geology*, **251**, 49-57.

Mazumder, R., Eriksson, P. G., De, S., Bumby, A. J., Lenhardt, N. 2012a. Palaeoproterozoic sedimentation on the Singhbhum craton: global context and comparison with Kaapvaal. In: Mazumder, R., Saha, D. (Eds.) Palaeoproterozoic of India. *Geological Society of London, Special Publications*, **365**, 51-76. <http://dx.doi.org/10.1144/SP365.4>.

Mazumder, R., Van Loon, A. J., Mallik, L., Reddy, S. M., Arima, M., Altermann, W., Eriksson, P. G., De, S., 2012b. Mesoarchaeoan-Palaeoproterozoic stratigraphic record of the Singhbhum Crustal Province, Eastern India: a synthesis. In: Mazumder, R., Saha, D. (Eds.), Palaeoproterozoic of India. *Geological Society of London, Special Publications*, **365**, 31-49. <http://dx.doi.org/10.1144/SP365.3>.

Mazumder, S. K. 1988: Crustal evolution of the Chhotanagpur Gneissic Complex and the Mica belt of Bihar. In: Mukhopadhyay, D. (Ed.) Precambrian of the Eastern India Shield, *Memoir, Geological Society of India*, **8**, 49–83.

McDonough, W. F., Sun, S.S., 1995. The composition of the Earth. *Chemical Geology*, **120**, 223–253.

Medaris, L. G. Jr., Fournelle, J. H., and Henry, D. J. 2003. Tourmaline-bearing quartz veins in the Baraboo quartzite, Wisconsin: Occurrence and significance of Foitite and “Oxy-Foitite.” *The Canadian Mineralogist*, **41**, 749–758.

Mehra, S., Banerjee, D. K. 1974. A note on the occurrence of apatite near Beldih, Purulia District, West Bengal. *Indian Minerals*, **28**, 88–90.

Michard, A., Albarcde, F. 1986, The REE content of some hydrothermal fluids. *Chemical Geology*, **55**, 51-60.

Migdisov, A.A., Boukhalfa, H., Timofeev, A., Runde, W., Roback, R., Williams-Jones, A.E., 2018a. A spectroscopic study of uranyl speciation in chloride-bearing solutions at temperatures up to 250° C. *Geochimica et Cosmochimica Acta*, **222**, 130–145.

Miller, S.R., Mueller, P.A., Meert, J.G., Kamenov, G.D., Pivarunas, A.F., Sinha, A.K., Pandit, M.K., 2018. Detrital Zircons Reveal evidence of Hadean Crust in the Singhbhum Craton. India. *The Journal of Geology*, **126**, 541–552.

Mishra, B., Pal, N., Ghosh, S. 2003. Fluid evolution of the Mosabani and Rakha copper deposits, Singhbhum district, Jharkhand: evidence from fluid inclusion study of mineralized quartz veins. *Journal of the Geological Society of India*, **61**, 51–60.

Mishra, B., Singh, R. K. 2003. Fluid evolution of the Jaduguda U–Cu deposit, Jharkhand. *Indian Journal of Geology*, **75**, 191–202.

Mishra, K. J., Bhattacharjee, S., Reddy, M. S., Praveen, M. N., Bhimte, A. D., Mahanta, N. 2018. Geology and tectonic implications of tourmaline bearing leucogranite of Bastipadu, Kurnool, Andhra Pradesh. *Journal of Earth System Science*, **127**, 1-18.

Mishra, S., Deomurari, M. P., Wiedenbeck, M., Goswami, J. N., Ray, S., Saha, A. K. 1999. <sup>207</sup>Pb/<sup>206</sup>Pb zircon ages and the evolution of the Singhbhum Craton, eastern India: an ion microprobe study. *Precambrian Research*, **93**, 139-151.

Möller, P., Stober, I., Dulski, P., 1997. Seltenerdelement-, Yttrium-Gehalte und Bleiisotope in Thermal- und Mineralwässern des Schwarzwaldes. *Grundwasser*, **3**, 118–132.

Moore, P.B. and Araki, T. (1978) Dumortierite, Si<sub>3</sub>B[A<sub>16.75</sub>□<sub>0.25</sub>O<sub>17.25</sub>(OH)<sub>0.75</sub>]: A detailed structure analysis. *Neues Jahrbuch für Mineralogie Abhandlungen*, **132**, 231–241.

Moore, J. N., Christenson, B. W., Allis, R. G., Browne, P. R. L., Lutz, S. J. 2004. The mineralogical consequences and behavior of descending acid-sulfate waters: An example from the Karaha – Telaga Bodas geothermal system, Indonesia. *Canadian Mineralogist*, **42**, 1483-1499.

Morgan, G. B., London, D. 1989. Experimental reactions of amphibolite with boron-bearing aqueous fluids at 200 MPa: implications for tourmaline. *Contributions to Mineralogy and Petrology*, **102**, 281–297.

Mukherjee, S., Dey, A., Sanyal, S., Ibanez-Mejia, M., Dutta, U., Sengupta, P. 2017. Petrology and U–Pb geochronology of zircon in a suite of charnockitic gneisses from parts of the Chotanagpur Granite Gneiss Complex (CGGC): evidence for the reworking of a Mesoproterozoic basement during the formation of the Rodinia supercontinent. In: Pant, N. C., Dasgupta, S. (Eds.) *Crustal Evolution of India and Antarctica: The Supercontinent Connection*, *Geological Society of London, Special Publications*, **457**, 197–231.

Mukhopadhyay, D. 1976. Precambrian stratigraphy of Singhbhum - The problems and the prospect. *Indian Journal of Earth Science*, **3**, 208–219.

Mukhopadhyay, D. 1984. The Singhbhum shear zone and its place in the evolution of the Precambrian mobile belt of North Singhbhum. Proc. Seminar on Crustal Evolution of the Indian Shield and its bearing on Metallogeny. *Indian Journal of Earth Science*, 205–212.

Mukhopadhyay, D. 1988. Precambrian of the Eastern Indian Shield - Perspective and Problems. In: Mukhopadhyay, D. (Ed.) *Precambrian of the Eastern Indian Shield*. *Memoir, Geological Society of India*, **8**, 1-12.

Mukhopadhyay, D. 1990. Precambrian plate tectonics in the Eastern Indian shield. In: Sychantharong, S. P. H. (Ed.) *Crustal Evolution and Orogeny*, *Oxford and IBH Publishing Co.*, New Delhi, 75-100.

Mukhopadhyay, D. 2001. The Archaean Nucleus of Singhbhum: The present state of knowledge. *Gondwana Research*, **4**, 307-318.

Mukhopadhyay, D., Deb, G. 1995. Structural and textural development in Singhbhum shear zone, eastern India. *Proceedings of the Indian Academy of Sciences- Earth and Planetary Sciences*, **104**, 385–405.

Mukhopadhyay, J., Ghosh, G., Zimmermann, U., Guha, S., Mukherjee, T., 2012. A 3.51Ga bimodal volcanics-BIF-ultramafic succession from Singhbhum Craton: implications for Palaeoarchaeon geodynamic processes from the oldest greenstone succession of the Indian subcontinent. *Geological Journal*, **47**, 284-311.

Naha, K. 1965. Metamorphic in relation to stratigraphy, structures and movements in part of East Singhbhum, Eastern India. *The Quarterly Journal of the Geological, Mining, and Metallurgical Society of India*, **37**, 41-81.

Nakano, T., Nakamura, E. 2001. Boron isotope geochemistry of metasedimentary rocks and tourmalines in a subduction zone metamorphic suite. *Physics of Earth and Planetary Interiors*, **127**, 233–252.

Naqvi, S. M., Rogers, J. J. W. 1987, Precambrian Geology of India. *Oxford University Press, New York*, 223.

Nelson, D., Bhattacharya, H. N., Thern, E. R., Altermann, W. 2014. Geochemical and ion-microprobe U–Pb zircon constraints on the Archaean evolution of Singhbhum Craton, eastern India. *Precambrian Research*, **255**, 412–432.

Nelson, D. R., Bhattacharya, H. N., Misra, S., Dasgupta, N., Altermann, W. 2007. New SHRIMP U-Pb zircon dates from the Singhbhum craton, Jharkhand-Orissa region, India. Abstract. In: Banerjee, S. (Ed.) *Abstracts International Conference on Precambrian Sedimentation and Tectonics and 2<sup>nd</sup> Global Precambrian Sedimentation Syndicate Meeting*. Indian Institute of Technology, Bombay, **47**.

Nemec, D. 1969. Fluorine in tourmalines. *Contributions to Mineralogy and Petrology*, **20**, 235–243.

Novák, M., Škoda, R., Filip, J., Macek, I., Vaculovic, T. 2011. Compositional trends in tourmaline from intragranitic NYF pegmatites of the Trebíč pluton, Czech Republic: an electron microprobe, Mössbauer and LA–ICP–MS study. *Canadian Mineralogist*, **49**, 359–380.

Olierook, H.K.H., Clark, C., Reddy, S.M., Mazumder, R., Jourdan, F., Evans, N.J., 2019. Evolution of the Singhbhum Craton and supracrustal provinces from age, isotopic and chemical constraints. *Earth Science Reviews*. **193** (2019), 237–259.

Orlando, A., Ruggieri, G., Chiarantini, L., Montegrossi, G., Rimondi, V., 2017. Experimental investigation of biotite-rich schist reacting with B-bearing fluids at upper crustal conditions and correlated tourmaline formation. *Minerals*. **7**,155. <https://doi.org/10.3390/min7090155>.

Ota, T., Kobayashi, K., Katsura, T., Nakamura, E. 2008. Tourmaline breakdown in a pelitic system: implications for boron cycling through subduction zones. *Contributions to Mineralogy and Petrology*, **155**, 19-32.

Pal, D. C., Barton, M. D., Sarangi, A. K. 2009. Deciphering a multistage history affecting U-Cu (-Fe) mineralization in the Singhbhum Shear Zone, eastern India using pyrite textures and compositions in the Turamdih U-Cu (-Fe) deposit. *Mineralium Deposita*, **44**, 61–80.

Pal, D. C., Trumbull, R. B., Wiedenbeck, M. 2010. Chemical and boron isotope compositions of tourmaline from the Jaduguda U (-Cu-Fe) deposit, Singhbhum shear zone, India: Implications for the sources and evolution of mineralizing fluids: *Chemical Geology*, **277**, 245–260.

Pal, D. C., Rhede, D 2013. Geochemistry and chemical dating of uraninite in the Jaduguda Uranium Deposit, Singhbhum Shear Zone, India—Implications for uranium mineralization and geochemical evolution of uraninite. *Economic Geology*. **108**, 1499–1515.

Palmer, M. R., Swihart, G. H. 1996. Boron isotope geochemistry: an overview. In: Grew, E. S., Anovitz, L. M. (Eds), *Boron: Mineralogy, Petrology and Geochemistry Reviews in Mineralogy and Geochemistry* **33**, 709-744.

Patel, S., Upadhyay, D., Mishra, B., Abhinay, K., Sarangi, A.K., 2021. Multiple episodes of hydrothermal alteration and uranium mineralization in the Singhbhum Shear Zone, eastern India: constraints from chemical and boron isotope composition of tourmaline. *Lithos*, **106084**,388–389.

Pesquera, A., Torres-Ruiz, J., Gil-Crespo, P. P., Jiang, S. Y. 2005. Petrographic, chemical and B-isotopic insights into the origin of tourmaline-rich rocks and boron recycling in the

Martinamor Antiform (Central Iberian Zone, Salamanca, Spain). *Journal of Petrology*, **46**, 1013-1044.

Pirajno, F., Smithies, R. H. 1992. The FeO / (FeO + MgO) ratio of tourmaline: A useful indicator of spatial variations in granite-related hydrothermal mineral deposits. *Journal of Geochemical Exploration*, **42**, 371-381.

Plimer, I. R., Lu, J., Kleeman, J. D. 1991. Trace and rare earth elements in cassiterite - sources of components for the 1086 tin deposits of the Mole Granite, Australia. *Mineralium Deposita*, **26**, 267-274. <https://doi.org/10.1007/BF00191072>.

Pouchou, J. L. Pichoir, F. 1984. A new model for quantitative X-ray microanalysis, Part I: Application to the analysis of homogeneous samples. *Recherche Aerospatiale*, **3**, 13-36.

Pouchou, J. L. 1985. " PAP" procedure for improved quantitative analysis. *Microbiology Analysis*, **20**, 104-105.

Pyne, T. K. 1992. The Proterozoic fold belt and the Chotanagpur Gneissic Complex in the Eastern Indian Sheild- a tectonometamorphic appraisal. *Indian Minerals*, **46**, 25-34.

Raith, J.G., Riemer, N., Meisel, S.T. 2004. Boron metasomatism and behaviour of rare earth elements during formation of tourmaline rocks in the eastern Arunta Inlier, central Australia. *Contributions to Mineralogy and Petrology*, **147**, 91-109.

Rao, N. K., Rao, G. V. U. 1983, Uranium mineralization in Singhbhum shear zone, Bihar: IV. Origin and geological time frame: *Journal of the Geological Society of India*, **24**, 615-627.

Ray, K. K., Ghosh-Roy, A. K., Sengupta, S. 1996. Acid volcanic rocks between the Dalma volcanic belt and the Chhotanagpur Gneissic Complex, East Singhbhum and Purulia districts of Bihar and West Bengal. *Indian Mineralogist*, **50**, 1-8.

Ray, S., Biswas, S., Chakraborty, M., Sanyal, S., Sengupta, P. 2012. Mass transport during fennitization of granite at the contact of carbonatite at Beldihi, Purulia, West Bengal, In: Rao,

N. V. C., Rao, K. S. P. (Eds.) *Recent advances and future challenges on Geochemistry and Geophysics: the Indian scenario, National Seminar Abstract*, Banaras Hindu University, **114**.

Ray, S. 2016. Petrology of carbonatite and alkaline rocks from parts of the South Purulia Shear Zone, East Indian Shield and their tectonic significance. PhD Thesis, Jadavpur University.

Ray Barman, T. K., Bishui, P. K. 1994. Dating of Chotanagpur gneissic complex of eastern Indian Precambrian shield. *Record, Geological Survey of India*, **127**, 25–27.

Reddy, S. M., Clarke, C., Mazumder, R. 2009a. Temporal constraints on the evolution of the Singhbhum Crustal Province from U-Pb SHRIMP data. In: Saha, D., Mazumder, R. (Eds.), *Paleoproterozoic Supercontinents and Global Evolution. International Association for Gondwana Research Conference Series, Abstract*, **9**, 17-18.

Reddy, S. M., Evans, D. A. D. 2009b. Palaeoproterozoic supercontinents and global evolution: correlations from core to atmosphere. In: Reddy, S. M., Mazumder, R., Evans, D. A. D., Collins, A. (Eds.), *Paleoproterozoic Supercontinents and Global Evolution. Geological Society of London, Special Publication*, **323**, 1-26.

Robinson, G. D., Healey, K., Kelly, V. C. 1988. Use of tourmaline in stream sediments to detect submarine exhalative sulfide deposits: example from central Virginia, USA. *Applied Geochemistry*, **3**, 225-230.

Roda-Robles, E., Pesquera, A., Gil-Crespo, P. P., Torres-Ruiz, J. 2012. From granites to highly evolved pegmatites: a case study of the Pinilla de Femoselle granite-pegmatite system (Zamora, Spain). *Lithos*, **153**, 192–207.

Roy, A. K. 1966. Orogenic-Plutonic Characters of Bengal Anorthorites. *Geological Survey of India. Miscellaneous Publication*, **23**, 255-266.

Roy, A. K. 1977. Structural and metamorphic evolution of the Bengal anorthosite and associated rocks. *Journal of Geological Society of India*, **18**, 203-223.

Roy, A., Sarkar, A., Jeyakumar, S., Aggrawal, S. K., Ebihara, M., 2002a. Sm–Nd age and mantle characteristics of the Dhanjori volcanic rocks, Eastern India. *Geochemical Journal*, **36**, 503–518.

Roy, A., Sarkar, A., Jeyakumar, S., Aggrawal, S. K., Ebihara, M. 2002b. Mid-Proterozoic plume-related thermal event in eastern Indian craton: evidence from trace elements, REE geochemistry and Sr-Nd isotope systematics of basic-ultrabasic intrusives from Dalma volcanic belt. *Gondwana Research*, **5**, 133-146.

Rudnick, R. L., Gao, S. 2003. Composition of the continental crust. In: Turekian, K., Holland, H. (Eds), *Treatise on geochemistry, 2nd edition, Elsevier, Amsterdam*, 1–64.

Ruiz, J.T., Pesquera, A., Gil-Crespo, P., Velilla, N., 2003. Origin and petrogenetic implications of tourmaline-rich rocks in the Sierra Nevada (Betic Cordillera, southeastern Spain). *Chemical Geology*, **197**, 55– 86.

Rustemeyer, P. 2003. *Faszination Turmalin*. Spektrum Akademischer Verlag, *Heidelberg–Berlin*, 309.

Saha, A. K. 1972. Petrogenetic and structural evolution of the Singhbhum Granitic Complex, Eastern India. *Proceedings of the 24th International Geological Congress*, **2**, 147–155.

Saha, A. K. 1994. Crustal evolution of Singhbhum-North, Orissa, eastern India. *Memoir, Geological Society of India*, **27**, 341.

Saha, A. K., Ray, S. L. 1984. The structural and geochemical evolution of the Singhbhum Granite batholithic complex, India. *Tectonophysics*, **105**, 163-176.

Saha, A. K., Ray, S. L., Sarkar, S. N. 1988. Early history of the Earth: Evidence from the Eastern Indian Shield. In: Mukhopadhyay, D. (Ed.) *Precambrian of the Eastern Indian Shield. Memoir, Geological Society of India*, **8**, 13-37.

Saikia, A., Gogoi, B., Kaulina, T., Lialina, L., Bayanova, T. Ahmad, M. 2017. Geochemical and U – Pb zircon age characterization of granites of the Bathani Volcano Sedimentary sequence, Chotanagpur Granite Gneiss Complex, eastern India: vestiges of the Nuna supercontinent in the Central Indian Tectonic Zone. In: Pant, N. C., Dasgupta, S. (Eds.) *Crustal Evolution of India and Antarctica: The Supercontinent Connection. Geological Society of London, Special Publications*, **457**, 233-252.

Sanyal, S., Sengupta, P. 2012. Metamorphic evolution of the Chhotanagpur Granite Gneiss Complex of the East Indian Shield: current status. *Geological Society of London, Special Publications*, **365**, 117-145. <http://dx.doi.org/10.1144/SP365.7>.

Sarkar, S. C. 1984. Geology and Ore Mineralisation Along the Singhbhum Copper–Uranium Belt, Eastern India. Ph. D. thesis, *Jadavpur University, Calcutta*, 263.

Sarkar, S. C. 2000. Crustal evolution and metallogeny in the Eastern Indian craton. *Special Publication, Geological Survey of India*, **55**, 169-194.

Sarkar, S.C., Gupta, A. 2012. Crustal evolution and metallogeny in India. *Cambridge University Press, New York*, 741.

Sarkar, S. C., Gupta, A., Basu, A. 1992. North Singhbhum Proterozoic mobile belt, eastern India: Its character, evolution and metallogeny. In: Sarkar, S. C. (Ed.) *Metallogeny related to tectonics of Proterozoic mobile belt, Oxford and IBH Publishing, New Delhi*, 271-304.

Sarkar, S.N., Saha, A. K. 1962. A revision of the Precambrian stratigraphy and tectonics of Singhbhum and adjacent region. *Quarterly Journal of the Geological, Mineralogical and Metallurgical Society of India*, **34**, 97-136.

Sarkar, S. N., Saha, A. K. 1977. The present status of the Precambrian stratigraphy, tectonics and geochronology of Singhbhum-Keonjhar-Mayurbhanj region, Eastern India. *Indian Journal of Earth Science*, **Ray, S. volume**, 37–65.

Sarkar, S. N., Saha, A. K. 1983. Structure and tectonics of the Singhbhum-Orissa Iron Ore Craton, Eastern India. Recent researches in Geology. *Hindustan Publishing, New Delhi*, **10**, 1-25.

Sauerer, A., Troll, G., 1990. Abundance and distribution of boron in the Hauzenberg (Bavaria) granite complex. *Geochimica et Cosmochimica Acta*, **54**, 49-55.

Searle, M. P., Fryer, B. J. 1986. Garnet, tourmaline and muscovite-bearing leucogranites, gneisses and migmatites of the Higher Himalayas from Zaskar, Kulu, Lahoul and Kashmir. *Geological Society of London, Special Publication*, **19**, 185-201.

Sen, S. 1947. A note on the Magma-tectonics of the Porphyritic Granite around Anara, Manbhum. *Read before the Society*, December, 1947.

Sengupta, N., Mukhopadhyay, D., Sengupta, P., Hoffbauer, R. 2005. Tourmaline-bearing rocks in the Singhbhum shear zone, eastern India: evidence of boron infiltration during regional metamorphism. *American Mineralogist*, **90**, 1241–1255.

Sengupta, N., Sengupta, P., Sachan, H. K. 2011. Aluminous and alkali-deficient tourmaline from the Singhbhum Shear Zone, East Indian shield: Insight for polyphase boron infiltration during regional metamorphism. *American Mineralogist*, **96**, 752–767.

Sengupta, N., 2012. Stability of chloritoid + biotite-bearing assemblages in some metapelites from the Palaeoproterozoic Singhbhum Shear Zone, eastern India and their implications: *Geological Society, London-Special Publications*, **365**, 91–116.

Sengupta, S., Sarkar, G., Ghosh Roy, A. K., Bhaduri, S. K., Gupta, S. N., Mandal, A. 2000. Geochemistry and Rb-Sr Geochronology of acid tuffs from the northern fringe of the Singhbhum craton and their significance in the Precambrian evolution. *Indian Minerals*, **54**, 43-56.

Shannon, R. D. 1976. Revised effective ionic radii and systematic studies of interatomic distances in halides and chalcogenides. *Acta crystallographica section A: crystal physics, diffraction, theoretical and general crystallography*, **32**, 751–767

Sharma, R. S. 2009. Cratons and fold belts of India. *Lecture Notes in Earth Sciences*, **127**, 304.

Sharma, M., Basu, A. R., Ray, S. L. 1994. Sm-Nd isotopic and geochemical study of the Archaean tonalite-amphibolite association from the eastern Indian Craton. *Contributions to Mineralogy and Petrology*, **117**, 45–55.

Shibata, S. N., Tanaka, T., Yamamoto, K., 2006. Crystal structure control of the dissolution of rare earth elements in water–mineral interactions. *Geochemical Journal*, **40**, 437–446.

Sibson, R.H. 1992. Implications of fault-valve behavior for rupture nucleation and recurrence. *Tectonophysics*, **211**, 283–293.

Singh, S. P. 1997. Geochemistry of Acid volcanics of the Dalma Group, Singhbhum, Eastern India. *Journal of the Geological Society of India*, **49**, 437– 41.

Singh, S. P. 1998. Precambrian stratigraphy of Bihar. In: Paliwal, B. S. (Ed.). *The Indian Precambrian*. Scientific Publishers, Jodhpur, India, 376–408.

Singh, S. P., De, A. K. 1990. The Precambrian stratigraphic sequences in Chhotanagpur Province. *Bulletin of Geological Mineralogical Metallurgical Society of India*, **56**, 21–22.

Slack, J. F. 1982. Tourmaline in Appalachian-Caledonian massive sulphide deposits and its exploration significance. *Institution of Mining and Metallurgy Transactions Section B Applied Earth Science*, **91**, 81-89.

Slack, J. F. 1993. Models for tourmalinite formation in the Middle Proterozoic Belt and Purcell supergroups (Rocky Mountains) and their exploration significance. *Current Research, Geological Survey of Canada*, **93-1E**, 33–40.

Slack, J. F. 1996. Tourmaline associations with hydrothermal ore deposits. In: Boron mineralogy, petrology and geochemistry. *Reviews in Mineralogy*, 33.

Slack, J. F., Trumbull, R. B. 2011. Tourmaline as a recorder of ore-forming processes. *Elements*, **7**, 321–326.

Slack, J. F., Herriman, N., Barnes, R. G., Plimer, I. R. 1984. Stratiform tourmalinites in metamorphic terranes and their geologic significance. *Geology*, **12**, 713-716.

Slack, J. F., Palmer, M. R., Stevens, B. P. J., Barnes, R. G. 1993. Origin and significance of tourmaline-rich rocks in the Broken Hill District, Australia. *Economic Geology*, **88**, 505-541.

Sperlich, R. 1990. Zoning and Crystal Chemistry of Tourmalines in Prograde Metamorphic Sequences of the Central Alps. Ph.D. thesis, *University of Basel, Basel, Switzerland*.

Sperlich, R., Gieré, R., Frey, M. 1996. Evolution of compositional polarity and zoning in tourmaline during prograde metamorphism of sedimentary rocks in the Swiss Central Alps. *American Mineralogist*, **81**, 1222–1236.

Spicer, E. M., Stevens, G., Buick, I. S. 2004. The low-pressure partial-melting behaviour of natural boron-bearing metapelites from the Mt. Stafford area, central Australia. *Contributions to Mineralogy and Petrology*, **148**, 160-179.

Sverjensky, D. A. 1984. Europium redox equilibria in aqueous solution. *Earth and Planetary Science Letters*, **67**, 70-78.

Tait, J., Zimmermann, U., Miyazaki, T., Presnyakov, S., Chang, Q., Mukhopadhyay, J., Sergeev, S. 2011. Possible juvenile Palaeoarchean TTG magmatism in eastern India and its constraints for the evolution of the Singhbhum Craton. *Geological Magazine*, **148**, 340–347.

Talapatra, A. K. 1968. Sulfide mineralization associated with migmatization in the south-eastern part of the Singhbhum shear zone, Bihar, India. *Economic Geology*, **63**, 156–165.

Talukdar, M., Chattopadhyay, N., Sanyal, S. 2012. Shear controlled Fe-mineralization from parts of South Purulia Shear Zone. *Journal of Applied Geochemistry*, **14**, 496–508.

Talukdar, M., Sanyal, S., & Sengupta, P. 2017. Metasomatic alteration of chromite from parts of the Late Archaean Sittampundi Layered Magmatic Complex (SLC), Tamil Nadu, India. *Ore Geology Reviews*, **90**, 148–165.

Torres-Ruiz, J., Pesquera, A., Gil-Crespo, P. P., Velilla, N. 2003. Origin and petrogenetic implications of tourmaline-rich rocks in the Sierra Nevada (Betic Cordillera, southeastern Spain). *Chemical Geology*, **197**, 55-86.

Torres-Roldan, R. L., Garcia-Casco, A., & Garcia-Sanchez, P. A. 2000. C Space: an integrated workplace for the graphical and algebraic analysis of phase assemblages on 32-bit Wintel platforms. *Computers & Geosciences*, **26(7)**, 779-793.

Upadhyay, D., Chattopadhyay, S., Kooijman, E., Mezger, K., Berndt, J. 2014. Magmatic and metamorphic history of Paleoproterozoic tonalite-trondhjemite-granodiorite (TTG) suites from the Singhbhum Craton, eastern India. *Precambrian Research*, **252**, 180–190.

Vapnik, Y., Bushmin, S., Chattopadhyay, A., Dolivo-Dobrovolsky, D. 2007. Fluid inclusion and mineralogical study of vein-type apatite ores in shear zones from the Singhbhum metallogenic province, West Bengal, India. *Ore Geology Reviews*, **32**, 412-430.

Van den Bleeken, G., Corteel, C., and Van den haute, P. 2007. Epigenetic to low-grade tourmaline in the Gdoutmont metaconglomerates (Belgium): A sensitive probe of its chemical environment of formation. *Lithos*, **95**, 165–176.

van Hinsberg, V. J. 2011. Preliminary experimental data on trace-element partitioning between tourmaline and silicate melts. *The Canadian Mineralogist*, **49**, 153– 163.

van Hinsberg, V. J., Marschall, H. R. 2007. Boron isotope and light element sector zoning in tourmaline: implications for the formation of B-isotopic signatures. *Chemical Geology*, **238**, 141–148.

van Hinsberg, V. J., Schumacher, J. C. 2007a. Using estimated thermodynamic properties to model accessory phases: The case of tourmaline. *Journal of Metamorphic Geology*, **25**, 769-779.

van Hinsberg, V. J., Schumacher, J. C. 2007b. Intersector element partitioning in tourmaline; a potentially powerful single-crystal thermometer. *Contributions to Mineralogy and Petrology*, **153**, 289-301.

van Hinsberg, V. J., Henry, D. J., Marschall, H. R. 2011a. Tourmaline; an ideal indicator of its host environment. *The Canadian Mineralogist*, **49**, 1-16.

van Hinsberg, V. J., Henry, D. J., Dutrow, B. L. 2011b. Tourmaline as a petrologic forensic mineral: a unique recorder of its geologic past. *Elements*, **7**, 327–32.

van Hinsberg, V. J., Schumacher, J. C., Kearns, S., Mason, P. R. D., Franz, G. 2006. Hourglass sector zoning in metamorphic tourmaline and resultant major and trace-element fractionation. *American Mineralogist*, **91**, 717- 728.

Vernon, R. H. 2004. A practical guide to rock microstructure. *Cambridge university press*, Cambridge, UK.

Voll, G. 1969. Klastische Mineralien aus den Sedimentserien der Schottischen Highlands und ihr Schicksal bei aufsteigender Regional- und Kontaktmetamorphose. Habilitations These, *Technische Universität Berlin*, Germany.

von Goerne, G., Franz, G., Wirth, R. 1999. Hydrothermal synthesis of large dravite crystals by the chamber method. *European Journal of Mineralogy*, **11**, 1061–1077.

von Goerne, G., Franz, G., van Hinsberg, V. J. 2011. Experimental determination of Na–Ca distribution between tourmaline and fluid in the system  $\text{CaO–Na}_2\text{O–MgO–Al}_2\text{O}_3\text{–SiO}_2\text{–B}_2\text{O}_3\text{–H}_2\text{O}$ . *Canadian Mineralogist*, **49**, 137–152.

Ward, C. D., McArthur, J. M., Walsh, J. N. 1992. Rare-earth element behaviour during evolution and alteration of the Dartmoor Granite, SW England. *Journal of Petrology*, **33**, 785–815.

Whitford, D. J., Korsch, M. J., Porritt, P. M., Craven, S. J., 1988. Rare earth element mobility around the volcanogenic polymetallic massive sulfide deposit at Que River, Tasmania, Australia. *Chemical Geology*, **68**, 105-119.

Winter, J. D. 2001. An introduction to Igneous and Metamorphic Petrology. *Prentice-Hall Inc.*, New Jersey.

Wolf, M. B., London, D. 1997. Boron in granitic magmas: stability of tourmaline in equilibrium with biotite and cordierite. *Contributions to Mineralogy and Petrology*, **130**, 12-30.

Xavier, R. P., Wiedenbeck, M., Trumbull, R. B., Dreher, A. M., Monteiro, L. V. S., Rhede, D., de Araújo, C. E. G., Torresi, I. 2008. Tourmaline B-isotopes fingerprint marine evaporites as the source of high-salinity ore fluids in iron oxide copper-gold deposits, Carajás Mineral Province (Brazil). *Geology*, **36**, 743- 746.

Yang, S. Y., Jiang, S. Y., Zhao, K. D., Dai, B. Z., Yang, T. 2015. Tourmaline as a recorder of magmatic–hydrothermal evolution: an in situ major and trace element analysis of tourmaline from the Qitianling batholith, South China. *Contributions to Mineralogy and Petrology*, **170**, 1–21.

Yavuz, F., Iskenderoglu, A., Jiang, S. Y. 1999. Tourmaline compositions from the Salikvan porphyry Cu–Mo deposit and vicinity, Northeastern Turkey. *Canadian Mineralogist*, **37**, 1007–1023.

Yavuz, F., Jiang, S. Y., Karakaya, N., Karakaya, M. C., Yavuz, R. 2011. Trace-element, rare-earth element and boron isotopic compositions of tourmaline from a veintype Pb–Zn–Cu ± U deposit, NE Turkey. *International Geological Reviews*, **53**, 1–24.

Zajacz, Z., Halter, W.E., Pettke, T., Guillong, M., 2008. Determination of fluid/melt partitioning coefficients by LA-ICPMS analysis of co-existing fluid and silicate melt inclusions: controls on element partitioning. *Geochimica et Cosmochimica Acta*, **72**, 2169–2197.

## **APPENDIX I: Analytical procedures**

### **Chemical Composition of Minerals: Electron Probe Micro Analyser (EPMA)**

Chemical compositions of the minerals were determined from carbon-coated thin sections by electron microprobe analysis (EMPA) with a CAMECA SX100 electron microprobe at the Central Petrological Laboratory, Geological Survey of India, Kolkata. The accelerating voltage used was 15 kV with a 12 nA current. Elements were analysed using natural standards were used for calibrations which included orthoclase (for K and Si), jadeite (Na), wollastonite (Ca), hematite (Fe), corundum (Al), rhodonite (Mn), apatite (P), barite (Ba), chromite (Cr) and sphalerite (Zn), except for Mn and Ti for which synthetic standards were used. The raw data were processed using the PAP procedure (Pouchou and Pichoir 1984). Beam diameters were varied from 1 to 3  $\mu\text{m}$ , with an accelerating voltage of 15 kV and a 12 nA beam current, several points were analyzed both under broad beam (10  $\mu\text{m}$ ) and narrow beam (1  $\mu\text{m}$ ), but no significant difference was observed. At least three analyses were done from each colour domain of a tourmaline grain, and at least five grains were measured from each sample.

Some minerals are analysed with CAMECA SX Five electron probe micro analyser (EPMA) at Department of Central Research Facility in ISM, Dhanbad. The instrument was operated with 15kV accelerating voltage, 1–2  $\mu\text{m}$  beam diameter and 15 nA current. Standards used for calibration were synthetic for Mn and Ti. Natural mineral standards were used to calibrate other elements (Si, Al, Cr, Fe, Zn etc.). Raw analyses were corrected by using PAP (Pouchou and Pichoir 1984)) method.

### **LA-ICPMS trace element measurement protocol**

Trace elements in minerals were measured in-situ using Laser Ablation-Inductively Coupled Plasma Mass spectrometry (LA-ICP-MS) at the Department of Geology and Geophysics, Indian Institute of Technology (IIT), Kharagpur. The analyses were done using a Cetac 213 nm Nd YAG laser ablation system coupled to a Varian 820 quadrupole ICP-MS. The ablation was done at 10 Hz pulse frequency, 50  $\mu\text{m}$  spot size and 730 V energy. Analyses were performed in peak hopping mode with each analysis consisting of a 20 s

background measurement with the laser turned off and 40 s peak signal measurement with the laser turned on. Calibration was done using NIST 612 glass and data were reduced using the Glitter© software (Griffin et al. 2008).

## **APPENDIX II: Normalization of tourmaline and associated minerals**

The complete tourmaline chemical composition cannot be obtained from EPMA analysis because (1) Li, H, B and O cannot be measured; and (2) it cannot differentiate the Fe valance state. Li content is insignificant in the analysed tourmaline grain because tourmaline compositions containing Mg >0.02 apfu typically has an insignificant amount of lithium in their structure (Henry and Dutrow 1996). In my study area all the tourmaline bearing assemblages contain a good amount of muscovite. Muscovite is strong sink of Li, preferentially fractionated into muscovite relative to Fe-Mg tourmaline (Dutrow et al. 1986; Guidotti et al. 2000; Medaris et al. 2003; Henry et al. 2003). Thus, all the analysed tourmaline are Li poor. The tourmaline compositions were normalized sum of T + Z + Y cations to 15 cations, assuming T-, Z-, and Y-sites are completely filled (i.e., no vacancies in these sites). This cation normalization procedure of tourmaline has the advantage of being independent of B, OH, O and the oxidation state of Fe in tourmaline (Henry and Dutrow, 1996). The amount of B<sub>2</sub>O<sub>3</sub> wt% is calculated from stoichiometric constraints to produce three B cations in the structural formula. In my study area tourmaline does not contain significant amount of Fe<sup>3+</sup> in their structure cause Fe<sup>3+</sup> bearing oxide mineral are not associated with tourmaline. Total Fe is expressed as FeO<sub>total</sub>. The sum of the cation-charges in the X + Y + Z + T sites exceeds 49 for most of the tourmaline compositions (Medaris et al. 2003; Torres-Ruiz et al. 2003). Si rarely exceeds 6 apfu (Van den Bleeken et al. 2007). This procedure of tourmaline normalization in several natural occurrences confirm these assumptions (Henry and Dutrow 1996; Hawthorne and Henry 1999; Henry et al. 2002, Henry et al. 2003).

Muscovite, biotite and pyrophyllite analyses were recalculated on the basis of 11 oxygen atoms. Plagioclase feldspar and K- feldspar analysis were recalculated on the basis of 8 oxygen atoms. Chlorite compositions were recalculated on 28 oxygen basis. Kyanite analysis were recalculated on 5 oxygen basis. Ilmenite compositions were recalculated on 3 oxygen basis. Rutile compositions were recalculated on 2 oxygen basis. Dumortierite compositions were calculated on the basis of 16.125 oxygens assuming one B and 0.75 OH per formula unit (after Moore and Araki,1978).

## APPENDIX III: C-Space programme

The computer programme C-Space is used in this study which is published by Torres-Roldan et al., 2000, to model the different reaction texture by the singular value decomposition (SVD) method of matrix operation. Singular value decomposition (SVD) is a simple but robust technique with minimal numerical errors that is widely used by the geoscientists for modelling different reaction texture.

If “m” and “n” represent the rows and columns of a given matrix, then A set of linearly independent relations will be as follows:

$$a_{11}X_1 + a_{12}X_2 + a_{13}X_3 + \dots + a_{1n}X_n = Y_1$$

$$a_{21}X_1 + a_{22}X_2 + a_{23}X_3 + \dots + a_{2n}X_n = Y_2$$

$$a_{31}X_1 + a_{32}X_2 + a_{33}X_3 + \dots + a_{3n}X_n = Y_3$$

.....

$$a_{m1}X_1 + a_{m2}X_2 + a_{m3}X_3 + \dots + a_{mn}X_n = Y_m$$

These equations can be expressed in the following matrix form :

$$A.X=Y \dots (1)$$

where, A,X and Y are as follows:

$$\begin{pmatrix} a_{11} & a_{12} & a_{13} \dots \dots \dots a_{1n} \\ a_{21} & a_{22} & a_{23} \dots \dots \dots a_{2n} \\ a_{31} & a_{32} & a_{33} \dots \dots \dots a_{3n} \\ \dots & \dots & \dots & \dots \\ a_{m1} & a_{m2} & a_{m3} \dots \dots \dots a_{mn} \end{pmatrix} = A \quad \begin{pmatrix} X_1 \\ X_2 \\ X_3 \\ \dots \\ X_m \end{pmatrix} = X \quad \begin{pmatrix} Y_1 \\ Y_2 \\ Y_3 \\ \dots \\ Y_m \end{pmatrix} = Y$$

Various techniques such as Gauss-Jordan elimination, the SVD etc are used to solve equation (1). Among the above techniques, the SVD is prominent method as it minimizes numerical errors and also provides solutions in cases where other methods.

From the SVD technique, an  $m \times n$  matrix  $A$  ( $m$ =number of rows,  $n$ =number of columns), where  $m \geq n$ , expressed as

$$A=U.W.V \dots(2)$$

where,

$U = m \times n$  column orthogonal matrix,

$W = n \times n$  diagonal matrix with positive or zero elements,

$V =$  transpose of an  $n \times n$  orthogonal matrix.

Therefore, from equation (1) and (2) it can be expressed as:

$$U.V.W.X = Y \dots(3)$$

The above equation can be re-written in the form:

$$W.z = d \dots(4)$$

where,

$$z = V^T . X,$$

$$d = U^T . Y$$

Thus the equation (4) may be solved to get the values of the unknowns  $X_1$  to  $X_n$ .

In geological problems, “ $m$ ” signifies the number of minerals and/or chemical phases and “ $n$ ” is the number of system components in terms of which composition of these minerals or phases can be expressed. These are used to generate an  $m \times n$  matrix as in  $A$  of equation (1). As described above, the SVD technique is applied to solve this matrix using equation (4).

From the SVD method it will generate all possible balanced chemical reactions involving a given set of mineral compositions or chemical species. Out of the possible balanced reactions, those that explain the textural relations are chosen. The chosen reactions must have predicted reactants and products on opposite sides and observed proportions of the phases match closely for the given assemblage.

## APPENDIX IV: List of abbreviations used

List of abbreviations for the mineral names mainly follows the list published by Kretz (1983) with recommendations by the IUGS sub-commission on the Systematics of Metamorphic Rocks (SCMR). Some mineral abbreviations are not included in the Kretz, 1983. The unlisted minerals (Kretz, 1983) are also presented which are used in this context. The abbreviations used are as follows:

<b>Mineral</b>	<b>Abbreviation</b>
Tourmaline	Tur
Muscovite	Mus
Biotite	Bt
Chlorite	Chl
Microcline	Mc
K-Feldspar	Kfs
Plagioclase feldspar	Pl
Feldspar	Fsp
Ilmenite	Ilm
Rutile	Rt
Kyanite	Ky
Dumortierite	Dum
Pyrophyllite	Pyro
Goethite	Goe
Albite	Ab
Quartz	Qtz